Mathematical Modeling and Analysis of Nanofluid Blood Flow Through Different Arteries Under Physiological Conditions

THESIS

Submitted in partial fulfilment of the requirements for the degree of

DOCTOR OF PHILOSOPHY

by

UMESH KHANDURI

(2019PHXF0070P)

Under the Supervision of

PROF. BHUPENDRA KUMAR SHARMA

BITS Pilani

Pilani | Dubai | Goa | Hyderabad | Mumbai

BIRLA INSTITUTE OF TECHNOLOGY AND SCIENCE, PILANI

2024

BIRLA INSTITUTE OF TECHNOLOGY & SCIENCE, PILANI

CERTIFICATE

This is to certify that the thesis titled **"Mathematical Modeling and Analysis of Nanofluid Blood Flow Through Different Arteries Under Physiological Conditions"** submitted by **Mr. Umesh Khanduri**, ID No. **2019PHXF0070P** for the award of Ph.D. of the institute embodies original work done by him under my supervision.

_____

Signature of the Supervisor
Name: **DR. BHUPENDRA KUMAR SHARMA**
Designation: **Professor**

Date: **20- 03- 2024**

Dedicated to

My Beloved Parents

And

All My Respected Teachers

Acknowledgements

Foremost, I express my gratitude to the Almighty for his blessings and love. I am privileged and pleased to acknowledge the contributions of numerous individuals who have been a great source of inspiration and support throughout my endeavors. They have endowed me with invaluable knowledge, paving the way for my success. The influence of these people is evident in my work, and for that, I am profoundly thankful.

I extend my heartfelt gratitude to Prof. Bhupendra Kumar Sharma, my esteemed supervisor, for his unwavering support during my Ph.D. studies and related research endeavors. I am profoundly indebted to him for his remarkable patience, constant motivation, and profound knowledge. His expert guidance proved invaluable throughout the entirety of my research journey, including the process of crafting this thesis. Throughout my Ph.D. tenure, Prof. Sharma has consistently been approachable and eager to assist, providing valuable direction, insightful suggestions, and dedicating extensive hours to discuss and review the intricate aspects of my work. His enduring belief in my abilities and relentless encouragement have inspired me to persevere, work diligently, and attain my academic goals. I am truly fortunate to have had such an exceptional advisor and mentor guiding my Ph.D. studies.

I wish to extend our sincere gratitude to my DAC members, Prof. Ashish Tiwari and Prof. Sangita Yadav. Their invaluable comments and suggestions throughout this period have greatly influenced the quality of my thesis work. Whenever I reached out to them, they exhibited exceptional humility and kindness, patiently addressing my doubts and clarifying them despite their busy schedules.

I express my profound gratitude to Prof. Devendra Kumar, the Head of the Mathematics Department, for graciously providing me with the essential resources for this research endeavor. I am sincerely thankful to the Department of Mathematics at BITS Pilani for granting me the opportunity and necessary facilities to conduct this investigation. Additionally, I extend my appreciation to SRCD and AGSRD for their invaluable support throughout this research process. I sincerely acknowledge the financial support provided by CSIR New Delhi, during the tenure of my doctoral research work.

I would like to acknowledge my deepest sense of gratitude to my parents Sh.Vijay Prasad Khanduri and Smt. Rajani Khanduri for their unconditional love, blessings and being with me in every aspect of my life. I would like to express my gratitude to my uncle, Sh. Jagdish Khanduri, and my aunt, Smt. Geeta Khanduri, as well as my brothers Kamlesh, Abhishek, and Akhilesh Khanduri, my sister-in-law Sonam, and my beloved sister Pooja, who have

consistently supported me through life's ups and downs. Finally, I extend my thanks to my PhD friends Sanjiv, Riya, Gourav, Amit, Shipra, Anshu, Ashvini, Yogesh, Ankit, my seniors Kapil, Chandan, Sajan, Sughanda, my colleague and junior Rishu, Anup, and Richa for the support and motivational strength they provided during this PhD journey. They have been like a small family, always there throughout this beautiful journey.

Place: BITS Pilani
Date: March 2024

Umesh Khanduri
(Department of Mathematics)

Abstract

This thesis delves into the mathematical modelling and solution of fluid flow issues concerning Newtonian and non-Newtonian fluids. The primary objective is to explore the hemodynamic properties of blood flow in stenosed arteries. The research aims to discern hemodynamic patterns in arteries with diverse shapes, taking into account the variable viscosity of blood and the characteristics of nanoparticles to replicate the realistic nature of blood flow. Additionally, this thesis investigates the two-phase nature of blood flow within arteries affected by different stenosis types. The problems addressed in this study hold potential applications in analyzing blood flow through arteries impacted by various pathological conditions, including stenosis, thrombosis, and aneurysms. The thesis comprises eight chapters, and a detailed summary of each chapter is provided:

The first chapter concisely outlines the key concepts in bio-fluid dynamics, blood rheology, physical parameters, numerical methodologies, and research gaps.

In the second chapter, an examination is carried out on magnetohydrodynamic (MHD) blood flow within a catheterized artery under pathological conditions, including multi-stenosis and thrombosis. The study treats blood as the base fluid and forms a hybrid nano-blood suspension by suspending Au and GO nanoparticles. A comprehensive hemodynamic mathematical model is developed to accurately simulate blood flow within the artery, accounting for various factors such as Joule heating, thermal radiation, Hall, and ion slip effects. The model also takes into consideration the influence of nanoparticle shape and variable viscosity based on hematocrit levels. By employing a curvilinear coordinate system and assuming mild stenosis, the study derives closed-form solutions. These reduced governing equations are effectively solved using the Crank-Nicolson scheme, enabling a detailed visualization of the impact of relevant parameters on flow patterns.

In the third chapter, an entropy generation analysis has been conducted on the flow of an electrically conductive fluid (blood) containing Al_2O_3-suspended nanoparticles through an irregular stenosed artery with thrombosis in the presence of a catheter. The fluid flow is influenced by various physical phenomena, including electroosmosis, radiation, Joule heating, and a uniform radial magnetic field. Different shapes and sizes of nanoparticles are considered using the Crocine model. The velocity, temperature, and concentration distributions are calculated using the Crank-Nicolson method within the framework of the Debye-Huckel linearization approximation.

In the fourth chapter, the influence of electroosmotic blood flow is explored in an Al_2O_3-Cu/Blood hybrid nanofluid containing gyrotactic microorganisms passing through a bifurcated artery. The overlapping stenosis in the parent artery and irregular stenosis in the daughter artery are taken into account. The flow experiences the effects of a uniform magnetic field, viscous dissipation, heat source, and electroosmotic force. The governing equations are normalized and transformed into a non-dimensional form, with a coordinate transformation applied to regularize the irregular boundaries. The resulting system of equations is solved utilizing the Crank–Nicolson method.

In the fifth chapter, an investigation is conducted on the flow characteristics and entropy analysis within a bifurcated artery system afflicted by pathological conditions. Specifically, aneurysm and stenosis are considered in the parent and daughter arteries, respectively. The governing equations are non-dimensionalized, and a coordinate transformation is applied to regularize the irregular boundaries. The Crank-Nicolson scheme models blood flow in the presence of a ternary hybrid nanofluid (Au-CuO-GO/Blood) within the arterial domain. The research sheds light on the intricate interplay involving stenosis, magnetohydrodynamic (MHD) flow, aneurysms, Joule heating, and the ternary hybrid nanofluid, providing valuable insights into these complex phenomena.

The sixth chapter presents an investigation into the two-phase nanofluid flow of blood through a stenosed artery influenced by magnetohydrodynamics. The study employs a two-phase fluid model, where the core region is modelled as a Power-law fluid and the plasma region as a Newtonian fluid. Furthermore, the analysis incorporates thermophoresis, Brownian motion, and activation energy. The primary focus of this research lies in exploring the potential of utilizing Al_2O_3 nanoparticles suspended in the blood as carriers for drug delivery due to their biocompatible and chemically stable properties. The governing equations, developed under the mild stenosis assumption, are solved using the Method of Lines approach, a versatile numerical methodology known for its precision and adaptability in addressing complex partial differential equations. This methodology serves as a valuable tool for the academic and scientific community.

In the seventh chapter, the effectiveness of targeted drug delivery mechanisms in the context of unsteady blood flow is investigated by introducing the infusion of Fe_3O_4 magnetic nanoparticles into a stenosed artery. This study utilizes a two-phase mathematical model, incorporating a power law fluid model for the core region and a Newtonian model for the plasma regions. Various crucial parameters are systematically examined, including Hall and ion effects, radiation, and viscous dissipation, to assess their impact on the diseased arterial segment. The governing equations are discretized and solved using the Method of Lines (MOL) approach, which transforms spatial and time variables into coupled ordinary

differential equations (ODEs) in the time domain.

At the conclusion of this comprehensive study, the summarized findings of the thesis and the potential avenues for future research are presented in the eighth chapter.

Contents

List of Figures

List of Tables

List of Symbols

^{nf}	Nanofluid
r	Radial direction
z	Axial direction
t	Time
$R_1(z)$	Radius of stenosis in core region
$R(z)$	Radius of stenosis in plasma region
R_0	Radius of the blood vessel without stenosis
L	Length of the blood vessel
d	Location of stenosis
R_c	Radius of curvature of curved artery
u_c, v_c, w_c	velocities of core region in r, θ, z directions, respectively
u_p, v_p, w_p	velocities of plasma region in r, θ, z directions, respectively
u, v, w	Velocities in curvilinear and cylindrical geometry
p_c, p_p	Pressures in core and plasma region, respectively
T_c, T_p	Temperature in core and plasma region, respectively
C_c, C_p	Concentration in core and plasma region, respectively
Gr	Thermal Grashof number
Gc	Solute Grashof number
M	Magnetic field
Nr	Thermal radiation parameter
$\tilde{Q}$	Heat source
h_m	Hematocrit level
κ_c, κ_p	Thermal conductivity in core and plasma region, respectively
$\tilde{C}_c, \tilde{C}_p$	Specific heat in core and plasma region, respectively
Re	Reynold number
Ec	Eckert number
Pr	Prandtl number
Br	Brinkman number

k_0	Thermal conductivity ratio
D_c, D_p	Mass diffusivity in core and plasma region, respectively
Sc	Schmidt number
Da	Darcy number (Permeability parameter)
Q^f	Volumetric flow rate
Nu	Nusselt number
E_g	Entropy generation
$\mathbf{J}$	Electric current density
β_e	Hall parameter
β_i	Ion parameter
U_{hs}	Helmholtz-Smoluchowski velocity
q	Electro-kinetic width (inverse Debye length)
$\mathbf{E}$	Electric field

Greeks letters

θ	Angular direction
δ^*, δ_1^*	Maximum height of stenosis
σ_c	Maximum height of clot
$\bar{\beta}$	Ratio of central core radius to normal artery radius
ω	Angular frequency of the forced oscillation
μ_c, μ_p	Viscosity in core and plasma region, respectively
ρ_c, ρ_p	Density in core and plasma region, respectively
ξ	Chemical reaction parameter
λ	Frictional resistance (impedance)
τ_w	Wall shear stress
ρ_0	Density ratio
μ_0	Viscosity ratio
σ	Electrical conductivity of fluid
Φ	Electro-osmotic potential
η_1	Bifurcation angle

Physical Parameters

Values of parameters		
Parameters	Values	Resources
Magnetic field strenght (M)	0.1-6.0	[1, 2]
Viscosity ratio (μ_0)	0.5-1	[3, 4]
Density ratio (ρ_0)	1.05	[4, 5]
Thermal Grashof number (Gr)	0-2	[6]
Steady pressure gradient (P_0)	1-10	[7, 8]
Curvature parameter (ε)	0-0.4	[9]
Activation energy parameter (E_a)	0.08-1.8	[1, 10]
Hematocrit parameter (h_m)	0-1	[11, 12]
Schmidth Number (Sc)	0.5-1.5	[7]
Heat source parameter (Q)	0-1	[13, 14]
Thermophoresis parameter (N_t)	0.1-0.8	[15, 16]
Brownian parameter (N_b)	0.1-0.8	[10, 15]
Solute Grashof number (Gc)	1-6	[7, 17]
Weissenberg number (We)	1.5-3.5	[18]

Table 1: Range of values of existing parameters with their resources

Chapter 1

Introduction

Biofluid mechanics is a captivating interdisciplinary field that combines fluid dynamics and biology principles to understand the fluid behaviour within biological systems. In the human body, fluids such as blood, cerebrospinal fluid and lymph play a crucial role in the physiological process, and the study of biofluid mechanics explains the forces' interaction between the fluid and biological tissues. The application of fluid dynamics in biological systems has significantly advanced medicine and bioengineering. The study of different factors like shear stress, pressure distribution and flow patterns within the cardiovascular system led scientists and researchers to gain insight into the functioning of the organs, the progression of diseases and the designing of medical devices. In the human body, the physiological circulation of biological fluid plays a pivotal role in sustaining life. The cardiovascular system, comprising three fundamental components—the heart, blood, and blood vessels—forms an intricate network that efficiently distributes oxygen, nutrients, hormones, and waste products throughout the body. This vital process is indispensable for the survival of every cell and organ, as it provides the essential substances necessary for energy production, growth, repair, and the elimination of waste.

1.1 Cardiovascular System

1.1.1 Heart

At the core of this system lies the heart, a hollow muscular organ serving as the central hub of the circulatory system. Its primary function is to tirelessly pump blood to all body parts through an extensive network of blood vessels. The heart generates electrical impulses that orchestrate its muscles' precise contraction and relaxation. This synchronization ensures a consistent heartbeat that adjusts according to the body's requirements, reflecting the remarkable precision of the cardiovascular system. Starting in the body tissues, the deoxygenated blood laden with waste enters the heart's right atrium. From here, it is propelled to the

right ventricle and then into the pulmonary artery, where it is transported to the lungs to release carbon dioxide and absorb life-giving oxygen. This oxygenated blood is transported from the lungs to the left atrium via the pulmonary artery and, subsequently, the left ventricle. Through powerful contraction, the heart expels this oxygenated blood into the aorta, commencing a journey that disseminates life-sustaining vitality to every corner of the body.

1.1.2 Blood and Its Components

Blood, the essential fluid flowing through the human body, is a remarkable and crucial element that profoundly contributes to sustaining health and balance. The heart pumps this bodily fluid to all parts of the body. The three major functions of blood are transportation, protection and regulation. Blood, the life-sustaining fluid that flows throughout our bodies, is a remarkable combination of cells, proteins, and other chemicals that support numerous biological activities. Blood protects the body from pathological diseases and kills microorganisms with the help of antibodies and other proteins. Additionally, blood has the property to coagulate itself to form a clot to prevent blood loss in situations like operations, accidents or injuries. Blood also regulates its pH value by interacting with various acids and bases to maintain the optimum heat and fluid essential for our body's functioning.

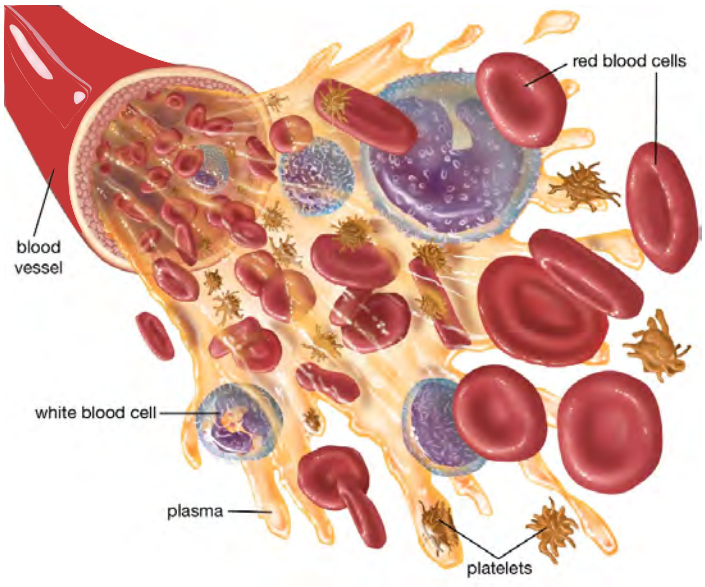

Figure 1.1: Blood and its constitutes

At its most fundamental level, blood comprises two primary constituents: formed elements and plasma. Plasma, a yellowish fluid present in blood, serves as the conduit for

transporting cells and various chemicals. It facilitates the circulation of vital nutrients, hormones, electrolytes, and waste products, ensuring an uninterrupted flow of essential substances required by the body. In a typical circulatory system, formed elements account for about 45% of the blood's composition, while plasma constitutes the remaining 55%, all within a total blood volume of 2.7-3.0 litres. The formed element of blood consists of cells and platelets (thrombocytes). At its core, blood consists of several key components, with each distinctive functioning. Red blood cells, or erythrocytes, dominate the bloodstream and transport oxygen from the lungs to tissues throughout the body. Their rich iron content gives blood its characteristic red colour and facilitates oxygen binding and release. White blood cells, or leukocytes, represent another vital component. They play a pivotal role in combating foreign substances within the body, contributing to the body's immune response and defence mechanisms.

1.1.3 Blood Vessels

Arteries serve as robust and resilient channels within the circulatory system, carrying oxygenated blood away from the heart to every part of the body. These vessels exhibit remarkable strength and flexibility, designed to withstand the powerful force exerted by the heart as it propels blood under high pressure. Arteries further divide into smaller vessels known as arterioles, all possessing muscular walls capable of adjusting their diameter to regulate blood flow in specific body areas. Conversely, blood from the body travels through capillaries to venules, which are tiny veins, and then into larger veins before returning to the heart. Unlike arteries, veins are crucial in transporting oxygen-depleted blood back to the heart for reoxygenation and recirculation. Veins can be distinguished from arteries by their thinner walls, lower pressure, and often appear blue or green due to the deoxygenated blood they carry. This intricate network ensures the continuous flow of blood, supporting various bodily functions and maintaining the delicate balance required for optimal health.

1.2 Fundamental Concept of Fluid Dynamics

The fundamental definition of a fluid asserts that it continuously deforms under the influence of tangential or shear stress, regardless of how minute the applied stress may be. Fluid dynamics, a sub-discipline of fluid mechanics, elucidates the behaviour of fluids and the forces acting upon them. Solids and fluids exhibit distinct behaviours when subjected to external forces. Unlike solids, where molecules are densely packed, fluid molecules are more loosely arranged. When shear stress is applied to a solid body, it breaks completely or

undergoes a specific angular deformation (say η). In contrast, in the case of fluids, there is no fixed η even for an infinitesimally small shear stress.

1.2.1 Continumm Hypothesis

A fluid or any substance in the matter comprises numerous minute particles in constant motion, undergoing continuous collisions. In principle, it is possible to study matter at the microscopic or discrete scales, as applied in kinetic theory or statistical mechanisms. This perspective, examining matter, is referred to as the microscopic viewpoint, wherein the primary emphasis is placed on the averaged behaviour of individual molecules within the substance. In general, our focus is observing the overall manifestation of molecular motion or the macroscopic behaviour of the fluid. In a macroscopic view, fluid behaviour is considered to conform to the continuum hypothesis when the Knudsen number, denoted as $(Kn = \frac{\lambda}{L})$ and calculated as the dimensionless ratio of the molecular mean free path (λ), representing the average distance travelled by a molecule between collisions, to a characteristic length scale (L) pertinent to the system, falls within the range of 0 to 0.01. This hypothesis essentially posits that the fluid is continuous and homogeneous. The continuum hypothesis allows the fluid to be treated as continuous or homogenous, meaning that its properties, such as density, velocity, and pressure, vary continuously from one point to another within the fluid. Consequently, this continuum assumption permits the utilization of differential equations and mathematical models to elucidate and anticipate fluid behaviour. Importantly, these models are formulated without needing to account for individual molecules' discrete, particle-based nature.

1.2.2 Blood Rheology

Blood rheology constitutes a crucial field of study in understanding blood flow, deformation behaviour, and its constituents under different physiological circumstances. The distinctive rheological properties of blood bear substantial implications for cardiovascular health, as any deviations in blood viscosity can significantly impact blood circulation, potentially leading to conditions such as thrombosis, atherosclerosis, and hypertension. Thus, it is necessary to understand the blood nature. The nature of the blood as a fluid is described below:

1.2.3 Newtonian Fluid

Viscosity is an intrinsic property of a fluid that quantifies the internal resistance encountered by its molecules as they undergo relative motion. According to Newton's hypothesis, a Newtonian fluid is characterized by a linear relationship between shearing stress and the

strain rate, with the proportionality constant designated as viscosity.

$$\tau = \mu \left(\frac{\partial u}{\partial y} \right), \tag{1.1}$$

where τ, μ, and $\frac{\partial u}{\partial y}$ are shear stress, viscosity and the velocity gradient, respectively. The blood depicts the Newtonian nature when it flows through the larger diameter arteries ($>$ 1mm) at, the higher shear rates (about 100/sec).

1.2.4 Non-Newtonian Fluid

Non-Newtonian fluids are a class of fluids that do not obey the linear relationship between the shear stress and strain rate, characteristic of Newtonian fluids. The fluid's viscosity is given by μ, which is treated as apparent viscosity. Non-Newtonian fluids exhibit varying viscosity under different conditions, making their flow behaviour more complex and diverse.

Some of the non-Newtonian fluid models to depict the blood characteristics are listed:

1.2.4.1 Power-Law Fluid

The mathematical model for the power law model is given as follows:

$$\frac{\tau}{\left(\frac{\partial u}{\partial y} \right)} = m \left(\frac{\partial u}{\partial y} \right)^{n-1}, \tag{1.2}$$

where, m and n represent the flow consistency and behaviour index, respectively.

- If $n < 1$, the fluid demonstrates shear-thinning behaviour, characterized as a pseudo-plastic fluid. In this case, the apparent viscosity decreases as the shear rate increases.

- If $n = 1$, the fluid becomes the Newtonian fluid.

- If $n > 1$, the fluid exhibits the shear thickening property and is known as dilant fluid, in which the apparent viscosity increases with enhancement in the shear rate.

1.2.4.2 Casson Fluid

The rheological equation of state for incompressible flow in the context of the Casson fluid model is expressed as follows:

$$\tau_{ij}^* = \begin{cases} 2\left(\mu_b^* + \frac{p_y^*}{\sqrt{2\pi^*}}\right)e_{ij}^*, & \pi^* > \pi_c^*, \\ 2\left(\mu_b^* + \frac{p_y^*}{\sqrt{2\pi_c^*}}\right)e_{ij}^*, & \pi^* \leq \pi_c^*, \end{cases} \tag{1.3}$$

where $\pi^* = e_{ij}^*.e_{ij}^*$ represent the multiplication of the deformation rate with itself , μ_b^* signifies the viscosity of the non-Newtonian fluid, p_y^* represents the yield stress of the fluid, and π_c^* denotes a critical value derived from the non-Newtonian model.
Equation (1.3) converted to the following form when $\pi^* \leq \pi_c^*$:

$$\tau_{ij}^* = 2\mu_b^*\left(1 + \frac{1}{\beta_1}\right)e_{ij}^*, \tag{1.4}$$

where $\beta_1 = \frac{\mu_b^*\sqrt{2\pi_c^*}}{p_y^*}$ denotes the Casson fluid parameter.

The nine quantities of rate strain components $e_{ij}^*(i, j = r, \theta, z)$ may be arranged as follows:

$$e^* = \begin{bmatrix} e_{rr}^* & e_{r\theta}^* & e_{rz}^* \\ e_{\theta r}^* & e_{\theta\theta}^* & e_{\theta z}^* \\ e_{zr}^* & e_{z\theta}^* & e_{zz}^* \end{bmatrix} \tag{1.5}$$

Similarly the stress comonents $\tau_{ij}^*(i, j = r, \theta, z)$ may be arranged as follows:

$$\tau^* = \begin{bmatrix} \tau_{rr}^* & \tau_{r\theta}^* & \tau_{rz}^* \\ \tau_{\theta r}^* & \tau_{\theta\theta}^* & \tau_{\theta z}^* \\ \tau_{zr}^* & \tau_{z\theta}^* & \tau_{zz}^* \end{bmatrix} \tag{1.6}$$

1.3 Mathematical Modeling

Mathematical modelling constitutes a precise method for describing real-world phenomena in the language of mathematics. These models are constructed based on a foundation of knowledge about the system and can be categorized as (i) Experimental, (ii) Theoretical, or (iii) a combination of both experimental and theoretical approaches. The relationships among the quantities employed in these models reflect essential phenomena relevant to the

intended purposes and are expected to hold true under diverse circumstances. A comprehensive comprehension of physiological systems empowers researchers to formulate mathematical models, enabling predictions about the system's behaviour under specific assumptions, utilizing carefully formulated concepts and data. Given biological organs' irregular and intricate shapes, explaining them accurately through mathematical means is challenging. In such instances, specific mathematical assumptions become necessary, guided by the inherent nature of the problem and justified within the research context.

1.3.1 Governing Equations of Fluid Dynamics

1.3.1.1 Continuity Equation or Conservation of Mass

The principle of the conservation of mass postulates that mass cannot be generated nor obliterated within an enclosed system. The aggregate mass within such a closed system remains constant over time. This concept is expressed mathematically through the equation of continuity, which asserts that the augmentation of mass within a closed surface is equivalent to the net mass flows into or out of that system.

$$\frac{\partial \rho}{\partial t} + \nabla \cdot (\rho \mathbf{V}) = 0, \tag{1.7}$$

where, $\rho, \mathbf{V} = (u, v, w)$ and ∇ are the density of the fluid, velocity vector and vector differential operator, respectively.

1.3.1.2 Conservation of Momentum

Every fluid particle at rest or in motion obeys Newton's second law of motion, which states that the time rate of change of momentum equals the external forces. The movement of the fluid is explained by the Navier-stokes equations, which are derived from the principle of Newton's second law of motion. The mathematical equation in the vector notation is written as:

$$\rho \left(\frac{\partial \mathbf{V}}{\partial t} + (\mathbf{V} \cdot \nabla)\mathbf{V} \right) = -\nabla p + \mu \nabla^2 \mathbf{V} + \rho F, \tag{1.8}$$

where, $\nabla p, F$ and ∇^2 are pressure gradient, external forces and Laplacian operator, respectively.

1.3.1.3 Conservation of Energy

The principle of energy conservation is a fundamental idea that the total energy within a closed system remains constant if no external work is applied to the system and no losses

occur due to friction, viscous dissipation, or other dissipative phenomena. It asserts mechanically that the rate of change of fluid energy inside a given volume V is equal to the negative outward flow of energy plus the work performed by different forces such as body forces, surface forces, thermal conduction, and chemical processes, if applicable. The following is the mathematical depiction of energy conservation for an incompressible fluid:

$$\rho C_p \left(\frac{\partial T}{\partial t} + (T \cdot \nabla) T \right) = \kappa \nabla^2 T + \frac{\partial Q}{\partial t}. \tag{1.9}$$

1.3.1.4 Conservation of Concentrated Species

Mass transfer is an essential phenomenon that is crucial for the transportation of mass from one location to another. It serves as a fundamental cornerstone within the domain of transport phenomena. When the principle of mass conservation is applied to a fluid with variable density, particularly when the fluid consists of two or more distinct fluids, it becomes necessary to extend this principle to the discrete constituents of the mixture. This extension allows for the application of mass transfer theory to compute the mass flux within the system and the distribution of species across both temporal and spatial dimensions within the system. The mathematical expression for the law of concentration conservation is expressed as follows:

$$\frac{\partial C}{\partial t} + (C \cdot \nabla) C = D_B \nabla^2 C + R_c, \tag{1.10}$$

where C, D_B and R_c represent the concentrations of components in the mixture, molecular diffusivity, and the chemical reaction parameter, respectively.

1.4 Dimensionless Parameter

Dimensionless parameters, also known as dimensionless numbers, represent physical quantities that illustrate the relationships among various variables used within a system. Unlike regular physical quantities, these parameters lack specific units. Scientists and engineers find them invaluable as they enable comparisons across different phenomena, eliminating the need to consider specific measurement units. Consequently, several dimensionless parameters exist to assist in rescaling problems as necessary. In this discussion, we will provide a brief overview of some of these parameters:

1.4.1 Reynolds Number (Re)

The Reynolds number, a dimensionless quantity, is defined as the ratio of inertial to viscous forces. This parameter is instrumental in predicting the flow regime, differentiating

between laminar and turbulent flows. In cases of low Reynolds numbers, the flow exhibits a laminar nature, where viscous forces prevail. Conversely, the flow becomes turbulent at higher Reynolds numbers, indicating the dominance of inertial forces. Mathematically, the Reynolds number is defined as follows:

$$Re = \frac{\text{inertial forces}}{\text{viscous forces}} = \frac{\rho v d}{\mu}, \tag{1.11}$$

where, v is the fluid velocity, d is the charaacteristic lenght, ρ and μ represents the fluid density and viscosity, respectivley.

1.4.2 Prandtl Number (Pr)

The Prandtl number is a dimensionless parameter that quantifies the relationship between a fluid's momentum and thermal diffusivity. It is mathematically represented as:

$$Pr = \frac{\mu C_p}{\kappa}. \tag{1.12}$$

In this equation, C_p represents the specific heat capacity at constant pressure, and κ denotes the thermal conductivity of the fluid.

1.4.3 Brinkmann Number

The Brinkmann number signifies the correlation between heat transferred through molecular conduction and the heat generated by viscous dissipation. It operates such that a higher Brinkmann number elevates the fluid temperature due to heat generation from viscous dissipation, as described by the equation:

$$Br = \frac{\mu v^2}{\kappa(T_w - T_0)}, \tag{1.13}$$

where T_w and T_0 represent the temperatures at the walls and the bulk temperature of the fluid, respectively.

1.4.4 Nusselt Number

The Nusselt number is a dimensionless parameter employed in heat transfer analysis to quantify the relationship between convective and conductive heat transfer within a boundary layer. Studying the Nusselt number holds significant value for researchers and scientists, providing insights into the blood flow patterns that directly impact heat transfer within blood

vessels.

$$Nu = \frac{h}{\kappa/L} = \frac{hL}{\kappa}, \tag{1.14}$$

where, h is the convective heat transfer coefficient.

1.4.5 Sherwood Number

Sherwood number is analogous to Nusselt number and is defined as the ratio of the mass transfer from convection to mass transfer by diffusion. This parameter holds significant relevance in biological contexts, elucidating the mass exchange between fluid and solid surfaces, which is crucial for studying the transportation phenomena of nutrients and other substances across biological membranes.

$$Sh = \frac{h}{D_B/L} = \frac{hL}{D_B}, \tag{1.15}$$

where, h is the convective mass transfer coefficient and D_B is the mass diffusivity.

1.5 Pathological Condtions

1.5.1 Cardiovascular Disease (CVD)

Cardiovascular disease (CVD) is a major public health concern due to its high morbidity and mortality rates [19]. This rates upshots in both developed and developing countries due to obesity and poor lifestyle. CVD encompasses a wide range of disorders, including cardiac muscle and vascular system diseases. It is widely recognised that arterial pathologies arise due to the degradation mechanisms involving cholesterol, lipoproteins, and diverse chemical components. These processes predominantly occur at the curvatures or bifurcation points of the arterial wall. Many researchers pointed out that hemodynamic factors play a significant role in the formation and progression of these diseases. Walsh and McLachlan [20] explained that stenosis and thrombosis result from vascular injury and inflammation. The clot develops due to internal damage to the arterial lumen, and additional clot formation results in stenosis or emboli. The shear stress and hemodynamic parameters affecting stenosis and thrombosis were investigated by Strony et al. [21]. They found that the shape of stenosis had a significant impact on platelet activation and thrombosis development in a diseased artery. Tanveer et al. [22] investigated the MHD (magneto hydrodynamics) Jeffery nanofluid in curved channel with convective boundary conditions. Ahmed and Nadeem [23] analysed the shape effect of copper nanoparticles through curved stenosed artery. The study conducted by Shahzadi and Kousar [24] focused on the development of a mathematical model

for analysing the behaviour of a bifurcated stenosed artery, with particular emphasis on incorporating slip effects into the model. The research findings indicated that the angle of bifurcation played a significant role in improving the distribution of shear stress within the main artery. Conversely, the daughter artery exhibited a contrasting pattern, with a decrease in shear stress as the bifurcation angle increased.

1.5.2 Magnetohydrodynamic (MHD)

MHD (magnetohydrodynamic) is a mathematical-physical framework encompassing a broad spectrum of physical phenomena, from liquid metal to space plasma. When a conductor moves into a magnetic field, the magnetic field is disturbed, resulting in an induced electric current. As a result, this action produces an internal magnetic field in the conductor that resists the external magnetic field. Conversely, when the magnetic field encourages the conductor to move in and out, the magnetic field is amplified. Reddy et al. (2016) interlinked the study of MHD and nanofluid on the boundary layer problem. They examined the effect of different shapes and size parameters of nanofluid on the boundary layer problem by considering the viscosity and conductivity as the function of the volume fraction of nanoparticles. Changdar and De [25] evaluated the discrete model on irregularly shaped stenosis artery to investigate the effect of gold nanoparticles on MHD blood flow. MHD blood flow was examined by Alghamdi et al. [26] using two parallel channels that resembled the microcirculatory system. They employed Cu/blood and Cu-Cuo/blood hybrid nanofluid that can be used for drug delivery in medical procedures. Sharma et al. [27] took into account MHD two-phase blood flow by looking at the core and plasma regions. They discovered that wall permeability and curvature increase the likelihood of atherosclerosis development, but heat source reduces it. Kumawat et al. [28] further extended the study by examining the entropy generation on the MHD two-phase blood with heat and mass transfer.

1.5.3 Electrokinetics

Electrokinetics refers to the phenomenon wherein particles are propelled in response to electrical potential differences. Electroosmosis is an electrokinetic phenomenon that arises from applying an external electric field to a charged surface. The flow of an electrically conductive fluid within the blood vessels establishes a net charge at the vessel walls. This, in turn, leads to the development of an opposite charge due to the principle of electro-neutrality within the electrical double layer in close proximity to the walls. The investigation conducted by Mekheimer et al. [29] focused on analysing the impact of electroosmotic and bifurcation effects on the hemodynamic flow in a bifurcated artery with stenosis along the

parent artery. Hybrid nanofluid flow through a diseased artery with aneurysmal and stenosed segments at the walls was discussed by Abdelsalam et al. [30]. The study's findings indicate a correlation between the nanoparticles shape factor and the fluid velocity profile. The study suggests that this information can be applied to improve drug delivery systems. Akhtar et al. [31] elucidated the electroosmotic modulated flow through an artery with multiple stenoses. The dependence of trapping symmetry on the symmetry of multiple stenoses and regulating fluid velocity, temperature, and velocity through electro-osmosis are notable findings in this study. In their research, Akram et al. [32] compared the Tiwari-Das model and the modified Buongiorno model to investigate the electroosmotic nanofluid flow under peristaltic pumping. In their study, Khanduri et al. [33] conducted a sensitivity analysis on the MHD fluid flow through a curved artery with stenosis at the wall and thrombosis at the catheter. The WSS profile exhibits a negatively correlated with the Debye-Huckel parameter and Hartmann number, whereas the impedance profile displays an opposite trend. The EMHD micropolar fluid was analysed by Manchi and Ponalagusamy [34] in the context of a bifurcated artery, taking into account the effects of Joule heating and body acceleration. The topic of discussion by Zaher et al. [35] pertained to the flow of non-Newtonian fluid with microorganisms in the presence of electroosmotic flow within the boundary layer. In non-Darcian fluid, the velocity is observed to be lower when compared to that of Darcian fluid.

1.5.4 Nanoparticles

Nanoparticles are microscopic particles with diameters ranging from 1 to 100 nanometers. These nanoparticles can be split into two categories. The first one is those made out of organic molecules such as liposomes, dendrites, etc. The second one is linked to inorganic molecules like metals and metal oxides. Nanofluids are the suspension of the nano-sized particles like liposomes, metals, nitrides, etc with the base fluid. This way it increases the thermal conductivity and heat transfer rate of the nanofluids as compared to the base fluid. By reengeering the nanoparticles properties, nanofluid can be used in any kind of diseases. Due to its small size, high efficacy, and higher thermal conductivity several researchers are paying more attention to it. Lee and Choi [36] were the first one to introduced the new class of engineered fluid and coined it as nanofluids. The impact of copper (Cu) nanoparticles with water as the base fluid on a stenosis artery with a permeable wall was studied by Akbar and Butt [37]. They discovered that pure water had a higher velocity than Cu-water due to the presence of Cu, which makes the arteries more flexible. Ahmed and Nadeem [23] investigated the effect of different shapes of Cu nanoparticles on the catheterized stenosis artery, such as bricks, cylinders, and platelets. They investigated the nanofluid's velocity,

impedance, and wall shear stress distribution using the perturbation approximation method with the variant curvature parameter. Shahzad et al. [38] developed a mathematical model to study the effect of entropy generation on the stenosis artery with permeable walls having single-wall and multiple-wall carbon nanotubes inside the blood (base fluid). Gandhi et al. [39] considered the bell-shaped artery to explore the effect of hybrid nanoparticles (Au-Al_2O_3) on the blood flow subject to temperature-dependent viscosity. Further, Sharma et al. [40] explored the entropy analysis on the MHD slip flow with tapered multiple-stenosis artery.

1.5.5 Entropy

In the biological system, metabolism is the central process, providing the energy needed to sustain life. The heat transfer and energy losses are incurred in this process causing the disorders (entropy). The entropy generation is associated with the thermodynamic irreversibility process that is associated with the second law of thermodynamics. The mitigation or reduction of the energy losses is desirable and one of the focus area in bio-inspired engineering system. The entropy generation is classified in two physical framework: reversible and irreversible process. The reversible process are those where change of entropy is zero and non-zero change in entropy signifies the irreversible process. Although, all the processes that occurs in nature are irreversible. Several factors associated in the biological process for production of entropy such as (viscosity) fluid friction, exposure to radiation and magnetic field (associated with iron particle present in hemoglobin molecule), electric field (associated with ions), etc. Bejan [41] pioneered the entropy analysis by studying the four fundamental way of heat conductive process. According to their study the thermal efficiency of the system can be optimized by reducing the overall entropy. Moreover, they concluded that the viscous dissipation and heat transfer were the crucial one for entropy generation in the system. Aoki [42] investigated the human body's entropy production at the basal conditions and calculated using the energetic data obtained from the respiration calorimeter. They determined that the impacts of the forced air current and clothes did not influence entropy creation. It's conceivable that there are physiological systems that can keep the body's entropy production at constant levels. For the analysis of entropy production utilising a ferromagnetic nanofluid, Akbar and Butt [43] employed the mathematical model of composite stenosis arteries with permeable walls. Gandhi et al. [44] took into account the various nanoparticle shapes effect on the multi-stenosed artery exposed to heat radiation to conduct their entropy study. Further theoretical investigation of the MHD two-phase across a permeable curved artery with varying viscosity and radiation was reported by

Kumawat et al. [28]. They found that arterial wall permeability and curvature are the most critical risk factors for atherosclerosis.

1.5.6 Two-Phase Blood Flow

Blood flow shows various features; one of its basic characteristics is the volume content of erythrocytes in the blood (hematocrit level). The blood rheological properties vary both in vivo and in vitro analysis as explained by:

1. **Fåhræus Effect** This phenomenon illustrates that blood viscosity diminishes in smaller blood vessels relative to larger ones, occurring in vessels larger than capillaries but smaller than major arteries or veins. It clarifies that the hematocrit level decreases when blood flows from wider-diameter vessels to narrower ones.

2. **Fåhræus-Lindqvist Effect** This phenomenon pertains to the reduction in blood viscosity observed in minuscule vessels like capillaries, where the diameter matches or is smaller than that of red blood cells. In these tiny vessels, the small size of red blood cells causes them to migrate towards the vessel wall, creating a central flow primarily composed of plasma with fewer red blood cells. As plasma has lower viscosity than whole blood, this alignment substantially decreases blood viscosity within these small vessels.

In small blood vessels, the Haynes [45] marginal theory elucidates the two-phase nature of blood flow. According to this theory, in two-phase blood flow, red blood cells (RBCs) tend to accumulate at the centre of the vessel, while plasma, devoid of RBCs, gathers at the vessel's periphery. Several mathematical models have been developed to investigate this phenomenon. Chebbi [46] expanded upon Haynes' work by directly comparing experimental data without adjusting any parameters for computation. His study sheds light on decreased apparent viscosity, reducing microvascular resistance and, subsequently, lowering blood pressure.

1.6 Methodology

Blood flow dynamics are primarily governed by the non-linear Navier-Stokes equations, constituting a set of complex partial differential equations. Due to their inherent non-linearity and the coupling of equations, deriving analytical solutions for these equations proves to be a formidable challenge. Therefore, numerical methods are employed as a reliable means of providing solutions to the governing equations.

1.6.1 Finite Difference Method (FDM)

In pursuing numerical solutions for the Navier-Stokes equation, the continuous data inherent in the exact solutions of partial differential equations (PDEs) are converted into the discretized form. The finite difference method approximates derivatives using finite difference equations derived from truncated Taylor series expansions. The endeavour to solve differential equations using difference equations was first undertaken by Euler. Today, with the advent of high-speed computers, sophisticated schemes have been developed to address the intricacies associated with solving nonlinear hydrodynamic equations and their corresponding boundary conditions. These advanced methods aim to minimize the error in the approximate solutions to fulfil the stability criteria, ensuring accuracy and reliability in computational fluid dynamics simulations.

Its ability to provide numerical solutions to a wide array of differential equations makes it an indispensable tool in the realm of computational science and engineering. In FDM, the spatial and time derivatives (if applicable) are finitely divided into grid/nodal points. The distance between the consecutive grid points is the step size, and the total number of grid points varies according to the step size and length of the domain into consideration. The finite difference method is applied to discretize the required differential equation at these grid points using Taylor's series expansion. The Taylor's series expansion of $w_{i+1,j}$ at the point (i, j) with step size of Δx is written as follows-

$$w_{i+1,j} = w_{i,j} + \left(\frac{\partial w}{\partial x}\right)_{i,j} \Delta x + \left(\frac{\partial^2 w}{\partial x^2}\right)_{i,j} \frac{(\Delta x)^2}{2!} + \left(\frac{\partial^3 w}{\partial x^3}\right)_{i,j} \frac{(\Delta x)^3}{3!} + \ldots, \tag{1.16}$$

From the equation (1.16), the first derivatice at (i, j) can be written as -

$$\left(\frac{\partial w}{\partial x}\right)_{i,j} = \underbrace{\frac{w_{i+1,j} - w_{i,j}}{\Delta x}}_{\text{Finite-diffrence representation}} \underbrace{- \left(\frac{\partial^2 w}{\partial x^2}\right)_{i,j} \frac{(\Delta x)}{2!} - \left(\frac{\partial^3 w}{\partial x^3}\right)_{i,j} \frac{(\Delta x)^2}{3!} - \ldots,}_{\text{Truncation error}} \tag{1.17}$$

and,

$$\left(\frac{\partial w}{\partial x}\right)_{i,j} \approx \frac{w_{i+1,j} - w_{i,j}}{\Delta x}, \tag{1.18}$$

where, the equation (1.18) is the first-order accurate with Taylor's series. The other representation for first-order differential equations is :

$$\left(\frac{\partial w}{\partial x}\right)_{i,j} = \begin{cases} \frac{w_{i+1,j}-w_{i,j}}{\Delta x} + O(\Delta x) & \text{Forward Difference,} \\ \frac{w_{i,j}-w_{i-1,j}}{\Delta x} + O(\Delta x) & \text{Backward Difference,} \\ \frac{w_{i+1,j}-w_{i-1,j}}{2\Delta x} + O(\Delta x)^2 & \text{Central Difference.} \end{cases} \tag{1.19}$$

Using the Taylor's series, the second order derivative $\left(\frac{\partial^2 w}{\partial x^2}\right)_{i,j}$ can also be derived as:

$$\left(\frac{\partial^2 w}{\partial x^2}\right)_{i,j} = \frac{w_{i+1,j} - 2w_{i,j} + w_{i-1,j}}{(\Delta x)^2} + O(\Delta x)^2. \tag{1.20}$$

In a similar manner, higher-order derivatives may be ascertained via Taylor's series expansion. After implementing the finite difference scheme in place of the derivative at discrete grid points, a system of algebraic equations emerges, which can be resolved using the tridiagonal matrix algorithm (TDMA) to obtain numerical solutions at these grid points. If the system of algebraic equations exhibits nonlinearity, the Newton-Raphson method is employed to address the corresponding equations, followed by the utilization of TDMA to procure numerical solutions.

1.6.1.1 Crank-Nicolson Method

The Crank-Nicolson method and its modified versions play a crucial role in CFD as a prominent numerical technique for obtaining finite-difference solutions to the boundary layer equations. This numerical technique, well-known for its numerical stability, was first introduced during the mid-20th century by John Crank and Phyllis Nicolson.

To elucidate the fundamental methodology of the Crank-Nicolson method, this discussion delves into the numerical solution of heat equations along with their corresponding boundary conditions.

$$\frac{\partial w}{\partial t} = \frac{\partial^2 w}{\partial x^2}, \tag{1.21}$$

where, the initial and boundary conditions are given as

$$\begin{cases} w(x,0) = \sin(\pi x), & \\ \frac{\partial w}{\partial x} = \pi e^{-\pi^2 t} & \text{for} \quad \text{x=0,} \\ w(x,t) = 0. & \text{for} \quad \text{x=1.} \end{cases} \tag{1.22}$$

The exact solution of the equation (1.21) with initial and boundary conditions (1.22) is expressed as $w(x,t) = \sin(\pi x)e^{-\pi^2 t}$. The right-hand side (RHS) of the equation (1.21) is

discretised using the spatial difference in terms of averaged properties of time levels n and $n+1$. The discretised form is given as:

$$\frac{w_i^{n+1}-w_i^n}{\Delta t}=\frac{1}{2}\left[\frac{w_{i+1}^{n+1}-2w_i^{n+1}+w_{i-1}^{n+1}}{(\Delta x)^2}+\frac{w_{i+1}^n-2w_i^n+w_{i-1}^n}{(\Delta x)^2}\right]. \tag{1.23}$$

Let $r=\frac{\Delta t}{2(\Delta x)^2}$, then the equation (1.23) becomes

$$-rw_{i+1}^{n+1}+(1+2r)w_i^{n+1}-rw_{i-1}^{n+1}=rw_{i+1}^n+(1-2r)w_i^n+rw_{i-1}^n. \tag{1.24}$$

The equations on the RHS are known and subsequently refined by incorporating boundary conditions. The resulting equations formed a tridiagonal structure, allowing for the straightforward solution of w_i^{n+1} by employing the Tridiagonal Matrix Algorithm (TDMA) approach.

1.6.1.2 Method of Lines (MOL)

The MOL is a powerful technique that transforms the PDE with two independent variables into the system of adjoint ODE in one of the independent variables. Especially in the parabolic equations, the spatial variable is discretized using the finite difference method while leaving the other spatial partial derivative or time partial derivative in continuous form.

Furthermore, the initial condition stated in equation (1.22) is rewritten in discrete form to be compatible with equation (1.21) as follows

The equation (1.21) after discretization in the spatial variable (x) takes the adjoint system of ODEs of the first order at i^{th} line.

$$\frac{dw_i}{dt}=\frac{w_{i+1}-2w_i+w_{i-1}}{(\Delta x)^2}\text{for}\quad i=2\ \text{ to }\ N. \tag{1.25}$$

1. At the first straight line $i=1$,

$$\frac{dw_1}{dt}=\frac{w_2-2w_1+w_0}{(\Delta x)^2}. \tag{1.26}$$

By introducing the BC at line $i=1$, equation (1.26) becomes

$$\frac{dw_1}{dt}=\frac{2w_2-2w_1-2\Delta x\pi e^{-\pi^2 t}}{(\Delta x)^2}. \tag{1.27}$$

2. At the second straight line $i=2$,

$$\frac{dw_2}{dt} = \frac{w_3 - 2w_2 + w_1}{(\Delta x)^2}. \tag{1.28}$$

3. At the straight line $i = N$,

$$\frac{dw_N}{dt} = \frac{-2w_N + w_{N-1}}{(\Delta x)^2}. \tag{1.29}$$

4. At the straight line $i = N+1$,

$$w_{N+1} = 0. \tag{1.30}$$

The resultant system of ODEs can be solved by the RK-4 method, Euler, etc. The solution of the equation (1.21) with corresponding BCs (1.22) with both the method are shown in figure 1.2.

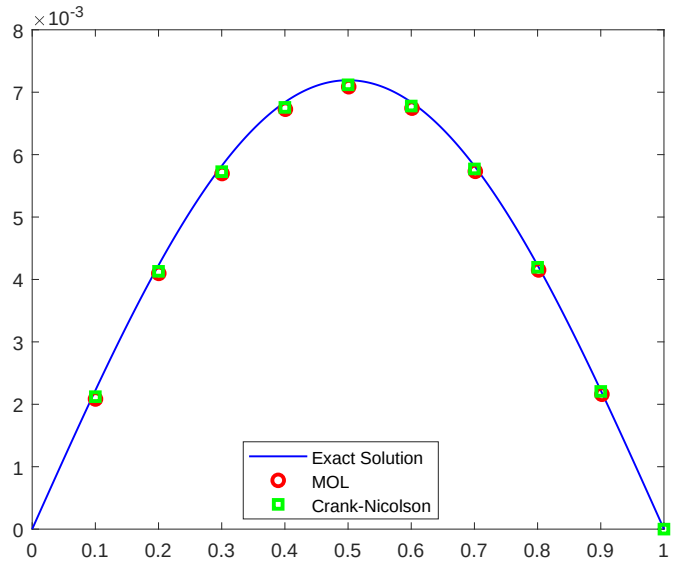

Figure 1.2: Solution of heat equation using Crank-Nicolson and MOL method

1.7 Research Gaps

As per the literature mentioned earlier and from many research articles, it is widely acknowledged that Cardiovascular Disease (CVD) remains a significant global health concern, leading to substantial morbidity and mortality. Its occurrence is frequently attributed to various factors, notably high blood pressure, elevated cholesterol levels, smoking, obesity, and diabetes. CVD encompasses a spectrum of disorders affecting the heart and blood vessels, including conditions such as heart disease, stroke, and heart failure.

Despite considerable research efforts in the biomedical field, particularly in investigating hemodynamic flow through stenosed arteries as documented in prior literature, the depth of knowledge in this area still needs to be improved. Developing theoretical or experimental models becomes imperative to comprehensively grasp the dynamic behaviour of blood flow. In this thesis, we have formulated mathematical models to explore the rheology of blood, incorporating key physical parameters such as magnetic field intensity, Joule heating, thermophoresis, Brownian motion, and magnetic drug targeting. It has been observed that certain aspects of blood flow have not been previously investigated:

1. Less attention has been given to the flow with hybrid nanofluid (Au-GO/Blood) flow through curved catheterized stenosed artery with thrombosis.

2. Earlier work has not paid much attention to the entropy generation optimization for the electroosmotic MHD flow on the catheterized stenosed artery with thrombosis.

3. Not much attention has been given to the hybrid nanofluid flow through the stenosed bifurcated artery containing gyrotactic microorganisms.

4. Less attention has been paid to the entropy generation analysis for the ternary hybrid nanofluid flow through the bifurcated artery with stenosis and aneurysm.

5. The effect of thermophoresis, Brownian motion and activation energy on the Two-phase blood model has not been covered so much.

6. Less attention has been given to magnetic targeting drug delivery on the two-phase blood flow model.

This thesis presents a comprehensive computational model that investigates blood flow dynamics within arteries across various physiological scenarios. The research focuses on understanding hemodynamic flow within arteries affected by different pathological conditions, including stenosis, thrombosis, and aneurysm. The study delves into the intricate behavior of blood, encompassing both Newtonian and non-Newtonian properties. The Casson fluid and power law fluid models have been employed to account for non-Newtonian characteristics. To underscore the varying viscosity of blood, various models are employed, such as hematocrit-dependent and temperature-dependent viscosity models. Additionally, the study explores the influence of nanoparticle shape and size on stenosed arteries, an area with limited existing research. Furthermore, the study includes an examination of a two-phase model. The hemodynamic flow model through diseased arteries is solved using the Method of Lines (MOL) technique, which has not been previously explored in this context.

This technique is valuable due to its robustness and effectiveness in solving the partial differential equations (PDEs) arising from the governing equations of the mathematical models.

The presented problem in the thesis are the theoretical model for which the experiment should be carried out to validate with the current model. Some of the findings from this thesis are compared with previous literature experiments, such as the utilization of the hematocrit-dependent viscosity model. In Chapters 2 and 3 of the thesis, a decreasing pattern in the velocity profile has been observed alongside an enhancement in the hematocrit parameter. This phenomenon is elucidated by the findings of [47] work, wherein it was demonstrated that viscosity increases with higher levels of hematocrit in the blood. Chapter 6 focuses on studying magnetic drug targeting in diseased arteries. Experimental data provided in [48] demonstrates that both fluid and particle velocity profiles decrease with an increase in the magnetic field parameter. Our computed results show similar outcomes.

The various types of nanoparticles, such as Au, GO, Al_2O_3, and CuO, have been selectively utilized based on their distinct physical properties. Au nanoparticles are favored for their inertness, low toxicity, and ease of fabrication, while GO nanoparticles exhibit potential in biomedical treatments. The incorporation of aluminum oxide nanoparticles in this study offers numerous applications in biomedicine and biosensing. Surface engineering techniques can enhance their stability, biocompatibility, and reactivity, rendering them effective for DNA sensing. The entropy generation has been studied in the present work that can be useful in the biomedical field showing the intricate complexities and behaviours inhernt in the biological system. Thus, can be utilized as a metric to quantitatively assesss the intrincsic randomness and disorder manifesting within the system. This research may also benefit radiological investigations like magnetic resonance angiography (MRA) for detecting arterial abnormalities. Thus, this work address the existing knowledge gaps and deepen our comprehension of magnetic drug targeting mechanisms within the complex dynamics of stenosed arteries. By doing so, we aim to provide valuable insights into biomedical fluid dynamics.

Chapter 2

Hall and Ion Slip Effects on Hybrid Nanoparticles (Au-GO/Blood) Flow Through a Catheterized Stenosed Artery with Thrombosis [1]

2.1 Introduction

According to WHO statistics [19] cardiovascular diseases are responsible for morbidity and mortality across the world. This led to an increasing trend to know the pathological blood flow behaviour in arteries, veins, and cardiovascular systems. Atherosclerosis is a condition that occurs due to the accrual of cholesterol and lipo-proteins inside the artery, leading to the formation of lesions that reduce blood flow. When this lesion further grows and narrows the blood flow. Then this term is known as stenosis. Deep vein thrombosis is a condition in which blood clots form in the veins that include areas like the lower legs, pelvis, and thighs, although blood clots can be formed at any other place in the body. The primary issue is the detachment of this clot and its possibility to move to different body organs leading to severe organ damage, renal failure, heart attack, strokes etc. The formation of stenosis and thrombosis (blood clot) are the result of vascular injuries. Doffin and Chagneau [49] developed an experimental model to demonstrate the oscillatory flow of blood between the stenosis and the clot model. In this model, he considered axisymmetrical stenosis with a blood clot at different positions on the centre of a small metallic rod. He concluded that the steady streaming could be a possible mechanism for the clotting effect that occurs due to the contact of the red blood cell and platelets with the walls or the obstacle at the centre. Vanherweghem [50] investigated that 35% of patients receiving subclavian dialysis catheters are more likely affected by stenosis or thrombosis in hemodialysis. In subclavian dialysis, oedema has occurred on the hand of the patient, leading to stenosis or thrombosis,

[1] A considerable part of this chapter is published in *Proceedings of the Institution of Mechanical Engineers, Part C: Journal of Mechanical Engineering Science*, 237(10), 2256–2278, 2023.

which can be removed by giving an anticoagulant with heparin. Walsh and McLachlan [20] studied that the endothelial cells exposed to low shear stress are responsible for these diseases. Elnaqeeb et al. [51] explored the effect of Cu nanoparticles on the catheterized stenotic artery with a varying shape parameter for the stenosis. Ahmed and Nadeem [52] investigated the Carreau nanofluid flow across an inclined artery with overlapping stenosis using the "homotopy perturbation" approach. Bhatti et al. [53] created a mathematical model of a blood clot and investigated the effects of viscosity and heat transfer. Saleem et al. [54] discussed the hemodynamic flow over the catherized artery having mild stenosis and clot at the center. Further, Akhtar et al. [55] examined the flow of Jeffery fluid within a tube with multiple thromboses to mimic the blood flow inside an artery. In this model, they considered the Peristaltic motion and viscous dissipation effects. Akhtar et al. [31] studied the electroosmotic effects on the stenosed artery. They considered the Casson flow model, and their study revealed that the enhancement in flow velocity is low for non-uniform shapes compared to uniform-shaped multiple stenoses. Further, Saleem et al. [56] studied the effect of Joule heating on the electro-osmotically flow over the symmetric and non-symmetric stenosed artery. Zidan et al. [57] explicated a study to show the effect of entropy generation in the artery having multiple stenoses at the outer wall and a thrombus at the centre. Further, Saleem et al. [58] explored the irreversibility impact of entropy by taking into account single-wall and multiple-wall carbon nanotubes inside an artery with thrombosis.

The importance of nanoparticles in the field of biomedicine has been emphasised by a combination of theoretical studies and empirical data. The studies shows the importance of nanoparticles to enhance the administration of diagnostic and therapeutic substances. Thus, numerous investigations have been conducted to explore molecular-level functionalities of nanoparticles in the field of life sciences. Shahzadi and Nadeem [59] conducted a series of studies to investigate the simulation of metallic nanoparticles located within eccentric annuli, while being subjected to the effects of a radial magnetic field. Moreover, a comparative analysis of copper nanoparticles was conducted in a separate study [60]. The study specifically examined the slip effect in oblique cylinders. Furthermore, Shahzadi et al. [61] conducted a study to examine the influence of different shapes of Ag nanoparticles, including platelets, bricks, and cylinders, within a curved artery. The results indicated that there was an increase in the velocity field as the curvature parameter was raised. In their study, Kumar et al. [62] performed an investigation on the features of flow and heat transfer within a porous medium, specifically focusing on the application of various hybrid nanofluids. On the other hand, the study conducted by Imran et al. [63] centred on the analysis of the flow of an incompressible Jeffrey nanofluid through a vertical tube. The results of their study revealed a positive relationship between velocity and nanoparticle concentration with

thermophysical parameters, while temperature showed a negative association. Jamil et al. [64], employed Caputo-Fabrizio fractional derivatives to examine the flow characteristics of Casson fluid within a constricted artery. The researchers observed that an increase in the Hartmann number resulted in an elevation of the concentration of magnetic particles, consequently leading to an augmentation of fluid viscosity and a decrease in fluid velocity. Hassan et al. [65] conducted an independent study to examine the characteristics of the boundary layer flow of nanofluid over a movable wedge. A decrease in the velocity field was observed as the nanoparticle volume fraction increased. Among the other nanoparticles, gold nanoparticles are proven to be helpful in biomedical treatment and diagnosis. Gold nanoparticles are inert, making them compatible with biological systems, and their use in small amounts has no noticeable adverse effects. Elnaqeeb et al. [66] analyzed the hemodynamic performance of gold nanoparticles in the stenosed artery. They found that fluid velocity increases in the Au blood model compared to TiO2 and Cu blood model. Further, Sarwar and Hussain [67] investigated the effect of the gold nanoparticles shape on the stenosed artery and compared the results with Cu and Al_2O_3-nanoparticles. Bhatti and Abdelsalam [68] investigated the peristaltic flow with Tantalum (Ta) and Gold (Au) nanoparticles (NPs) in a symmetric channel under the influence of thermal radiation and magnetic field effect. They discovered that the Tantalum and gold NPs size enhance the temperature profile. Khazayinejad et al. [69] developed a mathematical model to study the peristaltic motion of graphene-blood nanofluid in a wavy channel. Ocsoy et al. [70] created DNA-guided nanoparticles that are adsorbed on the surface of GO (graphene oxide) and can be modified by changing their shape and size. Some functional and biocompatible formations are Au-GO, Cu-GO, Ag-GO, etc. Kim et al. [71] studied the Au-GO nanomaterial composite to develop a diagnostic technique for virus detection. Kang et al. [72] formed the hybrid sheet of Au-GO nanoparticles to enhance the photothermic effect helpful in cancer therapy.

Generally, Ohm's law is neglected in the MHD flow due to the tenuous magnetic field. However, the influence of Hall and ion slip cannot be disregarded in the presence of a strong magnetic field. Blood contains ionized particles, and the existence of a strong electromotive force creates the induced electric current across the applied electric field. The three crucial factors that affect the ionised fluid are the magnetic force, the collision of the electron generating the Hall force, and the collision of the ions that produce the ion slip force. Mekheimer and Kot [73] studied the Hall effect on the MHD flow of blood over mild stenosis by varying the stenosis shape parameter. Using the implicit finite difference technique, Anika et al. [74] investigated the Hall and ion slip effects on the MHD Micropolar fluid on a vertical plate. Further, Mishra and Ghosh [75] introduced a mathematical framework to comprehend blood circulation dynamics from the parent artery to the capillary network, considering different

entry angles. The primary focus of the investigation revolved around the phenomenon of hematocrit reduction via plasma skimming and the mass flux occurring within the capillary system. The study's results highlighted that the lowest quantity of red blood cells passing from the main artery to the smaller capillary is observed when both vessels are positioned at a right angle. Ramzan et al. [76] investigated the three-dimensional nanofluid flow by considering the effect of Arrhenius activation energy, Cattaneo-Christov heat flux, and Hall and ion slip. Recently, Das et al. [77] used the Casson fluid model to show the rheology of blood, taking silver and aluminium oxide nanoparticles in the base fluid (blood) to construct a homogeneous ionised blood system and examine the Hall and ion slip effects. In the human circulatory system, blood flow is greatly influenced by pressure, viscosity, and other external or internal factors. The hemodynamic characteristic of blood continuously changes due to its shear-thinning property. As a result, blood viscosity cannot be considered to remain constant. Syndar [78] experimented on the lizard to study the influence of temperature and hemodynamic viscosity. The lizard was used for this experiment because it is easier to perceive temperature fluctuations in the lizard's body. Mishra et al. [75] developed a mathematical model by considering the Casson fluid to study the deprivation of hematocrit in the blood by the plasma skimming phenomena. Shit et al. [79] analytically solved the governing equations for blood flow through a stenotic artery with hematocrit dependent viscosity. They found that the composition of RBCs generates non-constant blood viscosity, which is reflected by the function of erythrocytes. Tripathi and Sharma [80] explored the effect of inclination with hematocrit dependent viscosity on the heat and mass characteristic of the MHD-blood flow. In addition, Kumawat et al. [12] conducted a mathematical study to investigate the influence of hematocrit dependent viscosity on two-phase blood flow. According to their findings, radial curvature raises the risk of atherosclerosis, whereas heat radiation lowers it.

The motivation of the present study is to analyze the effect of Hall and ion slips on the MHD blood flow through a multiple stenotic artery with clot at its center. The curvilinear coordinate system is adopted and the hematocrit dependent viscosity is considered to represent the more realistic situation of blood flow. The Au nanoparticles are utilized due to the their inert nature, low toxicity and easy fabrication property along with GO nanoparticles that can be applied in biomedical treatment. The present study may be helpful in radiological investigations such as magnetic resonance angiography (MRA) to capture the abnormalities of the artery. The effects of various pertinent parameter like radiation, Joule heating along with different shapes of nanoparticles are studied using the numerical technique. The governing equations representing the mathematical model is discretized and then solved by Crank-Nicolson method. The present investigation can help scientist and clinical

researchers to understand the effects of these parameter on stenotic artery with thrombosis.

The novelty of the present work includes:

- The influence of (Au-GO/blood) hybrid nanoparticles on the diseased segments containing both multiple stenosis and thrombosis has been discussed in this study.
- The hematocrit-dependent viscosity model and combined effects of thermal radiation, Joule heating, Hall and ion slip effect have been considered on the curved artery.
- The effect of arterial curvature and body acceleration in the velocity profile has been analyzed.

2.2 Mathematical Formulation

2.2.1 Geometry of the Model

Consider the flow of hybrid nanoparticles (Au-GO) in an incompressible, laminar blood flow inside two coaxial curved tubes of length L and radius R_0 from the point O. The flow is assumed to be Newtonian, and the curvilinear coordinate $(\tilde{r}, \tilde{\theta}, \tilde{z})$ is chosen as depicted in figure 2.1. The flow is independent in θ direction due to axi-symmetry blood flow in the artery. The magnetic Reynold is assumed to be small compared to the applied magnetic field so that induced magnetic field can be neglected. The outer tube has stenosis of radius $R^*(\tilde{z})$, whereas the inner tube contains a clot of radius $R_1^*(\tilde{z})$, and the mathematical expression for stenosed artery is given as [40]:

$$R^*(\tilde{z}) = \begin{cases} R_0 - 2\frac{\delta^*}{L_0}(\tilde{z} - L_0), & \tilde{d} \leq \tilde{z} \leq \tilde{d} + \frac{L_0}{2}, \\ R_0 + 2\frac{\delta^*}{L_0}(\tilde{z} - \tilde{d} - L_0), & \tilde{d} + \frac{L_0}{2} \leq \tilde{z} \leq \tilde{d} + L_0, \\ R_0 + \frac{\delta^*}{L_0} Sin(\pi(\tilde{z} - \tilde{d})), & \tilde{d} + L_0 \leq \tilde{z} \leq \tilde{d} + 2L_0, \\ R_0, & \text{otherwise.} \end{cases} \tag{2.1}$$

The geometry of the clot is given as [51]:

$$R_1^*(\tilde{z}) = \begin{cases} R_0(c + \sigma_c \exp(-\frac{\pi^2}{L_0^2}(\tilde{z} - \tilde{z}_d - 0.5)^2)), & \tilde{d} < \tilde{z} < \tilde{d} + \frac{3L_0}{2}, \\ cR_0, & \text{otherwise.} \end{cases} \tag{2.2}$$

Where, σ is the maximum height of the clot at the axial position $\tilde{z}_d$, cR_0 is the radius of the inner tube with $c << 1$. In equation (2.1), δ^* represents the maximum height of the stenosis, $\tilde{d}$ is the location of diseased segment.

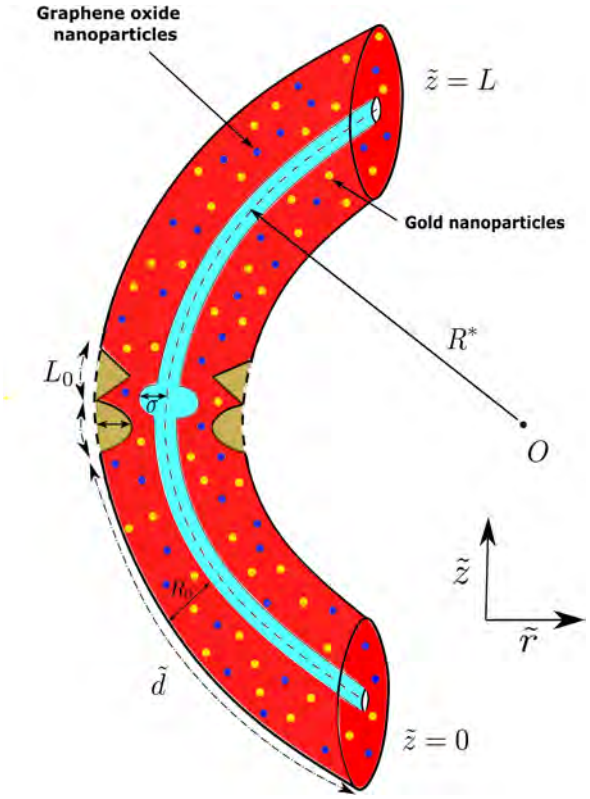

Figure 2.1: Diseased artery segment

2.2.2 Magnetohydrodynamics

Blood is the most complex biological fluid, comprising white blood cells, plasma, red blood cells, and other ionic components. The presence of hemoglobin in red blood cells makes it act like a magnetic fluid that may be regulated further using a magnetic field. Consider a flow subjected to a radial magnetic field $\mathbf{B} = (0, \frac{R^* B_0}{\tilde{r}+R^*}, 0)$, where, B_0 is constant. In the presence of ion slip and the Hall effect, the generalized Ohm law is given as:

$$\mathbf{J} = \sigma_{hnf}(\mathbf{E} + \mathbf{q} \times \mathbf{B}) - \frac{\beta_e}{\frac{R^* B_0}{\tilde{r}+R^*}}(\mathbf{J} \times \mathbf{B}) + \frac{\beta_e \beta_i}{B_0^2}[(\mathbf{J} \times \mathbf{B}) \times \mathbf{B}], \tag{2.3}$$

where $\mathbf{q}, \mathbf{E}, \mathbf{J}, \mathbf{B}, \beta_i, \beta_e$ denotes the velocity vector, the induced electric field vector, the current density vector, the magnetic field vector, ion slip parameter and Hall effect parameter.

The maxwell equations are given as [77]:

$$\nabla \times \mathbf{E} = -\frac{\partial B}{\partial t}, \quad \nabla \cdot \mathbf{B} = 0, \quad \nabla \cdot \mathbf{J} = 0. \tag{2.4}$$

Using the above equation in equation (2.3) yields [77]

$$(1+\beta_e\beta_i)J_{\tilde{z}}+\beta_e J_{\tilde{r}}=\sigma_{hnf}\left(E_{\tilde{z}}+\tilde{u}\frac{R^*B_0}{(\tilde{r}+R^*)}\right) \tag{2.5}$$

$$(1+\beta_e\beta_i)J_{\tilde{r}}-\beta_e J_{\tilde{z}}=\sigma_{hnf}\left(E_{\tilde{r}}-\tilde{w}\frac{R^*B_0}{(\tilde{r}+R^*)}\right). \tag{2.6}$$

Where, $(\tilde{u},\tilde{v},\tilde{w})$ are velocity component, $(J_{\tilde{r}},J_{\tilde{\theta}},J_{\tilde{z}})$ are current density components, and $(E_{\tilde{r}},E_{\tilde{\theta}},E_{\tilde{z}})$ are electric field components in $\tilde{r}$-direction, $\tilde{\theta}$-direction and $\tilde{z}$-direction, respectively. Assuming the induced magnetic field is very small which gives $E=0$. In the absence of external electric field, the expression for Lorentz force and current density as [77],[81]:

$$\mathbf{J}\times\mathbf{B}=\left(-\frac{\sigma_{hnf}B_0^2R^{*2}(\alpha_e\tilde{u}+\beta_e\tilde{w})}{(\alpha_e^2+\beta_e^2)(\tilde{r}+R^*)^2},0,\frac{\sigma_{hnf}B_0^2(R^*)^2(\beta_e\tilde{u}-\alpha_e\tilde{w})}{(\alpha_e^2+\beta_e^2)(\tilde{r}+R^*)^2}\right), \tag{2.7}$$

$$\frac{\mathbf{J}\cdot\mathbf{J}}{\sigma_{hnf}}=\frac{\sigma_{hnf}B_0^2(R^*)^2(\tilde{u}^2+\tilde{w}^2)}{(\alpha_e^2+\beta_e^2).(\tilde{r}+R^*)^2}, \tag{2.8}$$

where $\alpha_e=1+\beta_e\beta_i$ and β_e denotes the Hall parameter.

2.2.3 Governing Equations

Subject to the above mention assumption with the MHD flow interaction, the resultant governing equations becomes [22],[82]:

Continuity

$$\frac{\partial\tilde{u}}{\partial\tilde{r}}+\frac{\tilde{u}}{\tilde{r}+R^*}+\frac{R^*}{\tilde{r}+R^*}\frac{\partial\tilde{w}}{\partial\tilde{z}}=0. \tag{2.9}$$

Momentum ($\tilde{r}$-direction)

$$\rho_{hnf}\left[\frac{\partial\tilde{u}}{\partial\tilde{t}}+\tilde{u}\frac{\partial\tilde{u}}{\partial\tilde{r}}+\frac{\tilde{w}R^*}{\tilde{r}+R^*}\frac{\partial\tilde{u}}{\partial\tilde{z}}-\frac{\tilde{w}^2}{\tilde{r}+R^*}\right]=-\frac{\partial\tilde{p}}{\partial\tilde{r}}+\mu_{hnf}\left(\nabla^2\tilde{u}-\frac{\tilde{u}}{(\tilde{r}+R^*)^2}-\frac{2R^*}{(\tilde{r}+R^*)^2}\frac{\partial\tilde{w}}{\partial\tilde{z}}\right)$$
$$+\left(\frac{4}{3}\frac{\partial\tilde{u}}{\partial\tilde{r}}-\frac{2}{3}\left(\frac{R^*}{R^*+\tilde{r}}\frac{\partial\tilde{w}}{\partial\tilde{z}}+\frac{\tilde{u}}{R^*+\tilde{r}}\right)\right)\frac{\partial\mu_{hnf}}{\partial\tilde{r}}-\frac{\sigma_{hnf}B_0^2R^{*2}(\alpha_e\tilde{u}+\beta_e\tilde{w})}{(\alpha_e^2+\beta_e^2)(\tilde{r}+R^*)^2}. \tag{2.10}$$

Momentum ($\tilde{z}$-direction)

$$\rho_{hnf}\left[\frac{\partial\tilde{w}}{\partial\tilde{t}}+\tilde{u}\frac{\partial\tilde{w}}{\partial\tilde{r}}+\frac{R^*\tilde{w}}{\tilde{r}+R^*}\frac{\partial\tilde{w}}{\partial\tilde{z}}+\frac{\tilde{u}\tilde{w}}{\tilde{r}+R^*}\right]=-\left(\frac{R^*}{\tilde{r}+R^*}\right)\frac{\partial\tilde{p}}{\partial\tilde{z}}+\mu_{hnf}\left(\nabla^2\tilde{w}-\frac{\tilde{w}}{(\tilde{r}+R^*)^2}\right.$$
$$\left.+\frac{2R^*}{(\tilde{r}+R^*)^2}\frac{\partial\tilde{u}}{\partial\tilde{z}}\right)+\left(\frac{R^*}{R^*+\tilde{r}}\frac{\partial\tilde{u}}{\partial\tilde{z}}+\frac{\partial\tilde{w}}{\partial\tilde{r}}-\frac{\tilde{w}}{R^*+\tilde{r}}\right)\frac{\partial\mu_{hnf}}{\partial\tilde{r}}+g(\rho\beta)_{hnf}(\tilde{T}-\tilde{T}_0)$$
$$+G(\tilde{t})-\frac{\mu_{hnf}}{K_1}\tilde{w}+\frac{\sigma_{hnf}B_0^2(R^*)^2(\beta_e\tilde{u}-\alpha_e\tilde{w})}{(\alpha_e^2+\beta_e^2)(\tilde{r}+R^*)^2}. \quad (2.11)$$

Temperature Equation

$$(\rho_{cp})_{hnf}\left[\frac{\partial\tilde{T}}{\partial\tilde{t}}+\tilde{u}\frac{\partial\tilde{T}}{\partial\tilde{r}}+\frac{R^*}{\tilde{r}+R^*}\tilde{w}\frac{\partial\tilde{T}}{\partial\tilde{z}}\right]=\kappa_{hnf}\nabla^2\tilde{T}+\frac{\sigma_{hnf}B_0^2(\tilde{u}^2+\tilde{w}^2)}{(\alpha_e^2+\beta_e^2)}\left(\frac{R^*}{\tilde{r}+R^*}\right)^2$$
$$-\frac{1}{\tilde{r}+R^*}\left[\frac{\partial}{\partial\tilde{r}}(\{\tilde{r}+R^*\}q_r)\right]. \quad (2.12)$$

Where, $\nabla^2:=\frac{\partial^2}{\partial\tilde{r}^2}+\frac{1}{\tilde{r}+R^*}\frac{\partial}{\partial\tilde{r}}+\left(\frac{R^*}{\tilde{r}+R^*}\right)^2\frac{\partial^2}{\partial\tilde{z}^2}$.

The associate dimensional boundary conditions are:

$$\begin{cases}\tilde{w}=\tilde{T}=0 & \text{at} \quad \tilde{t}=0,\\ \tilde{w}=0,\tilde{T}=\tilde{T}_w & \text{at} \quad \tilde{r}=R^*(\tilde{z}) \text{ and } \tilde{r}=R_1^*(\tilde{z}).\end{cases} \quad (2.13)$$

The expression for axial pressure gradient is represented as:

$$-\frac{\partial\tilde{p}}{\partial\tilde{z}}=A_0+A_1\cos(\omega_p\tilde{t}), \quad \tilde{t}>0. \quad (2.14)$$

Where, $\omega_p=2\pi f_p$ with f_p as frequency, A_0 and A_1 represents the mean and pulsatile component of pressure gradient, respectively. The extrinsic body force acting on the axial direction is given by:

$$G(\tilde{t})=B_0\cos(\omega_q\tilde{t}+\psi), \quad (2.15)$$

where, ψ is the phase angle, $\omega_q=2\pi f_q$ with f_q as frequency and B_0 as the amplitude for body acceleration, respectively.

The hematocrit-dependent viscosity is considered in the model to account for the spatial variation of RBC present in blood and it is represented as(see [11], [83],[84]):

$$\mu_{bf}=\mu_f[1+\beta_1^*h(\tilde{r})], \quad (2.16)$$

Where, $h(\tilde{r}) = h_m[1-(\frac{\tilde{r}}{R_0})^m]$, h_m represent the maximum hematocrit with β_1^* as constant. Table 2.1 represents the thermophysical parameters for nanofluid and hybrid nanofluid . The radiative heat flux q_r is defined as [85]:

$$q_r = -\frac{4\sigma_e}{3k_e}\frac{\partial \tilde{T}^4}{\partial \tilde{r}}, \tag{2.17}$$

where k_e and σ_e are the mean absorption coefficient and the Stefan-Boltzmann constant.

Table 2.1: Thermophysical parameters of nanofluid and hybrid nanofluid

Properties	Mathematical expression for nanofluid and hybrid nanofluid
Viscosity	$\mu_{nf} = \frac{\mu_{bf}}{(1-\phi_1)^{2.5}}$ $\mu_{hnf} = \frac{\mu_{bf}}{(1-\phi_1)^{2.5}(1-\phi_2)^{2.5}}$
Density	$\rho_{nf} = (1-\phi_1)\rho_f + \phi_1\rho_{s_1}$ $\rho_{hnf} = [(1-\phi_2)\{(1-\phi_1)\rho_f + \phi_1\rho_{s_1}\}] + \phi_2\rho_{s_2}$
Heat Capacity	$(\rho C_p)_{nf} = (1-\phi_1)(\rho C_p)_f + \phi_1(\rho C_p)_{s_1}$ $(\rho C_p)_{hnf} = [(1-\phi_2)\{(1-\phi_1)(\rho C_p)_f + \phi_1(\rho C_p)_{s_1}\}]$
Thermal Conductivity	$\frac{k_{nf}}{k_f} = \frac{k_{s_1}+(m-1)k_f-(m-1)\phi_1(k_f-k_{s_1})}{k_{s_1}+(m-1)k_f+\phi_1(k_f-k_{s_1})}$ $\frac{k_{hnf}}{k_{bf}} = \frac{k_{s_2}+(m-1)k_f-(m-1)\phi_2(k_f-k_{s_2})}{k_{s_2}+(m-1)k_f+\phi_2(k_f-k_{s_2})}$ where $\frac{k_{bf}}{k_f} = \frac{k_{s_1}+(m-1)k_f-(m-1)\phi_1(k_f-k_{s_1})}{k_{s_1}+(m-1)k_f+\phi_1(k_f-k_{s_1})}$
Electrical Conductivity	$\frac{\sigma_{nf}}{\sigma_f} = \frac{\sigma_{s_1}+(m-1)\sigma_f-(m-1)\phi_1(\sigma_f-\sigma_{s_1})}{\sigma_{s_1}+(m-1)\sigma_f+\phi_1(\sigma_f-\sigma_{s_1})}$ $\frac{\sigma_{hnf}}{\sigma_{bf}} = \frac{\sigma_{s_2}+(m-1)\sigma_f-(m-1)\phi_2(\sigma_f-\sigma_{s_2})}{\sigma_{s_2}+(m-1)\sigma_f+\phi_2(\sigma_f-\sigma_{s_2})}$ where $\frac{\sigma_{bf}}{\sigma_f} = \frac{\sigma_{s_1}+(m-1)\sigma_f-(m-1)\phi_1(\sigma_f-\sigma_{s_1})}{\sigma_{s_1}+(m-1)\sigma_f+\phi_1(\sigma_f-\sigma_{s_1})}$
Thermal Expansion Coefficient	$\beta_{nf} = (1-\phi_1)\gamma_f + \phi_1\beta_{s_1}$ $\beta_{hnf} = [(1-\phi_2)\{(1-\phi_1)\beta_f + \phi_1\beta_{s_1}\}] + \phi_2\beta_{s_2}$

We assume the temperature differences within the flow are sufficiently small such that $\tilde{T}^4$ may be expressed as a linear function of temperature.

$$\tilde{T}^4 = \tilde{T}_0{}^3(4\tilde{T} - 3\tilde{T}_0). \tag{2.18}$$

Making use of equation (2.18) in equation (2.17), we obtain

$$q_r = -\frac{16\sigma_e \tilde{T}_0^3}{3k_e}\frac{\partial \tilde{T}}{\partial \tilde{r}}, \tag{2.19}$$

2.2.4 Non-Dimensional and Mild Stenosis Simplification

The governing equations are transformed into non-dimensionalize form by using the non-dimensionalize parameters discussed in the table 2.2. The non-dimensionalize form of diseased artery is given as follows (see [2],[40], [51]):

Stenosis Region:

$$R^*(z) = \begin{cases} 1-2\delta(z-d), & d \le z \le d+\frac{1}{2}, \\ 1+2\delta(z-d-1), & d+\frac{1}{2} \le z \le d+1, \\ 1+\delta\sin(\pi(z-d)), & d+1 \le z \le d+2, \\ 1, & \text{otherwise.} \end{cases} \tag{2.20}$$

Clot Region:

$$R_1^*(z) = \begin{cases} c+\sigma_c \exp(-\pi^2(z-\frac{z_d-0.5}{L_0})^2), & d < z < d+3/2, \\ c, & \text{otherwise.} \end{cases} \tag{2.21}$$

Table 2.2: Dimensionless parameters

$r = \frac{\tilde{r}}{R_0}$	$z = \frac{\tilde{z}}{L_0}$	$u = \frac{L_0\tilde{u}}{\delta^* U_0}$	$w = \frac{\tilde{w}}{U_0}$
$T = \frac{\tilde{T}-\tilde{T}_0}{\tilde{T}_w-\tilde{T}_0}$	$t = \frac{U_0\tilde{t}}{R_0}$	$R_c = \frac{R^*}{R_0}$	$p = \frac{R_0^2\tilde{p}}{\mu_f U_0 L_0}$
$\delta = \frac{\delta^*}{R_0}$	$M^2 = \frac{\sigma_f B_0^2 R_0^2}{\mu_f}$	$Gr = \frac{g(\rho\beta)_f R_0^2(\tilde{T}_w-\tilde{T}_0)}{\mu_f U_0}$	$\beta_e = \omega_e\tau_e$
$\alpha_e = 1+\beta_e\beta_i$	$Pr = \frac{\mu_f C_p}{\kappa_f}$	$Re = \frac{U_0\rho_f R_0}{\mu_f}$	$Nr = \frac{16\sigma_e\tilde{T}_0^3}{3\kappa_f\kappa_e}$
$Ec = \frac{U_0^2}{c_p(\tilde{T}_w-\tilde{T}_0)}$	$Br = EcPr = \frac{\mu_f U_0^2}{\kappa_f(\tilde{T}_w-\tilde{T}_0)}$	$Da = \frac{K_1}{R_0^2}$	$--$

Using the above non-dimensional parameters, neglecting the bar and assuming the assumption of fully developed flow, mild stenosis ($\delta << 1$) with $O(1) = \alpha = \frac{R_0}{L}$, the governing equations become:

$$\frac{\partial p}{\partial r} = 0, \tag{2.22}$$

$$\frac{\rho_{hnf}}{\rho_f} Re \frac{\partial w}{\partial t} = -\frac{R_c}{R_c + r}\frac{\partial p}{\partial z} + \frac{\mu_{hnf}}{\mu_f}\left(\frac{\partial^2 w}{\partial r^2} + \frac{1}{r+R_c}\frac{\partial w}{\partial r} - \frac{w}{(r+R_c)^2}\right) - \left(\frac{\partial w}{\partial r} + \frac{w}{R_c + r}\right)$$
$$\frac{m\beta_1^* h_m r^{m-1}}{(1-\phi_1)^{2.5}(1-\phi_2)^{2.5}} + \frac{(\rho\beta)_{hnf}}{(\rho\beta)_f} GrT - \frac{\sigma_{hnf}}{\sigma_f}\left(\frac{R_c}{r+R_c}\right)^2 \left(\frac{\alpha_e}{\alpha_e^2 + \beta_e^2}\right) M^2 w$$
$$+ G(t) - \frac{\mu_{hnf}}{\mu_f}\frac{w}{Da}, \tag{2.23}$$

$$\frac{(\rho C_p)_{hnf}}{(\rho C_p)_f}\frac{\kappa_f}{\kappa_{hnf}} PrRe \frac{\partial T}{\partial t} = \frac{\partial^2 T}{\partial r^2} + \frac{1}{r+R_c}\frac{\partial T}{\partial r} + \frac{\sigma_{hnf}}{\sigma_f}\frac{\kappa_f}{\kappa_{hnf}}\left(\frac{R_c}{r+R_c}\right)^2 \left(\frac{Br}{\alpha_e^2 + \beta_e^2}\right) M^2 w^2$$
$$+ \frac{\kappa_f}{\kappa_{hnf}} Nr\left[\frac{\partial^2 T}{\partial r^2} + \frac{1}{R_c + r}\frac{\partial T}{\partial r}\right]. \tag{2.24}$$

The associate boundary conditions are:

$$\begin{cases} w = T = 0 & \text{at} \quad t = 0, \\ w = 0, \;\; T = 1 & \text{at} \quad r = R^*(z) \;\text{ and }\; r = R_1^*(z). \end{cases} \tag{2.25}$$

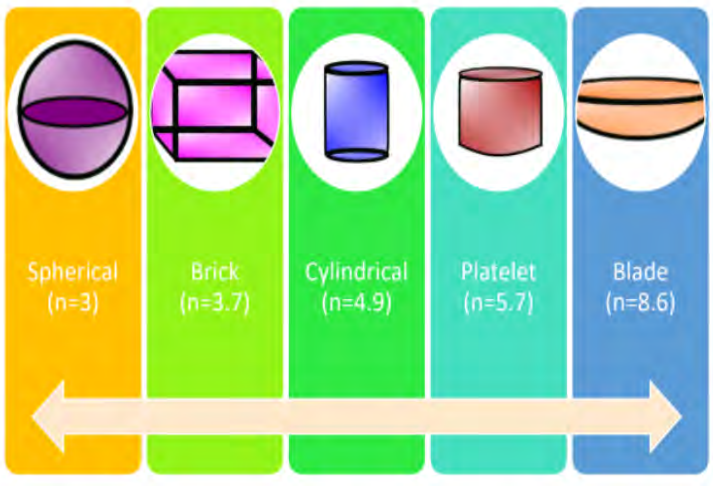

Figure 2.2: Various shapes of the Au-GO/blood hybrid nanoparticles

The non-dimensionalize formed for pressure gradient and body acceleration are given as follows:

$-\frac{\partial p}{\partial z} = B_1(1+e\cos(c_1 t))$, $G(t) = B_2\cos(c_2 t+\chi)$, where $B_1 = \frac{A_0 R_0^2}{\mu_f U_0}, e = \frac{A_1}{A_0}, B_2 = \frac{A_0 R_0^2}{\mu_f U_0}, c_2 = \frac{\omega_q R_0}{U_0}, c_1 = \frac{\omega_p R_0}{U_0}$.

The mathematical expression for important hemodynamical factors such as wall shear stress, flow rate and resistive impedance are illustrated as [39]:

$$\tau_w = -\left(\frac{\partial w}{\partial r}\right)_{r=R^*}, \tag{2.26}$$

$$Q^f = 2\pi \int_{R_1^*}^{R^*} wrdr, \tag{2.27}$$

$$\lambda = \frac{L(\frac{-\partial p}{\partial z})}{Q^f}. \tag{2.28}$$

2.3 Numerical Solution

2.3.1 Significance of Numerical Results

The governing equations (2.22) and (2.24) are non-linear coupled partial differential equations. In general, these equations don't admit exact solutions except in a few simple cases. Therefore, to solve these equations, various types of numerical methods have been designed. The usage of such technique is easier, handy and most importantly accurate due to availability of high speed computers and commercially available state of art softwares. As a result, the numerical approach should be used to deal with these equations. The Crank-Nicolson approach is an implicit strategy that has been proposed by various scholars in their research. It is the combination of the forward and backward Euler scheme at the n^{th} and $(n+1)^{th}$ level. Furthermore, it is second-order convergent in both space and time. After discretization and solving the resultant algebraic equations, we will get the velocity and temperature at the nodal points. Figures 2.2 depicts the Various shapes of the Au-GO/blood hybrid nanoparticles [86, 87].

Default values of parameters and thermodynamical properties of nanoparticles used in the present study are depicted in table 2.3 and the table 2.4 respectively.

Table 2.3: Default values of dimensionless parameters

parameter	B_2	Da	δ	h_m	Gr	Pr	Nr	Re	M	R_c	Br	β_i	β_e	e	B_1
Value	5	3	0.1	1	1	23	2	1	2	3	0.5	0.9	0.5	0.2	0.25

Table 2.4: Thermophysical Properties

Thermophysical Properties	Blood	Gold	Graphene
Density $[\rho(Kg/m^3)]$	1063	19320	1800
Electrical Conductivity $[\sigma(S/m)]$	6.67×10^{-1}	4.52×10^{7}	6.3×10^{7}
Thermal Expansion Coefficient $[\gamma * 10^{-}5(K^{-1})]$	0.18	1.4	28.4
Thermal conductivity $[\kappa(W/mK)]$	0.492	314	5000
Heat Capacity $[c_p(J/KgK)]$	3594	129	717

2.3.2 Discretization of Governing Equations

The governing equations are discretized as illustrated below:

$$\begin{aligned}
&\left[(1-\phi_2)\left[(1-\phi_1)+\phi_1\frac{\rho_{s1}}{\rho_f}\right]+\phi_2\frac{\rho_{s2}}{\rho_f}\right]Re\left[\frac{w_i^{k+1}-w_i^k}{dt}\right]=\frac{R_c}{R_c+r(i)}B_1[1+e\cos(c_1t^k)]\\
&+B_2\cos(c_2t^k+\chi)+\frac{[1+\beta_1^*h_m(1-(\frac{r(i)}{R_0})^m)]}{(1-\phi_1)^{2.5}(1-\phi_2)^{2.5}}\left[\frac{1}{2}\left(\frac{w_{i+1}^{k+1}-2w_i^{k+1}+w_{i-1}^{k+1}}{dx^2}+\frac{w_{i+1}^{k}-2w_i^{k}+w_{i-1}^{k}}{dx^2}\right)\right.\\
&\left.+\frac{1}{4(R_c+r(i))}\left(\frac{w_{i+1}^{k+1}-w_{i-1}^{k+1}}{dx}+\frac{w_{i+1}^{k}-w_{i-1}^{k}}{dx}\right)-\frac{(w_i^k+w_i^{k+1})}{2(R_c+r(i))^2}\right]\\
&-\frac{m\beta_1^*h_m(r(i))^{m-1}}{(1-\phi_1)^{2.5}(1-\phi_2)^{2.5}}\left[\frac{(w_{i+1}^{k+1}-w_{i-1}^{k+1}+w_{i+1}^{k}-w_{i-1}^{k})}{4dx}+\frac{(w_i^k+w_i^{k+1})}{2(R_c+r(i))}\right]+\\
&\left[(1-\phi_2)\left[(1-\phi_1)+\phi_1\frac{(\rho\beta)_{s1}}{(\rho\beta)_f}\right]+\phi_2\frac{(\rho\beta)_{s2}}{(\rho\beta)_f}\right](GrT_i^k))\Bigg)\\
&-\frac{1}{2}\frac{\sigma_{hnf}}{\sigma_f}M^2(w_i^k+w_i^{k+1})\left(\frac{\alpha_e}{\alpha_e^2+\beta_e^2}\right)\left(\frac{R_c}{R_c+r(i)}\right)^2-\frac{[1+\beta_1^*h_m(1-(\frac{r(i)}{R_0})^m)]}{(1-\phi_1)^{2.5}(1-\phi_2)^{2.5}}\frac{1}{2Da}(w_i^k+w_i^{k+1}),
\end{aligned}\tag{2.29}$$

$$\begin{aligned}
&\left[(1-\phi_2)\left[(1-\phi_1)+\phi_1\frac{(\rho C_p)_{s1}}{(\rho C_p)_f}\right]+\phi_2\frac{(\rho C_p)_{s2}}{(\rho C_p)_f}\right]\left[\frac{T_i^{k+1}-T_i^k}{dt}\right]=\frac{1}{RePr}\frac{\kappa_{hnf}}{\kappa_f}\Bigg[\\
&\left(\frac{T_{i+1}^{k+1}-2T_i^{k+1}+T_{i-1}^{k+1}}{2dx^2}+\frac{T_{i+1}^{k}-2T_i^{k}+T_{i-1}^{k}}{2dx^2}\right)+\frac{1}{4(R_c+r(i))}\left(\frac{T_{i+1}^{k+1}-T_{i-1}^{k+1}}{dx}\right.\\
&\left.+\frac{T_{i+1}^{k}-T_{i-1}^{k}}{dx}\right)\Bigg]+\frac{Nr}{RePr}\left[\frac{1}{2}\left(\frac{T_{i+1}^{k+1}-2T_i^{k+1}+T_{i-1}^{k+1}}{dx^2}+\frac{T_{i+1}^{k}-2T_i^{k}+T_{i-1}^{k}}{dx^2}\right)\right.\\
&\left.+\frac{1}{4(R_c+r(i))}\left(\frac{T_{i+1}^{k+1}-T_{i-1}^{k+1}}{dx}+\frac{T_{i+1}^{k}-T_{i-1}^{k}}{dx}\right)\right]+\frac{\sigma_{hnf}}{\sigma_f}\frac{\kappa_{hnf}}{\kappa_f}\frac{Ec}{Pr}\left(\frac{R_c}{R_c+r(i)}\right)^2M^2w_i^2,
\end{aligned}\tag{2.30}$$

The boundary and initial conditions associated with the governing equations are discretized as follows:

$$w_1^{k+1}=0,\quad T_1^{k+1}=1,\quad w_{N+1}^{k+1}=0,\quad T_{N+1}^{k+1}=1, w_i^1=0,\quad T_i^1=0. \tag{2.31}$$

The domain is divided into $N+1\times M+1$ grid points. The spatial variable is uniformly discretized into N+1 points as $x_i(i=1,2,...,N+1)$ with step-size of $\Delta x=1/(N+1)$. Similarly, time level is discretized into $M+1$ points as $t^k=(k-1)\Delta t$ with the time step as $\Delta t=1/(M+1)$. Although, this method is unconditionally stable for both value of Δx and Δt but we have chosen the step size as $\Delta t=10^{-4}$ and $\Delta x=10^{-4}$. The tridiagonal system of equations are obtained after implementing CN scheme, which is solved using the Tri-diagonal Matrix Algorithm (TDMA).

Eqn. (2.29) written in tri-diagonal system as:

$$R_i^k w_{i-1}^{k+1}+S_i^k w_i^{k+1}+U_i^k w_{i+1}^{k+1}=R_i^{'k} w_{i-1}^k+S_i^{'k} w_i^k+U_i^{'k} w_{i+1}^k+F_i^k, \tag{2.32}$$

where,

$$U_i^k=-\frac{[1+\beta_1^* h_m(1-(\frac{r}{R_0})^m)]}{(1-\phi_1)^{2.5}(1-\phi_2)^{2.5}}\left(\frac{dt}{2dx^2}+\frac{dt}{4(R_c+r(i))}\right)+\frac{m\beta_1^* h_m(r(i))^{m-1}}{(1-\phi_1)^{2.5}(1-\phi_2)^{2.5}}\left(\frac{dt}{4dx}\right),$$

$$\begin{aligned}S_i^k=Re\left[(1-\phi_2)\left[(1-\phi_1)+\phi_1\frac{\rho_{s1}}{\rho_f}\right]+\phi_2\frac{\rho_{s2}}{\rho_f}\right]-\frac{[1+\beta_1^* h_m(1-(\frac{r}{R_0})^m)]}{(1-\phi_1)^{2.5}(1-\phi_2)^{2.5}}\left(-\frac{dt}{dx^2}-\frac{dt}{2(R_c+r(i))^2}\right)\\ +\frac{m\beta_1^* h_m(r(i))^{m-1}}{(1-\phi_1)^{2.5}(1-\phi_2)^{2.5}}\left(\frac{dt}{2(R_c+r(i))}\right)+\frac{dt}{2}\frac{\sigma_{hnf}}{\sigma_f}M^2\frac{\alpha_e}{\alpha_e^2+\beta_e^2}\left(\frac{R_c}{R_c+r(i)}\right)^2\\ +\frac{[1+\beta_1^* h_m(1-(\frac{r(i)}{R_0})^m)]}{(1-\phi_1)^{2.5}(1-\phi_2)^{2.5}}\left(\frac{dt}{2Da}\right),\end{aligned}$$

$$R_i^k=-\frac{[1+\beta_1^* h_m(1-(\frac{r}{R_0})^m)]}{(1-\phi_1)^{2.5}(1-\phi_2)^{2.5}}\left(\frac{dt}{2dx^2}-\frac{dt}{4(R_c+r(i))}\right)+\frac{m\beta_1^* h_m(r(i))^{m-1}}{(1-\phi_1)^{2.5}(1-\phi_2)^{2.5}}\left(-\frac{dt}{4dx}\right),$$

$$U_i^{'k}=\frac{[1+\beta_1^* h_m(1-(\frac{r}{R_0})^m)]}{(1-\phi_1)^{2.5}(1-\phi_2)^{2.5}}\left(\frac{dt}{2dx^2}+\frac{dt}{4(R_c+r(i))}\right)-\frac{m\beta_1^* h_m(r(i))^{m-1}}{(1-\phi_1)^{2.5}(1-\phi_2)^{2.5}}\left(\frac{dt}{4dx}\right),$$

$$S_i^{\prime k} = Re\left[(1-\phi_2)\left[(1-\phi_1)+\phi_1\frac{\rho_{s1}}{\rho_f}\right]+\phi_2\frac{\rho_{s2}}{\rho_f}\right]+\frac{[1+\beta_1^* h_m(1-(\frac{r}{R_0})^m)]}{(1-\phi_1)^{2.5}(1-\phi_2)^{2.5}}\left(-\frac{dt}{dx^2}\right.$$
$$\left.-\frac{dt}{2(R_c+r(i))^2}\right)-\frac{m\beta_1^* h_m(r(i))^{m-1}}{(1-\phi_1)^{2.5}(1-\phi_2)^{2.5}}\left(\frac{dt}{2(R_c+r(i))}\right)-\frac{dt}{2}\frac{\sigma_{hnf}}{\sigma_f}M^2$$
$$-\frac{[1+\beta_1^* h_m(1-(\frac{r(i)}{R_0})^m)]}{(1-\phi_1)^{2.5}(1-\phi_2)^{2.5}}\left(\frac{dt}{2Da}\right),$$

$$R_i^{\prime k} = \frac{[1+\beta_1^* h_m(1-(\frac{r}{R_0})^m)]}{(1-\phi_1)^{2.5}(1-\phi_2)^{2.5}}\left(\frac{dt}{2dx^2}-\frac{dt}{4(R_c+r(i))}\right)+\frac{m\beta_1^* h_m(r(i))^{m-1}}{(1-\phi_1)^{2.5}(1-\phi_2)^{2.5}}\left(\frac{dt}{4dx}\right),$$

$$F_i^k = dt\frac{B_1 R_c}{(R_c+r(i))}[1+e\cos(c_1 t^k)]+B_2 dt\cos(c_2 t^k+\chi)+dt\left[(1-\phi_2)\left[(1-\phi_1)+\phi_1\frac{(\rho\beta)_{s1}}{(\rho\beta)_f}\right]\right.$$
$$\left.+\phi_2\frac{(\rho\beta)_{s2}}{(\rho\beta)_f}\right](GrT_i^k).$$

The tri-diagonal system corresponding to equation (2.30) is obtained as:

$$A_i^k T_{i-1}^{k+1}+B_i^k T_i^{k+1}+J_i^k T_{i+1}^{k+1} = A_i^{\prime k} T_{i-1}^k + B_i^{\prime k} T_i^k + J_i^{\prime k} T_{i+1}^k + D_i^k, \tag{2.33}$$

where,

$$A_i^k = -\frac{1}{RePr}\frac{\kappa_{hnf}}{\kappa_f}\left(\frac{dt}{2dx^2}-\frac{1}{4(R_c+r(i))}\frac{dt}{dx}\right)-\frac{Nr}{RePr}\left(\frac{dt}{2dx^2}-\frac{1}{4(R_c+r(i))}\frac{dt}{dx}\right),$$

$$B_i^k = \left[(1-\phi_2)\left[(1-\phi_1)+\phi_1\frac{(\rho C_p)_{s1}}{(\rho C_p)_f}\right]+\phi_2\frac{(\rho C_p)_{s2}}{(\rho C_p)_f}\right]+\frac{1}{RePr}\frac{\kappa_{hnf}}{\kappa_f}\frac{dt}{dx^2}+\frac{Nr}{RePr}\left(\frac{dt}{dx^2}\right),$$

$$J_i^k = -\frac{1}{RePr}\frac{\kappa_{hnf}}{\kappa_f}\left(\frac{dt}{2dx^2}+\frac{1}{4(R_c+r(i))}\frac{dt}{dx}\right)-\frac{Nr}{RePr}\left(\frac{dt}{2dx^2}+\frac{1}{4(R_c+r(i))}\frac{dt}{dx}\right),$$

$$A_i^{\prime k} = \frac{1}{RePr}\frac{\kappa_{hnf}}{\kappa_f}\left(\frac{dt}{2dx^2}-\frac{1}{4(R_c+r(i))}\frac{dt}{dx}\right)+\frac{Nr}{RePr}\left(\frac{dt}{2dx^2}-\frac{1}{4(R_c+r(i))}\frac{dt}{dx}\right),$$

$$B_i^{'k} = \left[(1-\phi_2)\left[(1-\phi_1)+\phi_1\frac{(\rho C_p)_{s1}}{(\rho C_p)_f}\right]+\phi_2\frac{(\rho C_p)_{s2}}{(\rho C_p)_f}\right] - \frac{1}{RePr}\frac{K_{hnf}}{K_f}\frac{dt}{dx^2} - \frac{Nr}{RePr}\left(\frac{dt}{dx^2}\right),$$

$$J_i^{'k} = \frac{1}{RePr}\frac{\kappa_{hnf}}{\kappa_f}\left(\frac{dt}{2dx^2}+\frac{1}{4(R_c+r(i))}\frac{dt}{dx}\right) + \frac{Nr}{RePr}\left(\frac{dt}{2dx^2}+\frac{1}{4(R_c+r(i))}\frac{dt}{dx}\right),$$

$$D_i^k = dt\frac{\sigma_{hnf}}{\sigma_f}\frac{\kappa_{hnf}}{\kappa_f}\frac{Ec}{Pr}\left(\frac{R_c}{R_c+r(i)}\right)^2 M^2 w_i^2$$

.

2.4 Results & Discussion

The current study is validated using the published work of Elnaqeeb et al. [51], as shown in figure 2.3 and figure 2.4. To validate the current study, the effect of radiation and multiple stenoses was ignored. The copper blood flow model is considered under the condition of a straight artery $(R_c = 0)$.

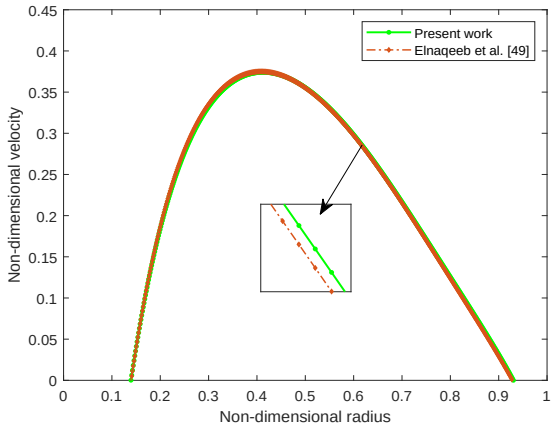

Figure 2.3: Velocity profile for $Gr = 5$

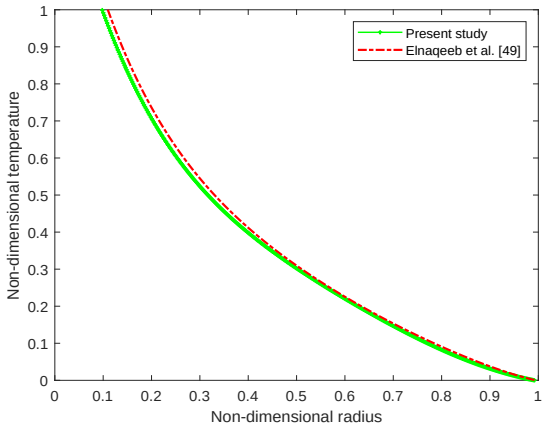

Figure 2.4: Temperature profile for $\sigma = 0.3$

The temperature at the clot is assumed to be the same as the stenosis wall. The velocity and temperature profiles are drawn by assuming the same set of values as in [51]. Figure 2.3 depicts the velocity profile for $Gr = 5$, and figure 2.4 replicates the validation of the present study for the temperature profile at clot height $\sigma = 0.3$. Both the figures in the present study are in good agreement with the [51] work.

2.4.1 Axial Velocity

The fluctuation of a velocity profile for different values of hematocrit viscosity is depicted in figure 2.5. In the physiological system, blood viscosity varies depending on the hematocrit level due to the composition of red blood cells. From the figure, it can be observed that the fluid velocity reduces as the hematocrit level increases. For a change of hematocrit level $h_m = 0.7$ to $h_m = 1$, blood velocity reduces to 24.81 % and 23.81 % at the maximum position $r = 0.5$ for stenosis and clot respectively. The influence of radius of curvature on velocity profile is seen in figure 2.6. Initially, the effect of curvature not comes into the picture till $z = 0.3$, after it the fluid velocity increases with the increase in its radius of curvature. The reason for this behaviour is that the curved channel shrinks to the straight tube as the value of R_c increases. The higher the value of R_c, the less obstruction comes into the fluid path, resulting in a higher fluid velocity. Figure 2.7 illustrates the declining effect of the magnetic field on the velocity profile. As the magnetic field parameter increases, it causes the magnetized particle present in the blood to flow in the rotational motion. The viscosity in blood plasma is suspended due to this irrotational motion of red blood cells, resulting in the formation of a resistive force known as Lorentz force. The shift in the velocity profile for both the hall and ion slip parameters is seen in figures 2.8 and 2.9. Both

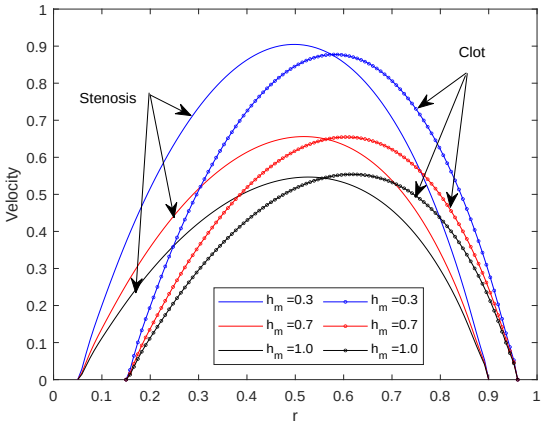

Figure 2.5: Velocity profile for varying h_m

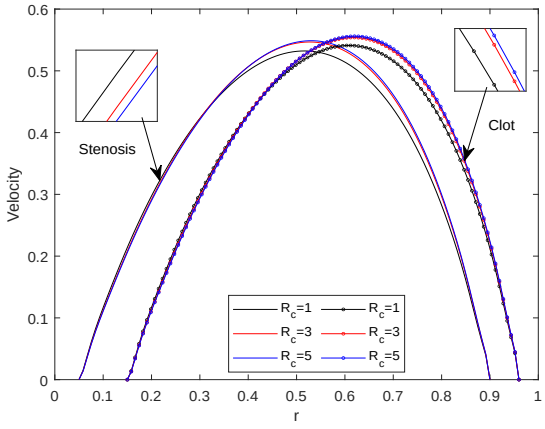

Figure 2.6: Velocity profile for varying R_c

parameters are inversely affected by the strength of the resistive Lorentzian drag due to the enhancement in the cyclotron frequency that result in an increase in the velocity profile. The influence of nanoparticle concentration on the velocity profile is seen in figure 2.10. The Au-GO/blood hybrid nanofluid has a higher velocity than the Au/blood and GO/blood nanofluids, indicating that the inclusion of additional nanoparticles can assist surgeons in

controlling blood flow. It can be inferred from the figure that the velocity profile enhances by 97.27% if only an Au nanoparticle is added to the base fluid (blood), while the change is approximately 200% for the GO nanoparticle. If both nanoparticles are added to the base fluid, then the velocity profile enhances by nearly 300%. This results reveals new insights for assessing the accuracy of theoretical studies of more complex in nature and to understand that how the particular nature of blood influences with different nanoparticle.

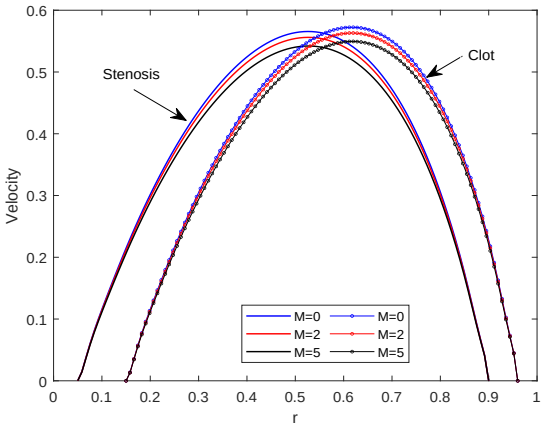

Figure 2.7: Velocity profile for varying M

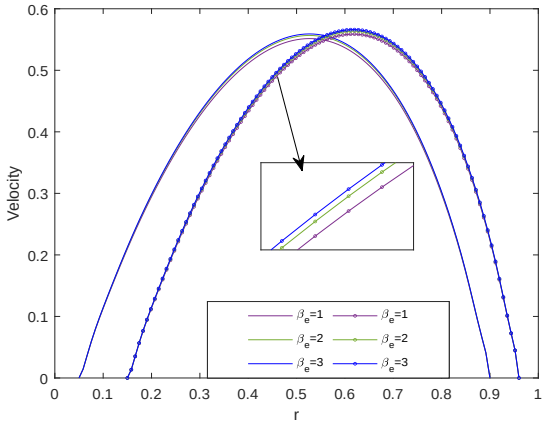

Figure 2.8: Velocity profile for varying β_e

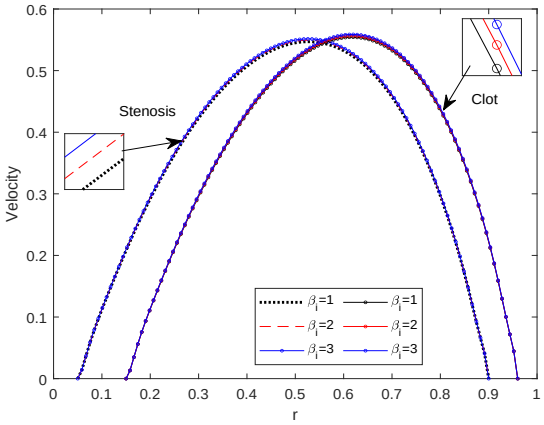

Figure 2.9: Velocity profile for varying β_i

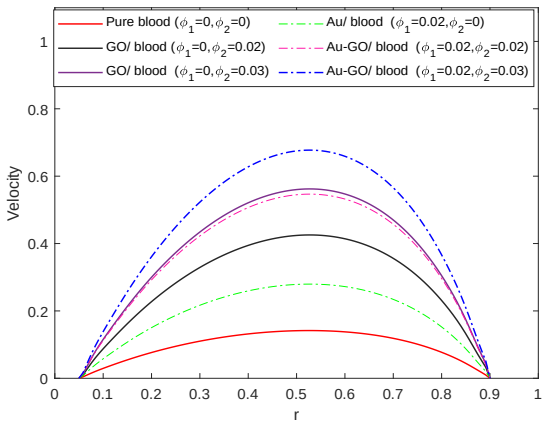

Figure 2.10: Variation in velocity with volume fraction of Au and GO

2.4.2 Temperature Profile

Figure 2.11 shows the effect of radiation on the temperature profile for both clot and stenotic region. From the figure, it can be observed that the temperature enhances if the radiation parameter is taken into consideration.

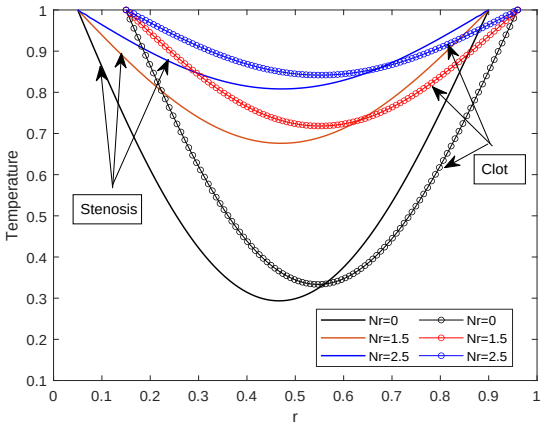

Figure 2.11: Temperature profile for varying Nr

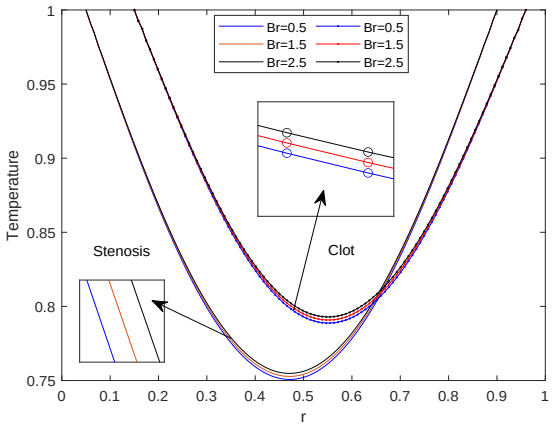

Figure 2.12: Temperature profile for varying Br

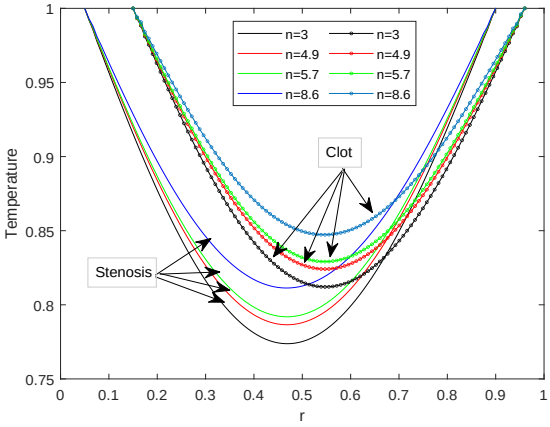

Figure 2.13: Temperature profile for varying nanoparticle shape parameter

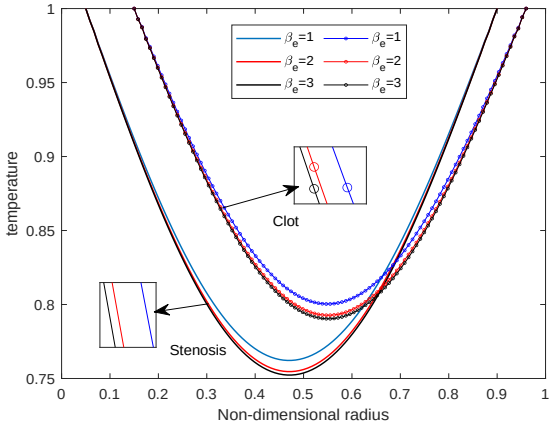

Figure 2.14: Temperature profile for varying β_e

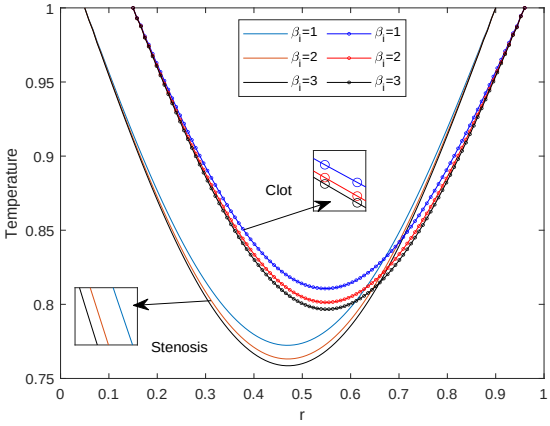

Figure 2.15: Temperature profile for varying β_i

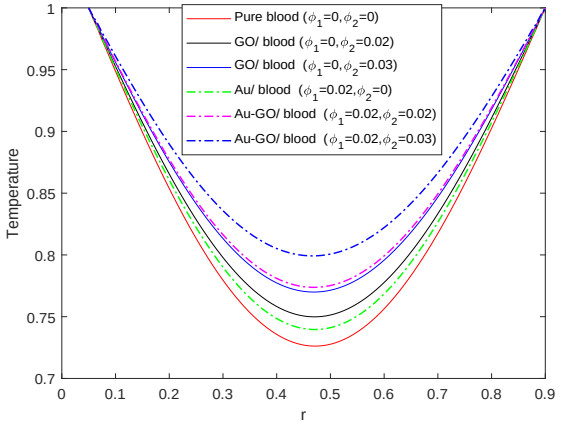

Figure 2.16: Variation in Temperature profile with volume fraction of Au and GO

The increment in temperature profile by 130% can be observed if the radiation effect is considered in the comparison of without radiation effect. The reason for this increase in the temperature profile is due to the generation of more thermal energy. Thus, it shows that the radiation parameter is an essential factor influencing the temperature profile. The outcome will be useful for measuring the rise of temperature during hyperthermia treatment of tumour and magnetic modified nanoparticles drug delivery system in diseased artery. In pathological circumstances, increasing the radiation dosage can assist surgeons in raising the temperature profile to eliminate cancerous cells while sparing healthy cells. Figure 2.12 illustrates the temperature profile for varying Br numbers. It is noted that the temperature profile enhances with an increase in the Br number. The Brinkman number is the ratio of heat generated by the viscous dissipation and heat produced by molecular conduction. So, for higher values of Br number, the heat generated by viscous dissipation is very small and slows the heat conduction, thus, raising the temperature profile. The advantage of nanotechnology is the ability to design and optimise nanoparticles to increase their functionalities and properties to meet different requirements. Nanotherapeutics rely on effective cellular uptake and tumour permeability of nanoparticles, both of which are affected by nanoparticle shape and size. A nanoparticle's optimal shape is also determined by the specific location and type of targeted tissue. Figure 2.13 illustrates how nanoparticle shape parameters ($n = 3$ sphere, $n = 4.9$ cylinder, $n = 5.7$ platelets, and $n = 8.6$ brick see figure 2.2) effect the temperature profiles in clot and stenotic arteries. The temperature profile will grow as the size of the nanoparticles rises due to the increase in its thermal conductivity. The significance of the role of shape of nanoparticles is shown graphically and it is observed that the temperature profile enhances by only 1.64% if cylindrical nanoparticles used in place of spherical nanoparticle shape, while, there is 4.85% enhancement is observed if the blade shape of the nanoparticles is taken in place of spherical nanoparticle. The impact of Hall and ion slip parameters on temperature profile are illustrated in figure 2.14 and figure 2.15, respectively. Due to the magnetic damping force, both parameters show the opposite effect with the temperature profile. Figure 2.16 illustrates the relationship between the nanoparticles and hybrid nanoparticles on the temperature profile. The temperature profile for pure blood is lower, but its temperature increases as the nanoparticles are added. The temperature profile for Au is lower than GO, and it gets further increases if hybrid nanoparticles are injected into the bloodstream. As a result, the surgeon will be able to regulate the blood flow during the surgical procedure.

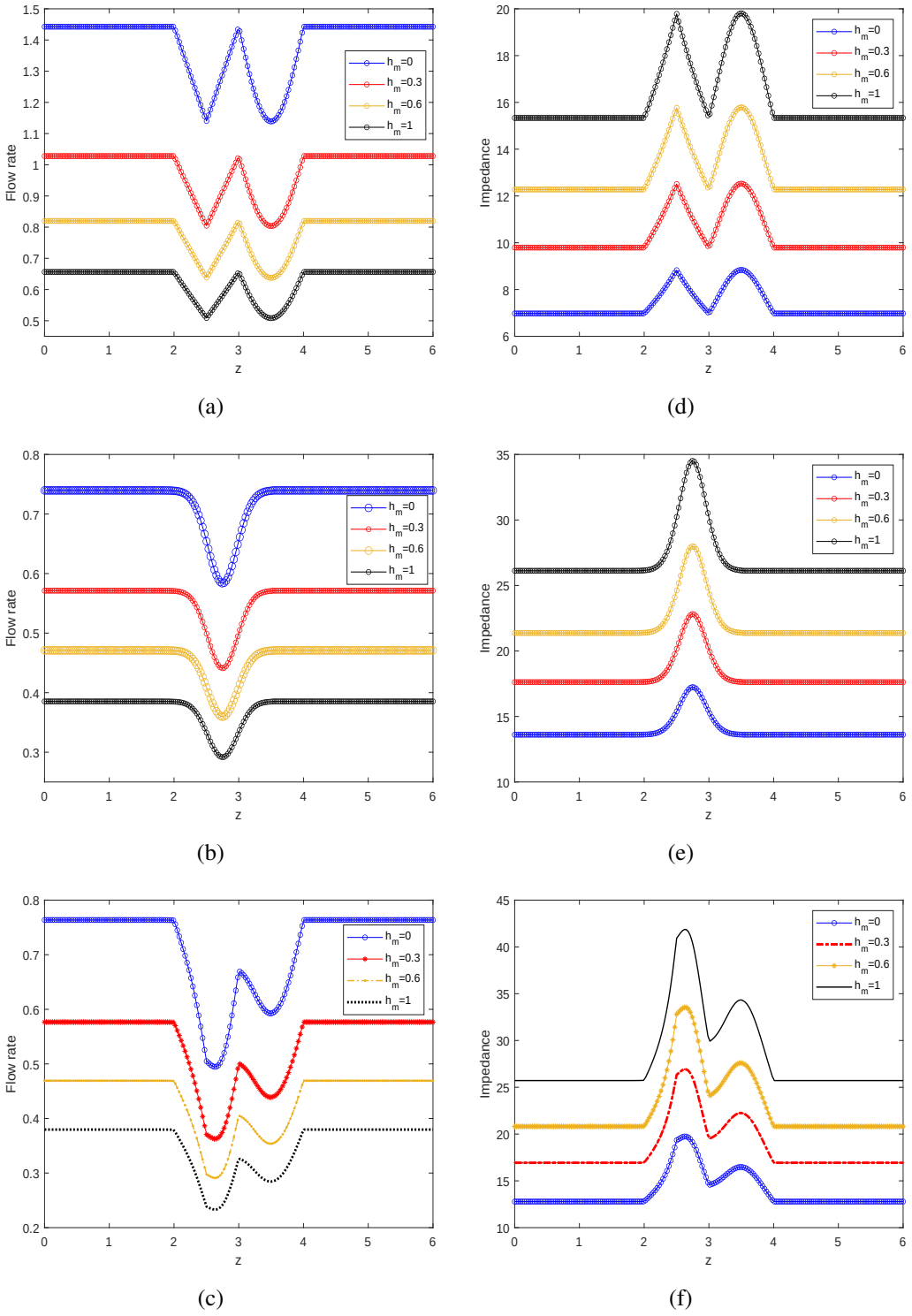

Figure 2.17: Flow rate and Impedance for varying h_m, (a) without clot, (b) without stenosis, (c) both clot and stenosis present, (d) without clot, (e) without stenosis, (f) both clot and stenosis present.

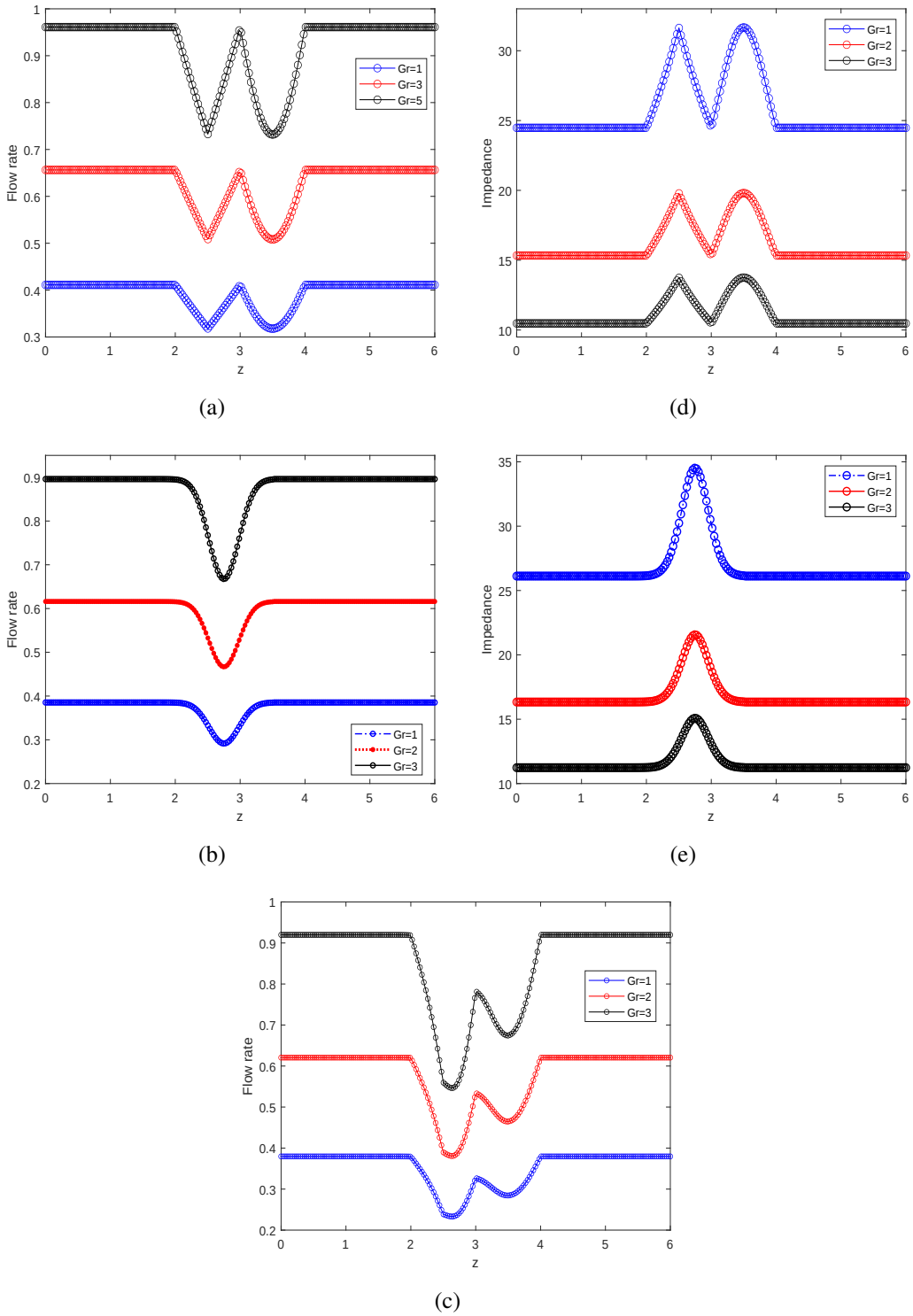

Figure 2.18: Flow rate and Impedance for *Gr*, (a) without clot, (b) without stenosis, (c) both clot and stenosis present, (d) without clot, (e) without stenosis, (f) both clot and stenosis present.

2.4.3 Resistance Impedence and Flow Rate

As given in equation (2.27), the volumetric flow rate is the quantity of fluid (blood) that goes through the bloodstream in a given amount of time. Due to the obstacles present in the artery, blood flow experiences resistance, known as resistance impedance, which impedes its flow. It is defined as the ratio of pressure drop to flow rate, essential for the body organs to regulate the blood flow. Figures 2.17(a)- 2.17(c) illustrate the relationship between flow rate and hematocrit dependent viscosity. From the figures, it can be observed that the flow rate decreases as the parameter h_m increases from 0 to 1. Figure 2.17(c) shows the flow rate in the presence of both clot and stenosis, whereas figures 2.17(a) and 2.17(b) show the flow rate in the absence of clot and stenosis, respectively. Flow rate decreases in the presence of both clot and stenosis compared to the other two cases. The flow rate decreases as the parameter h_m increases from 0 to 1. This increase in parameter h_m signifies a more concentration of red blood cells, which will increase its viscosity. Thus, it reduces the blood flow rate by offering more resistance to the flow; therefore, the resistance impedance increases as h_m increases, as shown in figures 2.17(d)-2.17(f). For increasing the value of Gr, 2.18(a)-2.18(c) and 2.18(d)-2.18(f) show the growing flow rate pattern and decreasing impedance profile, respectively. Consider the figures 2.18(c) and 2.18(f) for a particular value of $Gr = 1$. Initially, the flow rate and Impedance will be the same for all three cases until $z = 2$; afterwards, it changes due to a clot presence in the region $z = 2$ to $z = 3$. And the flow rate becomes the same again after $z = 4$. The concentration of nanoparticles in the bloodstream fluctuates, and an increase in Gr tends to increase buoyancy, which will lead to less resistance to the flow and thus, flow rate increases.

2.4.4 Wall Shear Stress

In an arterial flow, the force exerted by the wall on the per unit area of the fluid along the tangential direction is known as Wall shear stress (WSS). The disturbance in the normal hemodynamic flow is the primary cause of arterial diseases, for example, hypertension, cerebral strokes etc. Thus, it is essential to know blood flow behaviour at the walls and can easily be calculated by interpreting the velocity pattern along the arterial walls using equation 2.26. Figure 2.19 (a) depicts the WSS profile for hemodynamic viscosity parameter h_m. In the present study, both cases constant viscosity $h_m = 0$ and variable viscosity $h_m \neq 0$ are considered. The WSS profile decreases as the parameter h_m increases from 0 to 1. The sudden decrease in the WSS profile can be seen for a change of constant viscosity $h_m = 0$ to non-constant viscosity $h_m = 0.3$.

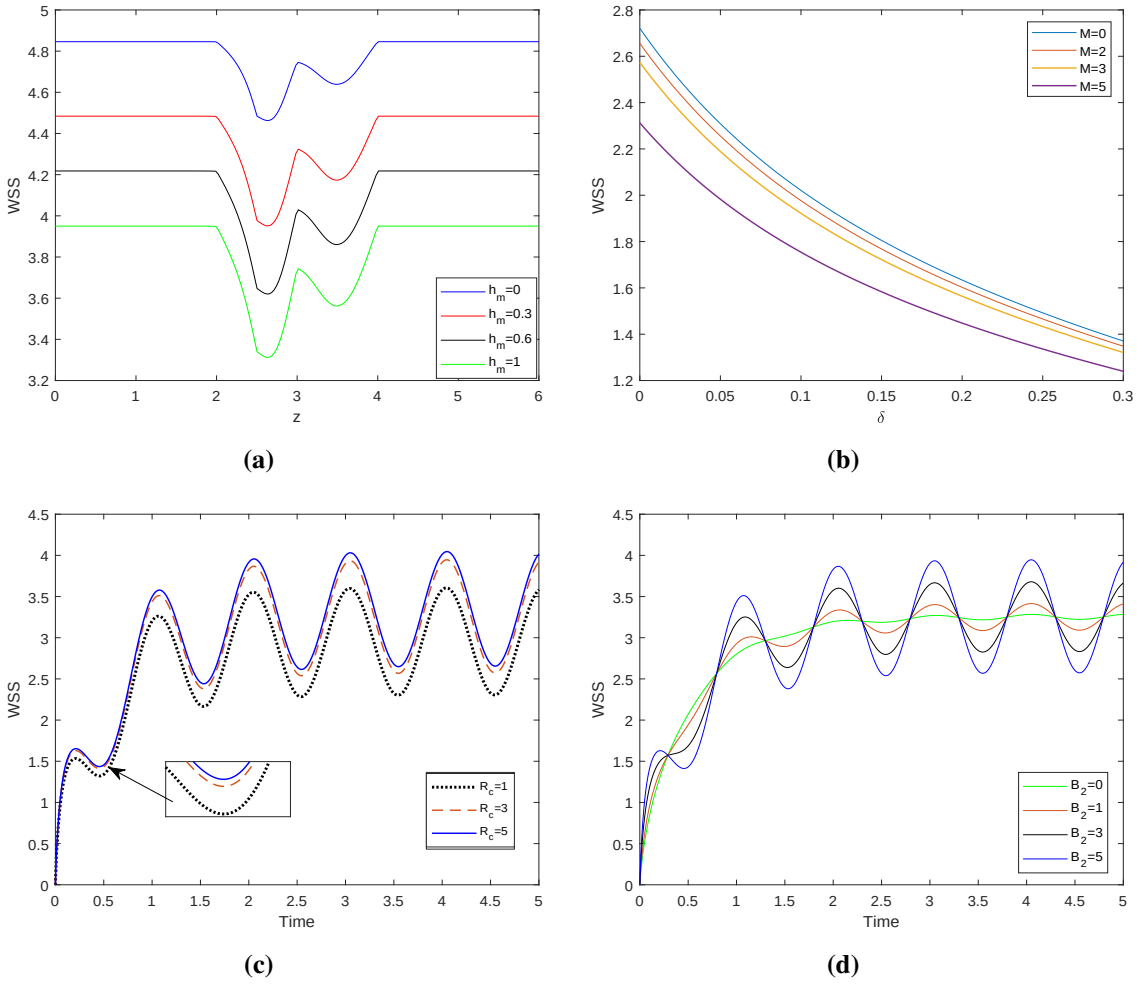

Figure 2.19: WSS of stenosis for different values of parameters, (a) Variation in WSS with h_m, (b) Variation in WSS with M and δ, (c) Variation in WSS with varying R_c , (c) Variation in WSS with varying B_2.

This sudden change is due to the shift in hematocrit level present in the blood, which causes the change in its viscosity that impedes its flow and is further responsible for the decline in the WSS profile. Figure 2.19 (b) portrays the declining profile for increasing values of M as well as stenotic depth. As the magnetic field parameter M increases, the resistive Lorentz force comes into the picture and resists the fluid flow. Similarly, with stenotic depth, the flow will experience more resistance in its path resulting in a decline in the WSS profile. Figure 2.19 (c) illustrates the time series graph for varying R_c. Initially, the WSS increases and afterwards, it shows the periodic pattern for different values of R_c. The WSS grows as the value of the R_c parameter increases, indicating that the curve artery will become a straight artery as the value of R_c increases. This change in artery shape shows the increased velocity along the arterial wall for the higher value of R_c, indicating that the WSS profile rises with an increase in R_c. Figure 2.19 (d) demonstrates the effect of body acceleration

on the WSS profile. The fluctuation in amplitude increases about the mean position as the parameter B_2 increases, as depicted in the graph, which shows the increasing WSS profile with an increase in the body acceleration term B_2 from 0 to 5. This rise in the WSS profile along the axial direction is caused by the higher velocity profile near the surface.

2.4.5 Velocity Contour

In this section, the velocity contour is drawn by varying different parameters. These contours give a pictorial representation of blood flow inside an artery, helpful in understanding the hemodynamic characteristics of the blood. Figure 2.20 show the velocity contour by changing the height of the clot and stenosis.

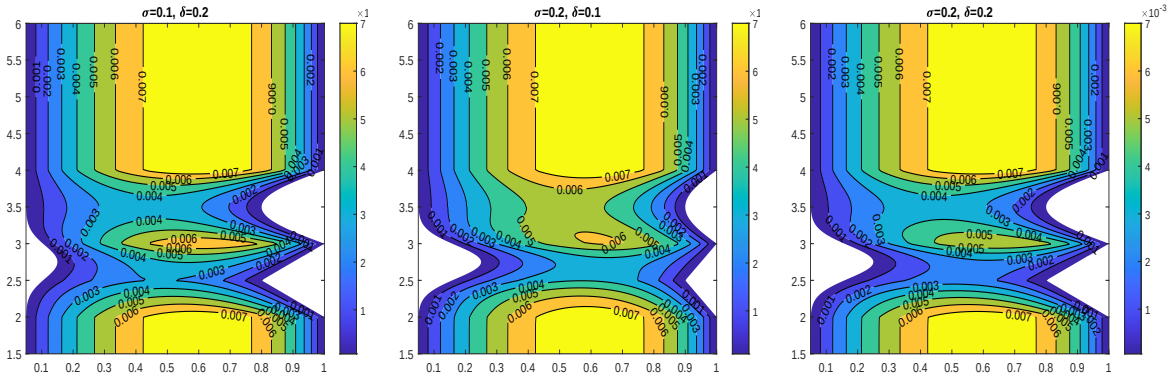

(a) **(b)** **(c)**

Figure 2.20: Variation in blood flow patterns for diseased artery segment (a) $\sigma = 0.1, \delta = 0.2$, (b) $\sigma = 0.2, \delta = 0.1$ (c) $\sigma = 0.2, \delta = 0.2$.

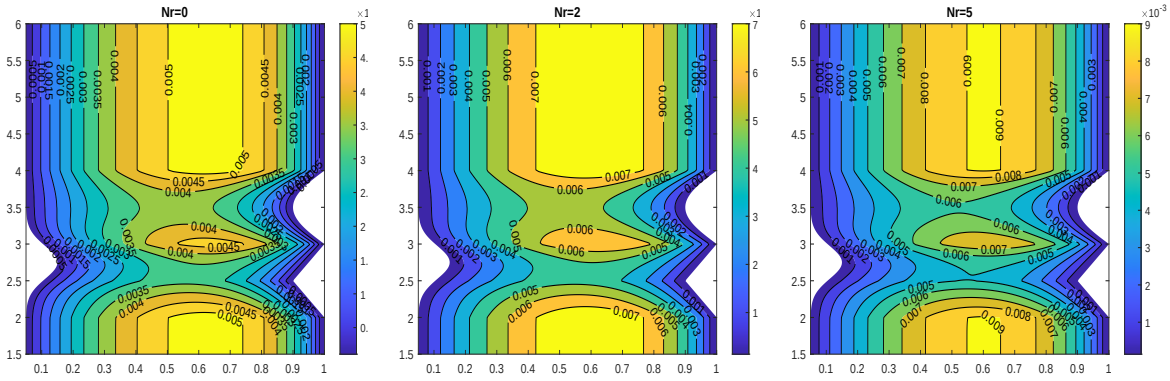

(a) **(b)** **(c)**

Figure 2.21: Variation in blood flow patterns for different values of radiation parameter, (a) $Nr = 0$, (b) $Nr = 2$, (c) $Nr = 5$.

The figure shows that the velocity profile decreases with increased clot and stenosis size. In all three cases, the maximum velocity attains by the blood is the same, which is 0.007. However, as we increase clot and stenosis size, the velocity profile decreases in the central region between clot and stenosis. Figure 2.20 (c) displays the velocity contour for the height of clot and stenosis with $\sigma = 0.2$ and $\delta = 0.2$, respectively.

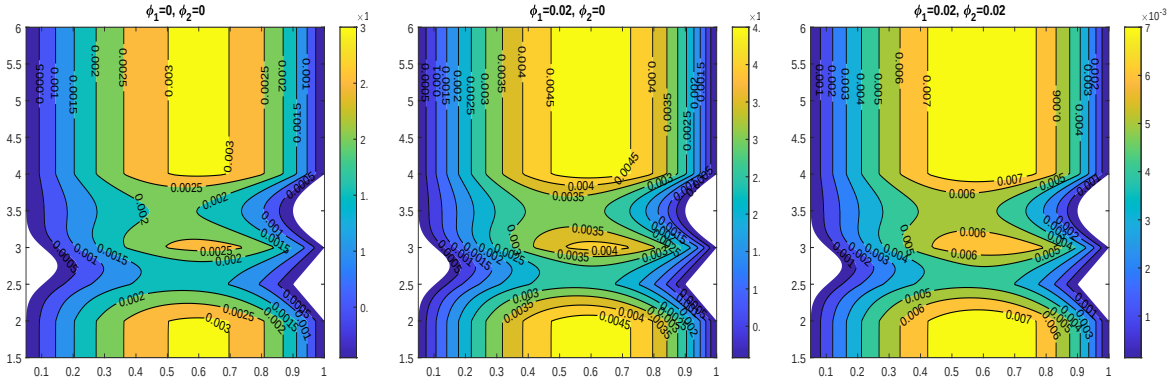

(a) **(b)** **(c)**

Figure 2.22: Variation in blood flow patterns for different volume fractions of nanoparticles, (a) $\phi_1 = 0, \phi_2 = 0$, (b) $\phi_1 = 0, \phi_2 = 0.02$, (c) $\phi_1 = 0.02, \phi_2 = 0.02$.

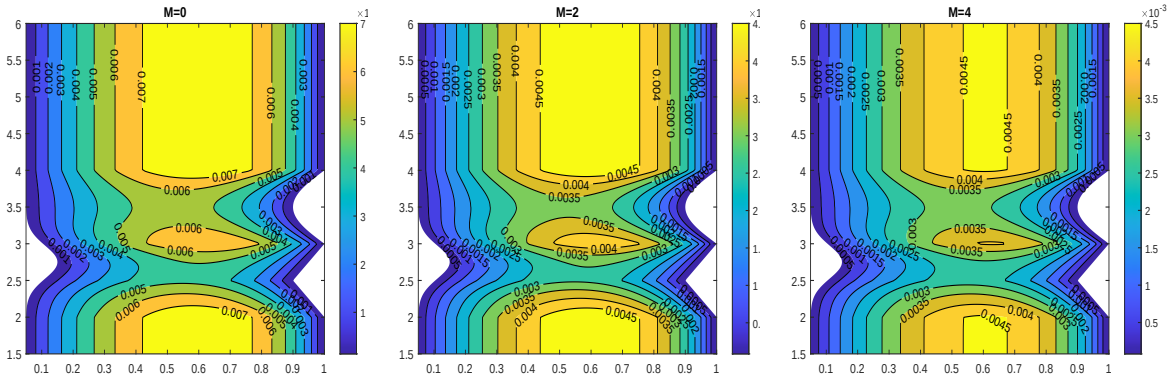

(a) **(b)** **(c)**

Figure 2.23: Variation in blood flow patterns for different magnetic field parameter, (a) $M = 0$, (b) $M = 2$, (c) $M = 4$.

From the comparison of velocity contour 2.20 (c) with 2.20 (a) and 2.20 (b), it is clearly noted that increasing the height of the clot and delta provides resistance to the flow and reduces the blood velocity. Figure 2.21 portrays the velocity contour for varying values of radiation parameter Nr. The maximum fluid velocity increases from 0.005 to 0.009. The fluctuation in the velocity pattern is caused by Nr indirect influence on the momentum equation. It can also be noticed from the figure that the stenosis and clot shape cause resistance

in the flow pattern. Figure 2.22 illustrates the velocity contour for varying concentrations of nanoparticles. Figure 2.22 displays the velocity pattern of pure blood, and the velocity pattern increases when the Au nanoparticle is added to the blood. Furthermore, the addition of second nanoparticles GO improves the flow pattern, as seen in figure 2.22 . Figure 2.23 depicts the decrease in velocity pattern as the magnetic field value M increases, which is consistent with figure 2.7. The maximum fluid velocity for $M = 0$ is 0.007, which decreases to 0.0045. The declination in the velocity profile results from the resistive Lorentz force.

2.5 Conclusion

A mathematical model portraying the multiple stenosis with thrombosis at the center of the artery has been analyzed in this paper. The flow is subjected to the strong magnetic field, and thermal radiation, Joule heating, Hall and ion slip effect have been considered. Au and GO nanoparticles are added along with the base fluid (blood). The hybrid nanoparticles are formed by integrating the multiple nanoparticles in the base fluid. The Au-GO hybrid nanoparticles and their different shapes have been considered in this study. The governing mathematical equations are simplified using the mild stenosis assumption and neglecting the induced magnetic field. The resulting equations are discretized and solved using the Crank-Nicolson method. The effect of different pertinent parameters on velocity, temperature, wall shear stress, Impedance and velocity contour is displayed. The significant outcomes of the study are summarized below:

- The velocity profile declines with an increase in the hematocrit dependent viscosity, Hall and ion slips parameter, whereas it shows the declining nature for radius of curvature and magnetic field parameter.
- The hybrid nanoparticles Au-GO/blood has higher temperature profile as compared to pure blood and unitary nanopartices as the thermal conductivity increases with an increase in nanoparticles concentration.
- Increasing the Grashof number Gr increases the fluid velocity, whereas the opposite trend is observed with Impedance.
- The significant decline in flow velocity is observed for an increase in the stenosis and clot height.
- Increasing the Hall and ion slips parameter causes the increment in the fluid velocity due to an enhancement in the cyclotron frequency of the particles.

- The thermal conductivity increases with an increase in the nanoparticles shapes, resulting in a higher temperature profile.

The present study may be helpful in radiological investigations such as magnetic resonance angiography (MRA) to capture the abnormalities of the artery. The hybrid nanoparticles Au-GO/blood have been considered due to their application in nanomedicine and the biomedical field. The Au nanoparticles have numerous applications due to their inert nature, stability, and anti-bacterial properties. Along with, the graphene oxide (GO) nanoparticles have been used, which has high drug loading efficiency, large surface area, and better controlled released property. These properties make the GO nanoparticles act like nanocarriers. The non-invasive nature of the strong magnetic field can guide the nanoparticles to reach the desired location. Thus, the present study gives insight into the treatment of stenosis and other abnormalities without surgery and reduces post-surgical complications.

Chapter 3

Entropy Generation Optimization for Electroosmotic MHD Fluid Flow over the Curved Stenosed Artery in the Presence of Thrombosis [1]

Young [88] analyzed the deposition of plaque along the lumen of the artery disturbed the blood flow and led to mechanical processes advancing in intimal cell proliferation. Flow separation is the main factor in the development of vascular disorders, suggested by Mustapha et al. [89] . They analyzed the unsteady MHD fluid flow through an irregular multi-stenosed arteries and concluded that the flow separation zone shrank with increasing the Hartmann number value. Changdar and De [25] discussed the nanoparticle application as drug delivery in the blood flow through an irregular stenosed artery by considering single- and discrete-phase models. Gandhi et al. [90] discussed magnetic hybrid nanoparticle (Au-Al_2O_3/blood) based drug delivery through a bell-shaped occluded artery with joule heating, viscous dissipation and variable viscosity. The application of blood with the applied magnetic field has extensive applications in the biomedical and engineering fields. Kolin [91] first introduced the concept of MHD in the medical field. The experimental results indicate that when a conducting fluid, such as human blood, is exposed to a magnetic field strength of 10 T, it experiences a retarding force that leads to a 30% decrease in flow. Moreover, the application of an external electric field results in the emergence of an electro-osmotic force, which in turn causes the migration of an electrolyte within a specific conduit. When the conduit is placed in an electrolytic medium, it induces an electrostatic response in which positively charged particles are drawn towards its surface. In contrast, negatively charged ions are pushed away. The Electric Double Layer (EDL) formation occurs due to this phenomenon. Initially, Melcher and Woodson [92] investigated electrically charged fluid dynamics, also known as electrokinetics or Electrohydrodynamics (EHD). The focus of their study lies in

[1] A considerable part of this chapter is published in *Scientific Reports.* 18;13(1):15441

the examination of the behaviour and relationships between ionised particles and the surrounding fluids. Additionally, they investigate the mechanisms that facilitate the movement of fluids, including electrostatics, electrophoresis, and electro-osmosis, among other related phenomena. Rice and Whitehead [93] applied the Debye-Huckel approximation for the electrokinetic flow through narrow capillaries. In a recent study, Nooren et al. [94] looked at how Joule heating and various zeta functions affected MHD nanofluid in a microchannel. Their study revealed that increases in the zeta potential retard fluid motion, an essential medical phenomenon, regulating blood flow. This retarding nature occurs due to the presence of impregnable EDL.

Abdelsalam et al. [30] investigated the hemodynamic characteristics of nanofluid flow in a diseased artery affected by both stenosis and aneurysm. The study also considered the influence of electroosmotic forces and the size of the nanoparticles. The study by Akram et al. [32] aimed to investigate the electroosmosis impact by comparing the modified Buongiorno and Tiwari-Das model. The investigation demonstrated that the modified Buongiorno model exhibits superior performance as a viscosity model compared to the Tiwari-Das model. Shahzadi et al. [95] conducted a study that aimed to examine the impact of electroosmotic force on the oblique stenosed aneurysmal artery. The researchers utilised a fractional model based on second-grade principles, incorporating ternary nano particles. They placed particular emphasis on the potential advantages of their study in augmenting drug transportation.

Blood is a very complex and marvellous fluid that nurtures life. Over the past few decades, scientists and researchers have been studying to uncover the perplexing behaviour of blood. It is essential to know the behaviour of blood to deal with the pathological conditions faced by animals and human beings. Examining fluid dynamics in a curved conduit is significant in biomedicine due to its ability to closely replicate the complex flow patterns observed in arterial blood vessels. These investigations are of great value in managing patients with coronary pathologies. In the study by Mekheimer and Kot [9], an examination was carried out to analyse the hemodynamic properties of fluid flow in a curved artery, specifically in the context of catheterisation. The researchers' study clarified that narrower arteries exhibit higher fluidic resistance than wider arteries. Additionally, they found that the velocity profile in non-curved arteries is more significant than that observed in curved arteries. Zaman et al. [96] examined the effect of different types of nanoparticles through curved stenosed channels. Their study exhibited that the curvature parameter influences the velocity profile, and the symmetric patterns reduce for a higher value of the curvature parameter. Sharma et al. [97] studied the MHD blood flow through a curved artery by considering the effect of heat transfer and body acceleration. Several other researchers [12, 27] scrutinized the blood flow through the curved stenosed artery. Majorly, researchers considered the blood

viscosity a constant, but in reality, it gets influenced by different factors like pressure, temperature and flow rate. Lih et al. [98] examined that blood viscosity at the low-shear region vary according to hematocrit and blood vessel diameter. The variable viscosity is essential whenever blood through a tube or channel is studied. Baskurt et al. [99] emphasized the variation in blood viscosity are influenced by hematocrit, RBCs (red blood cells) aggregation, shear stress and mechanical properties of RBCs. Ponalagusamy and Priyadharshini [11] developed the mathematical model of the two-fluid model in tapered arterial stenosis. They considered micropolar fluid in the core region and Newtonian fluid in the peripheral plasma region with variable viscosity.

Inspired by the aforementioned studies, the present research endeavours to investigate a previously unexplored domain, specifically examining the combined effects of nanoparticles' shape and size, alongside Joule heating, electroosmosis, radial magnetic fields, and radiation, on the blood flow dynamics within a curved stenosed artery with thrombosis. To fill this void in the existing research, we examined the flow of blood containing suspended Al_2O_3 nanoparticles through irregular stenosis while also considering the presence of thrombosis on the catheter walls. The nanoparticles under consideration are categorised as porous metallic oxides, known for their significant surface areas and impressive resistance to chemical and mechanical disturbances. The extensive accessibility of these nanoscale entities makes them economically feasible for incorporation into diverse biomedical applications.

This study examines the impact of a uniform radial magnetic field, electroosmosis , and radiation on a system. The hematocrit dependent viscosity model is taken into the consideration. In this study, we have chosen to adopt a curvilinear coordinate system along with mild stenosis assumptions to reduced the complexity of the governing equations. These governing equations are discretized using the Crank–Nicolson method and further solved in the MatLab under the appropriate boundary conditions.

The salient contributions of this research are as follows:

- Investigation of the impact of nanoparticle shape and size on the flow behavior within a curved artery.
- To investigate the impact of variable viscosity on the flow dynamics within a stenosed artery with thrombosis at the centre of the catheter wall, specifically by considering the hematocrit-dependent viscosity model.
- Entropy generation analyzation on the diseased artery by considering the combined effects of Joule heating, electro-osmosis, radial magnetic field and radiation.

3.1 Mathematical Formulation

A study is undertaken to examine the hemodynamics of blood flow in a pathological arterial segment that exhibits irregular stenoses and thrombosis at the central region of the catheterised tube. The flow is characterised by being unsteady, laminar, incompressible and fully developed, exhibiting an axisymmetric configuration. To enhance the analysis, a curvilinear coordinate system is employed, where the radial and axial coordinates are represented as $\tilde{r}$ and $\tilde{z}$ respectively. The adoption of axisymmetry enables the elimination of any dependence on the variable $\tilde{\theta}$ in the flow. The assumption is made that the induced magnetic field is very small, as it is considered insignificant in comparison with an applied magnetic field. As a component of the research, the introduction of aluminium oxide nanoparticles into the bloodstream is conducted to investigate their impact on the flow dynamics as they pass through the afflicted arterial vessel.

3.1.1 Geometrical Representation of the Model

The visual representation of the affected arterial structure is depicted in Figure 3.1. The depiction of the arterial configuration involves the use of two concentric tubes, where the radius is represented as R^*, originating from the central point O. The geometric characterization pertains to an irregularly shaped stenotic condition is given as follows: [44, 100]:

$$R^*(\tilde{z}) = \begin{cases} R_0 - 2\delta\left[\cos(\frac{2\pi}{L_0}(\frac{\tilde{z}-\tilde{d}}{2} - \frac{L_0}{4}) - \frac{7}{100}\cos(\frac{32\pi}{L_0}(\tilde{z}-\tilde{d}-\frac{L_0}{2}))\right] & \tilde{d} \le \tilde{z} \le \tilde{d}+L_0, \\ R_0 & \text{otherwise}, \end{cases} \tag{3.1}$$

Let R_1^* denote the radius of the stenotic segment, which possesses a length denoted by L. Additionally, d represents the distance of the stenotic segment from the initial position P. The geometric characteristics of the clot are described as follows:

$$R_1^*(\tilde{z}) = \begin{cases} R_0(c + \sigma\exp(-\frac{\pi^2}{L_0^2}(\tilde{z}-\tilde{z}_d-0.5L_0)^2)), & \tilde{d} < \tilde{z} \le \tilde{d}+\frac{3}{2}L_0, \\ cR_0, & \text{otherwise}, \end{cases} \tag{3.2}$$

where, cR_0 denotes the radius of the inner tube, or catheter, wherein the parameter c is significantly smaller than unity ($c << 1$). The clot axial displacement , with its utmost elevation denoted by σ, is represented by the variable $\tilde{z}_d$.

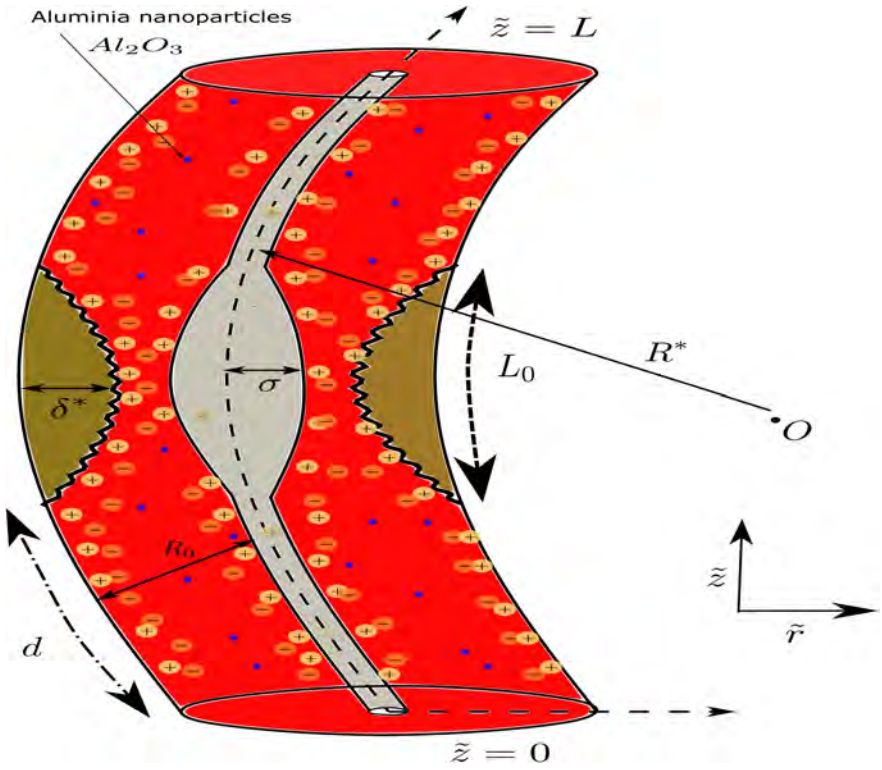

Figure 3.1: Physical sketch of the irregular-shaped constricted artery with Al_2O_3 nanoparticles.

3.1.2 Mathematical Formulation

3.1.2.1 Electrohydrodynamics (EHD)

Blood encompasses various ionic constituents like atoms or molecules that gain or lose electrons and thus carry an electric charge, which confers the properties of an electrically conducting fluid upon it. In consideration of this, we investigated the effects of introducing an electric field $(0,0,E_0)$ and an external magnetic field $\mathbf{B} = (\frac{R^*B_0}{\tilde{r}+R^*},0,0)$ subjected to the blood flow in the afflicted arterial, where B_0 remains constant. The current density and Lorentz force is given as [101]:

$$\frac{\mathbf{J}.\mathbf{J}}{\sigma_{nf}} = \sigma_{nf}\left(\frac{R^*B_0}{\tilde{r}+R^*}\right)^2(\tilde{w}^2) + \sigma_{nf}E_0^2, \tag{3.3}$$

$$\mathbf{J}\times\mathbf{B} = \left(0, \sigma_{nf}\left(\frac{R^*}{\tilde{r}+R^*}\right)B_0E_0, -\sigma_{nf}\left(\frac{R^*B_0}{\tilde{r}+R^*}\right)^2\tilde{w}\right), \tag{3.4}$$

where σ_{nf} and J signifies the electric conductivity and current density vector , respectively. The phenomenon of electroosmosis occurs in the present case as the solid conduct,

such as an arterial walls or a catheter, interfaces with an electrolyte solution, such as blood. The occurrence of this interaction results in the formation of an electrical double layer (EDL) in the proximity of the solid surface as a consequence of disparities in ion concentrations. The mathematical representation of the electroosmotic potential is given by the Poisson-Boltzmann equation as [29, 34]:

$$\nabla^2\tilde{\Phi} = -\frac{\rho_e}{\varepsilon}, \tag{3.5}$$

where, $\tilde{\Phi}$ denotes the electro-osmotic function, while ε represents the dielectric constant. The variable ρ_e is explicitly expressed as follows:

$$\rho_e = (n^+ - n^-)e_0 z_0. \tag{3.6}$$

The number density of cations and anions can be characterized by the Boltzmann distribution which is given as:

$$n^{\pm} = n_0 \exp(\mp\frac{e_0 z_0 \tilde{\Phi}}{k_B T_{avg}}), \tag{3.7}$$

where, k_B is Boltzmann constant , e_0 is electric constant, z_0 is the charge balance . Combining equations (3.6) and (3.7) and using the Debye-Huckel linearizion, we get:

$$\rho_e = -\frac{2e_0^2 z_0^2 n_0}{k_B T_{avg}}\tilde{\Phi}. \tag{3.8}$$

By using equations (3.5) and (3.8) , the Poisson equation takes the form:

$$\left(\frac{\partial^2}{\partial\tilde{r}^2} + \frac{1}{\tilde{r}+R^*}\frac{\partial}{\partial\tilde{r}} + \left(\frac{R^*}{\tilde{r}+R^*}\right)^2\frac{\partial^2}{\partial\tilde{z}^2}\right)\tilde{\Phi} = \frac{\tilde{\Phi}}{q_m^2}, \tag{3.9}$$

where $q_m = \frac{1}{e_0 z_0}\sqrt{\frac{\varepsilon k_B T_{avg}}{2n_0}}$.

3.1.2.2 Viscosity Model

Corcione [102] introduced a theoretical framework for investigating the interrelation between the diameters of nanoparticles (d_p) with nanofluid viscosity μ_{nf}.

$$\frac{\mu_{nf}}{\mu_{bf}} = \frac{1}{1 - 34.87(\frac{d_p}{d_f})^{-0.3}\phi_n^{1.03}}, \tag{3.10}$$

where, ϕ_n denots the volumetric concentration of nanoparticles, molecular diameter d_f of the base fluid is provided as follows:

$$d_f = \left[\frac{6M_1}{N_1 \pi \rho_{f_0}}\right]^{\frac{1}{3}}. \tag{3.11}$$

N_1 represents the Avogadro constant $(6.022 * 10^{23})$, applicable to nanoparticles within the size range of 25 to 200 nm and concentrations spanning from 0.01% to 7.1%.

The abundance of suspended entities within the circulatory system is primarily due to erythrocytes, also known as red blood cells or RBCs. These cells significantly impact the biomechanical properties of blood. The variability of blood viscosity is influenced by the spatial arrangement of its particles, which is a crucial factor examined in the subsequent model proposed in this study [82].

$$\mu_{bf} = \mu_f[1 + \beta_1^* h(\tilde{r})], \tag{3.12}$$

where, $h(\tilde{r}) = h_m[1 - (\frac{\tilde{r}}{R_0})^m]$, h_m signifies the maximum level of hematocrit with β_1^* as constant.

3.1.2.3 Governing Equations

Based on the previously mentioned assumption regarding magnetohydrodynamic (MHD) interaction, the governing equations are provided as follows [82, 103]:

Continuity Equation

$$\frac{\partial \tilde{u}}{\partial \tilde{r}} + \frac{\tilde{u}}{\tilde{r} + R^*} + \frac{R^*}{\tilde{r} + R^*}\frac{\partial \tilde{w}}{\partial \tilde{z}} = 0. \tag{3.13}$$

Momentum (in r_1^*-direction)

$$\rho_{nf}\left[\frac{\tilde{D}}{d\tilde{t}}\tilde{u} - \frac{\tilde{w}^2}{\tilde{r} + R^*}\right] = -\frac{\partial \tilde{p}}{\partial \tilde{r}} + \mu_{nf}\left(\nabla^2 \tilde{u} - \frac{\tilde{u}}{(\tilde{r} + R^*)^2} - \frac{2R^*}{(\tilde{r} + R^*)^2}\frac{\partial \tilde{w}}{\partial \tilde{z}}\right) + \left(\frac{4}{3}\frac{\partial \tilde{u}}{\partial \tilde{r}} - \frac{2}{3}\left(\frac{R^*}{R^* + \tilde{r}}\frac{\partial \tilde{w}}{\partial \tilde{z}} + \frac{\tilde{u}}{R^* + \tilde{r}}\right)\right)\frac{\partial \mu_{nf}}{\partial \tilde{r}}. \tag{3.14}$$

Momentum (in z_1^*-direction)

$$\rho_{nf}\left[\frac{\tilde{D}}{d\tilde{t}}\tilde{w}+\frac{\tilde{u}\tilde{w}}{\tilde{r}+R^*}\right]=-\left(\frac{R^*}{\tilde{r}+R^*}\right)\frac{\partial\tilde{p}}{\partial\tilde{z}}+\mu_{nf}\left(\nabla^2\tilde{w}-\frac{\tilde{w}}{(\tilde{r}+R^*)^2}+\frac{2R^*}{(\tilde{r}+R^*)^2}\frac{\partial\tilde{u}}{\partial\tilde{z}}\right)$$
$$+g(\rho\beta)_{nf}(\tilde{T}-\tilde{T}_0)+g(\rho\beta)_{nf}(\tilde{C}-\tilde{C}_0)+\left(\frac{R^*}{R^*+\tilde{r}}\frac{\partial\tilde{u}}{\partial\tilde{z}}+\frac{\partial\tilde{w}}{\partial\tilde{r}}-\frac{\tilde{w}}{R^*+\tilde{r}}\right)\frac{\partial\mu_{nf}}{\partial r}+\rho_eE_0$$
$$-\sigma_{nf}B_0^2\tilde{w}\left(\frac{R^*}{\tilde{r}+R^*}\right)^2. \quad (3.15)$$

Temperature Equation

$$(\rho C_p)_{nf}\frac{\tilde{D}\tilde{T}}{d\tilde{t}}=\kappa_{nf}\nabla^2\tilde{T}+\sigma_{nf}\left(\frac{R^*B_0}{\tilde{r}+R^*}\right)^2(\tilde{w}^2)+\sigma_{nf}E_0^2+F_{vd}-\frac{1}{\tilde{r}+R^*}\left[\frac{\partial}{\partial\tilde{r}}(\{\tilde{r}+R^*\}q_r)\right]. \quad (3.16)$$

Concentration Equation

$$\frac{\tilde{D}\tilde{C}}{d\tilde{t}}=D_m\nabla^2\tilde{C}-R_c(\tilde{C}-\tilde{C}_w). \quad (3.17)$$

Electroosmotic Equation

$$\nabla^2\tilde{\Phi}=-\frac{\tilde{\Phi}}{q_m^2}, \quad (3.18)$$

where $\nabla^2:=\frac{\partial^2}{\partial\tilde{r}^2}+\frac{1}{\tilde{r}+R^*}\frac{\partial}{\partial\tilde{r}}+\left(\frac{R^*}{\tilde{r}+R^*}\right)^2\frac{\partial^2}{\partial\tilde{z}^2}$, the material derivative is $\frac{\tilde{D}}{d\tilde{t}}:=\frac{\partial}{\partial\tilde{t}}+\tilde{u}\frac{\partial}{\partial\tilde{r}}+\frac{\tilde{w}R^*}{\tilde{r}+R^*}\frac{\partial}{\partial\tilde{z}}$ and the viscous dissipation term F_{vd} is given as:

$$F_{vd}=\mu_{nf}\left[2\left(\frac{\partial\tilde{u}}{\partial\tilde{r}}\right)^2+2\left(\frac{R^*}{\tilde{r}+R^*}\frac{\partial\tilde{w}}{\partial\tilde{z}}+\frac{\tilde{u}}{\tilde{r}+R^*}\right)^2+\left(\frac{\partial\tilde{w}}{\partial\tilde{r}}-\frac{\tilde{w}}{\tilde{r}+R^*}+\frac{R^*}{\tilde{r}+R^*}\frac{\partial\tilde{u}}{\partial\tilde{z}}\right)^2\right]. \quad (3.19)$$

The boundary conditions are given as:

$$\begin{cases}\tilde{w}=0, \quad \tilde{T}=\tilde{T}_0, \quad \tilde{C}=\tilde{C}_0 \quad \text{at} \quad \tilde{t}=0,\\ \tilde{w}=0, \quad \tilde{T}=\tilde{T}_w, \quad \tilde{C}=\tilde{C}_w \quad \text{at} \quad \tilde{r}=R^*(\tilde{z}) \text{ and } \tilde{r}=R_1^*(\tilde{z}).\end{cases} \quad (3.20)$$

The specification of boundary conditions pertaining to the potential function is as follows:

$$\begin{aligned}\tilde{\Phi}&=\tilde{\zeta}_2 \quad \text{on} \quad \tilde{r}=R^*(\tilde{z}),\\ \tilde{\Phi}&=\tilde{\zeta}_1 \quad \text{on} \quad \tilde{r}=R_1^*(\tilde{z}),\end{aligned} \quad (3.21)$$

where, zeta potential functions represented by $\tilde{\zeta}_1$ and $\tilde{\zeta}_2$ are specifically denoted with

respect to the arterial and catheter wall, respectively.

The pulsatile nature of blood flow is an inherent characteristic, primarily resulting from the continuous pumping action of the heart. The aforementioned phenomenon can be mathematically characterised in the subsequent manner [7, 104]:

$$-\frac{\partial \tilde{p}}{\partial \tilde{z}} = A_0 + A_1 \cos(\omega_p \tilde{t}), \tilde{t} > 0, \tag{3.22}$$

where, A_0 denotes the amplitude of the pressure gradient corresponding to the steady-state condition, while A_1 signifies the amplitude of the pressure gradient associated with the pulsatile state. The term $\omega_p = 2\pi f_p$ denotes the angular frequency pertaining to the heart.

Table 3.1: Dimensionless parameters

$r = \frac{\tilde{r}}{R_0}$	$z = \frac{\tilde{z}}{L_0}$	$u = \frac{L_0 \tilde{u}}{\delta^* U_0}$	$w = \frac{\tilde{w}}{U_0}$
$T = \frac{\tilde{T} - \tilde{T}_0}{\tilde{T}_w - \tilde{T}_0}$	$t = \frac{U_0 \tilde{t}}{R_0}$	$R_c = \frac{R^*}{R_0}$	$p = \frac{R_0^2 \tilde{p}}{\mu_f U_0 L_0}$
$\delta = \frac{\delta^*}{R_0}$	$M^2 = \frac{\sigma_f B_0^2 R_0^2}{\mu_f}$	$Gr = \frac{g(\rho\beta)_f R_0^2 (\tilde{T}_w - \tilde{T}_0)}{\mu_f U_0}$	$E_1 = \frac{R_0}{\sqrt{\mu_0 U_0}} E_0$
$Sc = \frac{\nu}{D_m}$	$Pr = \frac{\mu_f C_p}{\kappa_f}$	$Re = \frac{U_0 \rho_f R_0}{\mu_f}$	$Nr = \frac{16 \sigma_e \tilde{T}_0^3}{3 \kappa_f \kappa_e}$
$Ec = \frac{U_0^2}{c_p (\tilde{T}_w - \tilde{T}_0)}$	$Br = \frac{\mu_f U_0^2}{\kappa_f (\tilde{T}_w - \tilde{T}_0)}$	$Da = \frac{K_1}{R_0^2}$	$U_{hs} = \frac{\zeta \varepsilon E_0}{\mu_f U_0}$
$\xi = \frac{R_c \rho_f R_0^2}{\mu_0}$	$q_e = \frac{R_0}{q_m}$	$\Lambda = \frac{\tilde{C}}{(\tilde{C}_w - \tilde{C}_0)}$	$\Omega = \frac{\tilde{T}}{(\tilde{T}_w - \tilde{T}_0)}$

3.1.3 Non-Dimensionalization

In consideration of the dimensionless parameters delineated in the nomenclature, the pertinent equations ((3.13)-(3.21)) that govern the model under the assumption of mild stenosis ($\delta << 1$) and the condition $O(1) = \alpha = \frac{R_0}{L_0}$ can be expressed as follows [82]:

$$\frac{\partial p}{\partial r} = 0, \tag{3.23}$$

$$\frac{\rho_{nf}}{\rho_f}Re\frac{\partial w}{\partial t} = -\frac{R_c}{R_c+r}\frac{\partial p}{\partial z} + \frac{\mu_{nf}}{\mu_0}\left(\frac{\partial^2 w}{\partial r^2} + \frac{1}{r+R_c}\frac{\partial w}{\partial r} - \frac{w}{(r+R_c)^2}\right) + U_{hs}q_e^2\Phi$$
$$+\frac{(\rho\beta)_{nf}}{(\rho\beta)_f}(GrT+GcC) - \frac{m\beta_1^* h_m r^{*m-1}}{(1-34.87(\frac{d_p}{d_f})^{-0.3}\phi^{1.03})}\left(\frac{\partial w}{\partial r} - \frac{w}{R_c+r}\right) - \frac{\sigma_{nf}}{\sigma_f}\left(\frac{R_c}{r+R_c}\right)^2 M^2 w, \tag{3.24}$$

$$\frac{(\rho C_p)_{nf}}{(\rho C_p)_f}\frac{\kappa_f}{\kappa_{nf}}PrRe\frac{\partial T}{\partial t} = \frac{\partial^2 T}{\partial r^2} + \frac{1}{r+R_c}\frac{\partial T}{\partial r} + \frac{\sigma_{nf}}{\sigma_f}\frac{\kappa_f}{\kappa_{nf}}\left[\left(\frac{R_c}{r+R_c}\right)^2 BrM^2w^2 + S_z\right]$$
$$+\frac{\kappa_f}{\kappa_{hnf}}Nr\left[\frac{\partial^2 T}{\partial r^2} + \frac{1}{R_c+r}\frac{\partial T}{\partial r}\right] + \left(\frac{\kappa_f}{\kappa_{nf}}\right)\left(\frac{\mu_{nf}}{\mu_0}\right)Br\left[\frac{\partial w}{\partial r} - \frac{w}{r+R_c}\right]. \tag{3.25}$$

$$ReSc\frac{\partial C}{\partial t} = \frac{\partial^2 C}{\partial r^2} + \frac{1}{R_c+r}\frac{\partial C}{\partial r} - Sc\xi C, \tag{3.26}$$

$$\frac{\partial^2 \Phi}{\partial r^2} + \frac{1}{R_c+r}\frac{\partial \Phi}{\partial r} = q_e^2\Phi. \tag{3.27}$$

Associate boundary conditions are as follows:

$$\begin{cases} w = T = C = 0 & \text{at} \quad t = 0, \\ w = 0, T = 1, C = 1 & \text{at} \quad r = R_2^*(z) \ \text{ and } \ r = R_1^*(z). \end{cases} \tag{3.28}$$

Boundary condtion for electroosmotic function:

$$\begin{aligned} \Phi &= 0.1 \quad \text{on} \quad r = R_1^*(z), \\ \Phi &= 0.3 \quad \text{on} \quad r = R^*(z). \end{aligned} \tag{3.29}$$

The dimensionless expressions corresponding to the diseased artery are provided as:

Clot Region:

$$R_1^*(z) = \begin{cases} c + \sigma\exp(-\pi^2(z - z_d - 1/2)^2), & d < z < d + 3/2, \\ c, & \text{otherwise}, \end{cases} \tag{3.30}$$

Stenosis Region:

$$R_2^*(z) = \begin{cases} 1 - 2\delta\left[\cos(2\pi(\frac{z-d}{2} - \frac{1}{4}) - \frac{7}{100}\cos(32\pi(z - d - \frac{1}{2}))\right] & d \le z \le d + 1, \\ 1 & \text{otherwise}, \end{cases} \tag{3.31}$$

Parameters	Ranges	Sources
Thermal Grashof number (Gr)	0-6	[105, 106]
Nanoparticle shape parameter (n)	3-8.6	[23, 107]
Prandtl number (Pr)	0-4	[90, 107]
Radiation parameter (Nr)	0-3	[106, 108]
hematocrit parameter (h_m)	0-1	[11, 12]
Magnetic Number (M)	0-4	[1, 2]
Brinkmann number (Br)	0.1-2	[22, 107]

Table 3.2: Values of the physical parameters with their sources

where, σ represents the maximum clot height at the axial location z_d, while the inner tube radius is denoted as cR_0, where c is a considerably small value $(c << 1)$. Additionally, the maximum height of the stenosis is symbolized by parameter δ in equation (3.31), and the specific location of the affected segment is represented by the variable d.
The pressure component in dimensionless form is given as [82]:

$$-\frac{\partial p}{\partial z} = B_1(1 + e\cos(c_1 t)), \tag{3.32}$$

where, $B_1 = \frac{A_0 R_0^2}{\mu_f U_0}, e = \frac{A_1}{A_0}$, and $c_1 = \frac{2\pi R_0 f_p}{U_0}$.
The volumetric flow rate is defined as [107]:

$$Q^f = 2\pi \int_{R_1^*}^{R^*} wrdr. \tag{3.33}$$

In the afflicted arterial system, the impedance encountered by the blood flow is expressed as [107]:

$$\lambda = \frac{L(\frac{-\partial p}{\partial z})}{Q^f}. \tag{3.34}$$

Finally, the shear stress profile is given as [33]:

$$\tau_w = -\left(\frac{\partial w}{\partial r}\right)_{r=R^*}. \tag{3.35}$$

3.1.4 Entropy

Entropy is the measured of the irreversibility present in the system. The entropy is attribute to the change in the system cause by mass and thermal exchange. The overall entropy is the

sum of entropy produces by each individual process. The dimensional volumetric entropy generation is defined as [57, 109]:

$$E_g = \frac{\kappa_f}{\tilde{T}_0^2}\left[\frac{\kappa_{nf}}{\kappa_f}+\frac{16\sigma_e \tilde{T}_0{}^3}{3k_e\kappa_f}\right]\left(\frac{\partial \tilde{T}}{\partial \tilde{r}}\right)^2+\frac{\mu_{nf}}{\tilde{T}_0}\left(\frac{\partial \tilde{w}}{\partial \tilde{r}}\right)^2+\frac{\sigma_{nf}}{\tilde{T}_0}\left(\left(\frac{R^*}{\tilde{r}+R^*}\right)B_0^2\tilde{w}^2+E_0^2\right)+\frac{D_b}{\tilde{C}_w}\left(\frac{\partial \tilde{C}}{\partial \tilde{r}}\right)^2. \tag{3.36}$$

There are four components in the above equations. The first term on right hand side depicts the irreversibility due to heat transfer , the second term for the hydromagnetic, third term for the fluid friction and the last term for solute irreversibility. We simplified the above equation further, to get;

$$E_g = \frac{\kappa_f}{\tilde{T}_0^2}\frac{(\tilde{T}_w-\tilde{T}_0)^2}{R_0^2}\left\{\left[\frac{\kappa_{nf}}{\kappa_f}+\frac{16\sigma_e\tilde{T}_0^3}{3k_e\kappa_f}\right]\left(\frac{\partial T}{\partial r}\right)^2+\frac{\mu_{nf}U_0^2}{\kappa_f\Delta\tilde{T}}\left(\frac{\partial w}{\partial r}\right)^2\right.$$
$$\left.+\frac{\sigma_{nf}B_0^2U_0\tilde{T}_0R_0^2}{\kappa_f\Delta\tilde{T}}\left(\left(\frac{R_c}{r+R_c}\right)^2w^2+\left(\frac{E_0}{B_0U_0}\right)^2\right)+\frac{D_b}{\tilde{C}_w}\left(\frac{\Delta\tilde{C}}{R_0}\right)^2\frac{\tilde{T}_0^2}{\kappa_f}\frac{R_0^2}{\Delta\tilde{T}}\left(\frac{\partial C}{\partial r}\right)^2\right\}. \tag{3.37}$$

The dimensionless N_s defined as the ratio of total entropy generation to characteristic entropy transfer. It is defined as $N_s = \frac{\tilde{T}_0^2R_0^2}{\kappa_f(\Delta\tilde{T})^2}\times E_g$. Using equation above, we have

$$N_s = \left[\frac{\kappa_{nf}}{\kappa_f}+Nr\right]\left(\frac{\partial T}{\partial r}\right)^2+\frac{\mu_{nf}}{\mu_0}\left\{\left(\frac{\partial w}{\partial r}\right)^2\right\}\frac{Br}{\Omega}+\frac{\sigma_{nf}}{\sigma_f}\frac{M^2Br}{\Omega}\left(\left(\frac{R_c}{r+R_c}\right)^2w^2+E_1^2\right)$$
$$+\frac{\Lambda\Gamma}{\Omega}\left(\frac{\partial C}{\partial r}\right)^2, \tag{3.38}$$

where, $\Gamma = \frac{D_b\tilde{T}_0\Delta\tilde{C}}{\kappa_f\Delta\tilde{T}}$. The Bejan number is defined as the ratio of heat transfer irreversibility to total irreversibility. So, we have

$$Be = \frac{N}{N_s},$$
$$= \frac{\left[\frac{\kappa_{nf}}{\kappa_f}+Nr\right](\frac{\partial T}{\partial r})^2}{\left[\frac{\kappa_{nf}}{\kappa_f}+Nr\right]\left(\frac{\partial T}{\partial r}\right)^2+\frac{\mu_{nf}}{\mu_0}\left\{\left(\frac{\partial w}{\partial r}\right)^2\right\}\frac{Br}{\Omega}+\frac{\sigma_{nf}}{\sigma_f}\frac{M^2Br}{\Omega}\left(\left(\frac{R_c}{r+R_c}\right)^2w^2+E_1^2\right)+\frac{\Lambda\Gamma}{\Omega}\left(\frac{\partial C}{\partial r}\right)^2}. \tag{3.39}$$

3.2 Numerical Methodology

The mathematical model under consideration yields a set of non-linear coupled PDEs (partial differential equations), for which obtaining exact solutions proves to be challenging. In all but a few very basic circumstances, accurate solutions to these equations are impossible. As a result, several different numerical techniques have been developed to address these problems.

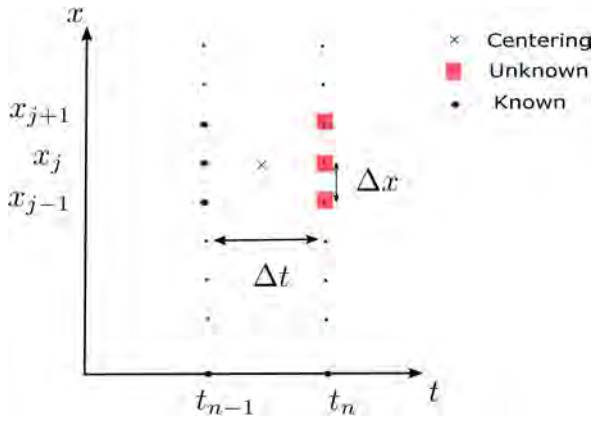

Figure 3.2: Grid for the Crank-Nicolson scheme

With today's fast computers and cutting-edge commercial software, such methods have become more straightforward and accurate. There have been a number of researchers that have suggested the Crank-Nicolson technique as an implicit strategy. It is second-order convergent in time. This method uses the finite difference grid as shown in figure 3.2 , replacing the spatial derivative at $\left(t_{n-1/2}, x_j\right)$ by taking the average of upstream and downstream values at t_{n-1} and t_n, respectively. In a similar manner, the time derivative can be substituted with the central difference formula at the point $\left(t_{n-1/2}, x_j\right)$.

3.2.1 Discretization of Governing Equations

In this study, we utilized the dimensional parameter and thermophysical parameters specified in table 3.1 and table 2.1, respectively. Additionally, the thermophysical properties of blood and nanoparticles, as presented in Figure 3.3, were taken into consideration, along with the physical parameters from table 3.2. The resulting discretized governing equations are displayed as follows:

$$\left[(1-\phi_1)+\phi_1\frac{\rho_{s_1}}{\rho_f}\right]Re\left[\frac{w_i^{k+1}-w_i^k}{\Delta t}\right]=\frac{R_c}{R_c+r(i)}D_1[1+e\cos(c_pt^k)]+\frac{[1+\beta_1^*h_m(1-(\frac{r(i)}{R_0})^m)]}{(1-34.87\left(\frac{d_p}{d_f}\right)^{-0.3}\phi_1^{1.03})}$$
$$\left[\frac{1}{2}\left(\frac{w_{i+1}^{k+1}-2w_i^{k+1}+w_{i-1}^{k+1}}{(\Delta x)^2}+\frac{w_{i+1}^k-2w_i^k+w_{i-1}^k}{(\Delta x)^2}\right)+\frac{1}{4(R_c+r(i))}\left(\frac{w_{i+1}^{k+1}-w_{i-1}^{k+1}}{\Delta x}+\frac{w_{i+1}^k-w_{i-1}^k}{\Delta x}\right)\right.$$
$$\left.-\frac{(w_i^k+w_i^{k+1})}{2(R_c+r(i))^2}\right]-\frac{m\beta_1^*h_m(r(i))^{m-1}}{(1-34.87\left(\frac{d_p}{d_f}\right)^{-0.3}\phi_1^{1.03})}\left[\frac{(w_{i+1}^{k+1}-w_{i-1}^{k+1}+w_{i+1}^k-w_{i-1}^k)}{4\Delta x}\right.$$
$$\left.-\frac{(w_i^k+w_i^{k+1})}{2(R_c+r(i))}\right]+\left[(1-\phi_1)+\phi_1\frac{(\rho\beta)_{s1}}{(\rho\beta)_f}\right](GrT_i^k+GcC_i^k)-\frac{1}{2}\frac{\sigma_{hnf}}{\sigma_f}M^2(w_i^k+w_i^{k+1})\left(\frac{R_c}{R_c+r(i)}\right)^2$$
$$+U_{hs}q_e^2\Phi_i^k, \quad (3.40)$$

$$\left[(1-\phi_1)+\phi_1\frac{(\rho C_p)_{s1}}{(\rho C_p)_f}\right]\left[\frac{T_i^{k+1}-T_i^k}{dt}\right]=\frac{1}{RePr}\frac{\kappa_{hnf}}{\kappa_f}\left[\left(\frac{T_{i+1}^{k+1}-2T_i^{k+1}+T_{i-1}^{k+1}}{2(\Delta x)^2}+\frac{T_{i+1}^k-2T_i^k+T_{i-1}^k}{2(\Delta x)^2}\right)\right.$$
$$\left.+\frac{1}{4(R_c+r(i))}\left(\frac{T_{i+1}^{k+1}-T_{i-1}^{k+1}}{\Delta x}+\frac{T_{i+1}^k-T_{i-1}^k}{\Delta x}\right)\right]+\frac{Nr}{RePr}\left[\frac{1}{2}\left(\frac{T_{i+1}^{k+1}-2T_i^{k+1}+T_{i-1}^{k+1}}{dx^2}+\frac{T_{i+1}^k-2T_i^k+T_{i-1}^k}{dx^2}\right)\right.$$
$$\left.+\frac{1}{4(R_c+r(i))}\left(\frac{T_{i+1}^{k+1}-T_{i-1}^{k+1}}{dx}+\frac{T_{i+1}^k-T_{i-1}^k}{dx}\right)\right]+\left(\frac{\mu_{nf}}{\mu_0}\right)\left(\frac{Br}{RePr}\right)\left[\frac{w_{i+1}^{k+1}-w_{i-1}^{k+1}+w_{i+1}^k-w_{i-1}^k}{4\Delta x}\right.$$
$$\left.-\frac{w_i^k+w_i^{k+1}}{2(R_c+r(i))}\right]^2+\frac{1}{PrRe}\left\{\frac{\sigma_{nf}}{\sigma_f}\frac{\kappa_f}{\kappa_{nf}}\left[\left(\frac{R_c}{R_c+r(i)}\right)^2BrM^2(w_i^2)^k+S_z\right]\right\}, \quad (3.41)$$

$$\left[\frac{C_i^{k+1}-C_i^k}{\Delta t}\right]=\frac{1}{ReSc}\left[\left(\frac{T_{i+1}^{k+1}-2T_i^{k+1}+T_{i-1}^{k+1}}{2(\Delta x)^2}+\frac{T_{i+1}^k-2T_i^k+T_{i-1}^k}{2(\Delta x)^2}\right)+\frac{1}{4(R_c+r(i))}\left(\frac{T_{i+1}^{k+1}-T_{i-1}^{k+1}}{\Delta x}\right.\right.$$
$$\left.\left.+\frac{T_{i+1}^k-T_{i-1}^k}{\Delta x}\right)\right]-\frac{\xi}{2Re}(C_i^k+C_i^{k+1}) \quad (3.42)$$

$$\frac{\Phi_{i+1}-2\Phi_i+\Phi_{i-1}}{h^2}+\frac{1}{R_c+r(i)}\{\frac{\Phi_{i+1}-\Phi_{i-1}}{2h}\}=q_e^2\Phi_i. \quad (3.43)$$

Here, ϕ_1 denotes the nanoparticles volumetric concentration. The discretized equations for the initial and boundary conditions are given as:

$$w_1^{k+1}=0,T_1^{k+1}=1,C_1^{k+1}=1, \quad w_{N+1}^{k+1}=0,T_{N+1}^{k+1}=1,C_{N+1}^{k+1}=1, \quad (3.44)$$
$$w_i^1=0,T_i^1=0,C_i^1=0, \quad \Phi_1=0.1,\Phi_{N+1}=0.3. \quad (3.45)$$

The tri-diagonal system obtained from Eqn. (3.40) is written as:

$$R_i^k w_{i-1}^{k+1} + S_i^k w_i^{k+1} + U_i^k w_{i+1}^{k+1} = R_i^{'k} w_{i-1}^k + S_i^{'k} w_i^k + U_i^{'k} w_{i+1}^k + F_i^k, \tag{3.46}$$

where,

$$U_i^k = -\frac{[1+\beta_1^* h_m(1-(\frac{r}{R_0})^m)]}{(1-34.87\left(\frac{d_p}{d_f}\right)^{-0.3}\phi_1^{1.03})}\left(\frac{\Delta t}{2(\Delta x)^2}+\frac{\Delta t}{4(R_c+r(i))}\right)+\frac{m\beta_1^* h_m(r(i))^{m-1}}{(1-34.87\left(\frac{d_p}{d_f}\right)^{-0.3}\phi_1^{1.03})}\left(\frac{\Delta t}{4\Delta x}\right), \tag{3.47}$$

$$S_i^k = Re\left[(1-\phi_1)+\phi_1\frac{\rho_{s1}}{\rho_f}\right]-\frac{[1+\beta_1^* h_m(1-(\frac{r}{R_0})^m)]}{(1-34.87\left(\frac{d_p}{d_f}\right)^{-0.3}\phi_1^{1.03})}\left(-\frac{\Delta t}{(\Delta x)^2}-\frac{\Delta t}{2(R_c+r(i))^2}\right)$$
$$-\frac{m\beta_1^* h_m(r(i))^{m-1}}{(1-34.87\left(\frac{d_p}{d_f}\right)^{-0.3}\phi_1^{1.03})}\left(\frac{dt}{2(R_c+r(i))}\right)+\frac{\Delta t}{2}\frac{\sigma_{nf}}{\sigma_f}M^2\left(\frac{R_c}{R_c+r(i)}\right)^2, \tag{3.48}$$

$$R_i^k = -\frac{[1+\beta_1^* h_m(1-(\frac{r}{R_0})^m)]}{(1-34.87\left(\frac{d_p}{d_f}\right)^{-0.3}\phi_1^{1.03})}\left(\frac{\Delta t}{2(\Delta x)^2}-\frac{\Delta t}{4(R_c+r(i))}\right)$$
$$+\frac{m\beta_1^* h_m(r(i))^{m-1}}{(1-34.87\left(\frac{d_p}{d_f}\right)^{-0.3}\phi_1^{1.03})}\left(-\frac{\Delta t}{4\Delta x}\right), \tag{3.49}$$

$$U_i^{'k} = \frac{[1+\beta_1^* h_m(1-(\frac{r}{R_0})^m)]}{(1-34.87\left(\frac{d_p}{d_f}\right)^{-0.3}\phi_1^{1.03})}\left(\frac{\Delta t}{2(\Delta x)^2}+\frac{\Delta t}{4(R_c+r(i))}\right)$$
$$-\frac{m\beta_1^* h_m(r(i))^{m-1}}{(1-34.87\left(\frac{d_p}{d_f}\right)^{-0.3}\phi_1^{1.03})}\left(\frac{\Delta t}{4\Delta x}\right), \tag{3.50}$$

$$S_i^{'k} = Re\left[(1-\phi_1)+\phi_1\frac{\rho_{s1}}{\rho_f}\right]+\frac{[1+\beta_1^* h_m(1-(\frac{r}{R_0})^m)]}{(1-34.87\left(\frac{d_p}{d_f}\right)^{-0.3}\phi_1^{1.03})}\left(-\frac{\Delta t}{(\Delta x)^2}-\frac{\Delta t}{2(R_c+r(i))^2}\right)$$
$$+\frac{m\beta_1^* h_m(r(i))^{m-1}}{(1-34.87\left(\frac{d_p}{d_f}\right)^{-0.3}\phi_1^{1.03})}\left(\frac{\Delta t}{2(R_c+r(i))}\right), \tag{3.51}$$

$$R_i^{'k}=\frac{[1+\beta_1^* h_m(1-(\frac{r}{R_0})^m)]}{(1-34.87\left(\frac{d_p}{d_f}\right)^{-0.3}\phi_1^{1.03})}\left(\frac{\Delta t}{2(\Delta x)^2}-\frac{\Delta t}{4(R_c+r(i))}\right)+\frac{m\beta_1^* h_m(r(i))^{m-1}}{(1-34.87\left(\frac{d_p}{d_f}\right)^{-0.3}\phi_1^{1.03})}\left(\frac{\Delta t}{4\Delta x}\right), \tag{3.52}$$

$$F_i^k=\Delta t\frac{D_1 R_c}{(R_c+r(i))}[1+e\cos(c_1 t^k)]+(\Delta t)\left[(1-\phi_1)+\phi_1\frac{(\rho\beta)_{s_1}}{(\rho\beta)_f}\right](GrT_i^k+GcC_i^k)+\Delta t U_{hs}q_e^2\Phi_i^k. \tag{3.53}$$

Using equation ((3.41)), we may derive the tridiagonal system:

$$A_i^k T_{i-1}^{k+1}+B_i^k T_i^{k+1}+H_i^k T_{i+1}^{k+1}=A_i^{'k}T_{i-1}^k+B_i^{'k}T_i^k+H_i^{'k}T_{i+1}^k+D_i^k, \tag{3.54}$$

where,

$$A_i^k=-\frac{1}{RePr}\frac{\kappa_{nf}}{\kappa_f}\left(\frac{\Delta t}{2(\Delta x)^2}-\frac{1}{4(R_c+r(i))}\frac{\Delta t}{\Delta x}\right)-\frac{Nr}{RePr}\left(\frac{dt}{2dx^2}-\frac{1}{4(R_c+r(i))}\frac{dt}{dx}\right), \tag{3.55}$$

$$B_i^k=\left[(1-\phi_1)+\phi_1\frac{(\rho C_p)_{s_1}}{(\rho C_p)_f}\right]+\frac{1}{RePr}\frac{\kappa_{nf}}{\kappa_f}\frac{\Delta t}{(\Delta x)^2}+\frac{Nr}{RePr}\left(\frac{\Delta t}{(\Delta x)^2}\right), \tag{3.56}$$

$$H_i^k=-\frac{1}{RePr}\frac{\kappa_{nf}}{\kappa_f}\left(\frac{\Delta t}{2(\Delta x)^2}+\frac{1}{4(R_c+r(i))}\frac{\Delta t}{(\Delta x)}\right)-\frac{Nr}{RePr}\left(\frac{dt}{2dx^2}+\frac{1}{4(R_c+r(i))}\frac{dt}{dx}\right), \tag{3.57}$$

$$A_i^{'k}=\frac{1}{RePr}\frac{\kappa_{nf}}{\kappa_f}\left(\frac{\Delta t}{2(\Delta x)^2}-\frac{1}{4(R_c+r(i))}\frac{\Delta t}{\Delta x}\right)+\frac{Nr}{RePr}\left(\frac{dt}{2dx^2}-\frac{1}{4(R_c+r(i))}\frac{dt}{dx}\right), \tag{3.58}$$

$$B_i^{'k}=\left[(1-\phi_1)+\phi_1\frac{(\rho C_p)_{s1}}{(\rho C_p)_f}\right]-\frac{1}{RePr}\frac{\kappa_{nf}}{\kappa_f}\frac{\Delta t}{(\Delta x)^2}-\frac{Nr}{RePr}\left(\frac{\Delta t}{(\Delta x)^2}\right), \tag{3.59}$$

$$H_i^{'k}=\frac{1}{RePr}\frac{\kappa_{nf}}{\kappa_f}\left(\frac{\Delta t}{2(\Delta x)^2}+\frac{1}{4(R_c+r(i))}\frac{\Delta t}{\Delta x}\right)+\frac{Nr}{RePr}\left(\frac{dt}{2dx^2}+\frac{1}{4(R_c+r(i))}\frac{dt}{dx}\right), \tag{3.60}$$

$$D_i^k=\left(\frac{\mu_{nf}}{\mu_f}\right)\left(\frac{Br\Delta t}{RePr}\right)\left[\frac{w_{i+1}^{k+1}-w_{i-1}^{k+1}+w_{i+1}^k-w_{i-1}^k}{4\Delta x}-\frac{w_i^k+w_i^{k+1}}{2(R_c+r(i))}\right]^2 + \frac{\Delta t}{RePr}\left[\frac{\sigma_{nf}}{\sigma_f}\left(\frac{Rc}{Rc+r(i)}\right)^2 BrM^2(w_i^k)^2+S_z\right]. \tag{3.61}$$

Using equation ((3.42)), we may derive the tridiagonal system as:

$$X_i^k C_{i-1}^{k+1}+Y_i^k C_i^{k+1}+W_i^k C_{i+1}^{k+1}=X_i^{'k}C_{i-1}^k+Y_i^{'k}C_i^k+W_i^{'k}C_{i+1}^k+E_i^k, \tag{3.62}$$

where,

$$X_i^k = \frac{1}{ReSc}\left[-\frac{\Delta t}{2(\Delta x)^2} + \frac{\Delta t}{4\Delta x}\frac{1}{(Rc + r(i))}\right], \tag{3.63}$$

$$Y_i^k = \frac{1}{ReSc}\left[ReSc + \frac{\Delta t}{2(\Delta x)^2} + Sc\xi\frac{\Delta t}{2}\right], \tag{3.64}$$

$$W_i^k = \frac{1}{ReSc}\left[-\frac{\Delta t}{2(\Delta x)^2} - ReSc\frac{\Delta t}{4\Delta x}\frac{1}{(Rc + r(i))}\right], \tag{3.65}$$

$$X_i^{'k} = \frac{1}{ReSc}\left[\frac{\Delta t}{2(\Delta x)^2} - \frac{\Delta t}{4\Delta x}\frac{1}{(Rc + r(i))}\right], \tag{3.66}$$

$$Y_i^{'k} = \frac{1}{ReSc}\left[ReSc - \frac{\Delta t}{2h^2} - Sc\xi\frac{\Delta t}{2}\right], \tag{3.67}$$

$$W_i^{'k} = \frac{1}{ReSc}\left[\frac{\Delta t}{2(\Delta x)^2} + ReSc\frac{\Delta t}{4\Delta x}\frac{1}{(Rc + r(i))}\right], \quad E_i^k = 0. \tag{3.68}$$

The flow region has been partitioned into a grid composed of $(N+1)\times(M+1)$ points. In our analysis, we have chosen to utilise temporal and spatial discretization with step sizes $\Delta t = 0.01$ and $\Delta x = 0.001$, respectively, while considering the Crank-Nicolson method, which is renowned for its second-order convergence.

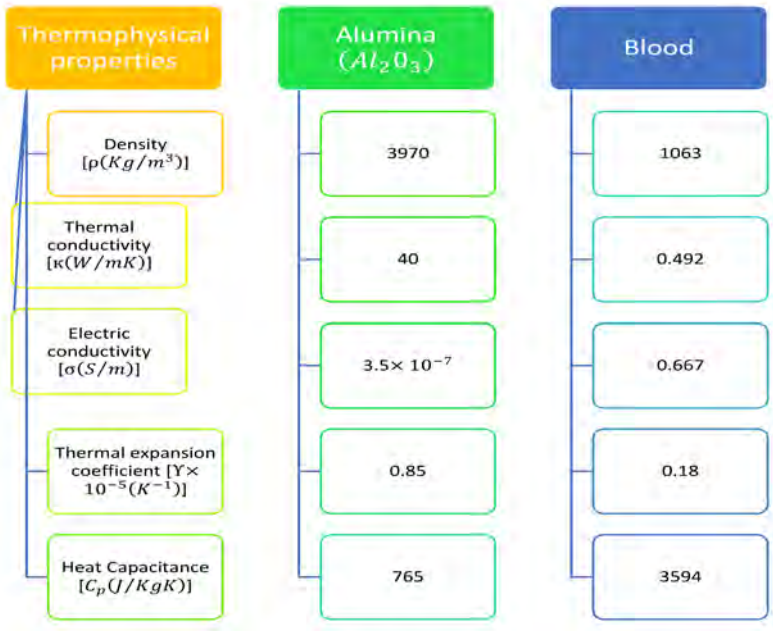

Figure 3.3: Thermophysical properties of blood and nanoparticle

In order to enhance the precision of our results, we have implemented a meshing scheme that ensures the attainment of a convergent solution. In order to perform numerical computations, a custom MATLAB code has been developed to solve for the distribution of velocity, temperature, electroosmotic, and concentration fields within the specified domain. It is worth noting that the electroosmotic equation is unaffected by changes in time, enabling us to effectively create a specialised function file that includes it in each temporal iteration.

3.3 Result & Discussion

3.3.1 Validation

This study aims to validate our model by comparing it to the previously published research conducted by Elnaqeeb et al. [51]. For the validation process, the radiation conditions and irregular stenosis were not considered.

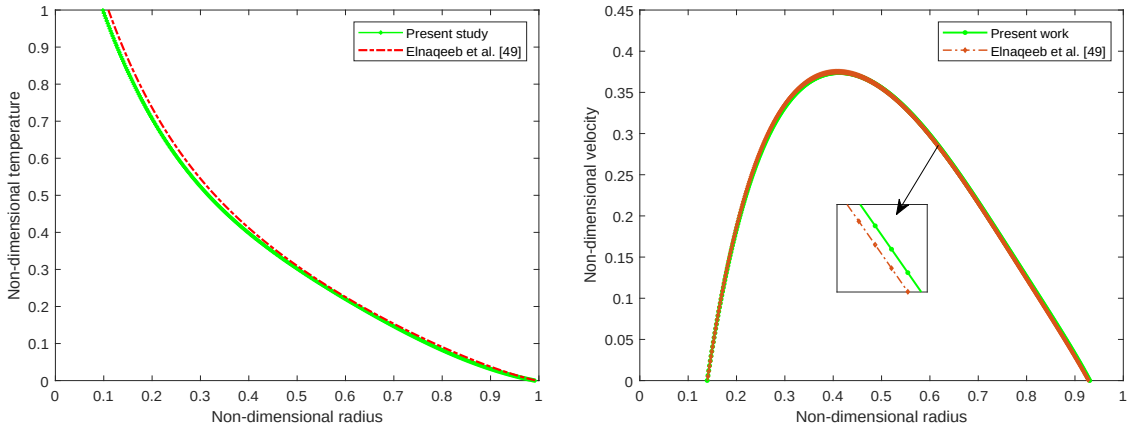

(a) **(b)**

Figure 3.4: Comparision for (a) Temperature distribution for $\sigma = 0.2$, (b) Velocity distribution for $Gr = 5$

To validate the findings, the primary objective was to analyse the behaviour of copper nanoparticles within the bloodstream when subjected to a straight artery ($R_c \neq 0$) while accounting for the source term in place of radiation. The boundary conditions utilised in this study for validation process were derived from the previously mentioned research conducted by Elnaqeeb et al. [51]. The temperature and velocity profiles for the fixed parameters $\sigma = 0.2$ and $Gr = 5$ are illustrated in Figures 3.4a and 3.4b, correspondingly. Significantly, the findings derived from this investigation demonstrate a substantial degree of concurrence with the outcomes presented in the research conducted by Elnaqeeb et al. [51].

3.3.2 Velocity Profile

Figure 3.5 depicts the impact of the different parameters on the velocity profile. The impact of magnetic field parameters and electric kinetic potential between the clot and stenotic zone is depicted in Fig. 3.5a. The analysis reveals that an increase in the magnetic field parameter leads to a decrease in the velocity profile, whereas a contrasting trend is observed in relation to the parameter q_e. The Debye-Huckel parameter q_e exerts a substantial influence on the fluid motion throughout the entire region being analysed. It is worth mentioning that an augmentation in the electro-kinetic parameter, which corresponds to a decrease in the electrical double layer (EDL) thickness, enhances the movement of fluid by reducing the drag force acting on it. The bulk fluid moves proportionately to the charged surface due to the applied electric field. Increasing the magnetic field parameter from $M = 0$ to $M = 4$ resists the fluid motion due to resistive Lorentz force. Figure 3.5b elucidates the effect of the shape and size of the nanoparticles on the velocity profile. According to several researchers, the velocity profile increases as particle size grows from 23 nm to 110 nm. The surface area ratio of a nanoparticle increases with nanoparticle size. Thus, reducing the nanoparticle size enhances the fluid's viscosity and impedes the fluid flow. Figure 3.5c depicts the increasing trend of the velocity profile for an enhancing Gc parameter $(Gc = 0, 1, 2, 3)$. The concentration profile is coupled with the velocity profile as seen in equation (3.24).

The solutal Grashof paramter is the ratio of solutal buoyancy with the hemodynamic viscous force. The buoyancy force depicts the dominant behavior as the value of Gc parameter increases and thus, shows the increasing the velocity profile. Figure 3.5d demonstrates the effect of radius of curvature on the velocity profile. It is observed from the graph that the velocity enhances as the radius of curvature parameter increases from 0 to 5. This phenomenon indicates that as the radius of curvature parameter increases, the artery tends to transform into a straight channel, resulting in reduced fluid obstruction near the wall and facilitating fluid motion. Figure 3.5e illustrates the velocity profile by varying the hematocrit dependent viscosity parameter. In the current study, the figure illustrates both scenarios, one with negligible viscosity ($h_m = 0$) and the other with varying viscosity ($h_m \neq 0$). The velocity profile demonstrates a decrease as the hematocrit parameter increases, primarily due to the concurrent increase in fluid viscosity. The velocity profile, as depicted in Figure 3.5f, showcases the cumulative effect of nanoparticle volumetric concentration and the Grashof number (Gr). It presents a comparative analysis between the velocity profiles of pure blood (devoid of any added nanoparticles) and Al_2O_3-blood (containing integrated nanoparticles). One can observed from the figure that the velocity distribution improves as the Grashof number or nanoparticles concentration enhances in the blood. Enhancing the Grashof number increases the velocity profile due to the dominating buoyancy force over the viscous force.

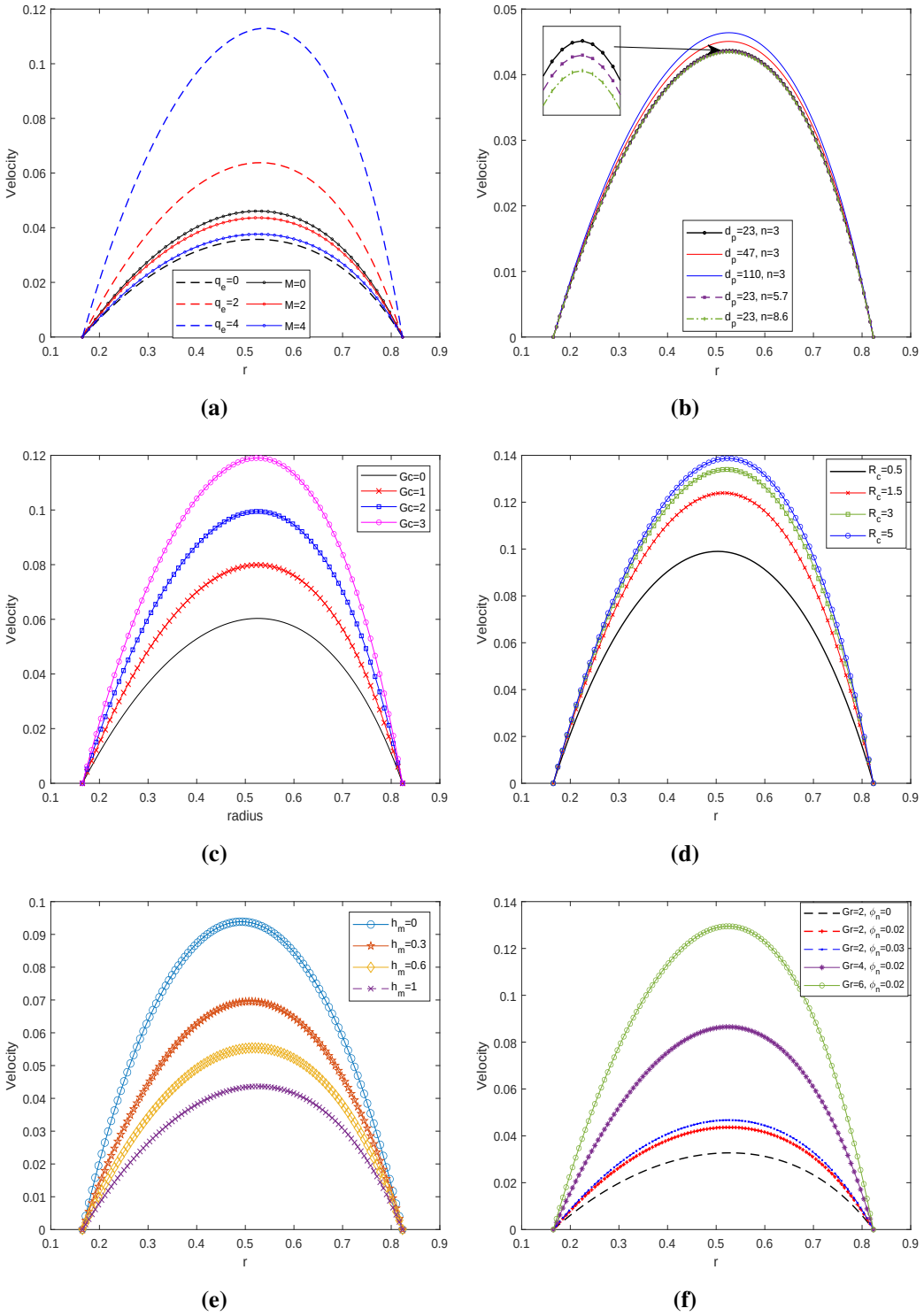

Figure 3.5: Velocity profile by varying (a) M and q_e, (b) d_p and n, (c) Gc, (d) R_c, (e) h_m, (f) Gr and nanoparticle concentration ϕ_1

3.3.3 Temperature Profile & Concentration profile

The temperature profile enhancement is depicted in Figure 3.6a, illustrating its dependence on the nanoparticle size d_p and the shape parameter. The shape parameter is denoted by n, where $n = 3$ corresponds to spheres, $n = 5.7$ and $n = 8.6$ represents for platelets and bricks, respectively. The findings suggest that the shape parameter significantly affects the temperature profile, while the size parameter has a relatively minimal impact. It is worth noting that an augmentation in the shape parameter enhances thermal conductivity, thereby resulting in an elevated temperature profile. The investigation focuses on the influence of two key parameters, namely the Prandtl number (Pr) and the radiation parameter (Nr), on the temperature profile within the context of Figures 3.6b. The provided figures demonstrate a noticeable increase in the temperature distribution as the radiation parameter (Nr) progresses from $Nr = 0$ (representing the absence of radiation) to $Nr = 2$. The observed escalation in temperature distribution can be ascribed to an accompanying surge in the generation of thermal energy, thereby contributing to an upward trajectory in the temperature profile. Therefore, Nr is considered to be a critical factor in determining the temperature profile. The implications of the findings presented in this study are of considerable importance across multiple domains. These endeavours encompass the observation of temperature elevations during hyperthermia therapy for cancer and the advancement of drug administration mechanisms that employ magnetically altered nanoparticles for damaged arterial structures. In certain pathological scenarios, surgeons may opt to administer a heightened dosage of radiation to enhance the thermal distribution, thereby selectively focusing on malignant cells while safeguarding the integrity of healthy ones. Moreover, the analysis presented in Figure 3.6b demonstrates that an augmentation in the Prandtl number (Pr) from 19 to 25 leads to a more advantageous thermal profile. The observed occurrence can be ascribed to the inverse correlation between the Prandtl number and the effective thermal conductivity. It may be noted that the rate at which heat is transmitted from the artery walls to the surrounding fluid (blood) is reduced for higher Prandtl numbers. This particular observation has the potential to play a crucial role in enhancing the efficiency of heat transfer mechanisms within a range of biomedical contexts.

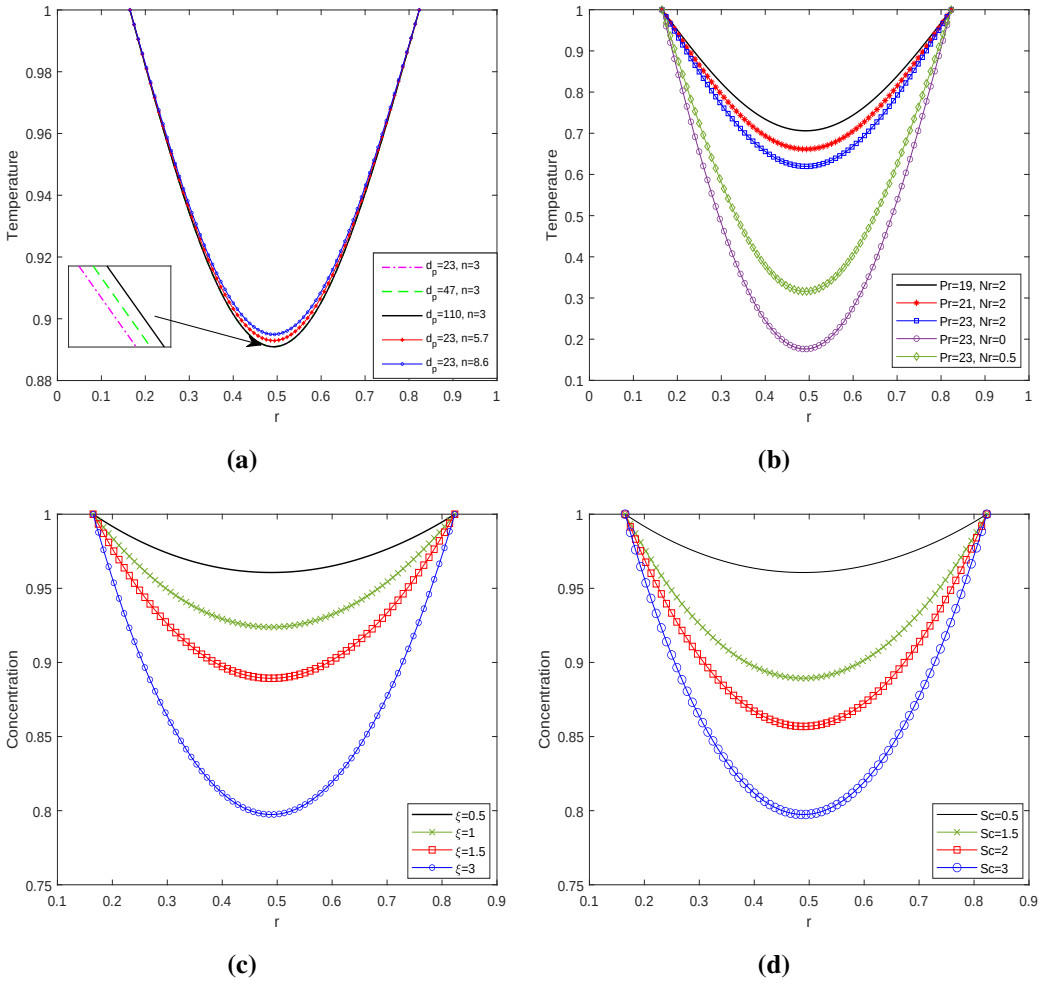

Figure 3.6: Temperature profile by varying (a) d_p and n, (b) Pr and Nr; Variation in concentration profile by varying (c) ξ, (d) Sc

The fact that the concentration profile has a suppressing effect for an increasing value in the chemical reaction parameter may be gleaned from figure 3.6c, as shown. This has occurred as a consequence of the low molecular diffusivity that rises as the value of ξ increases; as a result, less fluid diffuses through the artery wall. Therefore, this behaviour manifests itself everywhere across the flow field. The effect of Schmidt number on the concentration profile is illustrated in figure 3.6d. It is possible to deduce from the figure that the concentration profile will get lower as the Schmidt number gets higher. As the Schmidt number increases, there will be less mass diffusion, resulting in a lower concentration profile.

3.3.4 Flow Rate & Impedance

The present study illustrates the influence of the hematocrit parameter on the flow rate through the utilization of Figures 3.7a and 3.7b. In Figure 3.7a, the first scenario is depicted, wherein the clot is positioned on the left side of the stenosis. Conversely, Figure 3.7b portrays the second scenario, wherein both the clot's axial position and location remain consistent. Clearly, from the figures, it can be seen that the flow rate is less in figure 3.7a as compared to figure 3.7b at the axial position $z_1 = 2$ to $z_1 = 3$. This has happened due to hindrance observed by the flow from both clot and stenosis simultaneously, while the flow rate in figure 3.7a first reduces due to clot presence and then decreases due to stenosis presence. In both depicted illustrations, a noticeable decrement in the flow rate, accompanied by an enhancement in the hematocrit parameter. The observed phenomenon can be elucidated by the simultaneous increase in fluid viscosity resulting from higher levels of hematocrit concentrations in the blood. Similarly, from the figures 3.7c and 3.7d, we can observed that the impedance profile is higher for the case 2 as compared to case 1. In first case, fluid first experience the obstruction due to clot placed at the catheter, then due to stenosis at the arterial wall. In the second case, as the stenosis and clot are located at $z = 2.5$ (positioned at same axial position), so the fluid (blood) experience more hindrance due to their combined effect as compared to first case, where the hindrance in fluid path exists independently. In both the figures, the impedance profile shows increasing nature with respect to the hematocrit parameter. The fluid viscosity increases with an enhancement in the hematocrit parameter leading to show declination in the fluid velocity due to hindrance in its path. Figures 3.7e and 3.7f potrayed the flow rate and impedance profile for the distinct nanoparticle size , respectively. Clearly, from the figure, it can be inferred that flow rate increases as the nanoparticle size enhances as observed in the figure 3.7e, while shows the declining nature in the impedance profile as depicted by figure 3.7f. The smaller the size of the nanoparticle then fluid has more viscosity. Thus, increasing the nanoparticle size reduces the fluid viscosity leading to increasing the flow rate profile whereas decreasing impedance profile as less hindrance comes to the fluid path.

3.3.5 Nusselt Profile & Wall Shear Stress (WSS)

The profile of the Nusselt number for flow parameters like the Prandtl number and the radiation parameter are depicted in figure 3.8a and 3.8b, respectively. It may be noted from the figure 3.8a that the Nusselt profile at axial position $z_1 = 2.5$(peak value of stenosis), the change in Nusselt profile is nearly 65% for change in Pr from 19 to 23.

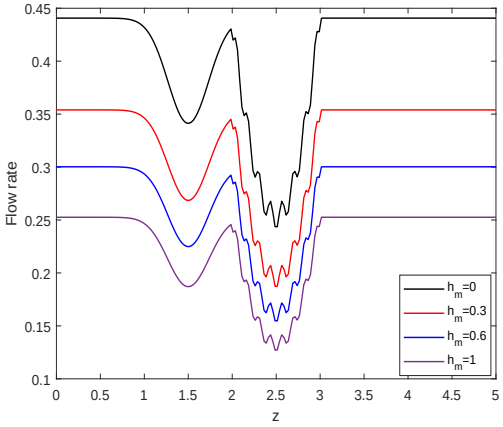

(a) Clot and stenosis at different axial position

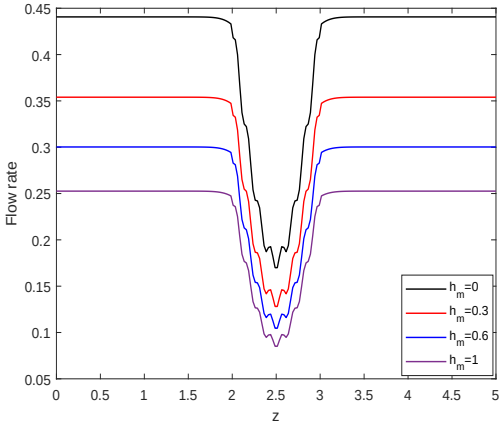

(b) Clot and stenosis at same axial position

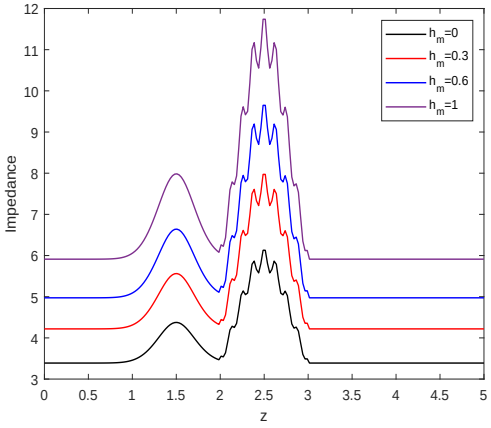

(c) Clot and stenosis at different axial position

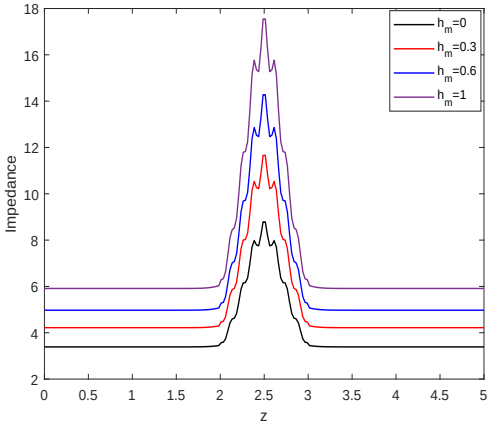

(d) Clot and stenosis at same axial position

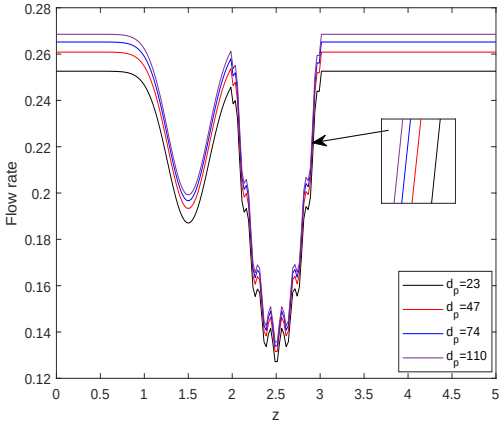

(e) Flow rate by varying d_p

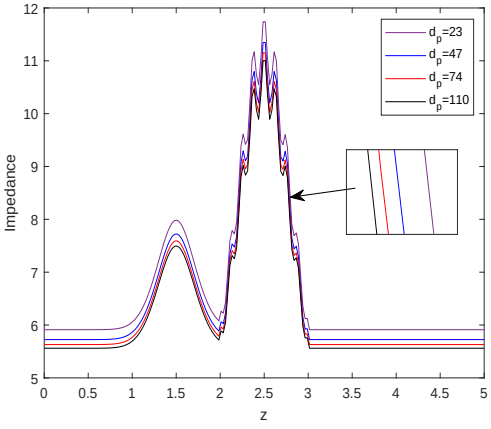

(f) Impedance profile by varying d_p

Figure 3.7: Flow rate by varying (a) h_m, (b) h_m, Impedance profile by varying (c) h_m, (d) h_m, (e)Flow rate by varying d_p, (f) Impedance profile by varying d_p

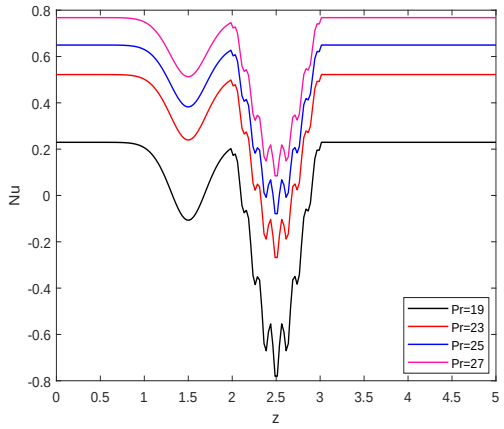

(a) Nusselt profile

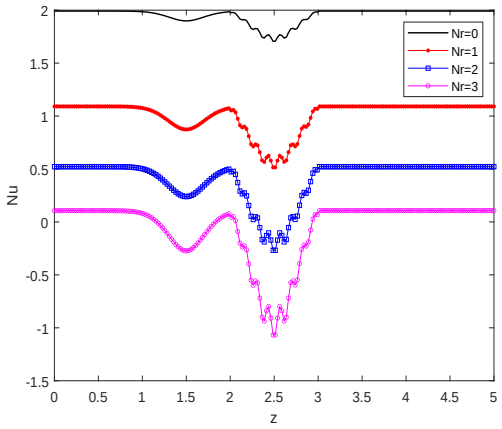

(b) Nusselt profile

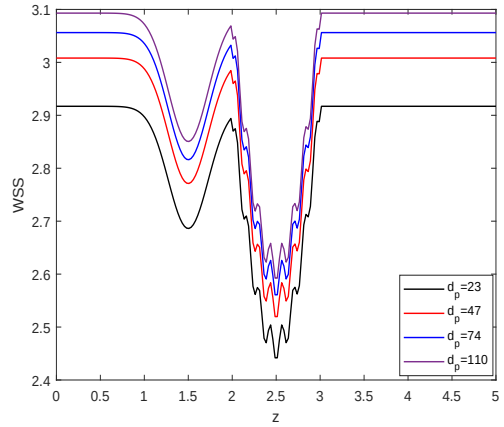

(c) WSS profile

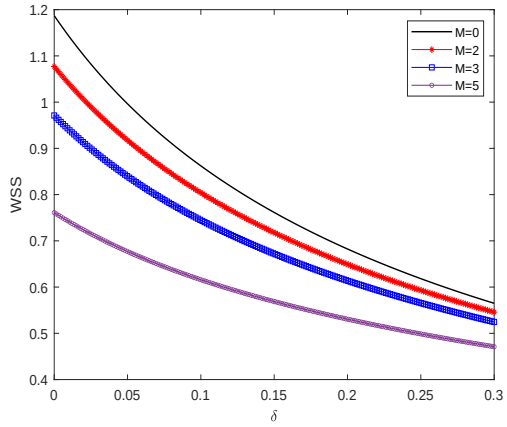

(d) WSS profile

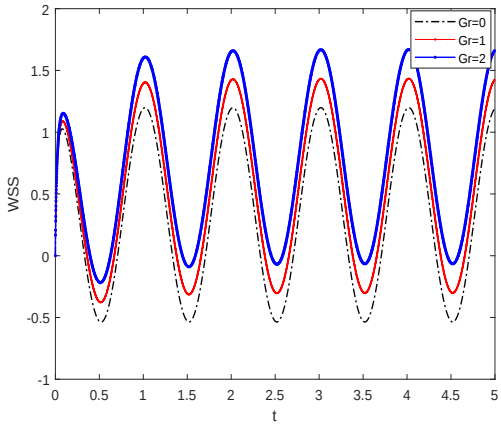

(e) WSS profile

Figure 3.8: Heat transfer coefficient profile by varying (a) Pr, (b) Nr, (c) WSS by varying d_p, (d) WSS by varying stenotic depth δ and M , (e) WSS by varying t and Gr

While, the enhancement is nearly 200% for change of Pr from 25 to 27. Similarly, we can observed from the graph that near the clot region (clot position shifted left of stenosis) at $z_1 = 1.5$, the change is nearly 300% for Pr ranging from 19 to 23 and nearly 35% for Pr ranging from 25 to 27. Also, we can inferred that the Nusselt profile rises to a higher level as the value of Pr is increased. It may be justified since there has been a drop in the thickness of the thermal boundary layer. The reduced temperature profile is the consequence of the reduction in thermal conductivity. As a result, the coefficient of heat transmission through the wall increases. The decrease in thermal conductivity that can be seen in figure 3.8b is shown to occur when the radiation parameter is increased. The reversal trend is seen as a result of an increase in the thickness of the thermal boundary layer close to the wall as Nr increases. Therefore, Nr brings about a decrease in the heat transmission coefficient. From the figure, we can observed that at the stenosis peak, the change in heat transfer profile is nearly 69% and nearly 300% for change in Nr from 0 to 1 and 2 to 3, respectively. While, near the clot region, the change in heat transfer profile is nearly 53% and nearly 200% for change in Nr from 0 to 1 and 2 to 3, respectively. The change in percentage value for both the figures can be occur due to amplifying nature of irregular stenosis and clot with change in the parameter values.

Fig. 3.8c shows how the size of the nanoparticles affects the WSS distribution. As the value of parameter d_p grows, a rising trend is seen in the WSS profile. This is because reducing the nanoparticles size has lowered down the fluid's viscosity, which has increased fluid flow and rendered WSS a growing function of nanoparticle size. When both the stenotic depth and the magnetic field parameter increase, the WSS profile decreases, as seen in Figure 3.8d. The fluid's velocity slows as a result of Lorentz force acting against it. As well as increasing the stenotic depth decreases the fluid velocity as it experiences hindrance in its path with an increase in the size of the stenosis. Grashof number's influence on the shear stress profile is seen in figure 3.8e. The amplitude develops slowly at first and then oscillates at regular intervals. As Gr increases from 0 to 2, the fluid flow enhances due to the generation of thermo buoyancy force.

3.3.6 Velocity Contour

The velocity contour provides a visual depiction of the flow, which may be used to analyse the effect of various parameters on the flow field. Velocity contours display the velocity magnitude at different arterial locations by the series of color-coded regions. The contour for a range of hematocrit values, from $h_m = 0$ to $h_m = 1$, is portrayed in figure 3.9a - 3.9c. The artery section consider here lies in the region of $z = 0.5$ to $z = 5$.

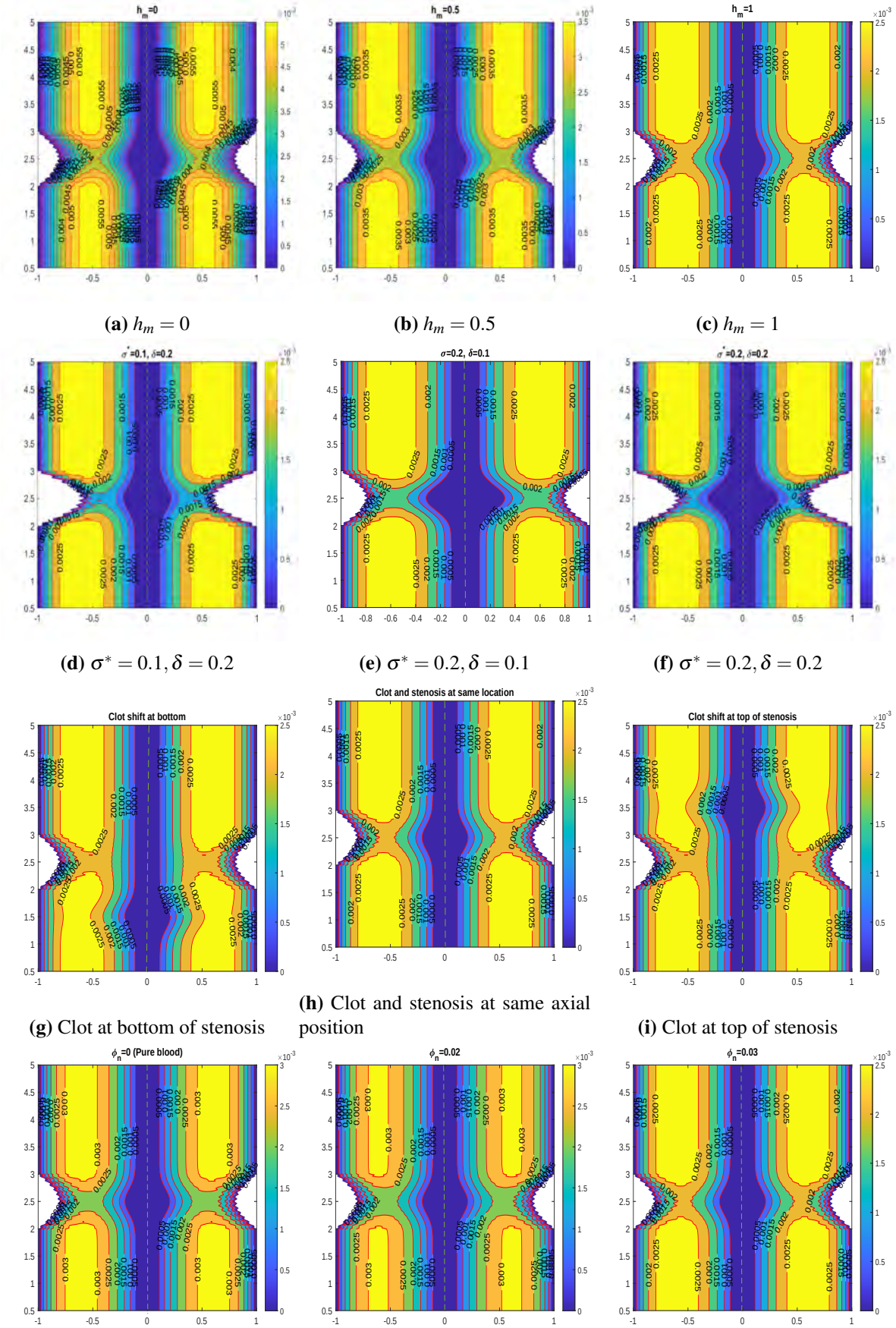

(a) $h_m = 0$ **(b)** $h_m = 0.5$ **(c)** $h_m = 1$

(d) $\sigma^* = 0.1, \delta = 0.2$ **(e)** $\sigma^* = 0.2, \delta = 0.1$ **(f)** $\sigma^* = 0.2, \delta = 0.2$

(g) Clot at bottom of stenosis **(h)** Clot and stenosis at same axial position **(i)** Clot at top of stenosis

(j) $\phi_1 = 0$ **(k)** $\phi_1 = 0.02$ **(l)** $\phi_1 = 0.03$

Figure 3.9: Velocity contour by varying hematocrit parameter, by varying stenosis and clot size, by varying the position of the clot, by varying nanoparticle concentration

It can be concluded from the figure that the velocity of the fluid reduces from 0.0055 to 0.0025. This declination is justified from the figure 3.9a, 3.9b and 3.9c as the magnitude of hematocrit parameter augmented the fluid viscosity also enhances that is depicted by the reduction in the flow rate. Figure 3.9d - 3.9f portrays the role of the size of the stenosis and clot on the hemodynamic flow. The fluid velocity reduces as the size of the stenosis or clot increases as depicted in the figure. If the figure 3.9d and 3.9e are compared with figure 3.9f, the reduction in the velocity can be observed near the region occupying the clot and stenosis in the span of $z = 2$ to $z = 3$.

The hindrance comes in the fluid path can be catastrophic as it reduced the blood flow through artery which is necessary for the basic functions of the body. Thus, it is necessary to address this behavior and proper cure for the disease at a right time. The impact of the clot location on the hemodynamic flow issue is shown in figure 3.9g - 3.9i. Although the maximum flow velocity remains the same in all three conditions, but the change in flow velocity in a certain region can be observed from the figure. In figure 3.9g, the position of the clot comes first afterwards, the stenosis. Similarly, in figure 3.9i, the position of the stenosis comes first afterwards the clot, while in figure 3.9h, the stenosis and clot are centered at the same axial position. In figure 3.9h, the stenosis and clot are centered at the same axial position. Compared to the other two situations, the flow velocity is lower in scenario 3.9h because the clot and stenosis act together to provide a multiplicative effect on the resistance to blood flow. Figure 3.9j - 3.9l depicts the velocity profile for different nanoparticle concentrations from 0 to 0.03. Figure 3.9j represents the arterial section when no nanoparticle is mixed with the blood, while the other two cases (see 3.9k and 3.9l) are for nanoparticle concentrations 0.02 and 0.03. As the concentration of nanoparticles in the blood increases, the velocity profile decreases. These methods may be beneficial for medical professionals and surgeons to slow the body's blood circulation.

3.3.7 Entropy

Figures 3.10a and 3.10b depict the effect of magnetic field parameter on the entropy generation N_G and Bejan number Be, respectively. The figure demonstrates a pattern in which the entropy initially decreases, followed by an increase, and ultimately reduces again as the magnetic field parameter is enhanced. While, the reversed behavior is observed with the Bejan number profile as depicted in figure 3.10b. It is noticed from figure 3.10a that the entropy generation profile decreases as the magnetic field parameter enhances near the arterial wall and catheter tube. This has happened due to the fluid friction irreversibility arises from the resistive Lorentz force.

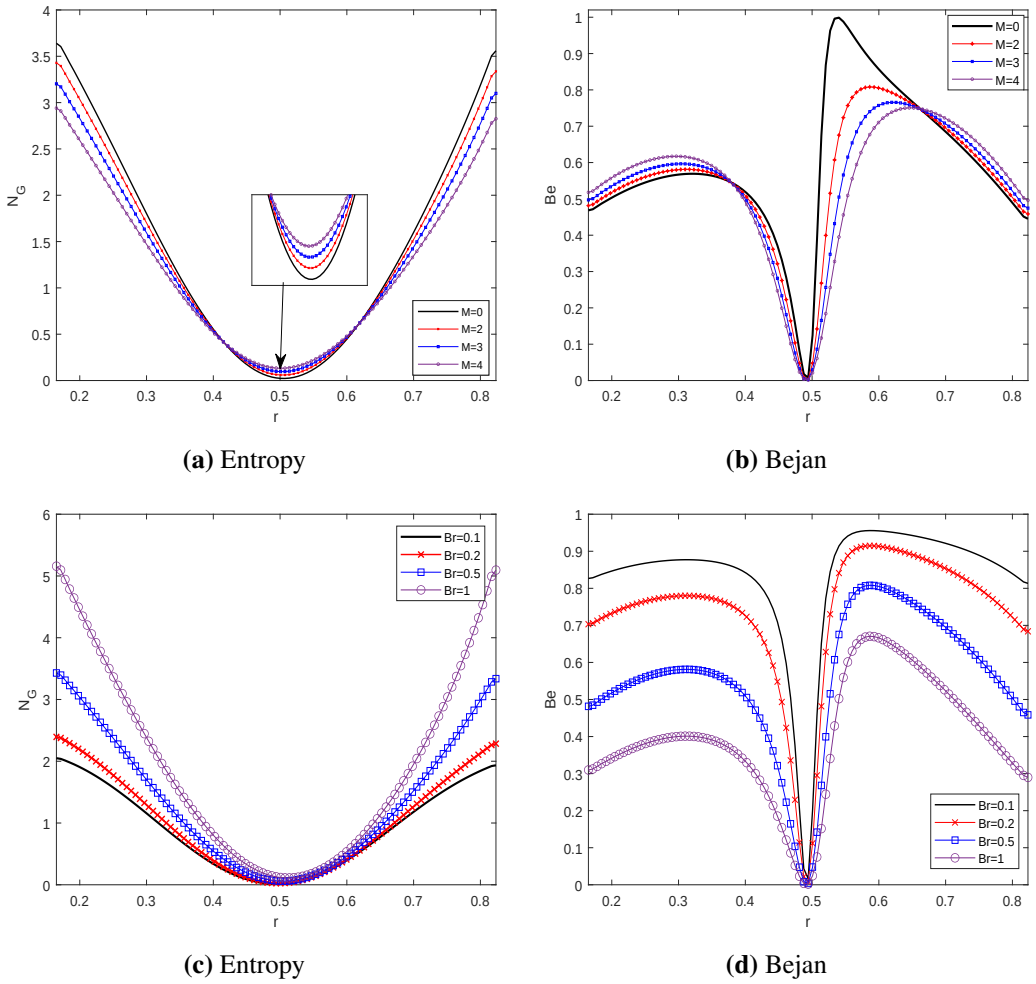

(a) Entropy **(b)** Bejan

(c) Entropy **(d)** Bejan

Figure 3.10: Entropy by varying (a) M, Bejan number by varying (b) M, Entropy by varying (c) Br, Bejan number by varying (d) Br

As, we move away from the walls near the center of the artery, the heat transfer irreversibility dominates due to presence of strong magnetic field which raises the temperature due to Ohmic heating. Hence, the entropy generation enhances near the center. Figure 3.10c elaborates the entropy generation profile for different values of the Brinkmann number Br. Brinkmann number is the ratio of heat generated due to viscous dissipation and heat transported by the molecular conduction. It is evident from the figure that there is a discernible correlation between the Brinkmann number and the enhancement of the entropy profile. This has happened due to the less prominent effect of viscous dissipation as compared heat transfer by molecular conduction. The substantial amount of heat generated between the layer of the fluid causing an enhancement in the entropy profile. The reverse behavior is observed in the Bejan number profile as depicted in the figure 3.10d. The declination in the Bejan profile can be explained by the fact that the less dominant effect of the molecular conduction as compared to viscous dissipation effect.

3.4 Conclusion

The present mathematical model provides the deep insight into the rheology of blood subject to pathological conditions such as stenosis and thrombosis and further helps scientists and researchers to understand the blood flow characteristics. The reduced form of governing equations are discretized using the Crank-Nicolson method and the relevant profile are computed. The salient findings are delineated as follows:

- The velocity distribution demonstrates an increase with an escalation in the nanoparticles volumetric concentration or the Grashof number, primarily due to the intensified effect of buoyant forces .

- The decrement in the WSS profile is observed with an increment in stenotic depth or the magnetic field parameter M.

- The velocity profile exhibits a negative correlation with the magnetic field intensity, while a positive correlation is observed between the velocity profile and the Debyle length parameter.

- Increasing the Brinkmann paramter Br enhances the entropy generation profile but shows the reverse trend with the Bejan number.

The current investigation entails the incorporation of aluminium oxide nanoparticles (AlNPs) into the base fluid medium. The nanoscale entities are categorized as porous metallic oxides, which possess significant surface areas and strongly resist chemical and mechanical disturbances. The extensive accessibility of these technologies makes them economically feasible for integration into the field of biomedical applications. In addition, the aluminium nanoparticles (AlNPs) exhibit significant chemical stability even under exposure to abrasive environments. Examining various dimensions and configurations of nanoparticles within the curved artery facilitates researchers in acquiring knowledge pertaining to the customization and production of pharmaceuticals to enhance drug delivery systems' efficacy. Entropy analysis allows researchers to quantitatively assess the degree of disorder or randomness displayed by flow patterns and evaluate energy dissipation within the system. The present study has primarily focused on standard wall conditions. It is imperative to extend the investigation by considering the permeable wall conditions to advance the research in this domain. To utilize the magnetic drug targeting to treat stenosed arteries with aneurysms and

other pathological conditions. The current study has yet to delve into the complexities of two-phase blood flow modelling. Incorporating the two-phase blood flow model to analyze the fluid flow and heat transfer in a curved tube with time-variant stenosis can significantly broaden the research.

Chapter 4

Simulation of Al_2O_3-Cu/Blood Hybrid Nanofluid Containing Gyrotactic Microorganisms Through the Multi-Stenosed Bifurcated Artery

4.1 Introduction

Numerous studies have been conducted to analyse the hemodynamic characteristics of blood flow through channels, pipes and tubes to understand the pathological mechanism that arises in the stenotic artery. The study provides researchers with insights into hemodynamic flow and facilitates the development of more effective preventative treatments for diseases. Arteriosclerosis, also known as stenosis, is a pathological phenomenon characterised by the accumulation of various substances such as lipids, proteins, fatty compounds, calcium, and other cellular debris along the walls of arteries. This accumulation can result in partial occlusion or complete blockage of the affected blood vessel. A mathematical model was developed by Young [88] to investigate the Newtonian flow within a time-dependent stenosed tube. The findings of the study indicate that the occurrence of stenosis within the artery disrupts the physiological processes of the cardiovascular system, ultimately resulting in severe pathological consequences. The study by Akbar et al. [110] delved into the intricacies of the non-Newtonian fluid model, specifically concerning blood flow within a tapered stenosed artery. The authors approached this investigation by considering blood as a Jeffery fluid. Shit and Roy [111] conducted a study on micropolar fluid to investigate the impact of induced magnetic fields on blood flow through the constricted artery. The study's findings indicate a positive correlation between the Hartman number and stenosis height with an enhancement in microcirculation. Tripathi and Sharma [17] developed a mathematical model to analyse the two-phase hemodynamic flow through a stenosed artery, incorporating chemical reactions and radiation effects. The study illustrated a reduction in blood velocity

adjacent to the arterial wall, as evidenced by the distortion of the velocity contour downstream and the shift of the tapering bolus towards the arterial wall. The study conducted by Khanduri and Sharma [107, 112] pertained to the examination of the impact of Hall effects on the flow of MHD fluid through a stenosed artery that has been affected by thrombosis. The study's findings indicate a decline in the WSS profile as the Hartman number and stenotic depth increase. This phenomenon is caused by a reduction in blood flow near the arterial walls.

The study revealed that atherosclerotic plaque, which obstructs blood flow in arteries, tends to manifest in regions of complex geometry, such as those proximal to bifurcations, junctions, or areas of high curvature. The presence of arterial curvature and variations in the size of the cross-section both had a role in the preferred localization of the plaque at the arterial walls. Tan et al. [113] explored the blood flow through the bifurcated artery under the gravity effect and irregular stenosis at the parent artery. Srinivasacharya and Rao [114] have designed a mathematical model to investigate the hemodynamic behaviour of blood flow containing copper nanoparticles within a constricted bifurcated artery. The study's findings indicate a notable alteration in the flow rate and impedance in the vicinity of the apex. This phenomenon is attributed to the occurrence of backflow at the junction and the presence of secondary flow in the region proximal to the apex. Moreover, the researchers [115] proceeded with their investigation by examining the behaviour of a couple's stress fluid within a bifurcated artery. Shahzadi et al. [13] conducted a theoretical investigation to examine the bio-nanofluid containing copper nanoparticles as a therapeutic agent in the bifurcated artery with compliant walls. The non-Newtonian Casson fluid was investigated by Shahzad et al. [116] in the context of a bifurcated channel featuring stenosis and elastic walls.

The study of blood rheology is affected by the application of external magnetic and electric fields, resulting in the reduction of the fluid flow, and such type of flow is commonly referred to as electro-magneto hydrodynamics (EMHD) flow. Kolin [91] introduced the concept of MHD in his medical research. The experiments demonstrate that applying a transverse magnetic field to an electrical field decelerates fluid motion. The empirical finding indicated a decrease of 30% in the volumetric blood flux within the duct subject to a high magnetic field of 10 Tesla. Ahmed and Nadeem [2] have constructed a mathematical model encompassing six distinct types of stenosis and have subsequently conducted an investigation on the effect of MHD and hybrid nanoparticles on micropolar fluid. The study revealed an increase in velocity and wall shear stress (WSS) with an enhancement in nanoparticle concentrations, while an inverse trend was observed for the impedance profile. The MHD

fluid flow in an artery was explored numerically by Joshua et al. [117] by employing a non-Newtonian Cross-rheological model. The researchers have considered the presence of multiple stenoses along the arterial walls and have conducted a comprehensive investigation by varying the magnetic parameter, Reynolds number, and stenosis height throughout the entire length of the artery. Kumar et al. [118] analysed MHD fluid flow in a bifurcated artery with permeability, considering the effect of heat source and chemical reaction. The EMHD flow of Au-blood through the inclined constricted artery under periodic body acceleration was investigated by Manchi and Ponalagusamy [119]. The researchers also placed emphasis on the shape of nanoparticles and concluded that the spherical nanoparticles exhibit a greater heat flux at the arterial walls in comparison with other nanoparticles shapes . Sharma et al. [27] formulated the MHD two-phase blood flow model by considering the variable viscosity in a curved artery. The study's findings suggest that atherosclerosis formation positively correlates with curvature and permeability, whereas the heat source parameter reduces the risk of atherosclerosis formation. The study conducted by Mishra et al. [120] delved into the characteristics of magnetohydrodynamic (MHD) nanofluid as it flows through a constricted artery while considering the Soret and Dufour effects. The optimisation of heat transfer in nanofluid blood flow through the stenosed artery was discussed by Sharma et al. [121]. The authors examined the hematocrit-dependent viscosity model and demonstrated that increased hematocrit level and stenotic depth leads to a reduction in the fluid velocity.

Both theoretical and experimental results have underscored the significance of nanoparticles in the biomedical domain, as they have been shown to augment the efficacy of delivering diagnostic and therapeutic agents. Numerous investigations have been undertaken to examine the novel potential of nanoparticles at the molecular scale within the realm of life sciences. The successful delivery of nanoparticles into the artery is primarily determined by their physical characteristics, including shape, size, and surface absorption properties. Nanofluid refers to a suspension of nanoparticles in a base fluid, whereas hybrid nanofluid pertains to a suspension of two or more types of nanoparticles in the base fluid. Synthesis of hybrid nanofluids offers the advantage of incorporating diverse materials' physical and thermal properties into a singular, homogeneous phase. This results in remarkable physicochemical properties in the resulting synthetic hybrid nanofluid. The hemodynamic flow through permeable walls was investigated by Ellahi et al. [122], employing the homotopy analysis method. The hybrid nanofluid flow through a stenosed artery was analysed by Gandhi et al. [39] in the presence of Joule heating and viscous dissipation. The findings of their research indicate that an increase in the Darcy number results in an enhancement of the

velocity profile. This can be attributed to the lower resistance offered by the medium permeability. The researcher, Basha et al. [123], analysed the inclined, uneven,and stenosed artery to investigate the biomagnetic blood flow of Au-Cu. The study conducted by Gandhi and Sharma [124] involved an investigation of the behaviour of Au-Cu hybrid nanoparticles in the context of blood flow through an artery with overlapping stenosis at the walls. The study revealed that an augmentation in the Casson fluid parameter results in the enhancement of both velocity and temperature. The researchers suggest that their findings may have potential applications in nano-pharmacology and biomedical sciences. In this study, we have selected Al_20_3-Cu nanoparticles for their remarkable anti-bacterial and anti-viral properties, which could be utilized in the biomedical field. The chemical stability and easy accessibility of these nanoparticles make them a perfect choice for our research.
Bioconvection refers to the phenomenon whereby the macroscopic motion of microorganisms occurs due to spatial variations in density. Microorganisms exhibit self-propulsion, whereas nanoparticles lack this capability. The phenomenon of bioconvection can be observed under conditions where the concentration of nanoparticles is relatively low. The phenomenon of bioconvection is observed due to the instability caused by spatial variation, which leads to the upward movement of microorganisms and the formation of a dense layer at the surface. This layer becomes unstable and results in the crumbling of microorganisms, further enhancing the bioconvection process. Bhatti et al. [125] have presented a discussion on the peristaltic motion of Jeffery nanofluid in the presence of microorganisms and a variable magnetic field. The bioconvection movement of microorganisms in a hybrid nanofluid through a porous stretching sheet was investigated by Alharbi et al. [126] . The study conducted by Sharma et al. [1] delved into the dynamics of magnetohydrodynamic (MHD) fluid flow in the presence of microorganisms over an inclined stretching sheet. Mekheimer et al. [127] conducted a study on the delivery of drugs via nanoparticles in the presence of hemodynamic flow within diseased organs. The study conducted by Mostapha and EL-Dabe [128] was a theoretical investigation of the flow of peristaltic-induced nanofluid, wherein motile gyrotactic microorganisms are observed to move through an endoscope. The study considered the effects of radiation and chemical interaction while incorporating the Soret and Dufour scheme.

The aforementioned study has served as inspiration and a basis for our current research on the hemodynamic behaviour of hybrid nanofluids in bifurcated arteries with mild stenosis in both parent and daughter arteries. This study presents a model that examines blood flow behaviour containing suspended nanoparticles of Al_2O_3-Cu, in the presence of gyrotactic microorganisms and electroosmotic force.The governing equations were rendered

non-dimensional and subsequently solved utilising the Crank-Nicolson scheme. The ensuing outcomes were analysed, and the effects of various parameters were elucidated by plotting velocity, temperature, concentration, microorganisms, flow rate, and WSS profiles.

4.2 Model Formulation

Consider a fully developed, unsteady, laminar, incompressible two-dimensional MHD blood flow passing through the stenosed bifurcated artery. The arteries are assumed to be straight, circular cylinder passing the center line of the parent artery. The bifurcated artery has overlapping stenosis at the parent artery while the irregular stenosis at the daughter arteries as shown in figure 4.1 . Let assumed the cylindrical coordinate system $\tilde{r}, \tilde{\theta}$ and $\tilde{z}$ to represent the material point in which $\tilde{z}$ is along the centerline of the parent artery and $\tilde{r}$ and θ are assumed to be radial and circumferential directions, respectively. The flow is assumed to be antisymmetric so all the variables are independent of $\tilde{\theta}$. A uniform magnetic field denoted by $\mathbf{B} = (B_0, 0, 0)$ and an electric field denoted by $\mathbf{E} = (0, 0, E_0)$ are applied to the flow of blood, where B_0 is constant. The gravitational force acts in the downward direction and induced magnetic field assumed to be negligible due to low magnetic Reynold's number assumption. The potential for a flow separation zone is eliminated with the incorporation of curvature at the lateral junction and bifurcation's apex.

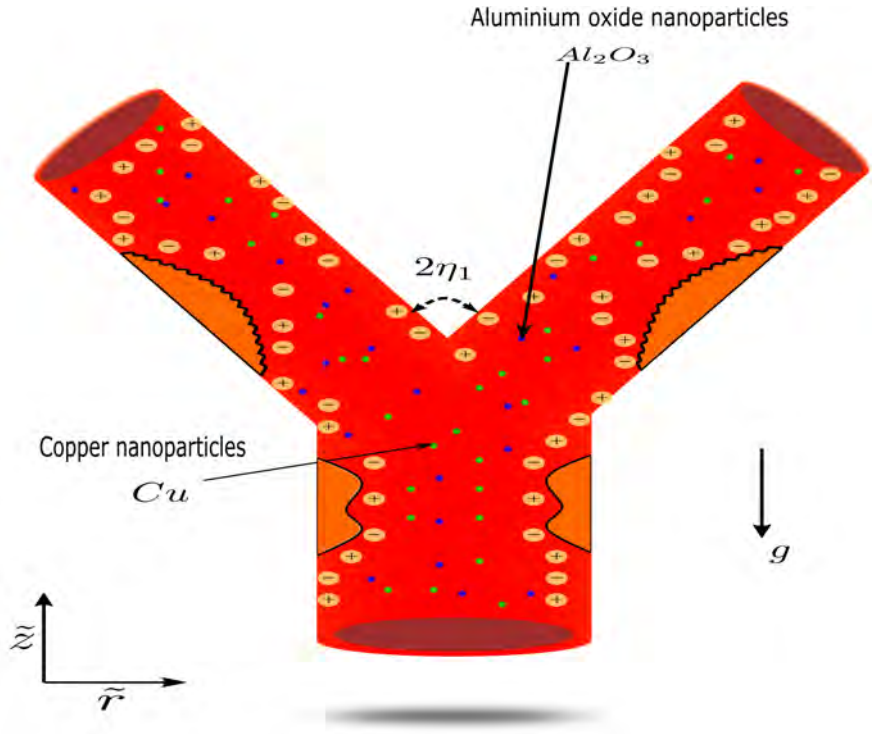

Figure 4.1: Representation of bifurcated stenosed artery

The geometry of the bifurcated artery with multi-stenosis in the parent artery and an overlapping stenosis in the daughter artery is expressed as follows [13]:

$$\tilde{\hat{R}}_1^*(\tilde{z}) = \begin{cases} R_0, & 0 < \tilde{z} \le \tilde{d} \\ R_0 - B^*, & \tilde{d} < \tilde{z} \le \tilde{d} + L_0 \\ R_0, & \tilde{d} + L_0 < \tilde{z} \le \tilde{z}_1 \\ R_0 + \tilde{r}_1 - \sqrt{\left(\tilde{r}_1^2 - \frac{R_0^2}{L_0^2}(\tilde{z} - \tilde{z}_1)^2\right)} & \tilde{z}_1 < \tilde{z} \le \tilde{z}_2 \\ 2r_0 sec\eta_1 + \frac{R_0}{L_0}\left(\tilde{z} - \tilde{z}_2\right)\tan\eta_1 & \tilde{z}_2 < \tilde{z} \le \tilde{z}_4 + 0.5L_0 \\ 2r_0 sec\eta_1 + \frac{R_0}{L_0}\left(\tilde{z} - \tilde{z}_2\right)\tan\eta_1 - A^* & \tilde{z}_4 + 0.5L_0 < \tilde{z} \le \tilde{z}_4 + 2.5L_0, \\ 2r_0 sec\eta_1 + + \frac{R_0}{L_0}\left(\tilde{z} - \tilde{z}_2\right)\tan\eta_1, & \tilde{z}_4 + 2.5L_0 < \tilde{z} \le z_{max} \end{cases} \tag{4.1}$$

Where,

$$A^* = 2\delta_1\left\{\cos\left(\frac{2\pi}{L_0}\left(\frac{\tilde{z} - \tilde{d}}{4}\right) - 0.25\right) - 0.07\cos\left(\frac{128\pi}{L_0}\left(\tilde{z} - \tilde{d} - 0.5L_0\right)\right)\right\}\tan(\eta_1),$$

$$B^* = \frac{6}{5L_0^4}\delta(11(\tilde{z} - \tilde{d})L_0^3 - 47(\tilde{z} - \tilde{d})^2L_0^2 + 72(\tilde{z} - \tilde{d})^3L_0 - 36(\tilde{z} - \tilde{d})^4)$$

And, Kroncecker delta function is defined as:

$$\delta_{ij} = \begin{cases} 0 & \text{for} \quad 0 < \tilde{z} \le \tilde{z}_3, \\ 1 & \text{for} \quad \tilde{z}_3 < \tilde{z} \le \tilde{z}_{max}, \end{cases} \tag{4.2}$$

The inner wall is represent as:

$$\tilde{\hat{R}}_2^*(\tilde{z}) = \begin{cases} 0, & 0 < \tilde{z} \le \tilde{z}_3, \\ \sqrt{\tilde{r}_1^{*2} - \left(R_0\left(\frac{\tilde{z} - \tilde{z}_3}{L_0}\right) - \tilde{r}_1^*\right)^2}, & \tilde{z}_3 < \tilde{z} \le \tilde{z}_4, \\ \frac{R_0}{L_0}(\tilde{z} - \tilde{z}_2)\tan\eta_1, & \tilde{z}_4 < \tilde{z} \le \tilde{z}_{max}. \end{cases} \tag{4.3}$$

Where, $\tilde{d}$ represent location of stenosis, $\tilde{z}_1$ denotes the location of insert lateral junction, $\tilde{z}_{max}$ signifies the maximum length of stenosis; $\tilde{r}_1$ denotes the daughter artery radius; The radii of curvature at the flow divider and at lateral junction is represented by:

$$\tilde{\tilde{r}}_1^* = \frac{(\tilde{z}_3 - \tilde{z}_2)R_0 \sin\eta_1}{L_0(1-\sin\eta_1)}, \;\; \tilde{r}_1 = \frac{R_0 - 2r_0 \sec\eta_1}{\cos\eta_1 - 1}, \;, \tag{4.4}$$

The positional of the lateral junction offset, apex, and curvature offset at the inner wall are presented as follows:

$$\tilde{z}_2 = \tilde{z}_1 + \tilde{r}_1 \left(\frac{L_0}{R_0}\right) \sin\eta_1, \tag{4.5}$$

$$\tilde{z}_3 = \tilde{z}_2 + q_1 L_0, \tag{4.6}$$

$$\tilde{z}_4 = \tilde{z}_3 + \tilde{\tilde{r}}_1^* \left(\frac{L_0}{R_0}\right)(1-\sin\eta_1). \tag{4.7}$$

Where η_1 is half of the bifurcation angle and value of q_1 lies between 0.1 and 0.5, z_{max} represents the finite length of the bifurcated artery.

4.2.1 Governing Equations

Assuming the aforementioned conditions and utilising the Boussinesq approximation, the equations dictating the flow can be expressed as follows [124]:

Continuity Equation:

$$\frac{\partial \tilde{u}}{\partial \tilde{r}} + \frac{\tilde{u}}{\tilde{r}} + \frac{\partial \tilde{w}}{\partial \tilde{z}} = 0, \tag{4.8}$$

Momentum Equation:
$\tilde{r}$-direction:

$$\rho_{hnf}\left[\frac{\partial \tilde{u}}{\partial \tilde{t}} + \tilde{u}\frac{\partial \tilde{u}}{\partial \tilde{r}} + \tilde{w}\frac{\partial \tilde{u}}{\partial \tilde{z}}\right] = -\frac{\partial \tilde{p}}{\partial \tilde{r}} + \frac{1}{\tilde{r}}\frac{\partial}{\partial \tilde{r}}\left[\mu_{hnf}\tilde{r}\frac{\partial \tilde{u}}{\partial \tilde{r}}\right] + \frac{1}{2}\frac{\partial}{\partial \tilde{z}}\left[\mu_{hnf}\left(\frac{\partial \tilde{w}}{\partial \tilde{r}} + \frac{\partial \tilde{u}}{\partial \tilde{z}}\right)\right] - \mu_{hnf}\frac{\tilde{u}}{\tilde{r}^2}, \tag{4.9}$$

$\tilde{z}$-direction:

$$\rho_{hnf}\left[\frac{\partial \tilde{w}}{\partial \tilde{t}}+\tilde{u}\frac{\partial \tilde{w}}{\partial \tilde{r}}+\tilde{w}\frac{\partial \tilde{w}}{\partial \tilde{z}}\right]=-\frac{\partial \tilde{p}}{\partial \tilde{z}}+\frac{1}{2}\frac{1}{\tilde{r}}\frac{\partial}{\partial \tilde{r}}\left[\mu_{hnf}\tilde{r}\left(\frac{\partial \tilde{u}}{\partial \tilde{z}}+\frac{\partial \tilde{w}}{\partial \tilde{r}}\right)\right]+\frac{\partial}{\partial \tilde{z}}\left[\mu_{hnf}\frac{\partial \tilde{w}}{\partial \tilde{z}}\right]$$
$$+(\rho\beta)_{hnf}g\left[(\tilde{T}-\tilde{T}_0)+(\tilde{C}-\tilde{C}_0)-(\tilde{n}^*-\tilde{n}_1^*)\right]\cos(\eta_1\delta_{ij})+G(\tilde{t})+\rho_e E_0-\sigma_{hnf}B_0^2\tilde{w}, \tag{4.10}$$

Energy Equation:

$$(\rho C_p)_{hnf}\left[\frac{\partial \tilde{T}}{\partial \tilde{t}}+\tilde{u}\frac{\partial \tilde{T}}{\partial \tilde{r}}+\tilde{w}\frac{\partial \tilde{T}}{\partial \tilde{z}}\right]=k_{hnf}\left[\frac{\partial^2 \tilde{T}}{\partial \tilde{r}^2}+\frac{1}{\tilde{r}}\frac{\partial \tilde{T}}{\partial \tilde{r}}+\frac{\partial^2 \tilde{T}}{\partial \tilde{z}^2}\right]+\tilde{Q}_0+\sigma_{hnf}B_0^2\tilde{w}^2+\sigma_{nf}E_0^2+\phi^*, \tag{4.11}$$

where,

$$\phi^*=2\mu_{hnf}\left[\left(\frac{\partial \tilde{u}}{\partial \tilde{r}}\right)^2+\left(\frac{\tilde{u}}{\tilde{r}}\right)^2+\left(\frac{\partial \tilde{w}}{\partial \tilde{z}}\right)^2+\frac{1}{2}\left(\frac{\partial \tilde{u}}{\partial \tilde{z}}+\frac{\partial \tilde{w}}{\partial \tilde{r}}\right)^2\right].$$

Concentration Equation:

$$\frac{\partial \tilde{C}}{\partial \tilde{t}}+\tilde{u}\frac{\partial \tilde{C}}{\partial \tilde{r}}+\tilde{w}\frac{\partial \tilde{C}}{\partial \tilde{z}}=D_b\left[\frac{\partial^2 \tilde{C}}{\partial \tilde{r}^2}+\frac{1}{\tilde{r}}\frac{\partial \tilde{C}}{\partial \tilde{r}}+\frac{\partial^2 \tilde{C}}{\partial \tilde{z}^2}\right]-R_c(\tilde{C}-\tilde{C}_0) \tag{4.12}$$

Microorganism Equation:

$$\frac{\partial \tilde{n}^*}{\partial \tilde{t}}+\tilde{u}\frac{\partial \tilde{n}^*}{\partial \tilde{r}}+\tilde{w}\frac{\partial \tilde{n}^*}{\partial \tilde{z}}+\frac{bW_c}{\tilde{C}_0-\tilde{C}_w}\left[\frac{\partial}{\partial \tilde{r}}\left(\frac{\tilde{n}^*\partial \tilde{C}}{\partial \tilde{r}}+\frac{\partial}{\partial \tilde{z}}\left(\frac{\tilde{n}^*\partial \tilde{C}}{\partial \tilde{z}}\right)\right)\right]=D_n\left[\frac{\partial^2 \tilde{n}^*}{\partial \tilde{r}^2}+\frac{1}{\tilde{r}}\frac{\partial \tilde{n}^*}{\partial \tilde{r}}+\frac{\partial^2 \tilde{n}^*}{\partial \tilde{z}^2}\right] \tag{4.13}$$

The boundary conditions are:

$$\tilde{w}=0,\ \ \tilde{T}=\tilde{T}_w,\ \ \tilde{C}=\tilde{C}_w,\ \ \tilde{n}^*=\tilde{n}_w^*,\ \ \text{at}\ \ \tilde{r}=\tilde{\tilde{R}}_1^*(\tilde{z})\quad \text{for all}\quad \tilde{z}, \tag{4.14}$$

$$\frac{\partial \tilde{w}}{\partial \tilde{r}}=0,\ \ \frac{\partial \tilde{T}}{\partial \tilde{r}}=0,\ \ \frac{\partial \tilde{C}}{\partial \tilde{r}}=0,\ \ \frac{\partial \tilde{n}^*}{\partial \tilde{r}}=0,\ \ \text{at}\ \ \tilde{r}=0\quad \text{for}\quad 0\le \tilde{z}\le \tilde{z}_3, \tag{4.15}$$

$$\tilde{w}=0,\ \ \tilde{T}=\tilde{T}_w,\ \ \tilde{C}=\tilde{C}_w,\ \ \tilde{n}^*=\tilde{n}_w^*\ \ \text{at}\ \ \tilde{r}=\tilde{\tilde{R}}_2^*(\tilde{z})\quad \text{for}\quad \tilde{z}_3\le \tilde{z}\le \tilde{z}_{max}. \tag{4.16}$$

The initial condition regarding velocity, temperature, concentration and microorganisms are considered as:

$$\tilde{w} = 0, \;\; \tilde{T} = 0, \;\; \tilde{C} = 0, \;\; \tilde{n}^* = 0 \;\text{ at }\; \tilde{t} = 0. \tag{4.17}$$

The body acceleration and pressure gradient terms are given as;

$$G(\tilde{t}) = B_0 \cos(\omega_q \tilde{t} + \psi) \tag{4.18}$$

$$-\frac{\partial \tilde{p}}{\partial \tilde{z}} = A_0 + A_1 \cos(\omega_p \tilde{t}) \tag{4.19}$$

Here, A_0 and A_1 are steady-state and amplitude of fluctuating component of pressure gradient, respectively. Where, $\omega_p = 2\pi f_p$, f_p is pulse frequency, B_0 is the body acceleration term, $\omega_q = 2\pi f_q$, f_q is frequency of body acceleration with ψ as a phase angle.

4.2.1.1 Electrohydrodynamics (EHD)

Blood is a complex physiological fluid consisting of haemoglobin, plasma, white blood cells, and various ionic components. Its unique composition enables it to function as an electrically conductive fluid. When the arterial walls are exposed to an electrolyte solution, a net charge is generated at the arterial walls. This leads blood to take the opposite charge near the arterial walls. Upon applying an electric field, the charged ion undergoes movement and subsequently induces fluid motion in its vicinity. This phenomenon is commonly referred to as electro-osmotic flow. The Poisson-Boltzmann equation provides the electro-osmotic potential function, as stated in work by Manchi et al. [34]:

$$\nabla^2 \tilde{\Phi} = -\frac{\rho_e}{\varepsilon}, \tag{4.20}$$

where, $\tilde{\Phi}$ is the electro-osmotic function, ε is dielectric constant, and ρ_e is given as:

$$\rho_e = (n^+ - n^-) e_0 z_0. \tag{4.21}$$

The Boltzmann distribution can effectively describe the determination of the number density of cations and anions as:

$$n^{\pm} = n_0 \exp\left(\mp \frac{e_0 z_0 \tilde{\Phi}}{k_B T_{avg}} \right), \tag{4.22}$$

where, z_0 is the charge balance, e_0 is electric constant, k_B is Boltzmann constant.

Using the Debye-Huckel linearizion, the Poisson equation takes the form:

$$\left(\frac{\partial^2}{\partial\tilde{r}^2}+\frac{1}{\tilde{r}}\frac{\partial}{\partial\tilde{r}}+\frac{\partial^2}{\partial\tilde{z}^2}\right)\tilde{\Phi}=\frac{\tilde{\Phi}}{q_m^2}, \tag{4.23}$$

where $q_m=\frac{1}{e_0 z_0}\sqrt{\frac{\varepsilon k_B T_{avg}}{2n_0}}$.

The boundary conditions for electro-osmotic equation are:

$$\begin{cases}\tilde{\Phi}=\tilde{\zeta}_1, & \text{at} \quad \tilde{r}=\tilde{\hat{R}}_1^*(\tilde{z}) \quad \text{for all} \quad \tilde{z},\\ \frac{\partial\tilde{\Phi}}{\partial\tilde{r}}=0, & \text{at} \quad \tilde{r}=0 \quad \text{for} \quad 0\le\tilde{z}\le\tilde{z}_3,\\ \tilde{\Phi}=\tilde{\zeta}_2, & \text{at} \quad \tilde{r}=\tilde{\hat{R}}_2^*(\tilde{z}) \quad \text{for} \quad \tilde{z}_3\le\tilde{z}\le z_{max}.\end{cases} \tag{4.24}$$

4.2.2 Non-Dimensionalization

It is necessary to convert the governing equations presented in (4.8)-(4.13) into dimensionless form in order to obtain a numerical solution. The introduction of non-dimensional variables is performed in the following manner:

$$u=\frac{L_0\tilde{u}}{\delta^* U_0}, t=\frac{U_0\tilde{t}}{R_0}, z=\frac{\tilde{z}}{L_0}, p=\frac{R_0^2\tilde{p}}{U_0 L_0\mu_0}, r=\frac{\tilde{r}}{R_0}, w=\frac{\tilde{w}}{U_0}, T=\frac{\tilde{T}-\tilde{T}_0}{\tilde{T}_w-\tilde{T}_0}, C=\frac{\tilde{C}-\tilde{C}_0}{\tilde{C}_w-\tilde{C}_0},$$
$$\tilde{\chi_1}^*=\frac{\tilde{n}^*-\tilde{n}_1^*}{\tilde{n}_w^*-\tilde{n}_1^*}, \hat{R}_i^*=\frac{\tilde{\hat{R}}_i^*}{R_0}(i=1,2), d=\frac{\tilde{d}}{L_0}, r_0=\frac{\tilde{r}_0}{R_0}, z_i=\frac{\tilde{z}_i}{L_0}(i=1,..,4), r_1=\frac{\tilde{r}_1}{R_0},$$
$$\tilde{r_1}^*=\frac{\tilde{\hat{r}}_1^*}{R_0}, Re=\frac{U_0\rho_f R_0}{\mu_f}, M^2=\frac{\sigma_f B_0^2 R_0^2}{\mu_f}, E_1^*=\frac{E_0}{B_0 U_0}, Gr=\frac{\rho_f R_0^2 g\beta_f(\tilde{T}_w-\tilde{T}_0)}{\mu_f U_0},$$
$$Gc=\frac{\rho_f R_0^2 g\beta_f(\tilde{C}_w-\tilde{C}_0)}{\mu_f U_0}, Rb=\frac{\rho_f R_0^2 g\beta_f(\tilde{n}_w^*-\tilde{n}_1^*)}{\mu_f U_0}, Ec=\frac{U_0^2}{C_p(\tilde{T}_w-\tilde{T}_0)}, Pr=\frac{\mu_f C_p}{k_f},$$
$$\tilde{Q}=\frac{\tilde{Q}_0 R_0^2}{\kappa_f(\tilde{T}_w-\tilde{T}_0)}, S_z=\frac{\sigma_f}{\kappa_f}\frac{R_0^2 E_0^2}{(\tilde{T}_w-\tilde{T}_0)}, q_e=\frac{q_m}{R_0}, Sc=\frac{\nu}{D_m}, Pe=\frac{bW_c}{D_n}, \sigma_1=\frac{\tilde{n}^*}{(\tilde{n}_w^*-\tilde{n}_1^*)},$$
$$\xi=\frac{R_c\rho_f R_0^2}{\mu_f}, \quad U_{hs}=-\frac{\zeta\varepsilon E_0}{\mu_f U_0}, \qquad R(z)=\hat{R}_1^*-\hat{R}_2^* \quad . \tag{4.25}$$

The aforementioned non-dimensional parameters mentioned in equation (4.25) are inserted into the governing equations (4.8)-(4.13). The mild stenotic hypotheses are applied, i.e., $\delta(=\delta^*/R_0)<<1$, and $\varepsilon(=R_0/L_0)=O(1)$. As a consequence of the aforementioned process, the governing equations (4.8)-(4.13) undergo modifications, which can be expressed as follows:

Momentum Equation:

r_1-direction:

$$\frac{\partial p}{\partial r} = 0, \tag{4.26}$$

z_1-direction:

$$Re\frac{\rho_{hnf}}{\rho_f}\frac{\partial w}{\partial t} = -\frac{\partial p}{\partial z} + \frac{1}{2r}\frac{\partial}{\partial r}\left[\frac{\mu_{hnf}}{\mu_f} r\frac{\partial w}{\partial r}\right] + \frac{(\rho\beta)_{hnf}}{(\rho\beta)_f}\left[GrT + GcC - Rb\tilde{\chi}_1\right]\cos\eta_1\delta_{ij} + U_{hs}q_e^2\Phi - \frac{\sigma_{hnf}}{\sigma_f}M^2 w. \tag{4.27}$$

Energy Equation:

$$\frac{(\rho C_p)_{hnf}}{(\rho C_p)_f}\frac{\partial T}{\partial t} = \frac{1}{RePr}\frac{k_{hnf}}{k_f}\left[\frac{\partial^2 T}{\partial r^2} + \frac{1}{r}\frac{\partial T}{\partial r}\right] + \frac{\sigma_{hnf}}{\sigma_f}\left[\frac{EcM^2}{Re}w^2 + \frac{(S_z + \tilde{Q})}{RePr}\right] + \frac{\mu_{hnf}}{\mu_f}\frac{Ec}{Re}\left[\left(\frac{\partial w}{\partial r}\right)^2\right]. \tag{4.28}$$

Concentration Equation:

$$ReSc\frac{\partial C}{\partial t} = \frac{\partial^2 C}{\partial r^2} + \frac{1}{r}\frac{\partial C}{\partial r} - Sc\xi C, \tag{4.29}$$

Microorganism Equation:

$$ReSb\frac{\partial \tilde{\chi}_1}{\partial t} = \frac{\partial^2 \tilde{\chi}_1}{\partial r^2} + \frac{1}{r}\frac{\partial \tilde{\chi}_1}{\partial r} - Pe\sigma_1\left(\frac{\partial \tilde{\chi}_1}{\partial r}\frac{\partial C}{\partial r} + (\sigma_1 + \tilde{\chi}_1)\frac{\partial^2 C}{\partial r^2}\right), \tag{4.30}$$

Electroosmotic Equation:

$$\frac{\partial^2 \Phi}{\partial r^2} + \frac{1}{r}\frac{\partial \Phi}{\partial r} = {q_e}^2\Phi. \tag{4.31}$$

Here, Reynold's viscosity model [129] has been utilised to illustrate the temperature-dependent viscosity. The model is expressed as follows:

$$\mu_{bf}(T) = \mu_f e^{-\beta_0 T} = \mu_f[1 - \beta_0 T] \text{ where } \beta_0 << 1 \tag{4.32}$$

Upon substituting dimensionless variables in equation (4.25), the resulting modified equation for the pressure gradient can be written as:

$$-\frac{\partial p}{\partial z} = B_1[1 + e\cos(c_1 t)], \tag{4.33}$$

where

$$e = \frac{A_1}{A_0}, \quad B_1 = \frac{A_0 R_0^2}{\mu_f U_0}, \quad c_1 = \frac{2\pi R_0 f_p}{U_0}.$$

Upon applying non-dimensional values to the body acceleration Eqn (4.19), the terms $B_2 = \frac{A_0 R_0^2}{\mu_f U_0}$ and $c_2 = \frac{w_q R_0}{U_0}$ has taken the following form. The resulting form of the equation, by removing the bars, is as follows.

$$G(t) = B_2 \cos(c_2 t + \psi), \qquad t > 0, \tag{4.34}$$

The dimensionless form of the arterial outer wall is expressed as follows:

$$\hat{R}_1^*(z) = \begin{cases} 1, & 0 < z \leq d \\ 1 - \frac{6\delta^*}{5}(11(z-d) - 47(z-d)^2 + 72(z-d)^3 - 36(z-d)^4), & d < z \leq d+1 \\ 1, & d+1 < z \leq z_1, \\ 1 + r_1 - \sqrt{\left(r_1^2 - (z-z_1)^2\right)}, & z_1 < z \leq z_2, \\ 2r_0 \sec\eta_1 + \left(z - z_2\right)\tan\eta_1, & z_2 < z \leq z_4 + 0.5, \\ 2r_0 \sec\eta_1 + \left(z - z_2\right)\tan\eta_1 - A^*, & z_4 + 0.5 < z \leq z_4 + 2.5, \\ 2r_0 \sec\eta_1 + \left(z - z_2\right)\tan\eta_1, & z_4 + 2.5 \leq z \leq z_{max}. \end{cases} \tag{4.35}$$

Where $A^* = 2\delta_1^* \left\{ \cos\left(2\pi\left(\frac{z-d}{4}\right) - 0.25\right) - 0.07\cos\left(128\pi\left(z - d - 0.5\right)\right)\right\}\tan(\eta_1)$.
The inner wall is represent as:

$$\hat{R}_2^*(z) = \begin{cases} 0, & 0 < z \leq z_3, \\ \sqrt{\tilde{r}_1^{*2} - \left((z-z_3)) - \tilde{r}_1^*\right)^2}, & z_3 < z \leq z_4, \\ (z-z_2)\tan\eta_1, & z_4 < z \leq z_{max}. \end{cases} \tag{4.36}$$

The lateral junction curvature r_1 and the flow divider radius $\tilde{r}_1$ in the dimensionless form (after ignoring bars) are given as:

$$r_1 = \frac{1 - 2r_0 \sec\eta_1}{\cos\eta_1 - 1}, \tag{4.37}$$

$$\tilde{r}_1^* = \frac{(z_3 - z_2)\sin\eta_1}{(1 - \sin\eta_1)}, \tag{4.38}$$

where z_2, z_3 and z_4 in the dimensionless form are specified as:

$$z_2 = z_1 + r_1 \sin\eta_1, \tag{4.39}$$

$$z_3 = z_2 + q_1, \tag{4.40}$$

and

$$z_4 = z_3 + \tilde{r}_1^*(1-\sin\eta_1). \tag{4.41}$$

4.2.3 Radial Coordinate Transformation

In order to obtain a rectangular domain, it is necessary to apply the transformation $\left(x_1 = \frac{r-\hat{R}_2^*(z)}{R(z)}\right)$ to the geometry under consideration. Upon implementation of the aforementioned transformation, the equations denoted by (4.27) through (4.31) undergo a modification as follows:

$$Re\frac{\rho_{hnf}}{\rho_f}\frac{\partial w}{\partial t} = B_1[1+e\cos(c_1 t)] + \frac{1}{2}\left(\frac{1-\beta_0 T}{(1-\phi_1)^{2.5}(1-\phi_2)^{2.5}}\right)\left[\frac{1}{R^2}\frac{\partial^2 w}{\partial x_1^2} + \left(\frac{1}{x_1 R+R_2}\right)\left(\frac{1}{R}\frac{\partial w}{\partial x_1}\right)\right] - \frac{\beta_0}{2R^2((1-\phi_1)^{2.5}(1-\phi_2)^{2.5})}\frac{\partial w}{\partial x_1}\frac{\partial T}{\partial x_1} + \frac{(\rho\beta)_{hnf}}{(\rho\beta)_f}\left[GrT+GcC-Rb\tilde{\chi}_1\right]\cos(\eta_1\delta_{ij}) + U_{hs}q_e^2\Phi - \frac{\sigma_{hnf}}{\sigma_f}M^2 w + G(t), \tag{4.42}$$

$$\frac{(\rho C_p)_{hnf}}{(\rho C_p)_f}\frac{\partial T}{\partial t} = \frac{1}{RePr}\frac{k_{hnf}}{k_f}\left[\frac{1}{R^2}\frac{\partial^2 T}{\partial x_1^2} + \left(\frac{1}{x_1 R+R_2}\right)\left(\frac{1}{R}\frac{\partial T}{\partial x_1}\right)\right] + \frac{\sigma_{hnf}}{\sigma_f}\left[\frac{EcM^2}{Re}w^2 + \frac{S_z+\tilde{Q}}{RePr}\right] + \frac{1}{R^2}\left(\frac{1-\beta_0 T}{(1-\phi_1)^{2.5}(1-\phi_2)^{2.5}}\right)\frac{Ec}{Re}\left[\left(\frac{\partial w}{\partial x_1}\right)^2\right], \tag{4.43}$$

$$ReSc\frac{\partial C}{\partial t} = \frac{1}{R^2}\frac{\partial^2 C}{\partial x_1^2} + \left(\frac{1}{x_1 R+R_2}\right)\frac{1}{R}\frac{\partial C}{\partial x_1} - Sc\xi C, \tag{4.44}$$

$$ReSb\frac{\partial \tilde{\chi}_1}{\partial t} = \frac{1}{R^2}\frac{\partial^2 \tilde{\chi}_1}{\partial x_1^2} + \left(\frac{1}{x_1 R+R_2}\right)\frac{1}{R}\frac{\partial \tilde{\chi}_1}{\partial x_1} - \frac{Pe\sigma_1}{R^2}\left(\frac{\partial \tilde{\chi}_1}{\partial x_1}\frac{\partial C}{\partial x_1} + (\sigma_1+\tilde{\chi}_1)\frac{\partial^2 C}{\partial x_1^2}\right), \tag{4.45}$$

$$\frac{1}{R^2}\frac{\partial^2 \Phi}{\partial x_1^2} + \left(\frac{1}{x_1 R+R_2}\right)\frac{1}{R}\frac{\partial \Phi}{\partial x_1} = {q_e}^2\Phi. \tag{4.46}$$

The boundary conditions specified in equations (4.14) and (4.17) have been reduced in the following manner:

$$w = 0,\ \ T = 1,\ \ C = 1,\ \ \tilde{\chi}_1 = 1,\ \ \text{at}\ \ x_1 = 1 \qquad \text{for all} \quad z, \tag{4.47}$$

$$\frac{\partial w}{\partial x_1} = 0,\ \ \frac{\partial T}{\partial x_1} = 0,\ \ \frac{\partial C}{\partial x_1} = 0,\ \ \frac{\partial \tilde{\chi}_1}{\partial x_1} = 0\ \ \text{at}\ \ x_1 = 0 \qquad \text{for} \quad 0 \le z \le z_3, \tag{4.48}$$

$$w = 0,\ \ T = 1,\ \ C = 1,\ \ \tilde{\chi}_1 = 1,\ \ \text{at}\ \ x_1 = 0 \qquad \text{for} \quad z_3 \le z \le z_{max}. \tag{4.49}$$

The wall shear stress at the outer wall of the bifurcated artery is given as below:

$$\tau_w = -\frac{1}{R}\left(\frac{\partial w}{\partial x_1}\right)_{x_1=1}, \tag{4.50}$$

The flow rate for the parent artery and daughter artery is defined as follows:

$$Q_d^f = 2\pi R \int_0^1 w(x_1 R + R_2) dx_1. \tag{4.51}$$

$$Q_p^f = \pi R \int_0^1 w(x_1 R + R_2) dx_1. \tag{4.52}$$

The resistance impedance for the the parent artery and daughter artery is given by:

$$\lambda_p = \left| \frac{z_3\left(-\frac{\partial p}{\partial z}\right)}{Q_p^f} \right|, \qquad \text{for} \quad z < z_3, \tag{4.53}$$

$$\lambda_d = \left| \frac{(z_{max} - z_3)\left(-\frac{\partial p}{\partial z}\right)}{Q_d^f} \right|, \qquad \text{for} \quad z \ge z_3. \tag{4.54}$$

The Nusselt number at the outer wall of the bifurcated artery is computed as follows:

$$Nu_x = -\frac{1}{R}\left(\frac{\partial T}{\partial x_1}\right)_{x_1=1}. \tag{4.55}$$

Similarly, the Sherwood number is given as:

$$Sh_x = -\frac{1}{R}\left(\frac{\partial C}{\partial x_1}\right)_{x_1=1}. \tag{4.56}$$

4.3 Solution Process

It is well established fact that there are several numerical technique to compute the partial differential equations but the finite difference scheme is the easiest and efficient technique for finding the solution these equations. In order to solve the PDEs, we adopted the Crank Nicolson scheme and taken step size of Δx in the radial direction with time step of $\Delta t = 0.001$ to acheive the convergence of the numerical scheme. It is also observed that further change in Δx and Δt doesn't bring any substantial changes in the results.

4.3.1 Discretization

The governing equations are discretized as:

$$\left[(1-\phi_2)\left[(1-\phi_1)+\phi_1\frac{\rho_{s1}}{\rho_f}\right]+\phi_2\frac{\rho_{s2}}{\rho_f}\right]Re\left[\frac{w_i^{k+1}-w_i^k}{dt}\right] = B_1[1+ecos(c_1t^k)]$$
$$\frac{1}{2}\left\{\frac{1-\beta_0 T}{(1-\phi_1)^{2.5}(1-\phi_2)^{2.5}}\right\}\left[\frac{1}{R^2}\left(\frac{w_{i+1}^{k+1}-2w_i^{k+1}+w_{i-1}^{k+1}}{dx^2}+\frac{w_{i+1}^{k}-2w_i^{k}+w_{i-1}^{k}}{dx^2}\right)+\frac{1}{R}\frac{1}{Rx_i+R_2}\right.$$
$$\left.\left(\frac{w_{i+1}^{k+1}-w_{i-1}^{k+1}}{2dx}+\frac{w_{i+1}^{k}-w_{i-1}^{k}}{2dx}\right)\right]-\frac{1}{2R^2}\left\{\frac{\beta_0}{(1-\phi_1)^{2.5}(1-\phi_2)^{2.5}}\right\}\left[\left(\frac{w_{i+1}^{k+1}-w_{i-1}^{k+1}}{2dx}\right.\right.$$
$$\left.\left.+\frac{w_{i+1}^{k}-w_{i-1}^{k}}{2dx}\right)\left(\frac{T_{i+1}^{k}-T_{i-1}^{k}}{2dx}\right)\right]+U_{hs}q_e^2\Phi+F_bcos(c_2t_k+\psi)+\left[(1-\phi_2)\left\{(1-\phi_1)+\phi_1\frac{(\rho\beta)_{s1}}{(\rho\beta)_f}\right\}\right.$$
$$\left.+\phi_2\frac{(\rho\beta)_{s_2}}{(\rho\beta)_f}\right]\left(GrT_i^k+GcC_i^k-Rb\tilde{\chi}_{1i}^{\ k}\right)\cos(\eta_1\delta_{ij})-\frac{1}{2}\frac{\sigma_{nf}}{\sigma_f}M^2(w_i^k+w_i^{k+1}), \tag{4.57}$$

$$\left[(1-\phi_2)\left\{(1-\phi_1)+\phi_1\frac{(\rho C_p)_{s_1}}{(\rho C_p)_f}\right\}+\phi_2\frac{(\rho C_p)_{s_2}}{(\rho C_p)_f}\right]\left[\frac{T_i^{k+1}-T_i^k}{dt}\right] = \frac{1}{RePr}\frac{k_{hnf}}{k_f}\left[\frac{1}{2R^2}\right.$$
$$\left.\left(\frac{T_{i+1}^{k+1}-2T_i^{k+1}+T_{i-1}^{k+1}}{dx^2}+\frac{T_{i+1}^{k}-2T_i^{k}+T_{i-1}^{k}}{dx^2}\right)+\frac{1}{2(Rx_i+R_2)}\left(\frac{T_{i+1}^{k+1}-T_{i-1}^{k+1}}{2dx}+\frac{T_{i+1}^{k}-T_{i-1}^{k}}{2dx}\right)\right]$$
$$+\frac{1}{R^2}\left\{\frac{1-\frac{\beta_0}{2}(T_i^{k+1}+T_i^k)}{(1-\phi_1)^{2.5}(1-\phi_2)^{2.5}}\right\}\frac{Ec}{Re}\left[\frac{1}{2}\left(\frac{w_{i+1}^{k+1}-w_{i-1}^{k+1}}{2dx}+\frac{w_{i+1}^{k}-w_{i-1}^{k}}{2dx}\right)\right]^2$$
$$+\frac{\sigma_{hnf}}{\sigma_f}\left[\left(\frac{1}{2}\frac{EcM^2}{Re}\left(w_i^{k+1}+w_i^k\right)\right)^2+\frac{S_z+\tilde{Q}}{RePr}\right],. \tag{4.58}$$

$$ReSc\left[\frac{C_i^{k+1}-C_i^k}{dt}\right]=\left[\frac{1}{2R^2}\left(\frac{C_{i+1}^{k+1}-2C_i^{k+1}+C_{i-1}^{k+1}}{dx^2}+\frac{C_{i+1}^{k}-2C_i^{k}+C_{i-1}^{k}}{dx^2}\right)+\frac{1}{2(Rx_i+R_2)}\left(\frac{C_{i+1}^{k+1}-C_{i-1}^{k+1}}{2dx}+\frac{C_{i+1}^{k}-C_{i-1}^{k}}{2dx}\right)\right]-\frac{Sc\xi}{2}\left[C_i^{k+1}+C_i^k\right], \quad (4.59)$$

$$ReSb\left[\frac{\tilde{\chi}_{1i}^{k+1}-\tilde{\chi}_{1i}^{k}}{dt}\right]=\left[\frac{1}{2R^2}\left(\frac{\tilde{\chi}_{1i+1}^{k+1}-2\tilde{\chi}_{1i}^{k+1}+\tilde{\chi}_{1i-1}^{k+1}}{dx^2}+\frac{\tilde{\chi}_{1i+1}^{k}-2\tilde{\chi}_{1i}^{k}+\tilde{\chi}_{1i-1}^{k}}{dx^2}\right)+\frac{1}{2(Rx_i+R_2)}\left(\frac{\tilde{\chi}_{1i+1}^{k+1}-\tilde{\chi}_{1i-1}^{k+1}}{2dx}+\frac{C_{i+1}^{k}-C_{i-1}^{k}}{2dx}\right)\right]-\frac{Pe\sigma_1}{2}\left[\left\{\frac{\tilde{\chi}_{1i+1}^{k+1}+\tilde{\chi}_{1i-1}^{k+1}}{2dx}+\frac{\tilde{\chi}_{1i+1}^{k}+\tilde{\chi}_{1i-1}^{k}}{2dx}\right\}\left(\frac{C_{i+1}^{k}-C_{i-1}^{k}}{2dx}\right)+\left\{\sigma_1+\frac{\tilde{\chi}_{1i}^{k+1}+\tilde{\chi}_{1i}^{k}}{2}\right\}\left(\frac{C_{i+1}^{k}-2C_i^{k}-C_{i-1}^{k}}{dx^2}\right)\right], \quad (4.60)$$

$$\frac{\Phi_{i+1}-2\Phi_i+\Phi_{i-1}}{dx^2}+\frac{1}{(Rx_i+R_2)}\left\{\frac{\Phi_{i+1}-\Phi_{i-1}}{2dx}\right\}=q_e^2\Phi_i. \quad (4.61)$$

The discretized governing equations (4.57) and (4.61) are then converted to a tri-diagonal system of equations which is subsequently solved through the utilization of the Tri-Diagonal Matrix Algorithm (TDMA).

4.4 Results and Graphical Analysis

A MATLAB-based computer code was developed to gain insight into the mathematical and physical aspects of the current problem being considered. The code was designed to generate graphical representations of velocity, temperature, concentration, microorganisms, flow rate, impedance, Nusselt, and Sherwood profiles. This study examines the hemodynamic characteristics and blood rheology in the presence of pathological conditions such as stenosis on the arterial walls of bifurcated arteries. The thermophysical characteristics of nanoparticles and the parameters of nanofluids are shown in Tables 4.1 and 4.2, respectively. Table 4.3 shows the possible values explored for the different flow parameters.

4.4.1 Validation

The validation of our work is consummated with the published work of Tripathi et al. [100]. The present study employs a finite difference methodology, specifically the Crank-Nicolson

Properties	Mathematical Expression for Nanofluid and Hybrid Nanofluid
Viscosity	$\mu_{nf} = \frac{\mu_f}{(1-\phi_1)^{2.5}}$ $\mu_{hnf} = \frac{\mu_f}{(1-\phi_1)^{2.5}(1-\phi_2)^{2.5}}$
Density	$\rho_{nf} = (1-\phi_1)\rho_f + \phi_1\rho_{s_1}$ $\rho_{hnf} = [(1-\phi_2)\{(1-\phi_1)\rho_f + \phi_1\rho_{s_1}\}] + \phi_2\rho_{s_2}$
Heat Capacity	$(\rho C_p)_{nf} = (1-\phi_1)(\rho C_p)_f + \phi_1(\rho C_p)_{s_1}$ $(\rho C_p)_{hnf} = [(1-\phi_2)\{(1-\phi_1)(\rho C_p)_f + \phi_1(\rho C_p)_{s_1}\} + \phi_2(\rho C_p)_{s_2}]$
Thermal Conductivity	$\frac{k_{nf}}{k_f} = \frac{k_{s_1} + (m-1)k_f - (m-1)\phi_1(k_f - k_{s_1})}{k_{s_1} + (m-1)k_f + \phi_1(k_f - k_{s_1})}$ $\frac{k_{hnf}}{k_{nf}} = \frac{k_{s_2} + (m-1)k_{nf} - (m-1)\phi_2(k_{nf} - k_{s_2})}{k_{s_2} + (m-1)k_{nf} + \phi_2(k_{nf} - k_{s_2})}$
Electrical Conductivity	$\frac{\sigma_{nf}}{\sigma_f} = \frac{\sigma_{s_1} + (m-1)\sigma_f - (m-1)\phi_1(\sigma_f - \sigma_{s_1})}{\sigma_{s_1} + (m-1)\sigma_f + \phi_1(\sigma_f - \sigma_{s_1})}$ $\frac{\sigma_{hnf}}{\sigma_{nf}} = \frac{\sigma_{s_2} + (m-1)\sigma_{nf} - (m-1)\phi_2(\sigma_{nf} - \sigma_{s_2})}{\sigma_{s_2} + (m-1)\sigma_{nf} + \phi_2(\sigma_{nf} - \sigma_{s_2})}$
Thermal Expansion Coefficient	$\frac{(\rho\beta)_{nf}}{(\rho\beta)_f} = [(1-\phi_1) + \phi_1\frac{(\rho\beta)_{s1}}{(\rho\beta)_f}]$ $\frac{(\rho\beta)_{hnf}}{(\rho\beta)_{nf}} = (1-\phi_2)[(1-\phi_1) + \phi_1\frac{(\rho\beta)_{s1}}{(\rho\beta)_f}] + \phi_2\frac{(\rho\beta)_{s2}}{(\rho\beta)_f}$

Table 4.1: Thermophysical parameters of nanofluid and hybrid nanofluid

Thermophysical Properties	**Blood**	**Al_2O_3**	**Cu**
Density $[\rho(kg/m^3)]$	1060	3970	8933
Thermal Expansion Coefficient $[\beta \times 10^{-5}(K^{-1})]$	0.18	0.85	5
Electrical Conductivity $[\sigma(S/m)]$	0.667	3.5×10^7	10×10^{-10}
Thermal Conductivity [K(W/mK)]	0.492	40	314
Heat Capacitance $[C_p(J/kgK)]$	3770	3970	8933

Table 4.2: Thermophysical properties of nanoparticles

Parameters	**Values**	**Refrences**
Magnetic field (M^2)	0-5	[106, 112]
Grashof number (Gr)	0-5	[6, 108]
Rayleigh number (Rb)	0-6	[1, 125]
Prandtl number (Pr)	14-25	[130]
Heat source parameter $(\tilde{Q})$	0-1	[13, 14]

Table 4.3: Default values of emerging parameters with their sources

method, to compute the governing equations. In contrast, the previously published work of [100] utilised the FTCS scheme.

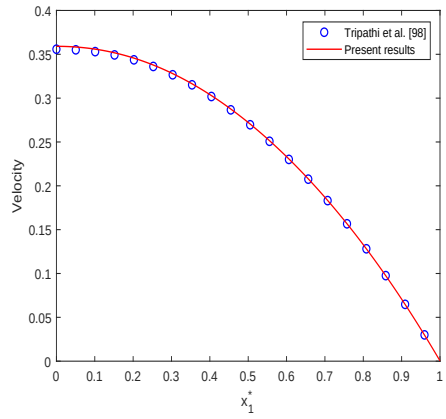

Figure 4.2: Velocity profile for pure blood

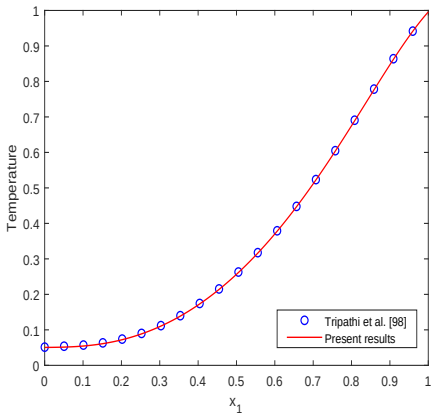

Figure 4.3: Temperature profile for pure blood

The present study compares two research works by analysing the impact of different parameters, namely Solutal Grashof number $(Gc = 0)$, Rayleigh number $(Rb = 0)$, magnetic field parameter $(M = 0)$, Debye-Huckel parameter $(q_e = 0)$, heat source $(\tilde{Q} = 0)$, Eckert number $(Ec = 0)$, and Joule heating parameter $(S_z = 0)$. Additionally, the inner wall $(R_2(z) = 0)$ has been considered. The velocity and temperature profile for pure blood (without the presence of nanoparticles) are illustrated in Figures 4.2 and 4.3, respectively. The graphical representations illustrate a high degree of concurrence between our study and prior research [100] concerning velocity and temperature profiles.

4.4.2 Velocity Profile

The composition of blood is multifaceted, encompassing haemoglobin, plasma, white blood cells, and diverse ionic constituents. The human circulatory system consists of millions of red blood cells and other ionic components, which render it capability to exhibit the biomagnetic properties. The primary objective of red blood cells (RBCs) is to transport oxygen to different tissues and organs within the human body. A comparative study was conducted to explored the impact of magnetic field parameters on the stenosed artery, motivated by its blood magnetic property. Figure 4.4a depicts the velocity profile variation for different magnetic field parameter values in both parent and daughter arteries. The maximum velocity of the fluid is achieved in the absence of the magnetic field that is $(M = 0)$, which reduces as the strength of the magnetic field enhances from $M = 0$ to $M = \sqrt{5}$. This has occurred due to the application of a transversal magnetic field in the direction of the flow, which produces the resistance Lorentz force and slows the fluid motion. The profile of the velocity for a variable electro-kinetic parameter, or Debye Huckel parameter q_e, is shown in Figure 4.4b. The enhancement in the velocity profile can be explained by the electro-kinetic acceleration term present in the momentum equation, i.e. $U_{hs}q_e^2\Phi$. The parameter known as the Debey Huckel parameter is expressed as the quotient of the radius of the tube denoted by R_0 and the Debye length represented by q_e. It has been observed that the Debey Huckel parameter exhibits an inverse relationship with the thickness of the electric double layer (EDL). Hence, raising the value of the Debey Huckel parameter reduces the EDL width, increasing the electro-osmotic forces that counteract fluid drag and boost fluid velocity. Bioconvection phenomena can be attributed to the upward swimming of motile microorganisms in a hybrid nanofluid solution. Typically, the density of microorganisms exhibits a slightly higher value than that of the hybrid nanofluid solution, resulting in the migration of microorganisms towards the upper surface of the solution. The observed phenomenon involves the generation of an uneven and unstable solution, resulting in the downward displacement of microorganisms and the subsequent initiation of a bioconvection process. The association between the bioconvection Rayleigh number and the momentum equation substantially impacted the velocity profile, as seen in Figure 4.4c. The increase in the Rayleigh number strengthens the microorganism's convection, which works against the buoyancy force acting on the fluid particles. This results in a decrement in the velocity profile. The variation in velocity profile by varying nanoparticle concentration is depicted in figure 4.4d. Nanoparticles play a critical role in the targeted delivery of therapeutic agents to affected tissues via the circulatory system, thereby enabling the treatment of a diverse array of medical ailments. Upon injection into the bloodstream, the copper oxide nanoparticles induce an increase in flow velocity, resulting in a heightened velocity profile relative to that of unadulterated blood.

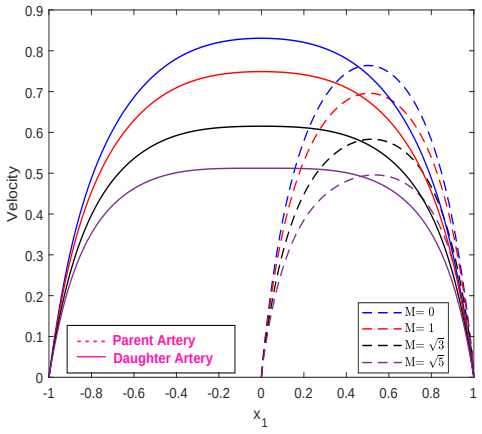

(a) Velocity profile by varying M

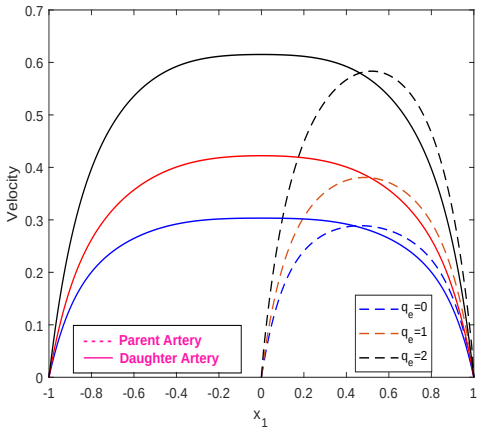

(b) Velocity profile by varying q_e

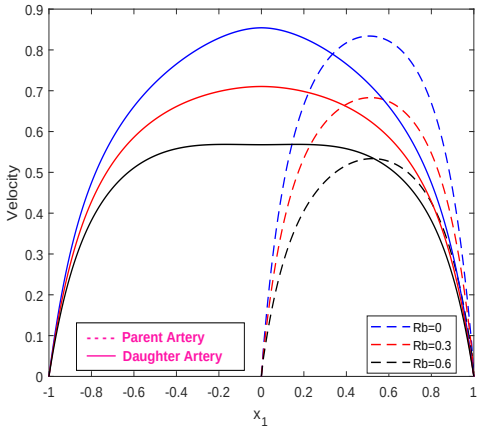

(c) Velocity profile by varying Rb

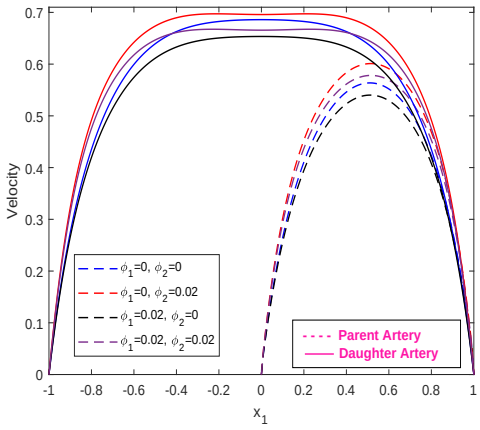

(d) Velocity profile by varying nanoparticle concentration

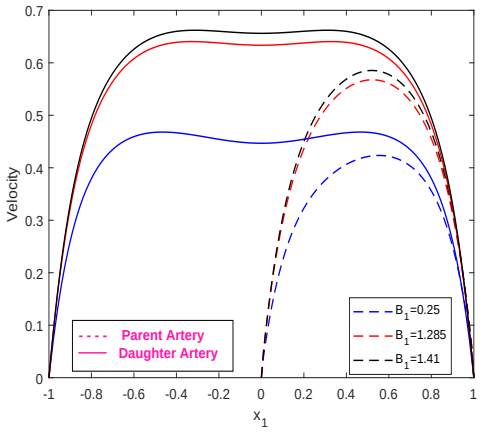

(e) Velocity profile by varying B_1

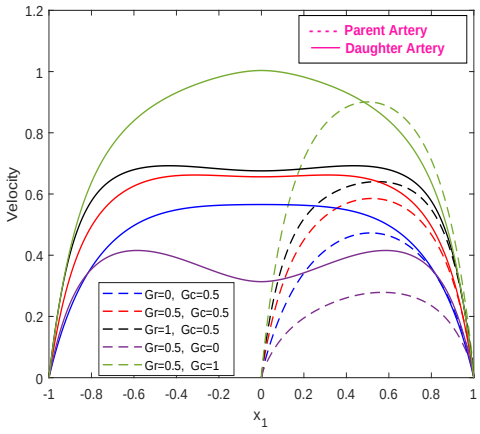

(f) Velocity profile by varying Gr and Gc

Figure 4.4: Velocity profile

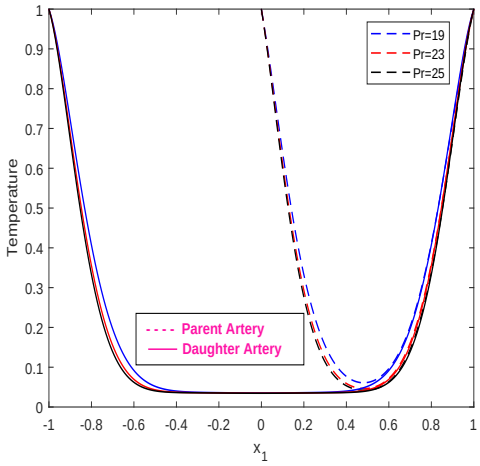

(a) Temperature profile by varying Pr

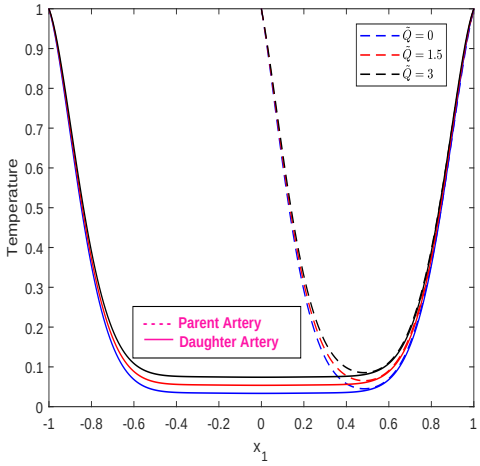

(b) Temperature profile by varying $\tilde{Q}$

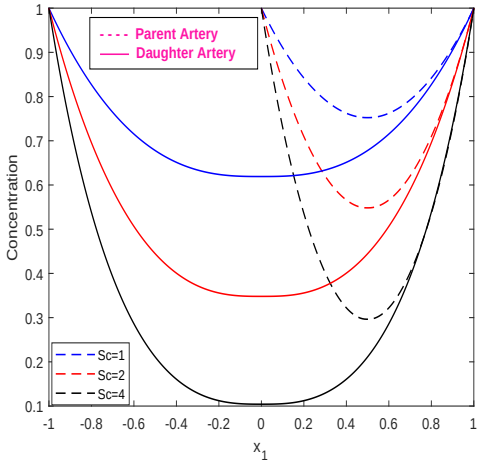

(c) Concentration profile by varying Sc

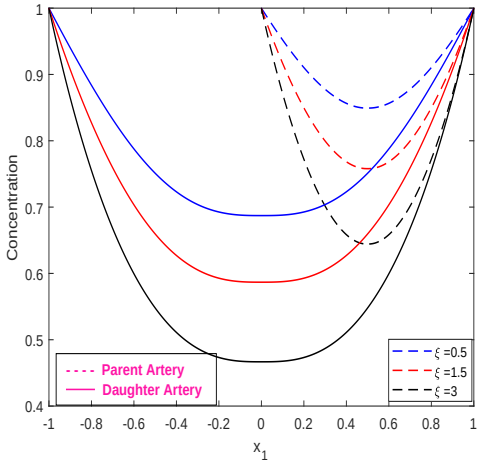

(d) Concentration profile by varying ξ

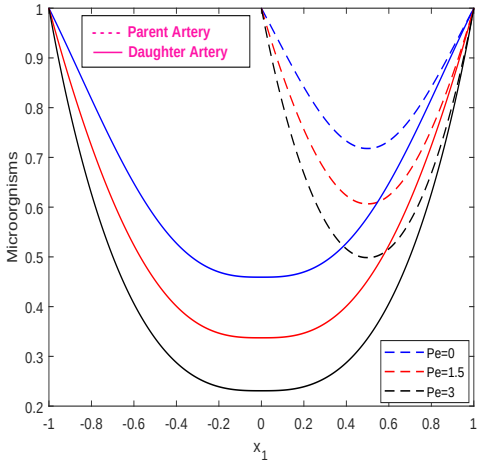

(e) Microorganisms profile by varying Pe

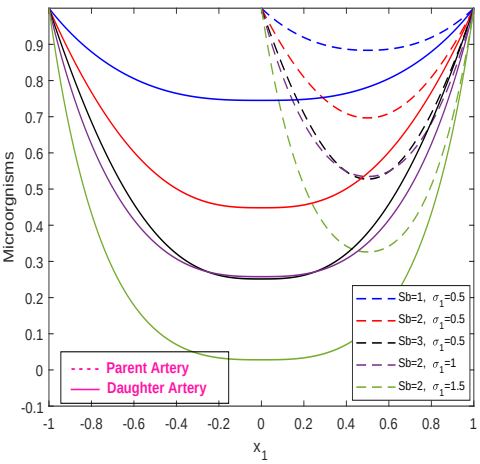

(f) Microorganisms profile by varying Sb

Figure 4.5: Temperature, Concentration and Microorganisms profile

It may be deduced from the figure that the velocity profile attains its highest magnitude upon the introduction of copper nanoparticles into the circulatory system, while the lowest velocity profile is observed for aluminium oxide nanoparticles. Figure 4.4e illustrates the velocity profile of parent and daughter arteries by considering the different artery diameters. In particular, the value of $B_1 = 1.41$ corresponds to the coronary artery, whereas the value of $B_1 = 6.6$ is indicative of the femoral artery. At the stenotic position, the velocity profile displays an augmentation in its profile for increasing artery diameter. The combined effect of the Grashof number and the solutal Grashof number is depicted in Figure 4.4f. Grashof number represent the ratio of buoyant force to viscous force. Clearly, it can be deduced that the fluid velocity enhances with an increment of Gr from 0 to 1. This has happened due to enhancement in the buoyant forces as compare to viscous forces which accelerates the fluid velocity. Similar trend is observed for solutal Grashof number Gc.

4.4.3 Temperature, Concentration and Microorganisms Profile

The variation in temperature for varying Prandtl number is depicted in figure 4.5a. In both parent and daughter artery, as the value of Pr enhances from 19 to 23, the temperature distribution decreases. Prandtl number represents the ratio of momentum and thermal diffusivity. The prandtl value for pure blood is 21, which is higher as compared to water and other base fluids. The smaller Prandtl number has higher thermal condutivity which signifies the heat transmitted faster from arterial wall as compared for higher-Pr fluids. Figure 4.5b signifies the argumentation in the temperature profile for an increasing heat source parameter. The enhancement is occur due to addition heat produces by the heat source that raises the temperature profile. The result of figure 4.5b may be serve as a promising application in the drug delivery system where the metallic nanoparticles can be used as carriers to treat cancerous cell. The tumor cell present in the downstream of the stenotic region can be treated by enhancing the temperature. Figure 4.5c and 4.5d depict the concentration profile for Schmidt and chemical reaction parameter, respectively. The concentration profile illustrates how a growing Schmidt number leads to a decreasing concentration. Sc denotes the ratio of the kinematic viscosity to the molecular diffusion coefficient. Since diffusivity is inversely proportional to Sc, this indicates that a lower Sc number leads to higher diffusivity. The more highly diffusive species have a more noticeable impact of slowing down the concentration distribution. As the parameter for the chemical reaction is increased, the concentration profile begins to fall. This has happened due to the consumption of additional species will lead to the suppressed concentration profile. The impact of bioconvective Pe on the microorganism's distribution is seen in Figure 4.5e. The Peclet number is the most prominent component that highly influences the density of microorganisms in the blood. Pe

was defined as the ratio of the maximal swimming speed of a cell to the diffusion rate of microorganisms. The process by which a substance moves from an area of higher concentration to a lower concentration is commonly known as diffusion. From the figure, there is a direct correlation between the rise in the Pe value from 0 to 3, which results in a reduction in the microbes' overall dispersion. It has been discovered that an increase in the bioconvective Peclet number results in an increase in the speed of motile microorganisms, which decreases the density of microorganisms. The combined impact of the bioconvective Lewis number and the microbial concentration differences parameter on the dispersion of microorganisms is shown in Figure 4.5f. The figure shows that the density decreases for an upsurge in magnitude of parameter σ_1. This results from a more significant density differential being formed between the gyrotactic microorganisms and the base fluid, which causes the gyrotactic bacteria to flow back and suppresses the concentration profile. The mounting value of Sb reduces the motile density of the fluid, and this has happened due to a decrease in the microorganism's diffusivity process. This shows that the microorganism's density reduces in both section of the bifurcated artery (parent and daughter arteries) as the magnitude of Sb and σ_1 enhances.

4.4.4 Flow Rate & Impedance Profile

In stenotic condition, the hemodynamic factors play a crucial role in assessing the risk of atherosclerosis progression induced by flow disorders. Thus, it is essential to study these factors to reduced its risk and addressed it at a correct time for better treatment. The volumetric flow rate is defined as the amount of fluid that passes through the arteries in a given amount of time whereas fluid resistance also known as Impedance is determined by the ratio of pressure drop to flow rate. Figure 4.6a shows the flow rate profile for varying magnetic field parameter. The flow rate profile depicts the declining nature as the magnetic field parameter enhances from $M = 0$ to $M = \sqrt{5}$. The flow rate is maximum in the absence of magnetic field ($M = 0$) which clearly shows that the flow rate can be regulated by the magnetic field. The fluid experiences the resistive Lorentz force that retard the fluid motion and from the figure, it can also be interpret that the fluid experiences the disturbance at the bifurcated point. Figure 4.6b illustrates the change in flow rate that occurs when the bifurcation angle is changed from $\pi/12$ to $\pi/6$. According to the inferences drawn from the figure, the flow rate profile remains unchanged in the parent artery but undergoes substantial changes following the bifurcation. The daughter artery's flow rate profile increases with enhancement in the bifurcation angle. The flow rate as a function of the Grashof number is seen in Figure 4.6c.

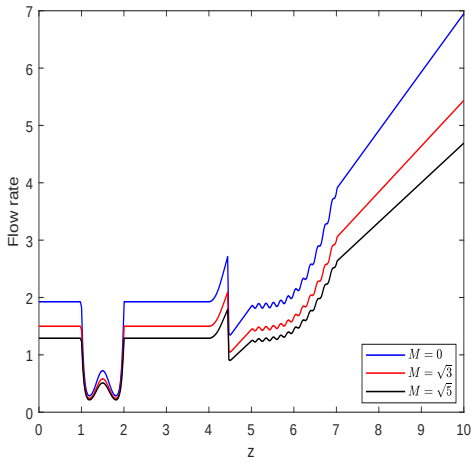

(a) Flow rate profile for varying M

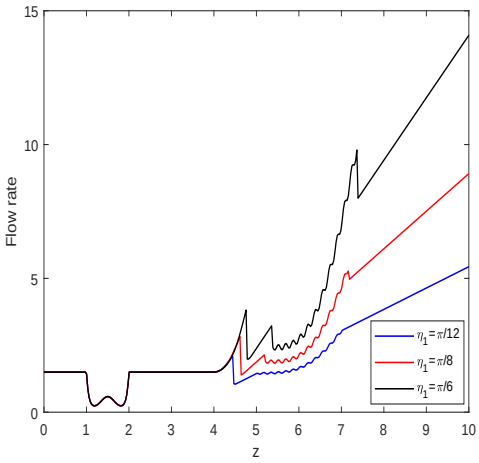

(b) Flow rate profile for varying η_1

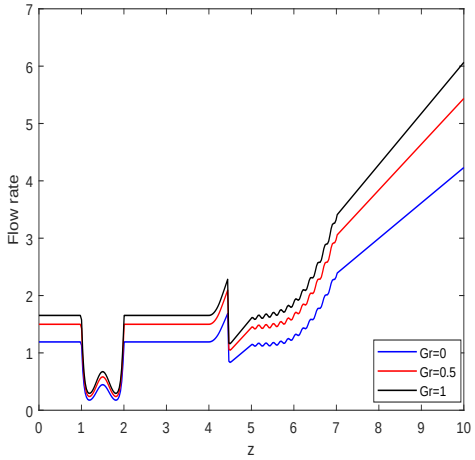

(c) Flow rate profile for varying Gr

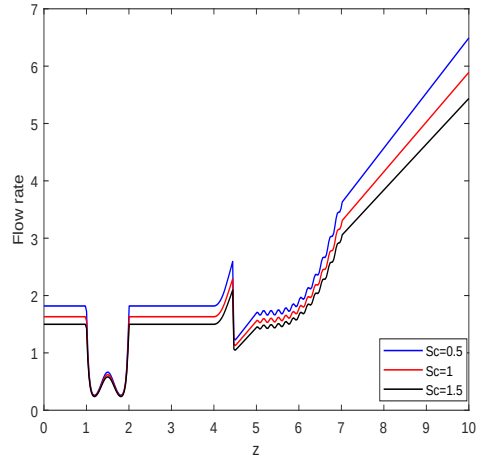

(d) Flow rate profile for varying Sc

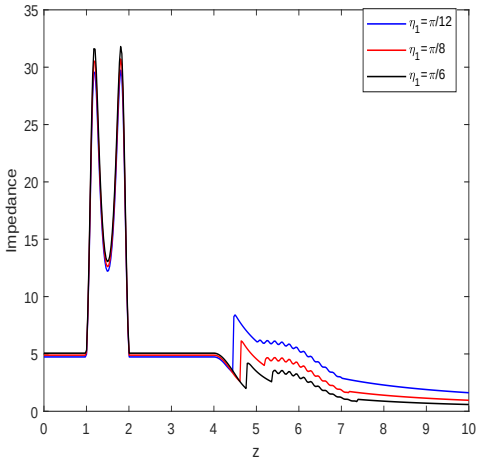

(e) Impedance profile by varying η_1

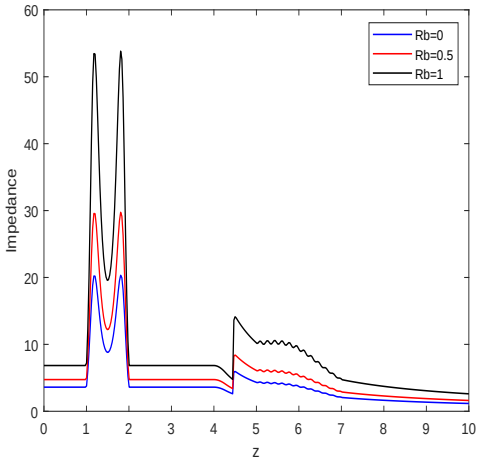

(f) Impedance profile by varying Rb

Figure 4.6: Flow rate and Impedance profile

This is the result of an increase in the temperature differential between the two regions, which has caused the buoyant force to predominate compared to the viscous forces. As a consequence, there has been an increase in the flow rate profile. The decrease in flow rate that occurs when the value of the Schmidt number grows from 0.5 to 1.5 is seen in Figure 4.6d. The reduction in molecular diffusion is shown physically by an increase in the value of Sc, whereas a reversal of behaviour was seen concerning the velocity profile, which led to a drop in the flow rate profile. Figure 4.6e illustrates the decrement in the velocity profile as the bifurcated angle increases from $\pi/12$ to $\pi/6$. Clearly, it can be observed that for change in the bifurcation angle, the impedance profile depicts no change in the parent artery but show the changes in the daughter artery as the bifurcated angle caused the fluid to change its behaviour and led the decreasing profile for an increasing bifurcation angle. Figure 4.6f shows the growing nature of the impedance profile by enhancing the Rayleigh number. The impedance profile is minimum when $Rb = 0$ and increases for a positive value of Rb. It has been noticed that the convection produced by microorganisms lowers the buoyant force that hinders the mobility of the fluid and raises the impedance distribution.

4.4.5 WSS, Nusselt Number and Sherwood Number

Wall shear stress (WSS) is defined as the force per unit area on the fluid produced by the arterial wall along the tangential direction. The research concluded that WSS is a critical component in the biomedical industry for elucidating the pattern of atherosclerotic lesion development. This research has clinical potential for assessing WSS's temporal and spatial distribution, which may aid in the early diagnosis of stenosis. Figure 4.7a depicts the WSS distribution by illustrating the effect of varying the stenotic depth in the bifurcated artery. In both sections of the arteries (parent and daughter arteries), the WSS profile decreases as the stenotic depth increases. The findings of this research corroborate those of Zhang's experimental work [131], which also found that arterial lesion development decreased WSS. Figure 4.7b indicates the influence of the solutal Grashof number on the WSS profile. The study reveals that the WSS profile rises as the parameter Gc increase from 0 to 1. WSS profile shows the minimum profile when $Gc = 0$ and increases as the Gc enhances, leading to the emergence of buoyant force that improves the flow near the arterial wall and enhances the WSS profile. The ratio of convective heat transmission to conductive heat transfer in the arterial walls is represented by the dimensionless Nusselt number. The decrease in the Nusselt number that occurs with an increasing Prandtl number is seen in Figure 4.7c. It can be inferred from the figure that the efficiency of transferring heat from the arterial wall to blood reduces as the Pr value enhances.

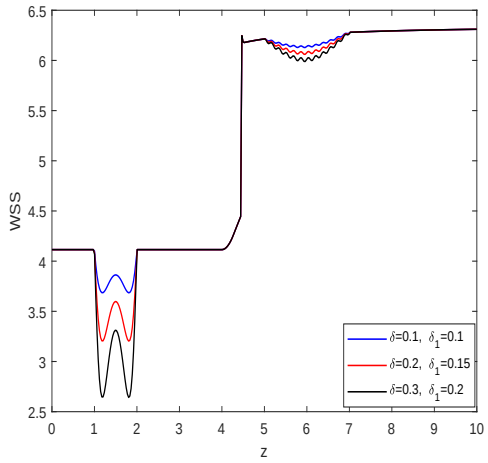

(a) Wall shear stress by varying stenotic depth

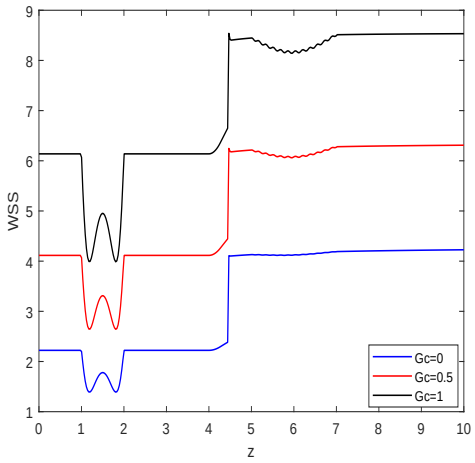

(b) Wall shear stress by varying Gc

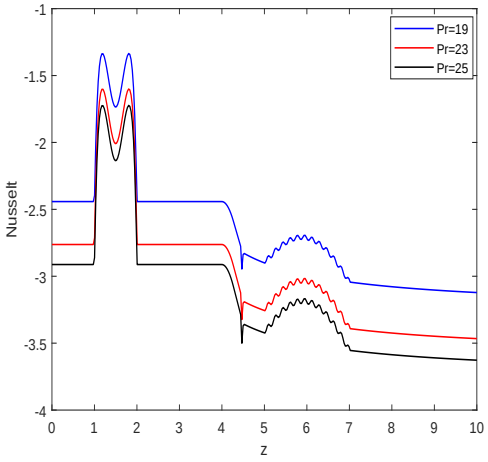

(c) Nusselt profile varying Pr

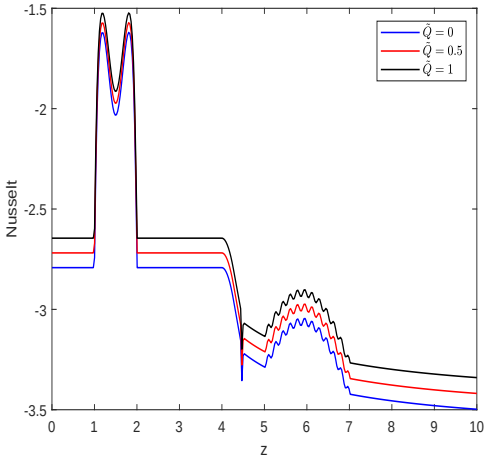

(d) Nusselt profile varying $\tilde{Q}$

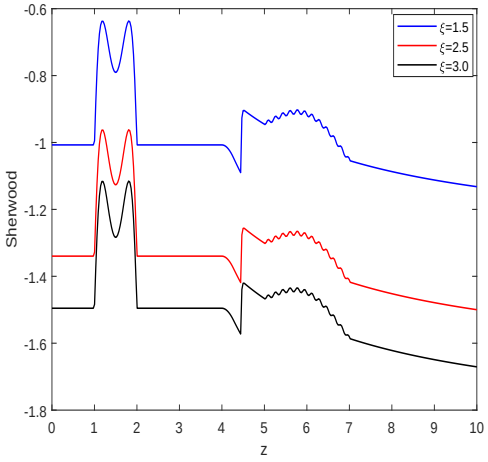

(e) Sherwood profile by varying ξ

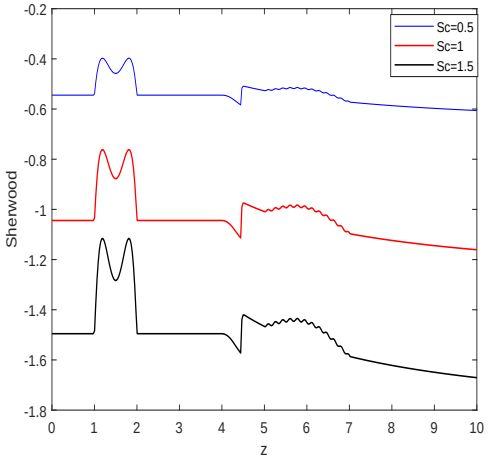

(f) Sherwood profile by varying Sc

Figure 4.7: WSS, Nusselt number and Sherwood profile

This has happened due to the low thermal conductivity of higher-Pr fluids. Figure 4.7c visually represents the relationship between the Nusselt number and the Prandtl number. The figure demonstrates that as the Prandtl number increases, there is a notable decrease in the Nusselt number. The observed pattern indicates that the efficiency of heat transfer from the arterial wall to the blood decreases as the Prandtl values increase. In the context of arterial heat transfer, it has been observed that fluids with higher Prandtl numbers tend to demonstrate diminished efficacy in the conduction of heat when compared to fluids possessing lower Prandtl numbers. Consequently, the Nusselt number decreases with increasing Prandtl number, indicating a reduced ability to transfer heat from the arterial wall to the blood. Figure 4.7d depicts the relation between the heat source parameter and Nusselt profile. The utilisation of a heat source has been found to have potential applications in therapeutic procedures. By selectively targeting the affected region, heat energy can be generated without causing harm to nearby tissues. This localised heating can serve multiple purposes, including the dilation of arteries to facilitate increased blood flow to the affected area. Therefore, it can be utilised as a potential intervention to mitigate stenosis. The reverse trend is observed in Figure 4.7d for the heat source parameter signifying that the higher Nusselt profile trend is observed with an increase in the heat source parameter. An increase in the heat source parameter from 0 to 1 induces a rise in the heat generation rate within the blood, thereby causing an escalation in the temperature leading to enhancing Nusselt number profile.

Thermal treatment is one of the finest ways to expose blood tissue and cancerous cells to high temperatures in biomedical area; nevertheless, it must be performed under safety recommendations to prevent damage to healthy tissues. The effect of the chemical reaction parameter and Schmidt number on the Sherwood profile is demonstrated in Figures 4.7e and 4.7f, respectively. The statistics suggest that nature is deteriorating, with a rise in ξ and Sc. This pattern may be described by the fact that the molecular diffusivity lowers, indicating a lesser mass transfer across the wall, which leads to a diminishing nature in the Sherwood profile.

4.4.6 Velocity Contour

This section presents visual representations of the velocity pattern as influenced by various parameters. This facilitates an enhanced visual and comprehensive depiction of the hemodynamic flow in close proximity to the constricted area along the walls of the bifurcated artery. The velocity contour for varying Grashof numbers is depicted in figure 4.8a-4.8c.

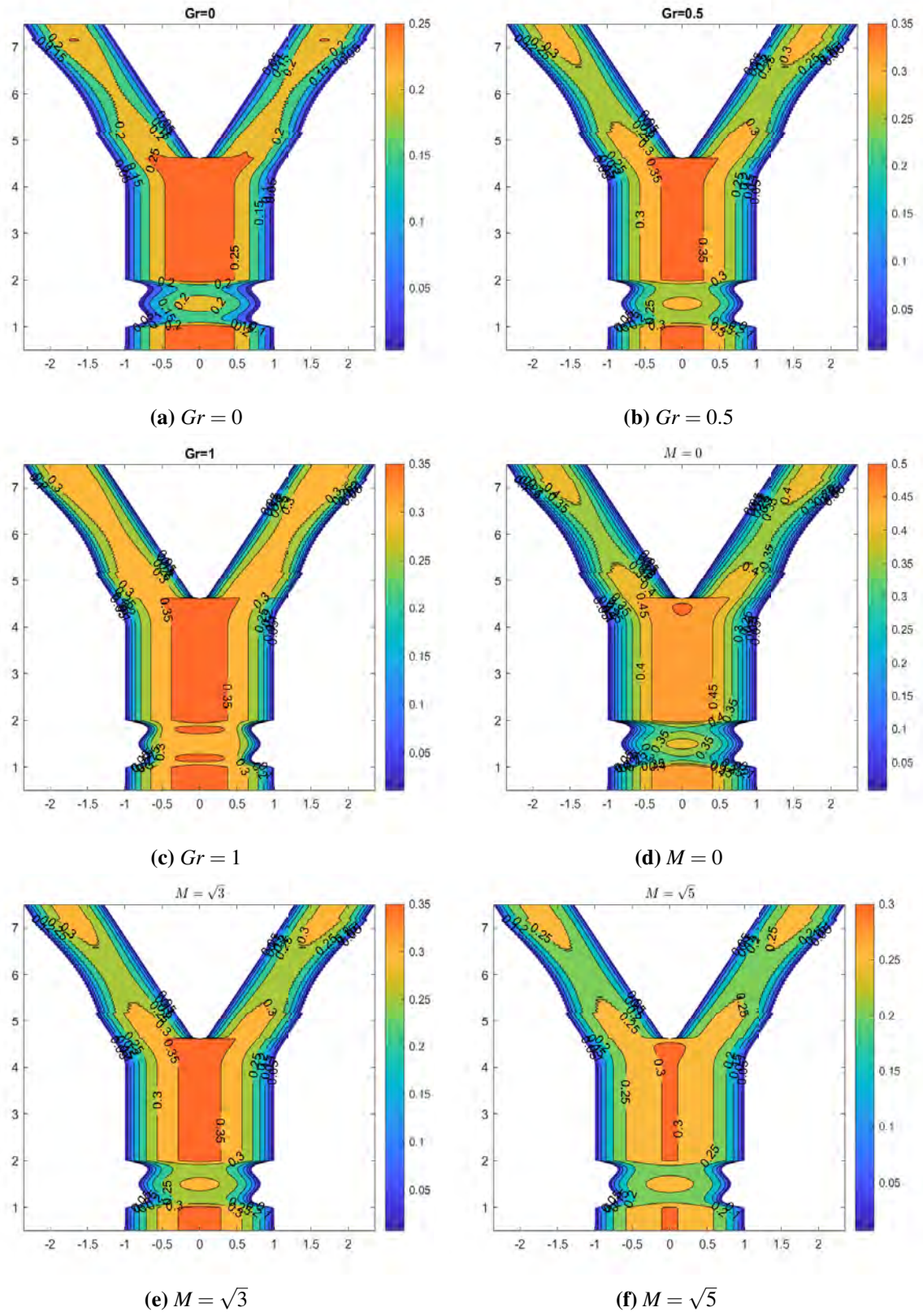

(a) $Gr = 0$ **(b)** $Gr = 0.5$

(c) $Gr = 1$ **(d)** $M = 0$

(e) $M = \sqrt{3}$ **(f)** $M = \sqrt{5}$

Figure 4.8: Velocity contour for Grashof number and Magnetic field parameter

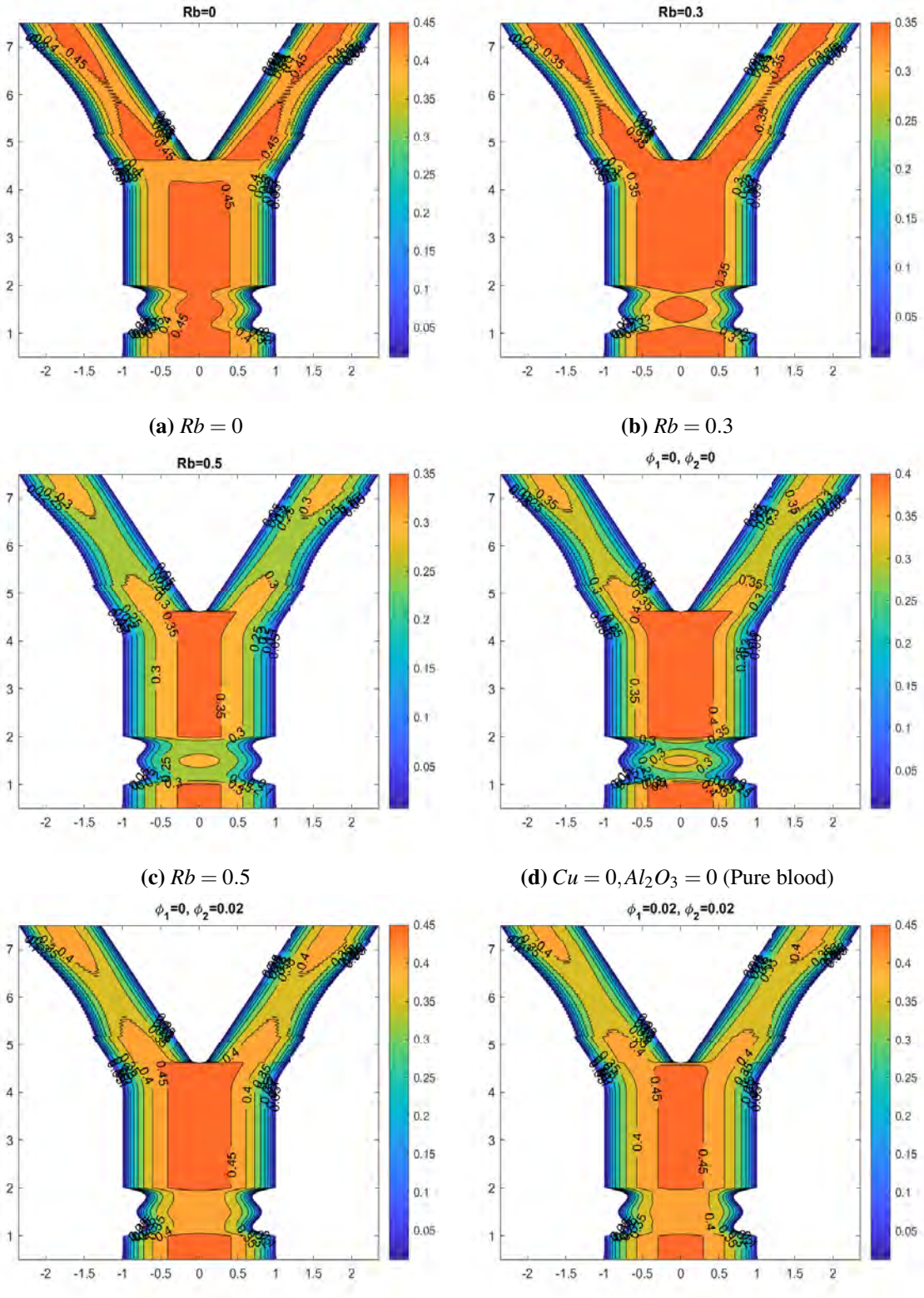

(a) $Rb = 0$

(b) $Rb = 0.3$

(c) $Rb = 0.5$

(d) $Cu = 0, Al_2O_3 = 0$ (Pure blood)

(e) $Cu = 0, Al_2O_3 = 0.02$

(f) $Cu = 0.02, Al_2O_3 = 0.02$

Figure 4.9: Blood flow patttern for Rayleigh number and nanoparticle volumetric concentration.

The figure demonstrates a positive correlation between the elevation of the trapping bolus and the magnitude of Gr. The maximum velocity achieved is 0.35 for both scenarios when the Grashof number (Gr) is equal to 0 and 0.5. Additionally, a maximum velocity of 0.25 is explicitly observed for the case when Gr is equal to 0. The maximum fluid speed is observed to occur in the parent region for all three cases. This phenomenon is attributed to the reduction in the value of Gr in the daughter artery, which is caused by the inclination angle $\eta_1/2$. The velocity contour demonstrates the relationship between the augmentation in velocity and the accompanying elevation in Gr, which can be ascribed to the amplification of the buoyant thermal force and its subsequent influence on the velocity profile. The effect of the magnetic field on the velocity contour is seen in Figure 4.8. Figure 4.8d – 4.8f show that the velocity field decreases when the magnetic field parameter increases. Without a magnetic field, the fluid can only reach a maximum speed of 0.5 , but when the magnetic field parameter is enhances, the fluid's speed reduces. The resistive Lorentz force is responsible for the declination in the velocity, which can be predicted by the velocity contour. The velocity contour for different values of Rb is depicted in Figure 4.9a-4.9c. The data suggest a negative correlation between velocity and Rb, indicating that an increase in Rb results in a decrease in velocity. In the context of Rb deficiency, it has been noted that the maximum velocity profile is achieved in both the parent and daughter arteries. According to our findings, maximum resistance resulting from the overlapping stenosis occurs at $Rb = 0.3$. In the region pertaining to the daughter, a decrease in the quantity of trapped bolus is observed as the value of Rb varies from 0.3 to 0.5. The presence of overlapping and irregular stenosis is observed to cause resistance and decrease fluid velocity in the vicinity of the affected segments. The observed decrease in velocity profile can be attributed to the strengthening of Rb, which resulted in the microorganism's convection counteracting the buoyancy force exerted on the fluid particles.

Figure 4.9d-4.9f displays the velocity contour related to manipulating volumetric nanoparticle concentration. The maximum velocity achievable by pure blood has been found to be 0.4. Additionally, the presence of trapped bolus can be observed in the vicinity of overlapping stenosis. Upon insertion of the copper nanoparticle into the bloodstream, there is an observed increase in the maximum velocity of the fluid, as illustrated in the Figure 4.9e. Figure 4.9f depicts the velocity contour of copper and aluminium oxide suspended in the base fluid (blood) . Although the maximum velocity remains constant in both cases 4.9e and 4.9f, the velocity profile is reduced when aluminium oxide nanoparticles are doped in copper/blood solution. These findings provide novel insights for evaluating the precision of theoretical investigations on complex systems and comprehending the impact of blood properties on diverse nanoparticles. Consequently, the surgeon surgeon possesses the ability to

regulate the blood flow during the surgical intervention.

4.5 Conclusion

The current study presents a mathematical model describing the hemodynamic flow through a bifurcated artery with overlapping and irregular stenosis at the parent and daughter arteries, respectively. The investigation has focused on implementing the Al_2O_3-Cu/Blood hybrid nanofluid in conjunction with electroosmotic force, a heat source, and microorganisms. Nanoparticles are colloidal suspensions composed of microscopic-shaped substances dispersed in a base fluid. The favourable heat transfer capabilities and stability of nanofluids make them an ideal choice for applications in the biomedical field. The pursuit of stable, non-aggregating, and bio-compatible medicines is a primary objective of researchers. The antibacterial and antiviral properties of copper nanoparticles are attributed to their large surface area-to-volume ratio. The chemical stability of aluminium oxide nanoparticles (AlNPs) in abrasive environments, their low cost, and ease of acquisition render them a viable option for application in biomedicine. The favourable characteristics exhibited by the nanoparticles have prompted us to investigate the potential of utilising the Al_2O_3-Cu/Blood hybrid nanofluid in the context of the bifurcated artery. The significant outcomes are outlined below:

- It is noticed that the velocity profile decreases in both parent and daughter artery with enhancement in magentic field parameter while reverse trend is observed for Debye-Huckel parameter.

- Temperature profile enhances with an upsurge in the heat source parameter.

- The mounting value of Sb reduces the motile density of the fluid, attributed to a reduction in microorganism diffusivity.

- Nusselt number profile decline with an enhancement in Pr while the opposite behaviour is observed for heat source parameter.

- Sherwood profile decreases with an enhancement in both chemical reaction parameter and Schmidt number due to lower molecular diffusivity.

Chapter 5

Entropy Generation Analysis of a Ternary Hybrid Nanofluid (Au-CuO-GO/Blood) Containing Gyrotactic Microorganisms in Bifurcated Artery [1]

5.1 Introduction

Stenosis and aneurysm are two distinct medical conditions of significant importance, as they can impact various human body regions. The presence of these abnormalities often results in the manifestation of a typical configurations within the vasculature, which can subsequently give rise to a range of health implications that may carry significant clinical significance [132]. Stenosis is a pathological condition characterised by the constriction or narrowing of blood vessels, primarily caused by the accumulation of various substances such as fatty plaques, cholesterol, cellular debris, and calcium on the inner lining of arteries [133]. On the contrary, an aneurysm denotes a condition characterised by the dilation or expansion of a blood vessel, which may heighten the likelihood of rupture, resulting in significant haemorrhaging and potential mortality [134]. The study conducted by Ahmed and Nadeem [2] seeks to explore the flow characteristics of the micropolar fluid and hybrid nanofluid through six different types of stenosis. This comparative study elucidates discernible variations in microrotation levels across different stenosis configurations. This comparative study revealed that irregular symmetric stenosis exhibits a higher microrotation than bell-shaped stenosis in micropolar fluid and hybrid nanofluid. Joshua et al. [117] comprehensively investigated unsteady blood flow characteristics in an inclined multiple stenosis configuration. The study encompassed the manipulation of numerous crucial parameters, precisely the Hartmann number, severity of stenosis, Power Law index, and Reynolds number. The study performed by Mishra et al. [120] focused on investigating the impact of the Soret and

[1] A considerable part of this chapter is published in *International Journal of Numerical Methods for Heat & Fluid Flow , Vol. 34 No. 2, pp. 980-1020*

Dufour effects on a MHD (magnetohydrodynamic) nanofluid with varying viscosity as it flows through a stenosed artery. Poonam et al. [82] conducted a numerical investigation to analyse the transport characteristics of a hybrid nanofluid within a curved artery with stenosis and aneurysm. The study incorporated multiple factors, such as hematocrit-dependent viscosity, external body acceleration, viscous dissipation, and Joule heating. The results of their study demonstrated that an elevation in the Hartmann number corresponded to a reduction in both wall shear stress and blood velocity. The investigation conducted by Shahzadi et al. [95] examined the impact of electroosmotic forces and slip conditions on the flow of a ternary nanofluid through an oblique stenosed aneurysmal artery. Numerous prior investigations [33, 121, 135, 136] have also examined the effects of MHD nanofluids related to arterial dieseases such as stenosis or aneurysms.

In recent years, MHD play a crucial role in the biomedical field. The human blood contains the ions and electrolytes which make them suitable to behave like an electrically conducting fluid. MHD is the interaction of the electric and magnetic field acting transversally to each other. While, electroosmosis is the interaction of charged particles on the action of an applied electric field. A thorough investigations helps the researchers to understand the application of MHD in the arterial diseases and open up new avenue for non-invasive and therapeutic interventions. Majee and Shit [137] performed a numerical investigation to examine the MHD flow within a stenosed artery. The findings of their investigation unveiled the existence of a region with reduced shear stress in the close vicinity of the stenosis's downstream area, suggesting a heightened probability of subsequent plaque accumulation. The research conducted by Abbas et al. [138] was centred on the study of MHD pulsatile flow through overlapping stenosis, taking into account body acceleration effects. Gandhi et al. [139] discussed Casson fluid's unsteady electromagnetic MHD flow through an irregular stenosed permeable artery. In their study, nanofluids' effective viscosity and thermal conductivity were determined using the Koo-Kleinstreuer-Li model, which incorporates the Brownian motion of nanoparticles. Sharma et al. [97] presented a comprehensive analysis of MHD blood flow within a curved arterial geometry, including the influence of heat transfer, body acceleration, and hybrid nanoparticles. In addition, the study integrated a viscosity model dependent on hematocrit levels to replicate the blood flow characteristics effectively. Dubey et al. [140] employed the finite element method to numerically investigate MHD fluid dynamics within a bifurcated artery containing a saccular aneurysm. Their findings indicated a reduction in the velocity profile with the rise in the magnitude of the magnetic field parameter , resulting in a drag force observed both at the saccular aneurysm and near the throat of the aneurysm.

The bifurcated artery is characterised by the anatomical phenomenon wherein the parent

artery undergoes division, forming branch-like structures referred to as daughter arteries. The bifurcated artery is a crucial component in the distribution of oxygen to different regions of the human body. It is present in key locations such as the aorta, carotid arteries, and coronary arteries. The present study primary focus to investigate Casson fluid's flow characteristics within a bifurcated artery configuration. Specifically, we examine scenarios where the parent artery contains an aneurysm while the daughter arteries exhibit mild overlapping stenosis. Vascular studies of this nature facilitate the examination and analysis of hemodynamic flow within diseased arteries, thereby contributing to the diagnostic process of various pathological conditions. Ponalagusamy and Priyadharshini [104] investigated the utilisation of the Casson fluid model in replicating the hemodynamic flow characteristics within a bifurcated artery having the permeable walls. The researchers analysed the transition from the Newtonian to the non-Newtonian blood flow model. Their findings indicate that this transition enhanced the flow rate and wall shear stress (WSS) profile. Shahzad et al. [116] constructed a mathematical model to investigate the phenomenon of fluid-structure interaction. Specifically, they focused on Casson fluid flow through elastic arterial walls. The observed trend indicates that an increase in both Bingham and Hartmann numbers corresponds to an increase in the load exerted on the walls. Hossain [141] explored the influence of a magnetic field on the flow of a two-phase bio-nanofluid through a bifurcated artery. The study highlighted that the presence of a magnetic source led to irregular flow patterns within the bifurcated artery. Manchi and Ponalagusamy [34] conducted a comprehensive investigation on the electromagnetic hydrodynamics (EMHD) micropolar fluid flowing through a porous bifurcated artery under the influence of body acceleration and Joule heating. Their study compared the heat transfer characteristics between two types of nanofluids: Ag/blood nanofluid and Ag-TiO2 hybrid nanofluid. The authors observed that the heat transfer rate increased with the Grashof number and decreased with increasing stenosis severity. Zain and Ismail [142] investigated the effects of MHD on blood flow through a bifurcated artery with overlapping-shaped stenosis. The authors suggested that an increase in the magnetic field parameter reduced the wall shear stress occurring at the constricted section of the stenosis throat. These findings contribute to the understanding of arterial flow dynamics and have implications for biomedical applications and the design of medical devices.

The concept of nanofluid entails the utilisation of minuscule nanoparticles that are evenly distributed within the base fluid, thereby exemplifying a pioneering technological advancement. The shape, size, and efficiency of nanoparticles play a significant role in the biomedical field as they contribute to the effectiveness of targeted drug delivery. Nanofluid flow via composite stenosis in permeable artery walls was studied by Ellahi et al. [143]. Sharifi et al. [144] proposed using nanofluid flow as a means of targeted drug delivery, specifically

within aneurysmal blood vessels, by employing a magnetic field. Therefore, the improvement of treatment protocols without the occurrence of adverse effects. Sowmya et al. [145] discussed the different shapes of nanoparticles through the radial porous fin. Their study revealed the enhancement in the heat transfer property by using the nanofluid. Gürbüz et al. [146] experimentally and numerically performed the simulation of CuO-Al_2O_3 water hybrid nanofluid through the U-type heat exchanger. The study suggested that adding fins and hybrid nanofluid can enhance the heat transfer rate in the heat exchanger. Sarwar and Hussain [67] examined the hemodynamic properties of a hybrid nanofluid comprising gold nanoparticles as it traverses a stenotic artery. This model presents the therapeutic application of gold nanoparticles in treating vascular diseases. Khanduri et al. [107, 112] examined the impact of Hall's effects on the stenotic artery. They specifically focused on utilising hybrid nanoparticles and a viscosity model that considers the dependence on hematocrit levels in the blood. The authors revealed that thrombosis within the catheterised artery impacts the hemodynamic flow characteristics.

Ternary hybrid nanoparticles, which have improved thermal conductivity and bio-stability over conventional nanofluids, provide a new opportunity for diagnosing and treating pathological disorders in the medical area. The combination of three distinct nanoparticles in a base fluid constitutes a ternary hybrid nanofluid. Therefore, by integrating these three characteristics of nanofluids, they may be employed as the targeted delivery drug. Comparative research between ternary hybrid nanofluids and hybrid and conventional nanofluids was conducted by Mahmood et al. [147]. The flow of ternary hybrid fluid passed through the stretching sheet under the influence of a magnetic field, suction and a heat source. Alnahdi et al. [148] discovered the influence of the flow characteristics of Casson fluid flow through the capillary tube and the governing equations arising from the model are computed using the homotopy analysis method. Their study predicted that the heat transfer rate increases with augmentation in the radiation parameter. In contrast, with an enhancement in the magnetic field parameter, a reverse trend is observed for the velocity profile. Fluid flow via the catheterized stenosed artery was explored by Dolui et al. [149], who looked at the impact of the induced magnetic field and radiation. The ternary hybrid nanoparticles are used in the composite stenosed artery and graphically portray the influence of different pertinent parameters. According to the investigation results, heat transfer and flow behaviour are improved within the stenotic artery. Thus, promising use of ternary hybrid nanofluids in healthcare and advancing state-of-the-art biomedical technologies.

Bioconvection is a naturally occurring phenomenon that arises as a result of density differences caused by the upward movement of microorganisms. The upward motion of microorganisms towards the surface led to an increased concentration of microorganisms in

that region, subsequently causing the downward movement of microorganisms due to the influence of gravity. Consequently, the phenomenon of bioconvection arises within the system. It is worth noting that microorganisms possess the ability to propel themselves through swimming, a characteristic that is absent in nanoparticles. In response to the aforementioned phenomena, Bhatti et al. [125] conducted a study to investigate the peristaltic motion of the Jeffery nanofluid within a system consisting of two coaxial tubes. The fluid flow is subjected to a significant magnetic field, and it has been observed that the density of motile microorganisms decreases as the Peclet number increases. Alharbi et al. [126]considered the porous stretching sheet to exhibit the microorganism's bioconvection phenomena in a hybrid nanofluid. The research conducted by Sharma et al. [1] delved into the intricate dynamics of magnetohydrodynamic (MHD) fluid flow when microorganisms are present in the vicinity of an inclined stretching sheet. The study conducted by Mekheimer et al. [127] focused on investigating the utilisation of nanoparticles for drug delivery in the context of hemodynamic flow within diseased organs. In their seminal work, Mostapha and EL-Dabe [128] conducted a comprehensive theoretical analysis to examine the intricate dynamics of nanofluid flow induced by peristalsis. Notably, their investigation considered the intriguing phenomenon of motile gyrotactic microorganisms within an endoscope. In addition to considering the impact of radiation and chemical interaction, the study also incorporated the Soret and Dufour scheme.

Entropy is a fundamental concept within the biomedical field, facilitating comprehension of the intricate complexities and behaviours inherent in biological systems. Amidst a dynamic environment, biological systems exhibit constant fluctuations, thereby warranting the utilization of entropy as a metric to quantitatively assess the intrinsic randomness and disorder manifesting within these systems [150]. Akbar et al. [151] explored the phenomenon of entropy in the peristaltic flow of a base fluid containing copper nanoparticles, considering the influence of an induced magnetic field. Tayebi and Chamkha [152] addressed the entropy analysis of MHD hybrid nanofluid in the wavy solid block under the influence of magnetic field. Marzougui et al. [153] discussed the entropy analysis of copper water nanofluid under the influence of magnetic field and nanoparticle volume fraction through porous medium. Zidan et al. [57] elucidated the concept of entropy generation and its relationship to the response surface methodology in blood flow through a catheterized arteries containing multiple stenoses. The authors aimed to understand how entropy is generated and distributed in the presence of these obstructions. Zaman et al. [96] addressed the topic of entropy generation in the presence of multiple stenoses in curved arteries, utilizing the Cross fluid model to represent blood flow. Algehyne et al. [154] focused on applying magnetized nanoparticles for drug delivery in composite stenosed arteries. The authors explored

the effects of magnetization on the behaviour of nanoparticles within the stenosed artery, explicitly investigating their potential for targeted drug delivery. Furthermore, Sharma et al. [109] conducted a numerical investigation on the entropy generation in a MHD power-law fluid flowing through a curved artery, considering the Hall effect and radiation. The authors discovered that entropy increases within the stenosed curved artery when the thermal radiation parameter is enhanced, suggesting that thermal radiation in therapies could potentially reduce the deposition of arteriosclerosis. Through diligent examination of entropy within the biomedical realm, researchers are empowered to garner invaluable insights into the efficiency, organization, and stability of various biological processes.

In light of the abovementioned study, a mathematical model was developed to analyze Casson fluid flow through a bifurcated artery, incorporating gyrotactic microorganisms. The study considers the presence of an aneurysm in the parent artery and stenosis in the daughter artery. The primary focus of this research revolves around examining the influence of entropy generation on the flow characteristics of a ternary hybrid nanofluid (Au-CuO-GO/Blood). Furthermore, the effects of viscous dissipation, Joule heating, and electroosmosis have been incorporated into the model. By incorporating these phenomena comprehensively, this study has achieved a deeper understanding of the multiphysics aspects associated with flow in bifurcated arteries. The insights gained hold significant implications for clinical settings and therapeutic interventions.

5.2 Model Formulation

In this study, we consider the analysis of a fully developed, unsteady, laminar, incompressible two-dimensional magnetohydrodynamic (MHD) blood flow within a stenosed bifurcated artery. The arterial system under investigation comprises straight, circular cylinders aligned along the centerline of the parent artery, exhibiting irregular aneurysm in the parent artery and overlapping stenosis in the daughter arteries (refer to Figure 5.1). To describe the system mathematically, we introduce a cylindrical coordinate system denoted by $\tilde{r}$, $\tilde{\theta}$, and $\tilde{z}$, where $\tilde{z}$ represents the coordinate along the centerline of the parent artery, while $\tilde{r}$ and $\tilde{\theta}$ denote the radial and circumferential directions, respectively. The flow characteristics are assumed to be antisymmetric, implying that all variables are independent of $\tilde{\theta}$. Furthermore, a uniform magnetic field $\mathbf{B} = (B_0, 0, 0)$ and an electric field $\mathbf{E} = (0, 0, E_0)$ are applied to the blood flow, with B_0 representing a constant magnetic field strength.

Considering the gravitational force acting in the downward direction, we neglect the contribution of the induced magnetic field due to the assumption of a low magnetic Reynolds number. In order to eliminate the potential for flow separation zones, curvature is introduced

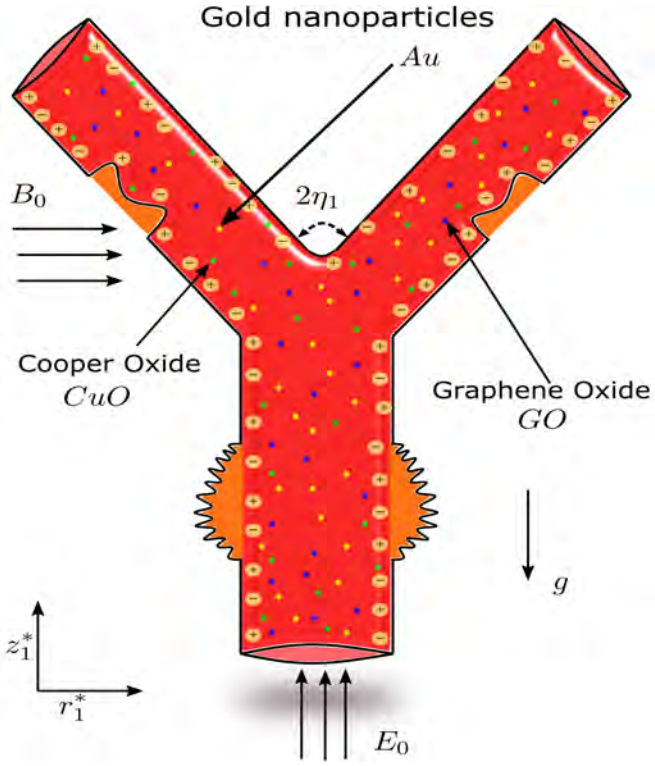

Figure 5.1: Representation of bifurcated artery with irregular aneurysm in the parent artery and overlapping stenosis in the daughter artery

at the lateral junction and the apex of the bifurcation. The geometry of the bifurcated artery with irregular aneurysm in the parent artery and an overlapping stenosis in the daughter artery is expressed as follows [13]:

$$\tilde{\bar{R}}_1^*(\tilde{z}) = \begin{cases} R_0, & 0 < \tilde{z} \leq \tilde{d}, \\ R_0 + A^*, & \tilde{d} < \tilde{z} \leq \tilde{d} + 2L_0 \\ R_0, & \tilde{d} + 2L_0, < \tilde{z} \leq \tilde{z}_1 \\ R_0 + \tilde{r}_1 - \sqrt{\left(\tilde{r}_1^2 - \frac{R_0^2}{L_0^2}(\tilde{z} - \tilde{z}_1)^2\right)}, & \tilde{z}_1 < \tilde{z} \leq \tilde{z}_2, \\ 2r_0 sec\eta_1 + \frac{R_0}{L_0}\left(\tilde{z} - \tilde{z}_2\right)\tan\eta_1, & \tilde{z}_2 < \tilde{z} \leq \tilde{z}_5 \\ 2r_0 sec\eta_1 + \frac{R_0}{L_0}\left(\tilde{z} - \tilde{z}_2\right)\tan\eta_1 - B^*, & \tilde{z}_5 < \tilde{z} \leq \tilde{z}_5 + L_0, \\ 2r_0 sec\eta_1 + \frac{R_0}{L_0}\left(\tilde{z} - \tilde{z}_2\right)\tan\eta_1, & \tilde{z}_5 + L_0 < \tilde{z} \leq \tilde{z}_{max}. \end{cases} \tag{5.1}$$

Where,

$$A^* = 2\delta_1^*\left\{\cos\left(\frac{2\pi}{L_0}\left(\frac{\tilde{z}-\tilde{d}}{4}\right)-0.25\right)-0.07\cos\left(\frac{128\pi}{L_0}\left(\tilde{z}-\tilde{d}-0.5L_0\right)\right)\right\}\tan(\eta_1),$$
$$B^* = \frac{6\delta^*}{5L_0^4}(11(\tilde{z}-\tilde{z}_5)L_0^3-47(\tilde{z}-\tilde{z}_5)^2L_0^2+72(\tilde{z}-\tilde{z}_5)^3L_0-36(\tilde{z}-\tilde{z}_5)^4).$$

And, Kroncecker delta function is defined as:

$$\delta_{ij} = \begin{cases} 0 & \text{for} \quad 0 \le \tilde{z} \le \tilde{z}_3, \\ 1 & \text{for} \quad \tilde{z}_3 \le \tilde{z} \le \tilde{z}_{max}, \end{cases} \tag{5.2}$$

The inner wall is represent as:

$$\tilde{R}_2^*(\tilde{z}) = \begin{cases} 0, & 0 < \tilde{z} \le \tilde{z}_3, \\ \sqrt{\tilde{r}_1^{*2} - \left(R_0\left(\frac{\tilde{z}-\tilde{z}_3}{L_0}\right) - \tilde{r}_1^*\right)^2}, & \tilde{z}_3 < \tilde{z} \le \tilde{z}_4, \\ \frac{R_0}{L_0}(\tilde{z}-\tilde{z}_2)\tan\eta_1, & \tilde{z}_4 < \tilde{z} \le z_{max}. \end{cases} \tag{5.3}$$

Where, $\tilde{d}$ represent location of stenosis, $\tilde{z}_1$ denotes the location of insert lateral junction, $\tilde{z}_{max}$ signifies the maximum length of stenosis; $\tilde{r}_1$ denotes the daughter artery radius; The radii of curvature at lateral junction and at the flow divider is represented by:

$$\tilde{r}_1 = \frac{R_0 - 2r_0\sec\eta_1}{\cos\eta_1 - 1},\ \tilde{r}_1^* = \frac{(\tilde{z}_3-\tilde{z}_2)R_0\sin\eta_1}{L_0(1-\sin\eta_1)}, \tag{5.4}$$

The spatial coordinates of the lateral junction offset, apex, and offset of curvature along the inner wall are expressed as follows:

$$\tilde{z}_2 = \tilde{z}_1 + \tilde{r}_1\left(\frac{L_0}{R_0}\right)\sin\eta_1, \tag{5.5}$$
$$\tilde{z}_3 = \tilde{z}_2 + q_1L_0, \tag{5.6}$$
$$\tilde{z}_4 = \tilde{z}_3 + \tilde{\tilde{r}}_1^*\left(\frac{L_0}{R_0}\right)(1-\sin\eta_1) \tag{5.7}$$
$$\tilde{z}_5 = \tilde{z}_4 + 0.5L_0. \tag{5.8}$$

Where η_1 is half of the bifurcation angle and value of q_1 lies between 0.1 and 0.5, $\tilde{d} = 1, \delta_1 = 0.2, \delta = 0.5$ and $\tilde{z}_{max}$ is the finite length of the bifurcated artery.

The rheological equation of state for incompressible flow in the context of the Casson fluid model is expressed as follows:

$$\tau_{ij}^{*}=\begin{cases}2\left(\mu_{b}^{*}+\frac{p_{y}^{*}}{\sqrt{2\pi^{*}}}\right)e_{ij}^{*}, & \pi^{*}>\pi_{c}^{*},\\ 2\left(\mu_{b}^{*}+\frac{p_{y}^{*}}{\sqrt{2\pi_{c}^{*}}}\right)e_{ij}^{*}, & \pi^{*}\leq\pi_{c}^{*},\end{cases} \tag{5.9}$$

where $\pi^{*}=e_{ij}^{*}.e_{ij}^{*}$ represent the multiplication of the deformation rate with itself , μ_{b}^{*} signifies the viscosity of the non-Newtonian fluid, p_{y}^{*} represents the yield stress of the fluid, and π_{c}^{*} denotes a critical value derived from the non-Newtonian model.
Equation (5.9) converted to the following form when $\pi^{*}\leq\pi_{c}^{*}$:

$$\tau_{ij}^{*}=2\mu_{b}^{*}\left(1+\frac{1}{\beta_{1}}\right)e_{ij}^{*}, \tag{5.10}$$

where $\beta_{1}=\frac{\mu_{b}^{*}\sqrt{2\pi_{c}^{*}}}{p_{y}^{*}}$ denotes the Casson fluid parameter.

5.2.1 Governing Equations

Given the aforementioned assumptions and with the application of the Boussinesq approximation, the governing equations that describe the flow can be expressed as follows:
Continuity Equation:

$$\frac{\partial\tilde{u}}{\partial\tilde{r}}+\frac{\tilde{u}}{\tilde{r}}+\frac{\partial\tilde{w}}{\partial\tilde{z}}=0, \tag{5.11}$$

Momentum Equation:
$\tilde{r}$-direction:

$$\rho_{thnf}\left[\frac{\partial\tilde{u}}{\partial t}+\tilde{u}\frac{\partial\tilde{u}}{\partial\tilde{r}}+\tilde{w}\frac{\partial\tilde{u}}{\partial\tilde{z}}\right]=-\frac{\partial\tilde{p}}{\partial\tilde{r}}+\frac{1}{\tilde{r}}\frac{\partial}{\partial\tilde{r}}\left[\mu_{thnf}\left(1+\frac{1}{\beta_{1}}\right)\tilde{r}\frac{\partial\tilde{u}}{\partial\tilde{r}}\right]+\frac{1}{2}\frac{\partial}{\partial\tilde{z}}\left[\mu_{thnf}\left(1+\frac{1}{\beta_{1}}\right)\left(\frac{\partial\tilde{w}}{\partial\tilde{r}}+\frac{\partial\tilde{u}}{\partial\tilde{z}}\right)\right]-\mu_{thnf}\left(1+\frac{1}{\beta_{1}}\right)\frac{\tilde{u}}{\tilde{r}^{2}}, \tag{5.12}$$

$\tilde{z}$-direction:

$$\rho_{thnf}\left[\frac{\partial\tilde{w}}{\partial\tilde{t}}+\tilde{u}\frac{\partial\tilde{w}}{\partial\tilde{r}}+\tilde{w}\frac{\partial\tilde{w}}{\partial\tilde{z}}\right]=-\frac{\partial\tilde{p}}{\partial\tilde{z}}+\frac{1}{2}\frac{1}{\tilde{r}}\frac{\partial}{\partial\tilde{r}}\left[\mu_{thnf}\left(1+\frac{1}{\beta_{1}}\right)\tilde{r}\left(\frac{\partial\tilde{u}}{\partial\tilde{z}}+\frac{\partial\tilde{w}}{\partial\tilde{r}}\right)\right]$$
$$+\frac{\partial}{\partial\tilde{z}}\left[\mu_{thnf}\left(1+\frac{1}{\beta_{1}}\right)\frac{\partial\tilde{w}}{\partial\tilde{z}}\right]+(\rho\beta)_{thnf}g\left[(\tilde{T}-\tilde{T}_{1})+(\tilde{C}-\tilde{C}_{1})-(\tilde{n}^{*}-\tilde{n}_{1}^{*})\right]\cos(\eta_{1}\delta_{ij})+G(\tilde{t})$$
$$+\rho_{e}E_{0}-\sigma_{thnf}B_{0}^{2}\tilde{w}, \tag{5.13}$$

Energy Equation:

$$(\rho C_p)_{thnf}\left[\frac{\partial \tilde{T}}{\partial \tilde{t}}+\tilde{u}\frac{\partial \tilde{T}}{\partial \tilde{r}}+\tilde{w}\frac{\partial \tilde{T}}{\partial \tilde{z}}\right]=k_{thnf}\left[\frac{\partial^2 \tilde{T}}{\partial r^2}+\frac{1}{\tilde{r}}\frac{\partial \tilde{T}}{\partial \tilde{r}}+\frac{\partial^2 \tilde{T}}{\partial \tilde{z}^2}\right]+\tilde{Q}_0+\sigma_{thnf}B_0^2\tilde{w}^2+\sigma_{thnf}E_0^2+\phi^*, \tag{5.14}$$

where,

$$\phi^*=2\mu_{thnf}\left(1+\frac{1}{\beta_1}\right)\left[\left(\frac{\partial \tilde{u}}{\partial \tilde{r}}\right)^2+\left(\frac{\tilde{u}}{\tilde{r}}\right)^2+\left(\frac{\partial \tilde{w}}{\partial \tilde{z}}\right)^2+\frac{1}{2}\left(\frac{\partial \tilde{u}}{\partial \tilde{z}}+\frac{\partial \tilde{w}}{\partial \tilde{r}}\right)^2\right].$$

Concentration Equation:

$$\frac{\partial \tilde{C}}{\partial \tilde{t}}+\tilde{u}\frac{\partial \tilde{C}}{\partial \tilde{r}}+\tilde{w}\frac{\partial \tilde{C}}{\partial \tilde{z}}=D_B\left[\frac{\partial^2 \tilde{C}}{\partial \tilde{r}^2}+\frac{1}{\tilde{r}}\frac{\partial \tilde{C}}{\partial \tilde{r}}+\frac{\partial^2 \tilde{C}}{\partial \tilde{z}^2}\right]-R_c(\tilde{C}-\tilde{C}_0) \tag{5.15}$$

Microorganism Equation:

$$\frac{\partial \tilde{n}^*}{\partial \tilde{t}}+\tilde{u}\frac{\partial \tilde{n}^*}{\partial \tilde{r}}+\tilde{w}\frac{\partial \tilde{n}^*}{\partial \tilde{z}}+\frac{bW_c}{\tilde{C}_0-\tilde{C}_w}\left[\frac{\partial}{\partial \tilde{r}}\left(\frac{\tilde{n}^*\partial \tilde{C}}{\partial \tilde{r}}+\frac{\partial}{\partial \tilde{z}}\left(\frac{\tilde{n}^*\partial \tilde{C}}{\partial \tilde{z}}\right)\right)\right]=D_n\left[\frac{\partial^2 \tilde{n}^*}{\partial \tilde{r}^2}+\frac{1}{\tilde{r}}\frac{\partial \tilde{n}^*}{\partial \tilde{r}}+\frac{\partial^2 \tilde{n}^*}{\partial \tilde{z}^2}\right] \tag{5.16}$$

The boundary conditions are:

$$\tilde{w}=0,\ \ \tilde{T}=\tilde{T}_w\ \ \tilde{C}=\tilde{C}_w\ \ \tilde{n}^*=\tilde{n}^*_w\ \text{ at }\ \tilde{r}=\tilde{\tilde{R}}_1(\tilde{z})\quad \text{for all}\quad \tilde{z}, \tag{5.17}$$

$$\frac{\partial \tilde{w}}{\partial \tilde{r}}=0,\ \ \frac{\partial \tilde{T}}{\partial \tilde{r}}=0\ \ \frac{\partial \tilde{C}}{\partial \tilde{r}}=0\ \ \frac{\partial \tilde{n}^*}{\partial \tilde{r}}=0\ \text{ at }\ \tilde{r}=0\quad \text{for}\quad 0\le \tilde{z}\le \tilde{z}_3, \tag{5.18}$$

$$\tilde{w}=0,\ \ \tilde{T}=\tilde{T}_w,\ \ \tilde{C}=\tilde{C}_w,\ \ \tilde{n}^*=\tilde{n}^*_w\ \text{ at }\ \tilde{r}=\tilde{\tilde{R}}_2(\tilde{z})\quad \text{for}\quad \tilde{z}_3\le \tilde{z}\le \tilde{z}_{max}. \tag{5.19}$$

The initial conditions regarding velocity, temperature, concentration and microorganisms are considered as:

$$\tilde{w}=0,\ \ \tilde{T}=0,\ \ \tilde{C}=0,\ \ \tilde{n}^*=0\ \text{ at }\ \tilde{t}=0. \tag{5.20}$$

The pulsatile nature of pressure gradient and body acceleration terms are given as;

$$G(\tilde{t})=B_0\cos(\omega_q\tilde{t}+\psi), \tag{5.21}$$

$$-\frac{\partial \tilde{p}}{\partial \tilde{z}}=A_0+A_1\cos(\omega_p\tilde{t}). \tag{5.22}$$

Here, A_0 and A_1 are steady-state and amplitude of fluctuating component of pressure gradient, respectively. Where, $\omega_p=2\pi f_p$, f_p is pulse frequency, B_0 is the body acceleration

term, $\omega_q = 2\pi f_q$, f_q is frequency of body acceleration with ψ as a phase angle.

5.2.1.1 Electrohydrodynamics (EHD)

Blood, a complex fluid composed of components such as haemoglobin, plasma, white blood cells, and various ions, exhibits unique electrical conductivity. In the presence of an electrolyte solution, the arterial walls experience generating a net charge, establishing opposite charge distribution in the blood near the walls. Applying an electric field induces the movement of charged ions, subsequently causing fluid motion in the vicinity of the walls. This phenomenon is commonly known as electro-osmotic flow. The electro-osmotic potential function is described by the Poisson-Boltzmann equation, as detailed in the research conducted by Manchi et al. [34]:

$$\nabla^2\tilde{\Phi} = -\frac{\rho_e}{\varepsilon}, \tag{5.23}$$

where, $\tilde{\Phi}$ denotes the electro-osmotic function, ε is dielectric constant, and ρ_e is given as:

$$\rho_e = (n^+ - n^-)e_0 z_0. \tag{5.24}$$

The number density of cation and anion can be defined by the Boltzmann distribution as:

$$n^{\pm} = n_0 \exp\left(\mp\frac{e_0 z_0 \tilde{\Phi}}{k_B T_{avg}}\right), \tag{5.25}$$

where, z_0 is the charge balance, e_0 is electric constant, k_B is Boltzmann constant.

Using the Debye-Huckel linearizion, the Poisson equation takes the form:

$$\left(\frac{\partial^2}{\partial\tilde{r}^2} + \frac{1}{\tilde{r}}\frac{\partial}{\partial\tilde{r}} + \frac{\partial^2}{\partial\tilde{z}^2}\right)\tilde{\Phi} = \frac{\tilde{\Phi}}{q_m^2}, \tag{5.26}$$

where $q_m = \frac{1}{e_0 z_0}\sqrt{\frac{\varepsilon k_B T_{avg}}{2 s_0}}$.

The boundary conditions for electro-osmotic equation are:

$$\begin{cases} \tilde{\Phi} = 0.3\zeta, & \text{at} \quad \tilde{r} = \tilde{\tilde{R}}_1(\tilde{z}) \quad \text{for all} \quad \tilde{z}, \\ \frac{\partial\tilde{\Phi}}{\partial\tilde{r}} = 0, & \text{at} \quad \tilde{r} = 0 \quad \text{for} \quad 0 \le \tilde{z} \le \tilde{z}_3, \\ \tilde{\Phi} = 0.1\zeta, & \text{at} \quad \tilde{r} = \tilde{\tilde{R}}_2(\tilde{z}) \quad \text{for} \quad \tilde{z}_3 \le \tilde{z} \le z_{max}. \end{cases} \tag{5.27}$$

5.2.2 Non-Dimensionalization

It is necessary to convert the governing equations presented in (5.11)-(5.16) into dimensionless form in order to obtain a numerical solution. The introduction of non-dimensional variables is performed in the following manner:

$$u=\frac{L_0\tilde{u}}{\delta^* U_0}, t=\frac{U_0\tilde{t}}{R_0}, z=\frac{\tilde{z}}{L_0}, p=\frac{R_0^2\tilde{p}}{U_0 L_0\mu_0}, r=\frac{\tilde{r}}{R_0}, w=\frac{\tilde{w}}{U_0}, T=\frac{\tilde{T}-\tilde{T}_0}{\tilde{T}_w-\tilde{T}_0}, C=\frac{\tilde{C}-\tilde{C}_0}{\tilde{C}_w-\tilde{C}_0},$$
$$\tilde{\chi_1}^*=\frac{\tilde{n}^*-\tilde{n}_1^*}{\tilde{n}_w^*-\tilde{n}_1^*}, \hat{R}_i^*=\frac{\tilde{\hat{R}}_i^*}{R_0}(i=1,2), d=\frac{\tilde{d}}{L_0}, r_0=\frac{\tilde{r}_0}{R_0}, z_i=\frac{\tilde{z}_i}{L_0}(i=1,..,4), r_1=\frac{\tilde{r}_1}{R_0},$$
$$\tilde{r_1}^*=\frac{\tilde{\tilde{r}}_1^*}{R_0}, Re=\frac{U_0\rho_f R_0}{\mu_f}, M^2=\frac{\sigma_f B_0^2 R_0^2}{\mu_f}, E_1^*=\frac{E_0}{B_0 U_0}, Gr=\frac{\rho_f R_0^2 g\beta_f(\tilde{T}_w-\tilde{T}_0)}{\mu_f U_0},$$
$$Gc=\frac{\rho_f R_0^2 g\beta_f(\tilde{C}_w-\tilde{C}_0)}{\mu_f U_0}, Rb=\frac{\rho_f R_0^2 g\beta_f(\tilde{n}_w^*-\tilde{n}_1^*)}{\mu_f U_0}, Ec=\frac{U_0^2}{C_p(\tilde{T}_w-\tilde{T}_0)}, Pr=\frac{\mu_0 C_p}{k_f},$$
$$\tilde{Q}=\frac{\tilde{Q}_0 R_0^2}{\kappa_f(\tilde{T}_w-\tilde{T}_0)}, S_z=\frac{\sigma_f}{\kappa_f}\frac{R_0^2 E_0^2}{(\tilde{T}_w-\tilde{T}_0)}, q_e=\frac{q_m}{R_0}, Sc=\frac{\nu}{D_m}, Pe=\frac{bW_c}{D_n}, \sigma_1=\frac{\tilde{n}^*}{(\tilde{n}_w^*-\tilde{n}_1^*)},$$
$$Pe=\frac{bW_c}{D_n}, \quad \xi=\frac{R_c\rho_f R_0^2}{\mu_f}, \quad U_{hs}=-\frac{\zeta\varepsilon E_0}{\mu_f U_0} \quad . \quad (5.28)$$

The aforementioned non-dimensional parameters mentioned in equation (5.28) are inserted into the governing equations (5.11)-(5.16) . The mild stenotic assumptions are employed, characterized by a maximal stenosis height that is significantly smaller than the radius of the artery, denoted as $\delta(=\delta^*/R_0) << 1$, a proportional relationship between the artery's radius and the length of the stenotic region, expressed as $\varepsilon(=R_0/L_0)=O(1)$. The governing equations (5.11)-(5.16) undergoes the modifications, which can be expressed as follows:

Momentum Equation:

***r*-direction:**

$$\frac{\partial p}{\partial r}=0, \quad (5.29)$$

z-direction:

$$Re\frac{\rho_{thnf}}{\rho_f}\frac{\partial w}{\partial t}=-\frac{\partial p}{\partial z}+\frac{1}{2r}\frac{\partial}{\partial r}\left[\frac{\mu_{thnf}}{\mu_f}\left(1+\frac{1}{\beta_1}\right)r\frac{\partial w}{\partial r}\right]-\frac{\sigma_{thnf}}{\sigma_f}M^2 w$$
$$+\frac{(\rho\beta)_{thnf}}{(\rho\beta)_f}[GrT+GcC+Rb\tilde{\chi}_1]\cos(\eta_1\delta_{ij})+U_{hs}q_e^2\Phi. \quad (5.30)$$

Energy Equation:

$$\frac{(\rho C_p)_{thnf}}{(\rho C_p)_f}\frac{\partial T}{\partial t} = \frac{1}{RePr}\frac{k_{thnf}}{k_f}\left[\frac{\partial^2 T}{\partial r^2}+\frac{1}{r}\frac{\partial T}{\partial r}\right]+\frac{\sigma_{thnf}}{\sigma_f}\left[\frac{EcM^2}{Re}w^2+\frac{S_z+\tilde{Q}}{RePr}\right] + \frac{\mu_{thnf}}{\mu_f}\left(1+\frac{1}{\beta_1}\right)\frac{Ec}{Re}\left[\left(\frac{\partial w}{\partial r}\right)^2\right]. \quad (5.31)$$

Concentration Equation:

$$ReSc\frac{\partial C}{\partial t} = \frac{\partial^2 C}{\partial r^2}+\frac{1}{r}\frac{\partial C}{\partial r}-Sc\xi C, \quad (5.32)$$

Microorganism Equation:

$$ReSb\frac{\partial \tilde{\chi}_1}{\partial t} = \frac{\partial^2 \tilde{\chi}_1}{\partial r^2}+\frac{1}{r}\frac{\partial \tilde{\chi}_1}{\partial r}-Pe\sigma_1\left(\frac{\partial \tilde{\chi}_1}{\partial r}\frac{\partial C}{\partial r}+(\sigma_1+\tilde{\chi}_1)\frac{\partial^2 C}{\partial r^2}\right), \quad (5.33)$$

Electroosmotic Equation:

$$\frac{\partial^2 \Phi}{\partial r^2}+\frac{1}{r}\frac{\partial \Phi}{\partial r} = {q_e}^2\Phi. \quad (5.34)$$

Here, Reynold's viscosity model [129] has been utilised to illustrate the temperature-dependent viscosity. The model is expressed as follows:

$$\mu_{bf}(T) = \mu_f e^{-\beta_0 T} = \mu_f[1-\beta_0 T] \text{ where } \beta_0 << 1 \quad (5.35)$$

Upon substituting dimensionless variables in equation (5.28), the resulting modified equation for the pressure gradient can be formulated as follows:

$$-\frac{\partial p}{\partial z} = B_1[1+e\cos(c_1 t)], \quad (5.36)$$

where

$$e = \frac{A_1}{A_0}, \quad B_1 = \frac{A_0 R_0^2}{\mu_f U_0}, \quad c_1 = \frac{2\pi R_0 f_p}{U_0}.$$

Upon applying non-dimensional values to the body acceleration Eqn (5.22), the terms $B_2 = \frac{A_0 R_0^2}{\mu_f U_0}$ and $c_2 = \frac{w_q R_0}{U_0}$ has taken the following form. The resulting form of the equation, by removing the bars, is as follows.

$$G(t) = B_2\cos(c_2 t+\psi), t > 0 \quad (5.37)$$

The dimensionless form of the stenosis geometry is expressed as follows:

$$\hat{R}_1^*(z) = \begin{cases} 1, & 0 < z \leq d \\ 1 + A^*, & d < z \leq d+2 \\ 1, & d+2 < z \leq z_1, \\ 1 + r_1 - \sqrt{\left(r_1^2 - (z-z_1)^2\right)}, & z_1 < z \leq z_2, \\ 2r_0 \sec\eta_1 + \left(z - z_2\right)\tan\eta_1, & z_2 < z \leq z_5, \\ 2r_0 \sec\eta_1 + \left(z - z_2\right)\tan\eta_1 - B^*, & z_5 < z \leq z_5 + 1, \\ 2r_0 \sec\eta_1 + \left(z - z_2\right)\tan\eta_1, & z_5 + 1 < z \leq z_{max}, \end{cases} \tag{5.38}$$

where,

$$A^* = 2\delta_1 \left\{ \cos\left(2\pi\left(\frac{z-d}{4}\right) - 0.25\right) - 0.07\cos\left(128\pi\left(z - d - 0.5\right)\right)\right\}\tan(\eta_1),$$

$$B^* = \frac{6\delta}{5}(11(z-z_5) - 47(z-z_5)^2 + 72(z-z_5)^3 - 36(z-z_5)^4)$$

The inner wall is represent as:

$$\hat{R}_2^*(z) = \begin{cases} 0, & 0 < z \leq z_3, \\ \sqrt{\tilde{r}_1^{*2} - \left((z-z_3)) - \tilde{r}_1^*\right)^2}, & z_3 < z \leq z_4, \\ (z-z_2)\tan\eta_1, & z_4 < z \leq z_{max}. \end{cases} \tag{5.39}$$

The lateral junction curvature r_1 and the flow divider radius $\tilde{r}_1$ in the dimensionless form (after ignoring bars) are given as:

$$r_1 = \frac{1 - 2r_0 \sec\eta_1}{\cos\eta_1 - 1}, \tag{5.40}$$

$$\tilde{r}_1^* = \frac{(z_3 - z_2)\sin\eta_1}{(1 - \sin\eta_1)}, \tag{5.41}$$

where z_2, z_3 and z_4 in the dimensionless form are specified as:

$$z_2 = z_1 + r_1 \sin\eta_1, \tag{5.42}$$

$$z_3 = z_2 + q_1, \tag{5.43}$$

and

$$z_4 = z_3 + \tilde{r}_1^*(1-\sin\eta_1). \tag{5.44}$$

5.2.3 Radial Coordinate Transformation

In order to obtain a rectangular domain, it is necessary to apply the transformation $\left(x_1 = \frac{r-\hat{R}_2^*(z)}{R(z)}\right)$ to the geometry under consideration. Upon implementation of the aforementioned transformation, the equations denoted by (5.30) through (5.34) undergo a modification as follows:

$$Re\frac{\rho_{thnf}}{\rho_f}\frac{\partial w}{\partial t} = B_1[1+e\cos(c_1 t)] + \frac{1}{2}\left(\frac{1-\beta_0 T}{(1-\phi_1)^{2.5}(1-\phi_2)^{2.5}(1-\phi_3)^{2.5}}\right)\left(1+\frac{1}{\beta_1}\right)\left[\frac{1}{R^2}\frac{\partial^2 w}{\partial x_1^2} + \left(\frac{1}{x_1 R+R_2}\right)\left(\frac{1}{R}\frac{\partial w}{\partial x_1}\right)\right] - \frac{\beta_0}{2R^2((1-\phi_1)^{2.5}(1-\phi_2)^{2.5}(1-\phi_3)^{2.5})}\frac{\partial w}{\partial x_1}\frac{\partial T}{\partial x_1} + \frac{(\rho\beta)_{thnf}}{(\rho\beta)_f}\left[GrT + Gc\tilde{\phi} - Rb\tilde{\chi}_1\right]\cos(\eta_1\delta_{ij}) + U_{hs}q_e^2\Phi - \frac{\sigma_{thnf}}{\sigma_f}M^2 w + G(t), \tag{5.45}$$

$$\frac{(\rho C_p)_{thnf}}{(\rho C_p)_f}\frac{\partial T}{\partial t} = \frac{1}{RePr}\frac{k_{thnf}}{k_f}\left[\frac{1}{R^2}\frac{\partial^2 T}{\partial x_1^2} + \left(\frac{1}{x_1 R+R_2}\right)\left(\frac{1}{R}\frac{\partial T}{\partial x_1}\right)\right] + \frac{\sigma_{thnf}}{\sigma_f}\left[\frac{EcM^2}{Re}w^2 + \frac{S_z+\tilde{Q}}{RePr}\right] + \frac{1}{R^2}\left(\frac{1-\beta_0 T}{(1-\phi_1)^{2.5}(1-\phi_2)^{2.5}(1-\phi_3)^{2.5}}\right)\left(1+\frac{1}{\beta_1}\right)\frac{Ec}{Re}\left[\left(\frac{\partial w}{\partial x_1}\right)^2\right], \tag{5.46}$$

$$ReSc\frac{\partial C}{\partial t} = \frac{1}{R^2}\frac{\partial^2 C}{\partial x_1^2} + \left(\frac{1}{x_1 R+R_2}\right)\frac{1}{R}\frac{\partial C}{\partial x_1} - Sc\xi C, \tag{5.47}$$

$$ReSb\frac{\partial \tilde{\chi}_1}{\partial t} = \frac{1}{R^2}\frac{\partial^2 \tilde{\chi}_1}{\partial x_1^2} + \left(\frac{1}{x_1 R+R_2}\right)\frac{1}{R}\frac{\partial \tilde{\chi}_1}{\partial x_1} - \frac{Pe\sigma_1}{R^2}\left(\frac{\partial \tilde{\chi}_1}{\partial x_1}\frac{\partial C}{\partial x_1} + (\sigma_1+\tilde{\chi}_1)\frac{\partial^2 C}{\partial x_1^2}\right), \tag{5.48}$$

$$\frac{1}{R^2}\frac{\partial^2 \Phi}{\partial x_1^2} + \left(\frac{1}{x_1 R+R_2}\right)\frac{1}{R}\frac{\partial \Phi}{\partial x_1} = {q_e}^2\Phi. \tag{5.49}$$

The boundary conditions specified in equations (5.17) and (5.20) have been reduced in the following manner:

$$w=0,\ \ T=1,\ \ C=1,\ \ \tilde{\chi}_1=1,\ \ \text{at}\ \ x_1=1 \qquad \text{for all} \quad z, \tag{5.50}$$

$$\frac{\partial w}{\partial x_1}=0,\ \ \frac{\partial T}{\partial x_1}=0,\ \ \frac{\partial C}{\partial x_1}=0,\ \ \frac{\partial \tilde{\chi}_1}{\partial x_1}=0\ \text{ at }\ x_1=0 \quad \text{for} \quad 0\le z\le z_3, \tag{5.51}$$

$$w=0,\ \ T=1,\ \ C=1,\ \ \tilde{\chi}_1=1,\ \text{ at }\ x_1=0 \quad \text{for} \quad z_3\le z\le z_{max}. \tag{5.52}$$

The wall shear stress at the outer wall of the bifurcated artery is given as below:

$$\tau_w=-\frac{1}{R}\left(\frac{\partial w}{\partial x_1}\right)_{x_1=1}, \tag{5.53}$$

The flow rate for the parent artery and daughter artery is defined as follows:

$$Q_d^f=2\pi R\int_0^1 w(x_1R+R_2)dx_1. \tag{5.54}$$

$$Q_p^f=\pi R\int_0^1 w(x_1R+R_2)dx_1. \tag{5.55}$$

The resistance impedance for the the parent artery and daughter artery is given by:

$$\lambda_p=\left|\frac{z_3\left(-\frac{\partial p}{\partial z}\right)}{Q_p^f}\right|, \quad \text{for} \quad z<z_3, \tag{5.56}$$

$$\lambda_d=\left|\frac{(z_{max}-z_3)\left(-\frac{\partial p}{\partial z}\right)}{Q_d^f}\right|, \quad \text{for} \quad z\ge z_3. \tag{5.57}$$

The Nusselt number at the outer wall of the bifurcated artery is computed as follows:

$$Nu_x=-\frac{1}{R}\left(\frac{\partial T}{\partial x_1}\right)_{x_1=1}. \tag{5.58}$$

Similarly, the Sherwood number is given as:

$$Sh_x=-\frac{1}{R}\left(\frac{\partial C}{\partial x_1}\right)_{x_1=1}. \tag{5.59}$$

5.3 Solution Process

It is widely acknowledged that there exist numerous numerical techniques for solving partial differential equations. Among these techniques, the finite difference scheme stands out as a remarkably accessible and efficient approach for solving such equations. We have implemented the Crank-Nicolson scheme to address the partial differential equations (PDEs) at hand. Specifically, we have chosen a step size of Δx in the radial direction while employing a time step of $\Delta t = 0.001$. This selection of parameters has been made to achieve convergence within the numerical scheme. It has been observed that additional variations in the values of Δx and Δt do not yield significant alterations in the outcomes.

5.3.1 Discretization

The governing equations are discretized as:

$$\begin{aligned}
&\left[(1-\phi_3)\left\{(1-\phi_2)\left[(1-\phi_1)+\phi_1\frac{\rho_{s_1}}{\rho_f}\right]+\phi_2\frac{\rho_{s_2}}{\rho_f}\right\}+\phi_3\frac{\rho_{s_3}}{\rho_f}\right]Re\left[\frac{w_i^{k+1}-w_i^k}{dt}\right]=B_1[1+e\cos(c_1t^k)]\\
&\quad+\frac{1}{2}\left\{\frac{1-\beta_0 T}{(1-\phi_1)^{2.5}(1-\phi_2)^{2.5}(1-\phi_3)^{2.5}}\right\}\left(1+\frac{1}{\beta_1}\right)\left[\frac{1}{R^2}\left(\frac{w_{i+1}^{k+1}-2w_i^{k+1}+w_{i-1}^{k+1}}{dx^2}\right.\right.\\
&\quad\left.\left.+\frac{w_{i+1}^{k}-2w_i^{k}+w_{i-1}^{k}}{dx^2}\right)+\frac{1}{R}\frac{1}{Rx_i+R_2}\left(\frac{w_{i+1}^{k+1}-w_{i-1}^{k+1}}{2dx}+\frac{w_{i+1}^{k}-w_{i-1}^{k}}{2dx}\right)\right]\\
&-\frac{1}{2R^2}\left\{\frac{\beta_0}{(1-\phi_1)^{2.5}(1-\phi_2)^{2.5}(1-\phi_3)^{2.5}}\right\}\left(1+\frac{1}{\beta_1}\right)\left[\left(\frac{w_{i+1}^{k+1}-w_{i-1}^{k+1}}{2dx}+\frac{w_{i+1}^{k}-w_{i-1}^{k}}{2dx}\right)\right.\\
&\quad\left.\left(\frac{T_{i+1}^k-T_{i-1}^k}{2dx}\right)\right]+U_{hs}q_e^2\Phi+F_b\cos(c_2t_k+\psi)\\
&\quad+\left[(1-\phi_3)\left\{(1-\phi_2)\left((1-\phi_1)+\phi_1\frac{(\rho\beta)_{s1}}{(\rho\beta)_f}\right)+\phi_2\frac{(\rho\beta)_{s_2}}{(\rho\beta)_f}\right\}+\phi_3\frac{(\rho\beta)_{s_3}}{(\rho\beta)_f}\right]\\
&\quad\left(GrT_i^k+GcC_i^k-Rb\tilde{\chi}_{1i}^{\,k}\right)\cos(\eta_1\delta_{ij})-\frac{1}{2}\frac{\sigma_{nf}}{\sigma_f}M^2(w_i^k+w_i^{k+1}) \quad (5.60)
\end{aligned}$$

$$\left[(1-\phi_3)\left\{(1-\phi_2)\left\{(1-\phi_1)+\phi_1\frac{(\rho C_p)_{s_1}}{(\rho C_p)_f}\right\}+\phi_2\frac{(\rho C_p)_{s_2}}{(\rho C_p)_f}\right\}+\phi_3\frac{(\rho C_p)_{s_3}}{(\rho C_p)_f}\right]\left[\frac{T_i^{k+1}-T_i^k}{dt}\right]=\frac{1}{RePr}$$
$$\frac{k_{thnf}}{k_f}\left[\frac{1}{2R^2}\left(\frac{T_{i+1}^{k+1}-2T_i^{k+1}+T_{i-1}^{k+1}}{dx^2}+\frac{T_{i+1}^{k}-2T_i^{k}+T_{i-1}^{k}}{dx^2}\right)+\frac{1}{2(Rx_i+R_2)}\left(\frac{T_{i+1}^{k+1}-T_{i-1}^{k+1}}{2dx}\right.\right.$$
$$\left.\left.+\frac{T_{i+1}^{k}-T_{i-1}^{k}}{2dx}\right)\right]+\frac{1}{R^2}\left\{\frac{1-\frac{\beta_0}{2}(T_i^{k+1}+T_i^k)}{(1-\phi_1)^{2.5}(1-\phi_2)^{2.5}(1-\phi_3)^{2.5}}\right\}\left(1+\frac{1}{\beta_1}\right)\frac{Ec}{Re}\left[\frac{1}{2}\left(\frac{w_{i+1}^{k+1}-w_{i-1}^{k+1}}{2dx}\right.\right.$$
$$\left.\left.+\frac{w_{i+1}^{k}-w_{i-1}^{k}}{2dx}\right)\right]^2+\frac{\sigma_{thnf}}{\sigma_f}\left[\left(\frac{1}{2}\frac{EcM^2}{Re}\left(w_i^{k+1}+w_i^k\right)\right)^2+\frac{S_z+\tilde{Q}}{RePr}\right]. \quad (5.61)$$

$$ReSc\left[\frac{C_i^{k+1}-C_i^k}{dt}\right]=\left[\frac{1}{2R^2}\left(\frac{C_{i+1}^{k+1}-2C_i^{k+1}+C_{i-1}^{k+1}}{dx^2}+\frac{C_{i+1}^{k}-2C_i^{k}+C_{i-1}^{k}}{dx^2}\right)+\frac{1}{2(Rx_i+R_2)}\right.$$
$$\left.\left(\frac{C_{i+1}^{k+1}-C_{i-1}^{k+1}}{2dx}+\frac{C_{i+1}^{k}-C_{i-1}^{k}}{2dx}\right)\right]-\frac{Sc\xi}{2}\left[C_i^{k+1}+C_i^k\right] \quad (5.62)$$

$$ReSb\left[\frac{\tilde{\chi}_{1_i}^{k+1}-\tilde{\chi}_{1_i}^{k}}{dt}\right]=\left[\frac{1}{2R^2}\left(\frac{\tilde{\chi}_{1_{i+1}}^{k+1}-2\tilde{\chi}_{1_i}^{k+1}+\tilde{\chi}_{1_{i-1}}^{k+1}}{dx^2}+\frac{\tilde{\chi}_{1_{i+1}}^{k}-2\tilde{\chi}_{1_i}^{k}+\tilde{\chi}_{1_{i-1}}^{k}}{dx^2}\right)\right.$$
$$\left.+\frac{1}{2(Rx_i+R_2)}\left(\frac{\tilde{\chi}_{1_{i+1}}^{k+1}-\tilde{\chi}_{1_{i-1}}^{k+1}}{2dx}+\frac{C_{i+1}^{k}-C_{i-1}^{k}}{2dx}\right)\right]-\frac{Pe\sigma_1}{2}\left[\left\{\frac{\tilde{\chi}_{1_{i+1}}^{k+1}+\tilde{\chi}_{1_{i-1}}^{k+1}}{2dx}+\frac{\tilde{\chi}_{1_{i+1}}^{k}+\tilde{\chi}_{1_{i-1}}^{k}}{2dx}\right\}\right.$$
$$\left.\left(\frac{C_{i+1}^{k}-C_{i-1}^{k}}{2dx}\right)+\left\{\sigma_1+\frac{\tilde{\chi}_{1_i}^{k+1}+\tilde{\chi}_{1_i}^{k}}{2}\right\}\left(\frac{C_{i+1}^{k}-2C_i^{k}-C_{i-1}^{k}}{dx^2}\right)\right] \quad (5.63)$$

$$\frac{\Phi_{i+1}-2\Phi_i+\Phi_{i-1}}{dx^2}+\frac{1}{(Rx_i+R_2)}\left\{\frac{\Phi_{i+1}-\Phi_{i-1}}{2dx}\right\}=q_e^2\Phi_i \quad (5.64)$$

The discretized governing equations (5.60) and (5.64) are then converted to a tri-diagonal system of equations and solved using Tri-Diagonal Matrix Algorithm (TDMA).

5.4 Entropy Generation

Entropy is a measure used to quantify the degree of irreversibility present in a given system. The concept of entropy is closely associated with changes occurring within a system due to the transfer of mass and thermal energy. The precise definition of dimensional entropy generation is as follows:

$$E_g = \underbrace{\frac{k_f}{\tilde{T}_1^{*2}}\left(\frac{k_{thnf}}{k_f}\right)\left(\frac{\partial \tilde{T}}{\partial \tilde{r}}\right)^2}_{\text{Thermal irreversibility}} + \underbrace{\frac{\mu_{thnf}}{\tilde{T}_1^*}\left(1+\frac{1}{\beta_1}\right)\left(\frac{\partial \tilde{w}}{\partial \tilde{r}}\right)^2}_{\text{Viscous irreversibility}} + \underbrace{\frac{\sigma_{thnf}}{\tilde{T}_1^*}(B_0\tilde{w}^2+E_0^2)}_{\text{Joule heating irreversibility}} + \underbrace{\frac{D_B}{\tilde{C}_1}\left(\frac{\partial \tilde{C}}{\partial \tilde{r}}\right)^2}_{\text{Solute irreversibility}} \tag{5.65}$$

The dimensionless variables mentioned in Equation (5.28) are substituted in Equation (5.65) to obtain:

$$E_g = \frac{k_f}{\tilde{T}_0^2}\frac{(\tilde{T}_w-\tilde{T}_0)^2}{R_0^2}\left(\frac{k_{thnf}}{k_f}\right)\left(\frac{\partial T}{\partial r}\right)^2 + \frac{\mu_{thnf}U_0^2}{\tilde{T}_0 R_0^2}\left(1+\frac{1}{\beta_1}\right)\left(\frac{\partial w}{\partial r}\right)^2 + \frac{\sigma_{thnf}R_0^2}{\tilde{T}_0}(U_0B_0w^2+E_0^2) + \frac{D_b}{\tilde{C}_0}\left(\frac{(\tilde{C}_w-\tilde{C}_0)}{R_0}\right)^2\left(\frac{\partial C}{\partial r}\right)^2 \tag{5.66}$$

The non-dimensional form of entropy generation number is defined as $N_s = \frac{\tilde{T}_0^2 R_0^2}{k_f(\tilde{T}_w-\tilde{T}_0)^2}E_g$. Then on using Equation (5.66), we have:

$$N_s = \left(\frac{k_{thnf}}{k_f}\right)\left(\frac{\partial T}{\partial r}\right)^2 + \frac{\mu_{thnf}}{\mu_f}\left(1+\frac{1}{\beta_1}\right)\frac{Br}{\Omega}\left(\frac{\partial w}{\partial r}\right)^2 + \frac{\sigma_{thnf}}{\sigma_f}\frac{M^2Br}{\Omega}(w^2+E_1^2) + \frac{\Lambda\Gamma}{\Omega}\left(\frac{\partial C}{\partial r}\right)^2 \tag{5.67}$$

On employing coordinate transformation as defined earlier, the expression for entropy generation is:

$$N_s = \left(\frac{k_{thnf}}{k_f}\right)\left(\frac{1}{R^2}\right)\left(\frac{\partial T}{\partial x_1}\right)^2 + \frac{\mu_{thnf}}{\mu_f}\left(1+\frac{1}{\beta_1}\right)\frac{Br}{\Omega}\left(\frac{1}{R^2}\right)\left(\frac{\partial w}{\partial x_1}\right)^2 + \frac{\sigma_{thnf}}{\sigma_f}\frac{M^2Br}{\Omega}(w^2+E_1^2) + \frac{\Lambda\Gamma}{\Omega}\left(\frac{1}{R^2}\right)\left(\frac{\partial C}{\partial x_1}\right)^2 \tag{5.68}$$

The mathematical expression for Bejan number is given as:

$$Be = \frac{N}{N_s}, \tag{5.69}$$

where, $N = \left(\frac{k_{thnf}}{k_f}\right)\left(\frac{1}{R^2}\right)\left(\frac{\partial T}{\partial x_1}\right)^2$.

Thermophysical Properties	Blood	Au	CuO	GO
Density $[\rho(kg/m^3)]$	1060	19320	6500	1800
Thermal Conductivity [K(W/mK)]	0.492	314	18	5000
Electrical Conductivity $[\sigma(S/m)]$	0.667	4.10×10^7	1×10^{-10}	6.3×10^7
Thermal Expansion Coefficient $[\beta \times 10^{-5}(K^{-1})]$	0.18	1.4	0.5	28.4
Heat Capacitance $[C_p(J/kgK)]$	3770	129	540	717

Table 5.1: Thermophysical properties of nanoparticles

Parameters	Values	Refrences
Magnetic field (M^2)	0-5	[106, 112]
Grashof number (Gr)	0-5	[108]
Prandtl number (Pr)	14-25	[130]
Casson fluid parameter (β_1)	0.1-10	[155]
Rayleigh number (Rb)	0-6	[1, 125]

Table 5.2: Default values of emerging parameters with their sources

5.5 Results and Graphical Analysis

This section illustrates the influence of different parameters on the hemodynaimc flow through a bifurcated artery. The Crank-Nicolson scheme is employed to discretize the governing equations and MATLAB code is developed to perform full investigation of the pertinent parameters on the velocity, temperature, concentration, microorganisms, flow rate, Nusselt and Sherwood profile. The thermophysical parameters and properties of nanofluid and the nanoparticles are shown in Tables 4.1 and 5.1, respectively. Table 5.2 shows the possible values explored for the different flow parameters with their sources.

5.5.1 Validation

The validation of this work is accomplished through a comparison with the published study conducted by Tripathi et al. [100]. The Crank-Nicolson technique, a finite difference methodology, is employed in this study to solve the governing equations, while Tripathi et al. [100] used the FTCS scheme. By analyzing the impact of various pertinent parameters, including the Solutal Grashof number ($Gc = 0$), Rayleigh number ($Rb = 0$), magnetic field parameter ($M = 0$), Debye-Huckel parameter ($q = 0$), heat source ($Q = 0$), Eckert number ($Ec = 0$), Joule heating parameter ($S_z = 0$), and considering the inner wall ($R_2(z) = 0$), a comparison is made between the present study and the previous work [100]. The velocity and temperature profiles for pure blood (without the presence of nanoparticles) are depicted

in Figures 5.2 and 5.3, respectively. The graphical representations demonstrate a high degree of agreement between this study and the prior research by Tripathi et al. [100] for the velocity and temperature profiles.

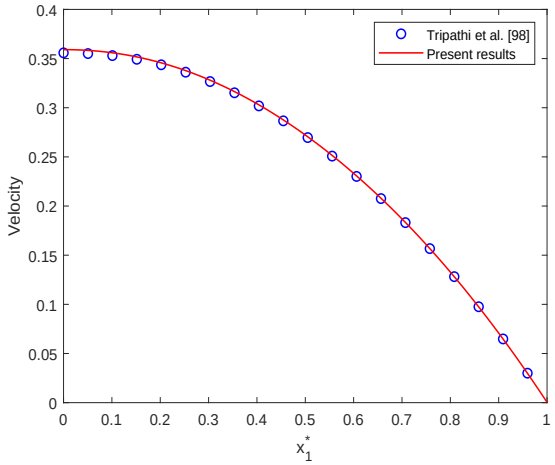

Figure 5.2: Velocity profile for pure blood

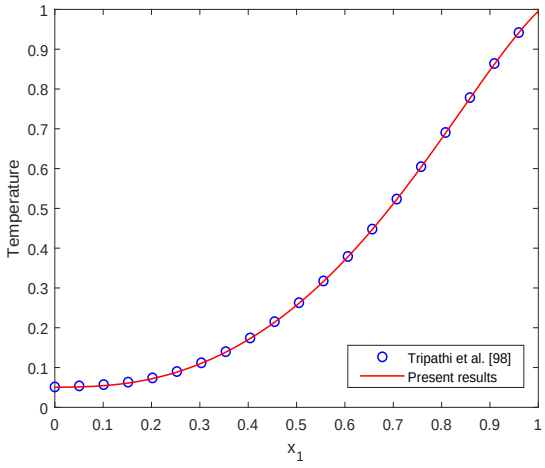

Figure 5.3: Temperature profile for pure blood

5.5.2 Velocity Profile

The influence of a magnetic field on fluid velocity is particularly noteworthy in the case of electrically conductive fluids. The observed phenomenon under discussion is commonly referred to as MHD.

It encompasses the intricate interplay between magnetic fields and the dynamic behaviour of conductive fluids. In the realm of MHD, the motion of the fluid is subject to the influence of the Lorentz force. This force emerges as a consequence of the interplay between the magnetic field and the electrically charged particles present within the fluid. The Lorentz force has the potential to serve as an additional force that either propels or hinders the fluid, thereby modifying its velocity profile. Figure 5.4a depicts the influence of magnetic field parameter on the velocity profile in both parent and daughter artery. The comparisional study has been performed to show the velocity distribution in both Au-CuO hybrid nanofluid and Au-CuO-GO ternary hybrid nanofluid. It can be observed from the figure that the velocity enhances in the ternary hybrid nanofluid as compared to hybrid nanofluid. The fluid velocity declines as the magnetic field parameter enhances due to the resisitive Lorentz force which resists the fluid motion and depicts the declining nature for the velocity profile. The drag force experienced by an object moving through a fluid can be described as directly proportional to several key factors, namely the velocity of the fluid, the strength of the magnetic field, and the electrical conductivity of the fluid. The fluid velocity enhances as

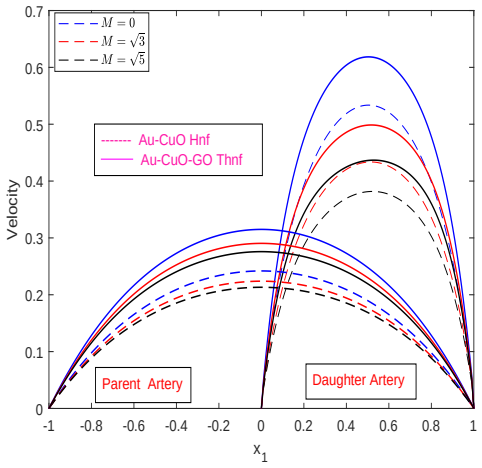

(a) Velocity profile by varying M

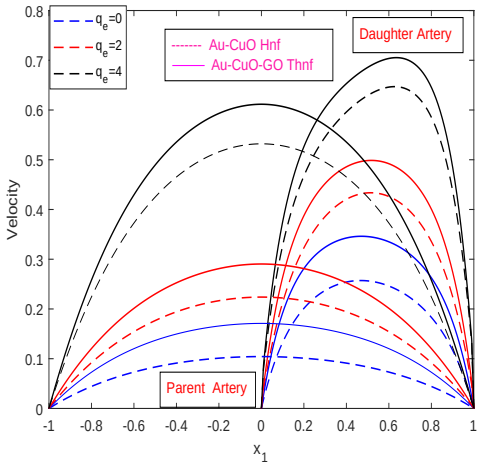

(b) Velocity profile by varying q_e

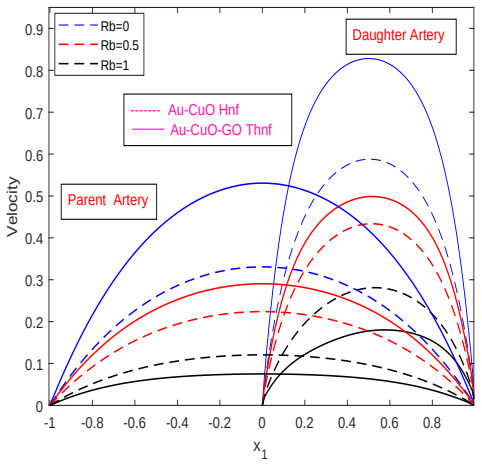

(c) Velocity profile by varying Rb

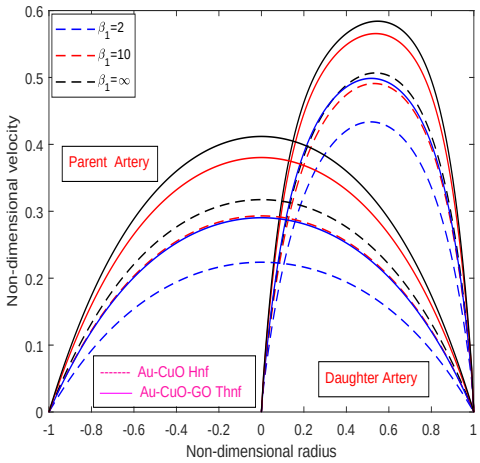

(d) Velocity profile by varying Casson fluid parameter

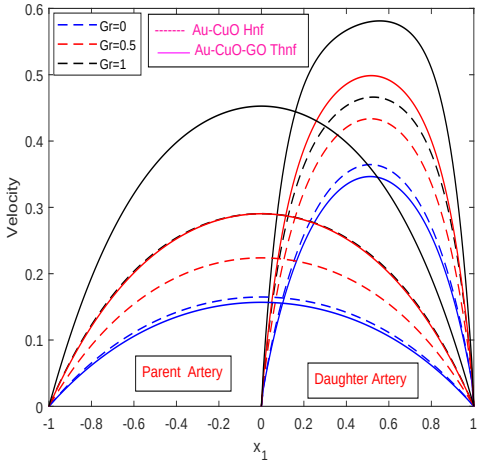

(e) Velocity profile by Grashof number Gr

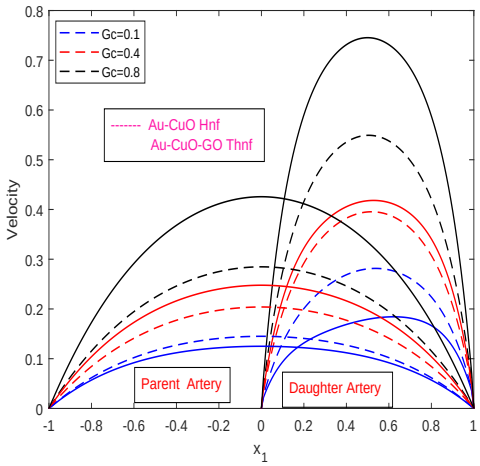

(f) Velocity profile by varying solutal Grashof number

Figure 5.4: Velocity profile

the Debye-Hückel parameter enhaces from $q_e = 0$ to $q_e = 2$ as depicted in figure 5.4b. The Debye-Hückel parameter, denoted as q_e, is a dimensionless parameter widely employed in scientific research to elucidate the impact of ionic strength on the behaviour of charged particles within a given solution. When the Debye-Hückel parameter is observed to increase, it signifies a higher concentration of charged particles within the solution. Consequently, this leads to an augmentation in the electric conductivity of the fluid, as a larger number of ions become available to facilitate the conduction of electric current. The modification of intermolecular forces has the potential to exert an impact on the flow characteristics of the fluid, potentially resulting in an augmentation of its velocity. Bioconvection is a phenomenon characterised by the coordinated movement of microorganisms or biological particles, leading to the emergence of well-organised patterns or structures in a fluid medium. The occurrence of this phenomenon is frequently documented in microbial suspensions or ecosystems, wherein the existence of motile microorganisms instigates the formation of convective flow patterns. The fundamental mechanism underlying bioconvection is predicated upon the intricate interplay between the swimming behaviour of microorganisms and their surrounding fluid environment. The association between the bioconvection Rayleigh number and the momentum equation substantially impacted the velocity profile, as seen in Figure 5.4c. The increase in the Rayleigh number strengthens the microorganism's convection, which works against the buoyancy force acting on the fluid particles. This results in a decrement in the velocity profile. The effect of Casson fluid parameter is depicted in the figure 5.4d. It can be observed from the figure that the fluid velocity increases as the Casson fluid parameter enhances from $\beta_1 = 2$ to $\beta_1 = \infty$. The Casson fluid model is a well-established framework within non-Newtonian fluid dynamics. It is specifically designed to capture the unique characteristics of specific fluid systems that demonstrate yield stress behaviour. As the magnitude of the coefficient β_1 tends towards infinity, the observed behaviour will exhibit Newtonian characteristics. The findings of the comparative analysis conducted on Au-CuO/Blood hybrid nanofluid and Au-CuO-GO/Blood ternary hybrid nanofluid indicate that the inclusion of GO nanoparticles in the Au-CuO/Blood solution leads to an enhancement in fluid velocity. The potential utility of this innovation lies in its capacity to enable surgeons and researchers to modulate blood flow within the human body effectively. Blood flow regulation is a complex and multidimensional field of study that encompasses a wide range of applications. Through acquiring an enhanced comprehension of the intricate mechanisms and multifaceted factors implicated in regulating blood flow, researchers endeavour to cultivate groundbreaking interventions to diagnose, treat, and averter a diverse array of cardiovascular and circulatory disorders. This collective pursuit ultimately aspires to ameliorate the overall state of human health and well-being. Figures 5.4e and 5.4f

illustrate the velocity profile under different conditions of the Grashof number and solutal Grashof number, respectively. The Grashof number (Gr), a dimensionless parameter in the field of fluid dynamics, serves as a quantitative measure of the relative significance of buoyancy forces compared to viscous forces within a fluid flow. The utilisation of this method is frequently observed in examining and projecting natural convection phenomena, wherein fluid movement is propelled by variances in density resulting from temperature fluctuations. The Grashof number is a crucial parameter that notably influences natural convection phenomena. The empirical evidence consistently indicates a positive correlation between the fluid velocity and the magnitude of the Grashof number. As the Grashof number increases, there is an observed increase in flow circulation. This can be attributed to the prevailing influence of buoyancy forces over viscous forces. It is imperative to acknowledge that the precise correlation between the Grashof number and the velocity profile is contingent upon the particular geometric configuration, boundary conditions, and fluid characteristics inherent to the given system. The comprehensive examination of velocity profiles in complex scenarios necessitates the utilisation of numerical simulations or experimental inquiries specifically designed to address the unique characteristics of the given situation. Similarly, when the solutal Grashof number increases, it signifies an escalation in the magnitude of buoyancy-driven convection owing to amplified disparities in solute concentration. In the domain of fluid dynamics, it is worth noting that an augmentation in the solutal Grashof number can induce alterations in the velocity profile. Buoyancy-driven convection is a phenomenon characterised by the fluid motion that emerges due to density variations induced by concentration differences. As the solutal Grashof number experiences an increase, it is observed that the buoyancy force exhibits a heightened strength in comparison to the viscous forces. This phenomenon subsequently results in a more prominent convective flow pattern, as visually represented in figure 5.4f.

5.5.3 Temperature, Concentration & Microorganisms Profile

The impact of the Prandtl number (Pr) on the temperature profile is visually depicted in figure 5.5a. The Prandtl number, a frequently used dimensionless parameter in fluid mechanics, evaluates the relative importance of momentum diffusivity (viscosity) and thermal diffusivity (thermal conductivity) within a fluid. A higher Prandtl number indicates a scenario where thermal diffusivity assumes a more prominent role than momentum diffusivity. In alternative terms, the fluid exhibits a higher degree of effectiveness in facilitating heat conduction than momentum transfer. The manifestation of this particular attribute becomes apparent upon scrutinising the temperature distribution of the fluid. As depicted in figure 5.5a, it can be observed that there is a decrement in temperature profile as the magnitude of

Prandtl number enhances within the range of 19 to 25. This observation suggests that the fluid exhibits enhanced efficacy in transmitting momentum, a phenomenon primarily driven by its flow or motion, as opposed to its ability to transfer heat. As a result, the temperature gradient, which refers to the rate of temperature change within the fluid, becomes less prominent.

The observed trend in the temperature profile, as depicted in figure 5.5b, indicates the positive correlation between the heat source and the Casson fluid parameter. Specifically, an increase in both factors leads to a rise in the temperature profile. The confluence of the thermal energy source and the augmented Casson fluid parameter synergistically facilitates the enhancement of convective heat transfer. The convection of heat within the fluid is facilitated by the enhanced fluid flow and improved mixing, in addition to the temperature gradient generated by the heat source. In the context of stenosis, the targeted temperature elevation can be accomplished by applying a heat source in the constricted area. Various methods can be employed to achieve this objective, including laser ablation, radiofrequency ablation, and thermal therapy techniques. The primary objective of localised heating is to achieve precise and targeted thermal treatment in the stenotic region while concurrently ensuring the preservation of the structural and functional integrity of the adjacent healthy tissues. Figure 5.5c depicts the influence of nanoparticles shape on the temperature profile. Nanoparticles with intricate or irregular shapes have larger surface areas than simpler ones, facilitating stronger interactions with the surrounding fluid or medium. However, the additional thermal resistance introduced can affect overall thermal performance. The presence of irregularities within the system hinders efficient heat transfer, leading to a decline in the temperature profile. This hindrance is caused by pockets or barriers within complex shapes that impede heat transfer effectiveness. In summary, intricate or irregular-shaped nanoparticles have increased surface area, enhancing interactions with the medium but introducing thermal resistance that affects heat transfer efficiency. The presence of pockets or barriers within complex shapes further impedes heat flow, resulting in a decreased temperature profile. The trend in fluid temperature is directly impacted by the increase in both the Eckert number (Ec) and Joule heating parameter, as shown in figure 5.5d. The Eckert number is a dimensionless parameter that quantifies the correlation between kinetic energy and enthalpy change in fluid flow. When the Eckert number increases, it signifies a higher proportion of kinetic energy relative to the enthalpy change depicting that kinetic energy converted into thermal energy as the Eckert number rises. Consequently, this transformation results in an evident enhancement of the temperature distribution within the fluid. The excess kinetic energy is converted into thermal energy, leading to an overall increase in temperature profile.

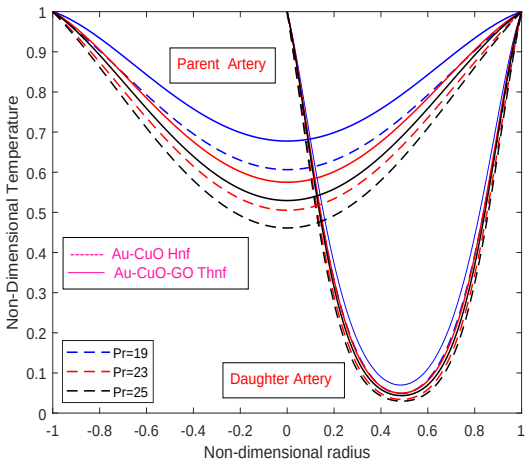

(a) Temperature profile by varying Pr

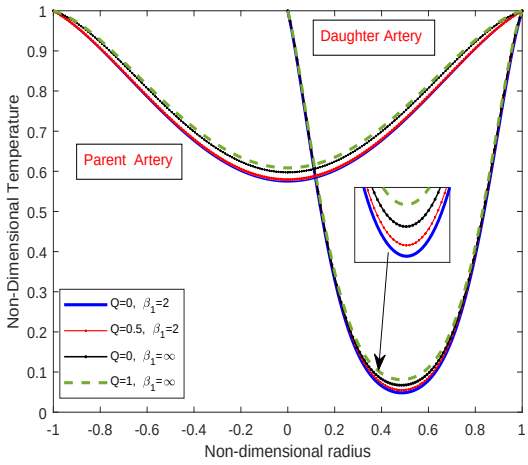

(b) Temperature profile by varying Q and Casson fluid parameter

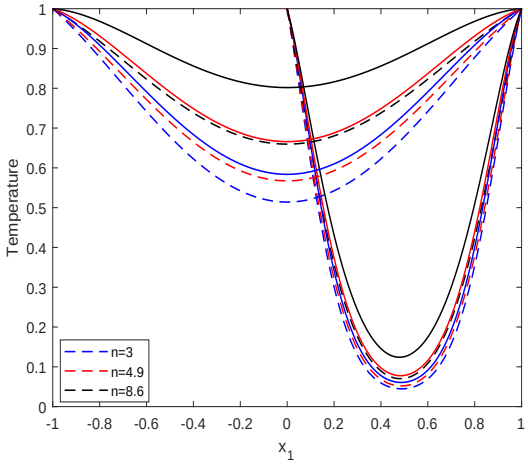

(c) Temperature profile by varying nanopartilces shape

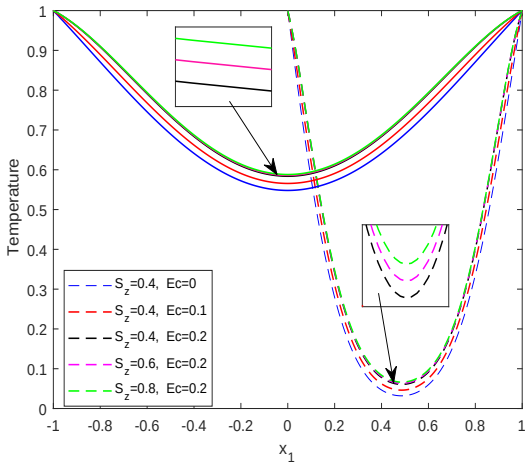

(d) Temperature profile by varying S_z and Ec

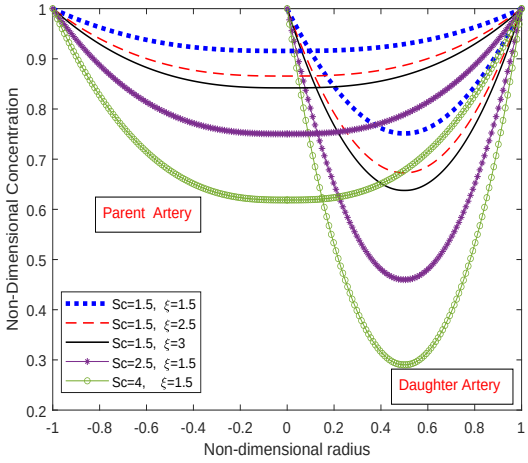

(e) Concentration profile by varying Sc and ξ

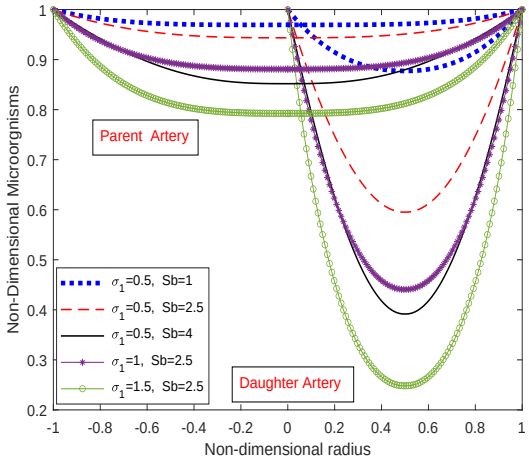

(f) Microorganisms profile by varying Sb and σ_1

Figure 5.5: Temperature, Concentration and Microorganisms profile

The temperature distribution is further influenced by the Joule heating parameter, which takes into account thermal generation. The presence of thermal gradients and variations in the fluid contributes to an appreciable improvement in the temperature profile.

The concentration profile in a fluid is observed to increase as the Schmidt number increases, as depicted in figure 5.5e. The Schmidt number, denoted as Sc, is a dimensionless quantity that characterises the relative importance of momentum diffusivity (kinematic viscosity) to mass diffusivity (molecular diffusivity) in a fluid. The Schmidt number, denoted as Sc, is a dimensionless quantity used in fluid dynamics to characterise the relative rates of mass transfer and momentum transfer in a fluid system. A higher value of Sc indicates that the mass transfer process is comparatively faster than the momentum transfer process. The observed phenomenon indicates that the fluid's capacity for momentum transport via convection or flow is more prominent compared to its capacity for mass or concentration transport. Consequently, the concentration gradient within the fluid experiences a reduction in its steepness, resulting in a decrease observed in the concentration profile. The diminution of the concentration profile becomes apparent as the chemical reaction parameter undergoes augmentation, transitioning from a value of 1.5 to 3. The augmentation of a parameter in a chemical reaction can engender a decline in the concentration profile of specific species. The decline in concentration is a consequence of the heightened reaction rate, which leads to the utilisation of supplementary species. Bioconvection refers to the fluid motion that occurs due to density gradients caused by the collective behaviour of microorganisms. The bioconvective Lewis number is a crucial parameter that quantifies the significance of thermal and mass diffusion processes in a given system. A higher bioconvective Lewis number implies that thermal diffusion is more significant than mass diffusion. In contrast, a lower bioconvective Lewis number indicates a greater significance of mass diffusion than thermal diffusion. The figure 5.5f demonstrates a consistent decrease in density as parameter σ_1 increases. The decrease observed can be explained by an increase in σ_1, resulting in a greater density contrast between the gyrotactic microorganisms and the surrounding fluid medium. The density difference among gyrotactic bacteria leads to a flow reversal, suppressing microorganisms' concentration profile. In contrast, an increase in the bioconvective Lewis number (Sb) reduces the density of motile entities in the fluid. The decrease in density is due to a reduction in the diffusivity process of the microorganisms. The density of microorganisms decreases in both the parent and daughter arteries as Sb and σ_1 increase.

5.5.4 Flow Rate & Impedance Profile

The influence of the Casson fluid parameter on the flow rate profile is depicted in figure 5.6a. The experimental findings indicate that the Casson fluid demonstrates increased resistance

under low shear rates. However, once the critical shear rate is attained, its behaviour starts to resemble that of a Newtonian fluid. The observed transition is concomitant with a notable reduction in the apparent viscosity, leading to a corresponding augmentation in the flow rate, as visually depicted in Figure 5.6a. The parameter β_1, known as the Casson fluid parameter, exhibits a range of values from 2, which signifies non-Newtonian behaviour, to $\beta_1 \to \infty$, indicating a Newtonian fluid. This parameter directly impacts the flow rate profile, increasing its magnitude.

The bifurcation angle refers to the angle of division at which a blood vessel or pipe separates into multiple branches. It has a notable impact on the flow characteristics in the bifurcation system. Understanding and analysing fluid dynamics in branching systems necessitates thoroughly considering this crucial aspect. Figure 5.6b presents a graphical representation of the influence of the bifurcation angle on the flow rate. The figure suggests that the flow rate also increases as the bifurcation angle increases from $\eta_1 = \pi/12$ to $\eta_1 = \pi/6$. The aforementioned observation suggests a direct correlation between modifications in the bifurcation angle and the resultant flow rate. Upon conducting a more comprehensive examination, it has been ascertained that the flow rate profile exhibits a sustained level of consistency within the parent artery. However, notable fluctuations in the flow characteristics become apparent subsequent to the occurrence of bifurcation. In accordance with the fundamental principle of conservation of mass, it is imperative to ensure that the volume of flow originating from the parent artery remains constant as it is distributed among the daughter arteries. As a result, it can be observed that the cross-sectional area of the daughter arteries exhibits an increase in proportion to the increment of the bifurcation angle. The observed phenomenon of increased flow rate profile can be attributed to the expansion in the cross-sectional area, which occurs in conjunction with an increase in the bifurcation angle. Hence, it is imperative to acknowledge the significant influence exerted by the bifurcation angle on the intricate interplay of flow dynamics and the subsequent dispersion of flow throughout the branching network. The impact of the Grashof number (Gr) on the flow rate profile is visually depicted in figure 5.6c. The observed phenomenon can be ascribed to the relatively prevailing impact of buoyancy forces in relation to viscous forces. Consequently, with an increase in the Grashof number (Gr), the resultant temperature variation initiates density disparities, which act as propelling factors and enhance the flow rate distribution, as depicted in figure 5.6c. The exploration of employing a magnetic field within a constricted artery to study the kinetics of blood flow and the characteristics of magnetic particles within the circulatory system is a crucial topic in the research field. Blood is a complex mixture of different components, one of which is haemoglobin.

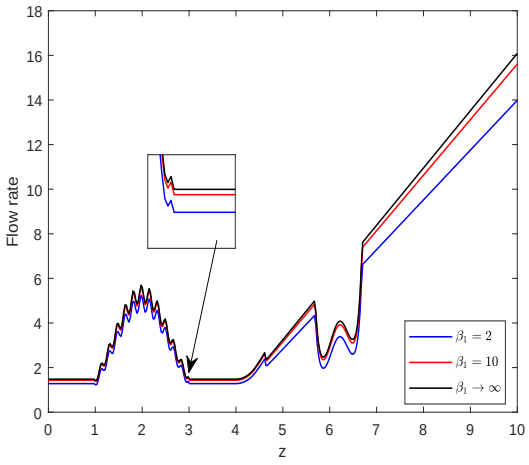

(a) Flow rate by varying β_1

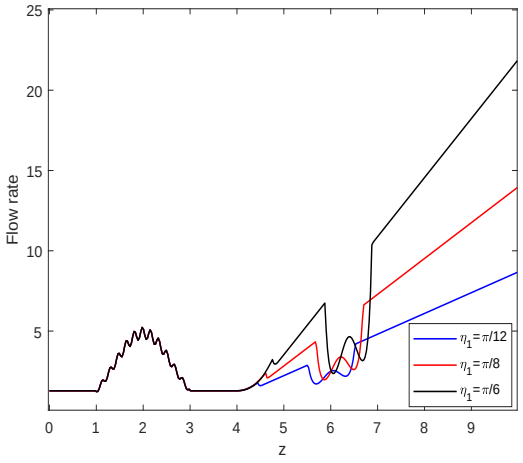

(b) Flow rate by varying η_1

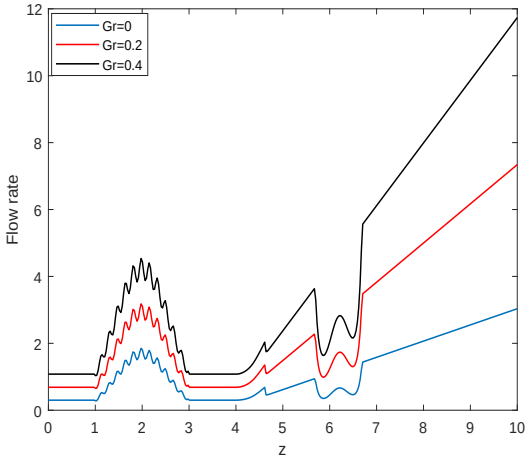

(c) Flow rate by varying Gr

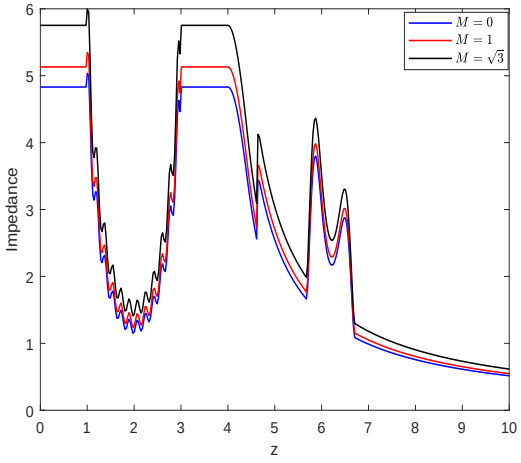

(d) Impedance profile by varying M

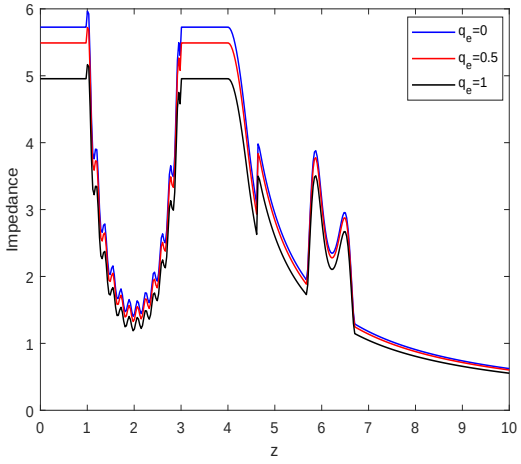

(e) Impedance profile by varying q_e

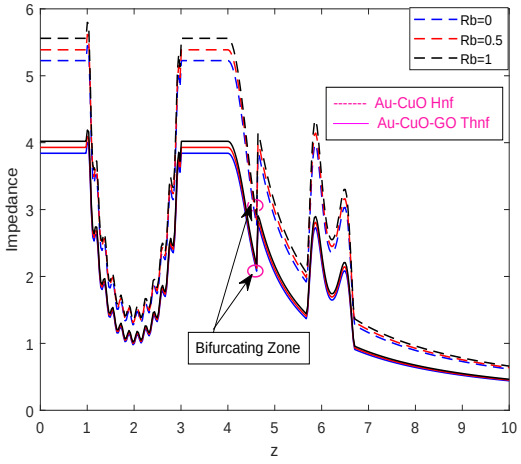

(f) Impedance profile by varying Rb

Figure 5.6: Flow rate and impedance profile

Haemoglobin exhibits properties similar to those of small magnetic particles and is susceptible to the influence of magnetic fields. The impedance profile illustrated in figure 5.6d portrays the impact of altering the magnetic field parameter. Upon careful examination of the provided figure, it is evident that the impedance profile exhibits a noticeable augmentation as the magnetic field parameter number progressively escalates from $M = 0$ to $M = \sqrt{3}$. Clearly, the observed phenomenon can be ascribed to the manifestation of the Lorentz force exerted by the magnetic field upon the conductive fluid. The counteracting force exerted by the Lorentz force contributes to an increased level of resistance and elevates the impedance profile within a stenosis. The impact of the Debye-Huckel parameter on the impedance profile illustrated in figure 5.6e is being examined. The impedance profile exhibits a negative correlation with the Debye-Huckel parameter, as the latter experience an increase. This phenomenon can be attributed to amplifying the screening effect within the solution. The observed increase in the screening effect results in a reduction of the strength of interactions between the charged particles, ultimately causing a decrease in the impedance profile. The illustration presented in figure 5.6f showcases the influence of Rb on the impedance characteristics while conducting a comparative analysis between the hybrid nanofluid composed of Au-CuO and blood and the ternary hybrid nanofluid consisting of Au-CuO-GO and blood. The figure reveals the increment in the impedance profile as the magnitude of Rb enhances from 0 to 1. The augmentation of the Rayleigh number amplifies the convective behaviour of the microorganism, thereby counteracting the buoyancy force exerted on the fluid particles. The observed outcome leads to a reduction in the velocity profile. Hence, the resistance encountered by the blood flow is heightened, escalating the impedance profile.

5.5.5 WSS, Nusselt & Sherwood Number

The investigation of wall shear stress (WSS) is essential in comprehending the hemodynamic flow dynamics and pathological manifestations of stenosis. The endothelium, which refers to the cellular layer lining the interior of blood vessels, is commonly impacted by WSS. The endothelial cells are subjected to and react to the mechanical forces exerted by the blood flow, such as WSS. The presence of an aberrant WSS induces endothelial dysfunction, thereby facilitating the development of atherosclerotic plaque. Therefore, it is imperative to investigate the impact of WSS on the hemodynamics of blood flow. Figure 5.7a illustrates the effects of the magnetic field parameter on the wall shear stress (WSS) profile. Evidently, the observed phenomenon demonstrates a decrease in the WSS profile as the magnetic field strength is increased.

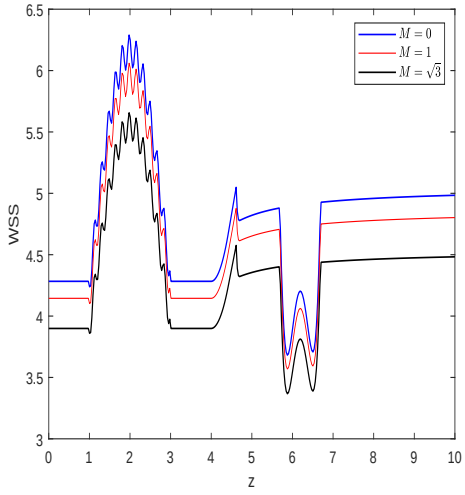

(a) WSS profile by varying M

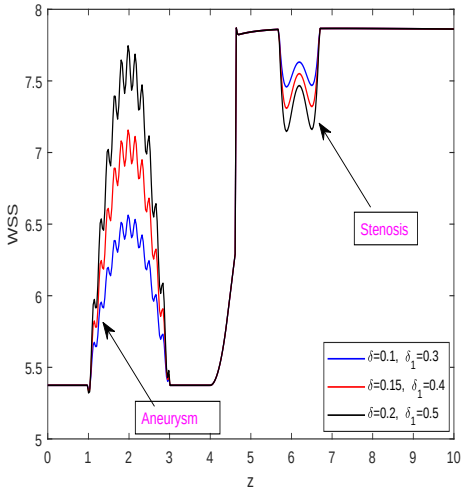

(b) WSS profile by varying stenotic depth and aneurysm height

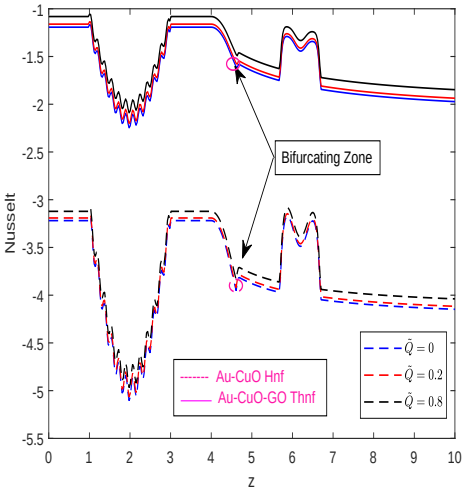

(c) Nusselt profile by varying Q

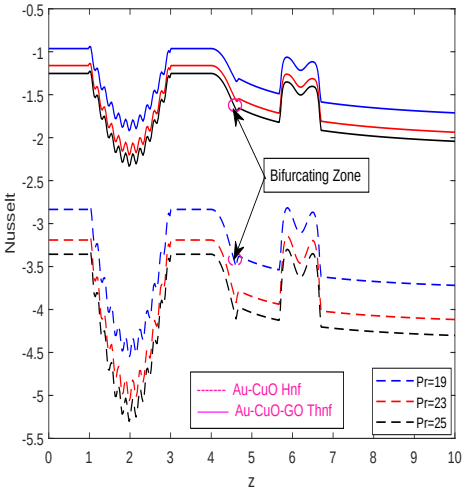

(d) Nusselt profile by varying Pr

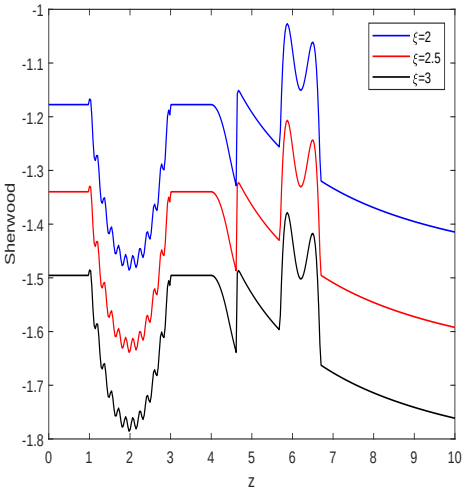

(e) Sherwood profile by varying ξ

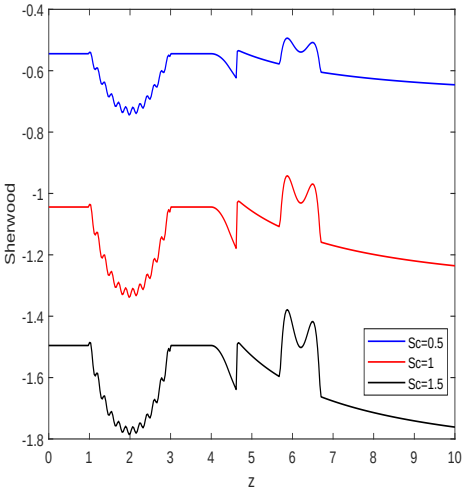

(f) Sherwood profile by varying Sc

Figure 5.7: WSS, Nusselt and Sherwood profile

The increment of the Hartman number yields an increase in the Lorentz force, which subsequently causes the redirection of the fluid flows away from the stenotic region. This redirection ultimately leads to a reduction in the WSS profile. The distribution of WSS is depicted in figure 5.7b, which investigates the consequences of modifying the stenotic and aneurysm depth in the arterial segment. Significantly, the WSS profile demonstrates the inverse correlation with the progressive increase in stenotic depth observed in the arterial sections, while the reverse trend is observed for aneurysm. The observations made in this study are consistent with the previous experimental investigations conducted by Zhang [131], which similarly documented a decrease in WSS as a consequence of the development of arterial lesions. The concurrence observed between the present study and Zhang's research provides additional substantiation for the hypothesis that augmented stenotic depth is a contributing factor to diminished WSS levels. Figure 5.7c illustrates the impact of the heat source parameter Q on the Nusselt profile while presenting a comparative analysis conducted between hybrid and ternary hybrid nanofluids. The comparative analysis reveals that the Nusselt number profile exhibits greater magnitudes for ternary hybrid nanofluids than hybrid nanofluids. The heat source parameter indicates the elevated heat production within the system, resulting in amplified temperature differences between the heated surface and the adjacent fluids. This phenomenon generates a strong convective force and amplifies the Nusselt number profile. Figure 5.7d visually represents the relationship between the Nusselt number and the Prandtl number. The figure demonstrates that as the Prandtl number increases, there is a notable decrease in the Nusselt number. The observed pattern indicates that the efficiency of heat transfer from the arterial wall to the blood decreases as the Prandtl values increase. In the context of arterial heat transfer, it has been observed that fluids with higher Prandtl numbers tend to demonstrate diminished efficacy in the conduction of heat when compared to fluids possessing lower Prandtl numbers. Consequently, the Nusselt number decreases with increasing Prandtl number, indicating a reduced ability to transfer heat from the arterial wall to the blood. Figure 5.7e illustrates the chemical reaction parameter's influence on the Sherwood profile. The augmentation of the Sherwood profile becomes apparent as the chemical reaction parameter undergoes an increase from 2 to 3. The observed phenomenon can be attributed to alterations in the concentration gradients, which serve as the driving force for mass transfer. As the value of ξ decreases, the rate of mass transfer also decreases, resulting in a decline in the Sherwood profile. The Sherwood profile exhibits a decreasing trend with increasing Schmidt number, as illustrated in figure 5.7f. The enhancement in Sc results in a decrease in mass transfer rate relative to diffusivity. Thus, the concentration is not fully exploited, which leads to a lower mass transfer rate and a decline in the Sherwood profile.

5.5.6 Velocity Contour

The analysis of velocity contours holds great importance within scientific research, as it enables researchers to effectively visualise and map blood flow distribution along the inner surface of blood vessels. This technology can facilitate diagnosing, evaluating, and strategising treatment plans for stenotic lesions. The contour analysis yields qualitative outcomes for computational simulations and provides further insight into the complex flow within the stenotic vessel. The impact of the Casson fluid parameter on the velocity contour is depicted in figure 5.8 . From figure 5.8a, we can inferred that the more trapped bolus formed near the aneurysm region and the maximum velocity attain by the fluid is 0.5 which further increases after it enters in the parent artery. Although, the maximum velocity remain same in both figures 5.8b and 5.8c but trapped bolous increases as the Casson fluid parameter enhances from $\beta_1 = 10$ to $\beta_1 \to \infty$.

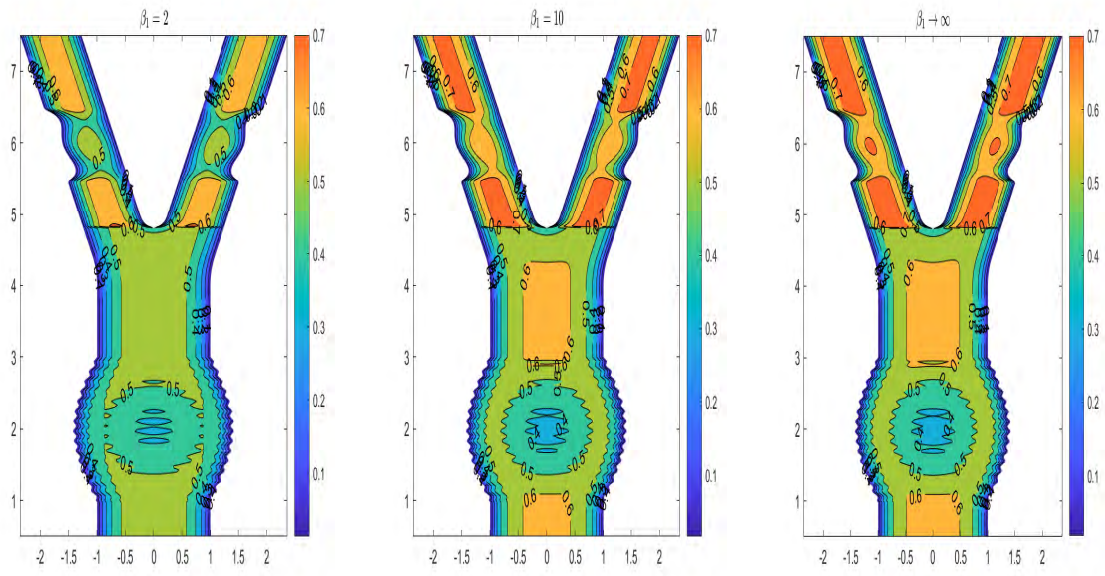

(a) **(b)** **(c)**

Figure 5.8: Velocity contour for varying Casson fluid parameter (a) $\beta_1 = 2$ (b) $\beta_1 = 10$ (c) $\beta_1 \to \infty$

Figure 5.9 illustrates the influence of bifurcation angle in the velocity contour profile. Clearly, it can be observed from the figure also that the flow behavior remains the same in parent artery for all the three cases but varies as it enters in the daughter artery. According to the principle of conservation of mass, the volume of flow from the parent artery must be conserved in the daughter arteries. Consequently, the cross-sectional area of the daughter arteries increases with an increasing bifurcation angle. This expansion in the cross-sectional area leads to an enhanced flow rate profile as the bifurcation angle increases.

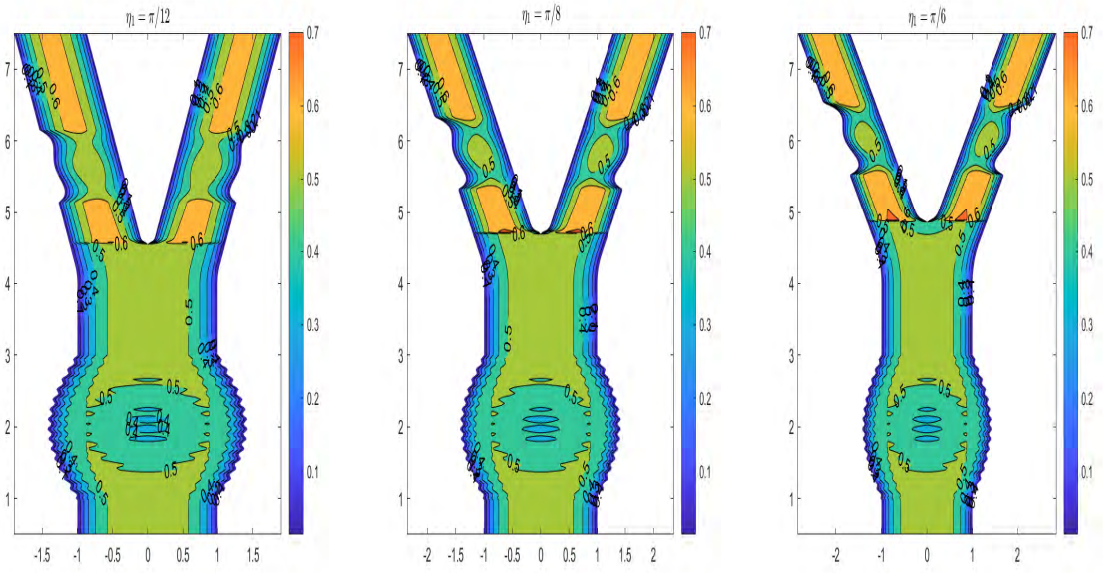

(a) **(b)** **(c)**

Figure 5.9: Velocity contour for varying bifurcating angle (a) $\eta_1 = \pi/12$ (b) $\eta_1 = \pi/8$ (c) $\eta_1 = \pi/6$

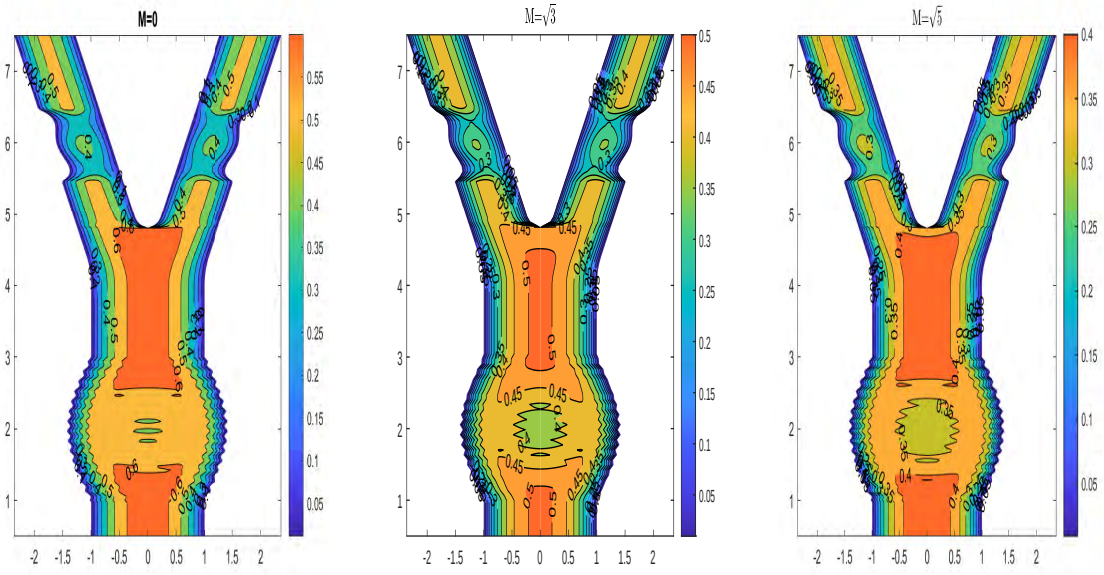

(a) **(b)** **(c)**

Figure 5.10: Velocity contour for varying magnetic field parameter (a) $M = 0$ (b) $M = \sqrt{3}$ (c) $M = \sqrt{5}$

The velocity contour for the enhancement in the magnetic field parameter from 0 to $\sqrt{3}$ is depicted in figure 5.10. In the absence of a magnetic field, the fluid achieves a maximum velocity of 0.6, as illustrated in figure 5.10a. Based on the observations made in figures

5.10b and 5.10c, it can be deduced that the maximum velocities achieved are 0.5 and 0.4, respectively. The observed phenomenon exhibits a correlation between the augmentation of the magnetic field parameter and the subsequent manifestation of a diminished velocity profile. The empirical occurrence can be ascribed to the manifestation of the Lorentz force exerted by the magnetic field upon the conductive fluid. The Lorentz force, when applied, exerts a counteracting influence that leads to a reduction in the velocity field. This phenomenon becomes more pronounced as the magnetic field parameter increases.

5.5.7 Entropy

Entropy is a fundamental thermodynamic property that provides insight into the degree of randomness and disorder within the blood vessel. The phenomenon of entropy generation arises due to the conversion of kinetic energy into heat, which occurs due to viscous dissipation or flow disturbances. Stenosis refers to the pathological condition characterised by the constriction or narrowing of a blood vessel. On the other hand, an aneurysm is an abnormal dilation or bulging formation that occurs within an artery, leading to disruptions in the normal flow pattern and an increase in resistance along the flow pathway. The aforementioned disruption has the potential to induce alterations in the generation of entropy within the system. Figures 5.11a and 5.11b depict the influence of Brinkmann number on the Entropy generation profile N_G on parent and daughter artery, respectively. Form the figure it can be inferred that the N_G profile show the increasing trend as the magnitude of the parameter Br enhances from 6.65 to 8.75. This has happened due to dominant effect of viscous dissipation over the thermal conduction which results in conversion of orderly energy into disordered energy and further lead to development of entropy generation profile. The influence of Br on the Bejan profile in the parent artery is illustrated in figure 5.11c. The Bejan number is a dimensionless parameter that quantifies the relative significance of convective heat transfer compared to conductive heat transfer within a given system. As the Brinkman number (Br) increases, a noticeable transition occurs where the influence of viscous dissipation becomes increasingly dominant compared to thermal conduction. The prevalence of viscous effects in this scenario gives rise to intensified convective processes, thereby leading to an augmented Bejan profile. Figure 5.11d demonstrates the impact of Br on the Bejan profile in the daughter artery. Analysis of the figure reveals distinct trends based on the proximity to the artery walls and the central region. The Bejan profile increases with Br in the vicinity of the arterial walls, but the reverse trend is observed at the centre. This behaviour can be attributed to the dominant influence of viscous dissipation in the vicinity of the walls that led to enhancement in the convective heat transfer process and further enhanced the Be profile. Conversely, the central region of the daughter artery exhibits a reverse trend as viscous

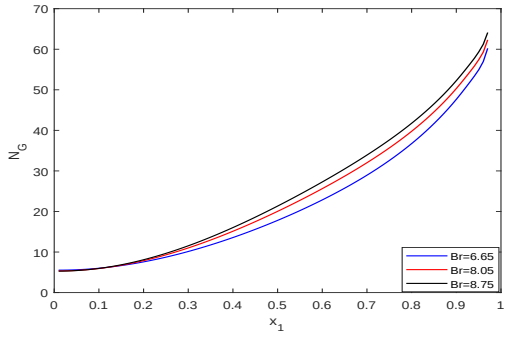

(a) Entropy in parent artery

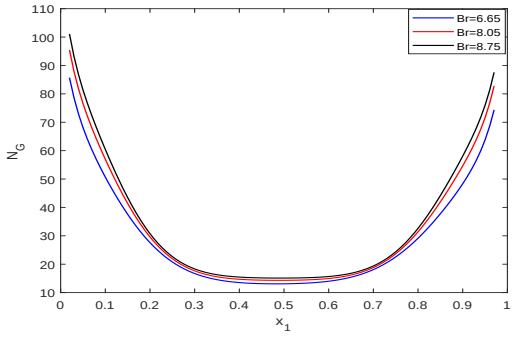

(b) Entropy in daughter artery

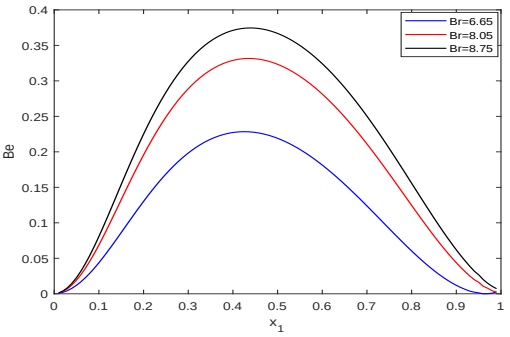

(c) Bejan number in parent artery

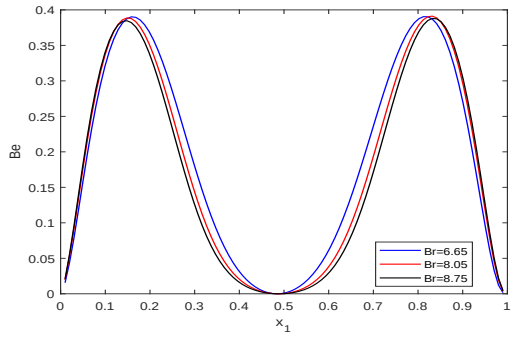

(d) Bejan number in daughter artery

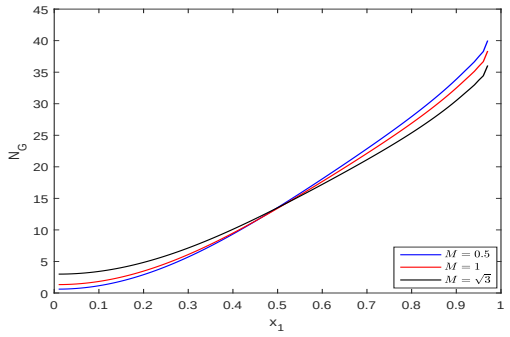

(e) Entropy in parent artery

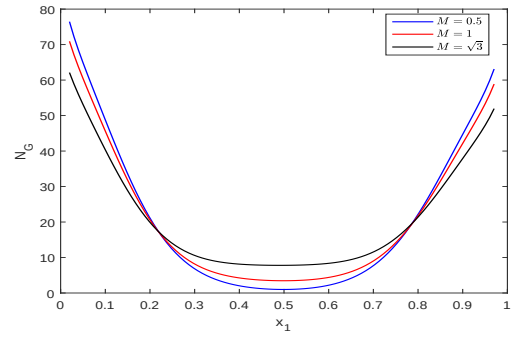

(f) Entropy in daughter artery

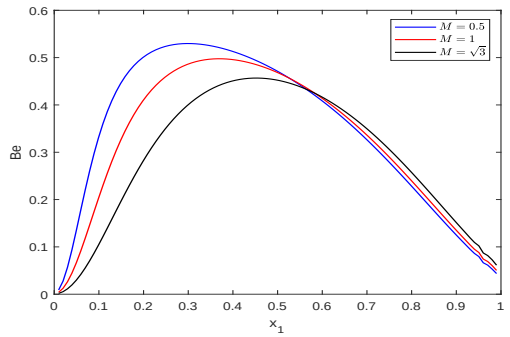

(g) Bejan number in parent artery

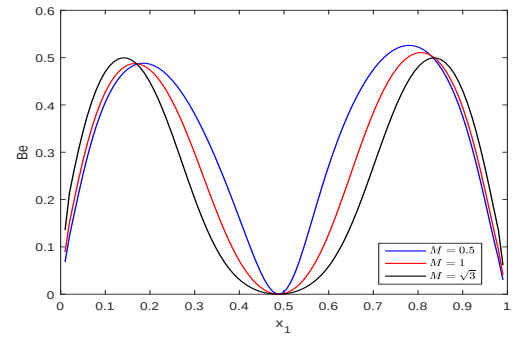

(h) Bejan number in daughter artery

Figure 5.11: Entropy and Bejan number by varying different parameters

dissipation's dominance weakens compared to thermal conduction, leading to decreasing Be profile. The influence of magnetic field parameter on the Be profile in the parent and daughter artery is depicted in figure 5.11e and 5.11f, respectively. In the vicinity of the arterial walls, the prevalence of the magnetic field results in a generation of resistive Lorentz forces, leading to a reduction in the N_G profile. Conversely, towards the centre, the magnetic field may weaken, thereby enabling the manifestation of dominance effects through viscous dissipation or thermal conduction. In instances of this nature, it is plausible for the entropy to demonstrate a counteractive pattern, wherein it may escalate with an augmenting magnetic field parameter. The Bejan profile trends near the arterial walls and at the centre in response to the magnetic field parameter are illustrated in figures 5.11g and 5.11h, respectively. In both the parent and daughter arteries, there is an observed increasing trend in proximity to the arterial walls, while a reverse trend is observed towards the central region. The observed behaviour can be attributed to the prominent effect of the magnetic field parameter close to the walls, which gradually diminishes its strength towards the centre. The convective heat transfer process is enhanced by a magnetic field, leading to an increase in the Bejan profile close to the walls. In contrast, it is worth noting that the prevalence of viscous dissipation in the central region results in a decrease in the Bejan profile.

5.5.8 Conclusion

The present study investigates pathological conditions such as stenosis and aneurysms in the bifurcated artery. The Casson fluid model is employed instead of the Newtonian fluid model to simulate blood flow properties like viscosity and flow rate accurately. Furthermore, the study examines the influence of entropy generation on flow attributes by utilizing a ternary hybrid nanofluid. The governing equations are simplified by applying the mild stenosis assumption, followed by discretization using the Crank-Nicolson scheme. This discretized model allows for the graphical representation of the influence of relevant parameters on the flow distribution. The findings obtained from this study are as follows:

- Enhanced Brinkmann number (Br) increases entropy generation by promoting dominant viscous dissipation over thermal conduction, leading to the conversion of ordered energy into disordered energy.

- The WSS profile decreases with the augmentation with the stenosis size .

- The velocity contour depicts the decreasing pattern in the velocity profile with enhancing values of magnetic field parameter.

- Nusselt number profile exhibits greater magnitudes for ternary hybrid nanofluids than hybrid nanofluids.

- Enhancement in the Eckert number and Joule heating parameter facilitates the conversion of surplus kinetic energy into thermal energy, consequently causing a rise in the temperature profile.

The ternary hybrid nanofluid (Au-CuO-GO/Blood) offers several advantages, including enhanced thermal conductivity and biocompatibility, which make it suitable for various applications such as diagnosis, drug delivery, bioimaging, and tissue engineering. Owing to these characteristics, the ternary hybrid nanofluid holds great potential for advancing biomedical research and clinical practices. Furthermore, entropy is a fundamental concept within biomedicine, enabling a deeper understanding of biological systems' intricate complexities and behaviours. By carefully examining entropy in the context of biomedicine, researchers gain valuable insights into the efficiency, organization, and stability of diverse biological processes.

Chapter 6

Method of Lines Analysis of MHD Two-Phase Blood Flow with Al_2O_3 Nanofluid Through Overlapping Stenosed Artery with Activation Energy

6.1 Introduction

Within the domain of numerical analysis and computational mathematics, the Method of Lines (MOL) emerges as a potent and adaptable approach for resolving partial differential equations (PDEs). Partial differential equations (PDEs) are widely used mathematical models that describe various natural phenomena accurately. These equations have proven invaluable tools in various scientific disciplines, such as physics, biophysics, fluid dynamics, and chemistry. The elucidation of partial differential equations (PDEs) provides a comprehensive framework for comprehending many phenomena that necessitate analytical or numerical solutions to these equations. The inherent intricacy and non-linearity of partial differential equations (PDEs) make solving them quite formidable. In this context, the Method of Lines offers a valuable tool owing to its intrinsic versatility, adaptability, and precision, affording a practical avenue for addressing complex PDEs within the academic and scientific community [156]. Nowak et al. [157] adopted the MOL method to solve the mathematical equations arising from the problem associated with reverse flow in the fixed bed reactor and initialization process of automobile catalytic converters. They adopted the adaptive algorithm to solve the problem as it relieves the user from manually selecting the necessary quantity of grid points and meticulously adjusting the tuning parameters. The application of the Method of Lines (MOL) as a computational technique was explored by Subramanian and White [158]. They utilised this method to solve a non-linear elliptical equation that emerged from mathematical modelling related to the steady-state mass and energy transport phenomena occurring within solid materials. Ozen and Selçuk [159] employed the MOL to get the efficient solutions for the wall fluxes and source term distributions in the fluidized

bed combustors containing particle laden combustion gases. Pantoleontos et al. [160] considered the mass-continuity equations associated with laminar flow within a membrane contractor, focusing specifically on lumen boundary conditions. Their inquiry concentrates on utilising a carbon-capture membrane-based gas absorption technique, which involves considering different boundary conditions to accommodate the wide range of membrane-based processes. To effectively handle the inherent non-linearity of the given boundary conditions, the application of the Method of Lines (MOL) approach was employed by the researchers.

Stenosis is a medical condition characterised by fatty acids, lipids, and cholesterol accumulating within the walls of arteries, leading to the eventual blockage of blood flow. The aforementioned medical condition represents a significant and urgent matter of public health that necessitates immediate attention and intervention. An investigation was conducted by Misra and Chakravarty [161] to explore the hemodynamic phenomena occurring in arterial segments affected by stenosis. In this study, the arterial wall was represented as an elastic tube, while blood was assumed to exhibit Newtonian fluid behaviour. Siddiqui et al. [162] undertook a comprehensive investigation that centred on the dynamics of the pulsatile flow of Casson fluid within an artery afflicted with stenosis. The study conducted by the researchers placed considerable emphasis on elucidating the oscillatory characteristics of wall shear stress that can give rise to fatigue and, eventually, loss of the permeability and elasticity of walls. The influence of a magnetic field on composite stenosis with permeable walls was investigated by Akbar and Butt [37]. Their research unveiled that the velocity profile increased when copper nanoparticles were introduced into the base fluid. Shit and Roy [111] delved into the effects of an induced magnetic field on blood flow through a constricted artery. Their findings demonstrated that microcirculation increased with higher magnetic field strength and stenosis height, shedding light on the interplay between magnetic fields and arterial hemodynamics. Zaman et al. [163] investigated the influence of entropy generation and magnetohydrodynamics (MHD) in channels with curved stenosis. Their findings demonstrated that applying a magnetic field resulted in a notable decrease in the velocity profile. The Hall effect on the magnetohydrodynamic (MHD) nanofluid flow through the stenosed artery was investigated by Sharma et al. [121]. The study encompassed a thorough sensitivity analysis to elucidate the influence of the Brinkmann number and the Hall parameter on the Nusselt number and the shear stress profile within the system.

Nanofluid have emerged as a groundbreaking class of heat transfer fluid that garnered the attention of various researchers and scientist. The nanoparticles are the colloidal suspension of nanoparticles ,ranging from 1 to 100 nanometer in size dispersed in the base fluid such as glycol, water or oil etc. The small size of nanoparticles allow it for suitably used for improving image resolution and drug delivery precision. Ponalagusamy and Priyadharshini [164]

undertook an investigation with the objective of evaluating the impact of a magnetic field and body acceleration on the pulsatile flow characteristics of a Casson nanofluid within an inclined stenosed artery. Majee and Shit [165] have undertaken a study wherein they formulated a mathematical model to investigate the potential application of magnetic nanoparticles in targeted drug delivery, specifically within stenosed arteries. The study's findings demonstrated a positive correlation between the concentration of nanoparticles and the Nusselt number. This observation holds potential implications in the field of biomedicine, particularly in treating tumour and cancer cells. Zaman et al. [166] undertook simulations to investigate the behaviour of hybrid nanoparticles (Ag, Al_2O_3) within stenosed arteries. The researchers aimed to provide a comparative analysis between these hybrid nanoparticles and silver (Ag) nanoparticles. The present study yielded valuable insights into the efficacy of these nanoparticles within the realm of biomedicine. Dubey et al. [6] explored the effect of metallic nanoparticle within the hemodynamic flow through the dieseased artery subject to thermophoresis and Brownian motion. Their study revelaed that the study may be beneficial for transport phenomena in pharmacology and in nano-drug delivery. Varmazyar et al. [167] utilised magnetic nanoparticles (MNP) as a means of drug delivery. The researchers injected the drug at locations preceding the plaque and tumour sites. It has been determined that the drug becomes entrapped in close proximity to the plaque, resulting in a diminished efficacy of drug delivery to the tumour site. The investigation conducted by Khanduri and Sharma [107] delved into the intricate realm of the influence exerted by Hall and ion slip effects on hybrid nanoparticles within a catheterized stenosed artery with thrombosis. To replicate the inherent properties of blood, the researchers opted to employ the hematocrit-dependent viscosity model. Additionally, Khanduri et al. [33] conducted a sensitivity analysis on the magnetohydrodynamic (MHD) fluid flow within a curved stenosed artery, considering the influence of electroosmosis and radiation effects. Several researchers [143, 168, 23, 120, 154] explored the study of nanofluid through the stenosed artery.

The blood circulation within the intricate networks of microvessels, including arterioles, capillaries, and venules, demonstrates discernible characteristics when contrasted with the larger conduits found in the circulatory system. The interactions of different microscopic properties of blood affect the nature of blood flowing through these microvessels. Investigating this phenomenon, researchers have delved into the dual-phase nature of blood flow within these vessels. Specifically, the plasma-rich region demonstrates Newtonian behaviour, while the core region displays non-Newtonian characteristics, shedding light on the complex rheological properties of blood within the microvascular system. An investigation

was conducted by Sachin and Murthy [169] to examine the trajectory of drug-bound magnetic nanoparticles in a two-phase fluid environment within microvessels, where the dynamics were influenced by an external magnetic field. Tiwari and Chauhan [84], in a separate study, employed a two-phase fluid model to explore the pulsatile behavior of blood with varying viscosity within blood vessels. Tripathi et al. [7] conducted a comprehensive examination of magnetohydrodynamic (MHD) two-phase blood flow through stenosed arteries, considering the effects of viscous dissipation, Joule heating, and k-th order chemical reactions. Their study also accounted for temperature-dependent viscosity in the core region and constant viscosity in the plasma region. Kumawat et al. [12] delved into the topic of two-phase blood flow within curved stenosed arteries, where the viscosity of the core region was dependent on hematocrit levels, and the viscosity of the plasma region varied with temperature. Furthermore, Sharma et al. [109] undertook a numerical investigation into the study of two-phase MHD power-law fluid flow within stenosed arteries, considering the presence of the Hall effect and a magnetic field. These scholarly inquiries collectively contribute to our understanding of complex fluid dynamics in various biomedical and engineering contexts.

The biomedical field encompasses a significant research domain centred around thermophoresis and Brownian motion. Within the context of drug delivery, these phenomena hold notable potential for the targeted transport of drug carriers, specifically nanoparticles, to precise anatomical sites or for the controlled dispersion of pharmaceutical agents at designated locales. Nadeem and Ijaz [170] investigated blood flow through overlapping stenoses under the influence of thermophoresis and Brownian motion. Additionally, Ponalagusamy and Priyadharshini [164] explored the intricate interplay of magnetic fields and body acceleration in the pulsatile flow of Casson fluid within inclined arteries. Their research illuminated an augmentation in temperature and concentration profiles with increasing Brownian motion parameters. Prasad and Yasa [171] developed a theoretical model to investigate micropolar fluid behaviour in arteries afflicted by multiple stenoses. Their findings underscored an enhancement in wall shear stress with increasing Brownian parameters, while a converse trend was observed concerning thermophoresis parameters. In a more recent study, Hussain et al. [172] delved into the effects of these parameters on pulsatile nanofluid flow within curved arteries, contributing to our understanding of their implications in biomedical contexts. Chemical reactions within the bloodstream have emerged as a critical factor, influencing phenomena such as blood clot formation (thrombosis) and playing a pivotal role in drug delivery applications, especially within stenosed arteries. A minimum energy threshold, known as activation energy, must be exceeded to initiate chemical reactions. Ibrahim et al. [173] recently explored the impact of activation energy on hemodynamic flow. Their

investigations unveiled the notable effect of activation energy in enhancing nanoparticle velocity, thereby facilitating their transport to the cervical canal. Saleem et al. [10] undertook a comprehensive study examining entropy generation in the context of nanoparticle-laden fluid flow within ciliated channels, accounting for the influence of activation energy and magnetic fields.

Inspired by the insightful investigation mentioned above, the present work delves into an in-depth exploration of Magnetohydrodynamic (MHD) two-phase blood flow within a stenosed arterial conduit. In our study, we model the core region of the fluid as an Ostwald-DeWaele power-law fluid, while the plasma region is represented as a Newtonian fluid. This choice of modeling reflects the complex rheological characteristics exhibited by blood in real physiological scenarios. Furthermore, the present study aims to broaden the investigation by integrating the impact of thermophoresis, Brownian motion, and activation energy into the analysis of flow dynamics. This approach acknowledges the crucial role of these factors in comprehending the intricate transport phenomena occurring within biological systems. In order to address the complex network of partial differential equations that emerge from these considerations, the Method of Lines is employed as a robust and versatile approach for numerical solution, ensuring the accuracy and reliability of our results.

6.2 Mathematical Model

Consider the continuous model of unsteady, laminar, incompressible blood flow through a stenosed artery of length L, as depicted in Figure 1. We simulate the blood flow model using the Ostwald-DeWaele power-law fluid model. In this two-phase blood flow model, the core region contains erythrocytes (a suspension with a uniform hematocrit of viscosity $(\mu_f)_c$), while the viscosity of the cell-depleted plasma layer in the plasma region is denoted as $(\mu_f)_p$. A cylindrical coordinate system $(\tilde{r}, \tilde{\theta}, \tilde{z})$ is adopted, assuming axi-symmetric flow, which results in the independence of all variables with respect to $\tilde{\theta}$. An external magnetic field B_0, applied perpendicular to the flow, leads to the neglect of the induced magnetic field $Re_M << 1$ due to its significantly lower magnitude compared to the applied magnetic field.

6.2.1 Geometry

The geometry of the stenosis in the core region is considered as [28, 34]:

$$\tilde{R}(\tilde{z}) = \begin{cases} R_0 - \frac{6\delta^*}{5L_0^4}A^*, & \text{for} \quad \tilde{d} < \tilde{z} \leq \tilde{d} + L_0 \\ R_0, & \text{otherwise} \end{cases} \tag{6.1}$$

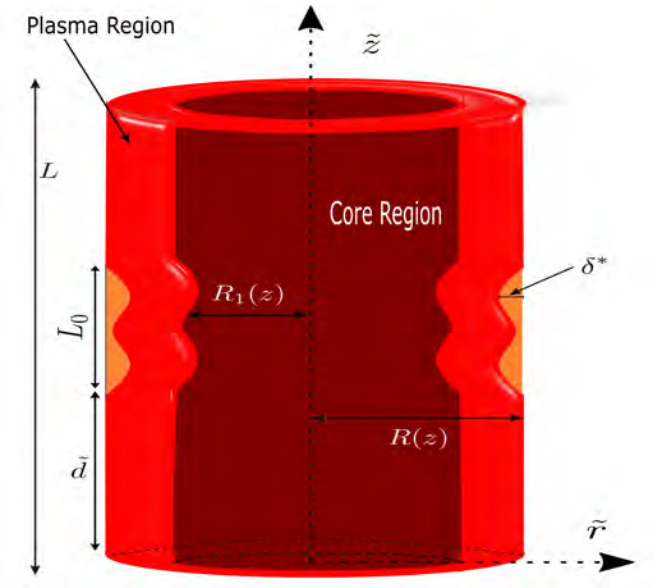

Figure 6.1: Pictorial representation of diseased artery

The geometry of the stenosis in the plasma region is considered as:

$$\tilde{R}_1(\tilde{z}) = \begin{cases} \bar{\beta}R_0 - \frac{6\delta^*}{5L_0^4}A^*, & \text{for} \quad \tilde{d} < \tilde{z} \leq \tilde{d} + L_0 \\ \bar{\beta}R_0, & \text{otherwise} \end{cases} \tag{6.2}$$

where, $R(z)$ represent the radius of the artery, R_0 is the radius of normal artery, L_0 signifies the length of the stenosis, d is the location of stenosis and δ^* is the stenosis height. Furthermore, the term A^* is defined as $A^* = 11(\tilde{z}-\tilde{d})L_0^3 - 47(\tilde{z}-\tilde{d})^2L_0^2 + 72(\tilde{z}-\tilde{d})^3L_0 - 36(\tilde{z}-\tilde{d})^4$.

6.2.1.1 Governing Equations

Consider the blood flow through an artery as bidirectional and unsteady. The velocity along the radial $\tilde{r}$ and axial direction $\tilde{z}$ are represented as $\tilde{u}_{\wp}$ and $\tilde{w}_{\wp}$, respectively. The governing mathematical equations are given as:

Continuity:

$$\frac{\partial \tilde{u}_{\wp}}{\partial \tilde{r}} + \frac{\tilde{u}_{\wp}}{\tilde{r}} + \frac{\partial \tilde{w}_{\wp}}{\partial \tilde{z}} = 0. \tag{6.3}$$

Energy Equation:

$$((\rho Cp)_{nf})_{\wp}\left[\frac{D\tilde{T}_{\wp}}{D\tilde{t}}\right]=(\kappa_{nf})_{\wp}\left[\nabla^2\tilde{T}_{\wp}\right]+(\rho C_p)_s\left[(D_B)_{\wp}\left\{\left(\frac{\partial\tilde{C}_{\wp}}{\partial\tilde{r}}\frac{\partial\tilde{T}_{\wp}}{\partial\tilde{r}}\right)+\left(\frac{\partial\tilde{C}_{\wp}}{\partial\tilde{z}}\frac{\partial\tilde{T}_{\wp}}{\partial\tilde{z}}\right)\right\}+\frac{(D_T)_{\wp}}{\tilde{T}_0}\left(\left(\frac{\partial\tilde{T}_{\wp}}{\partial\tilde{r}}\right)^2+\left(\frac{\partial\tilde{T}_{\wp}}{\partial\tilde{z}}\right)^2\right)\right]+\sigma_{nf}B_0^2\tilde{w}_{\wp}^2-\frac{1}{\tilde{r}}\left\{\frac{\partial}{\partial\tilde{r}}(\tilde{r}q_r)\right\}+\phi^*, \tag{6.4}$$

where, the radiation term [33, 174],

$$q_r=-\frac{16\sigma_e\tilde{T}_0^3}{3k_e}\frac{\partial\tilde{T}_{\wp}}{\partial\tilde{r}} \tag{6.5}$$

and, viscous dissipation term is defined as:

$$\phi^*=(\mu_{nf})_{\wp}\left[2\left(\frac{\partial\tilde{u}_{\wp}}{\partial\tilde{r}}\right)^2+\left(\frac{\partial\tilde{u}_{\wp}}{\partial\tilde{z}}+\frac{\partial\tilde{w}_{\wp}}{\partial\tilde{r}}\right)^2+2\left(\frac{\partial\tilde{w}_{\wp}}{\partial\tilde{z}}\right)^2\right], \tag{6.6}$$

Concentration Equation:

$$\left[\frac{D\tilde{C}_{\wp}}{D\tilde{t}}\right]=(D_B)_{\wp}\left[\nabla^2\tilde{C}_{\wp}\right]+\frac{(D_T)_{\wp}}{\tilde{T}_0}\left[\nabla^2\tilde{T}_{\wp}\right]-k_r^2\frac{\tilde{T}_{\wp}}{\tilde{T}_0}\left(\tilde{C}_{\wp}-\tilde{C}_0\right)e^{\left(-\frac{E_a}{k\tilde{T}_{\wp}}\right)}, \tag{6.7}$$

Here, the operators $\frac{D}{D\tilde{t}}\equiv\left[\frac{\partial}{\partial\tilde{t}}+\tilde{u}_{\wp}\frac{\partial}{\partial\tilde{r}}+\tilde{w}_{\wp}\frac{\partial}{\partial\tilde{z}}\right]$ and $\nabla^2\equiv\left[\frac{\partial^2}{\partial\tilde{r}^2}+\frac{1}{\tilde{r}}\frac{\partial}{\partial\tilde{r}}+\frac{\partial^2}{\partial\tilde{z}^2}\right]$.
The paramter $\wp$ is represented as:

$$\wp=\begin{cases}c, & \text{if } 0<\tilde{r}\le\tilde{R}_1(\tilde{z}) \qquad \text{(Core region)}\\ p, & \text{if } \tilde{R}_1(\tilde{z})<\tilde{r}\le\tilde{R}(\tilde{z}) \text{ (Plasma region)}\end{cases} \tag{6.8}$$

For core region:

Momentum ($\tilde{r}$-direction):

$$(\rho_{nf})_c\left[\frac{\tilde{D}\tilde{u}_c}{\tilde{D}\tilde{t}}\right]=-\frac{\partial\tilde{p}_c}{\partial\tilde{r}}+\left[\frac{1}{\tilde{r}}\frac{\partial}{\partial\tilde{r}}(\tilde{r}S_{\tilde{r}\tilde{r}})+\frac{\partial}{\partial\tilde{z}}(S_{\tilde{r}\tilde{z}})\right]. \tag{6.9}$$

Momentum ($\tilde{z}$-direction):

$$(\rho_{nf})_c\left[\frac{\tilde{D}\tilde{w}_c}{\tilde{D}\tilde{t}}\right]=-\frac{\partial\tilde{p}_c}{\partial\tilde{z}}+\left[\frac{1}{\tilde{r}}\frac{\partial}{\partial\tilde{r}}(\tilde{r}S_{\tilde{r}\tilde{z}})+\frac{\partial}{\partial\tilde{z}}(S_{\tilde{z}\tilde{z}})\right]+\tilde{F} \tag{6.10}$$

For plasma region:

Momentum ($\tilde{r}$-direction):

$$(\rho_{nf})_p\left[\frac{\tilde{D}\tilde{u}_p}{\tilde{D}\tilde{t}}\right]=-\frac{\partial\tilde{p}_p}{\partial\tilde{r}}+\frac{1}{\tilde{r}}\frac{\partial}{\partial\tilde{r}}\left\{\mu_{nf}\frac{\partial\tilde{u}_p}{\partial\tilde{r}}\right\}+\frac{\partial}{\partial\tilde{z}}\left\{\mu_{nf}\left(\frac{\partial\tilde{u}_p}{\partial\tilde{z}}+\frac{\partial\tilde{w}_p}{\partial\tilde{r}}\right)\right\}-2\mu_{nf}\frac{\tilde{u}_p}{\tilde{r}^2} \quad (6.11)$$

Momentum ($\tilde{z}$-direction):

$$(\rho_{nf})_p\left[\frac{\tilde{D}\tilde{w}_p}{\tilde{D}\tilde{t}}\right]=-\frac{\partial\tilde{p}_p}{\partial\tilde{z}}+\frac{1}{\tilde{r}}\frac{\partial}{\partial\tilde{r}}\left\{\tilde{r}\mu_{nf}\left(\frac{\partial\tilde{u}_p}{\partial\tilde{z}}+\frac{\partial\tilde{w}_p}{\partial\tilde{r}}\right)\right\}+\frac{\partial}{\partial\tilde{z}}\left\{2\mu_{nf}\left(\frac{\partial\tilde{w}_p}{\partial\tilde{z}}\right)\right\}+\tilde{F} \quad (6.12)$$

The body force term $\tilde{F}$ defined in the equations (6.10) and (6.12) is expressed as:

$$\tilde{F}=-(\sigma_{nf})_{\wp}B_0^2\tilde{w}_{\wp}+((\rho\beta)_{nf})_{\wp}g(\tilde{T}_{\wp}-\tilde{T}_0)+((\rho\beta)_{nf})_{\wp}g(\tilde{C}_{\wp}-\tilde{C}_0)-\frac{(\mu_{nf})_{\wp}}{K_1}. \quad (6.13)$$

The blood flow has the pulsatile nature due to the pumping action of the blood. Therefore, the pressure gradient can be taken in the following form:

$$-\frac{\partial\tilde{p}}{\partial\tilde{z}}=A_0+A_1\cos(\omega_p\tilde{t}),\tilde{t}>0. \quad (6.14)$$

Where, $\omega_p=2\pi f_p$, the terms A_0 and A_1 signifies the amplitude of steady-state and pulsatile component. The term f_p signifies for heart pulse frequency. Figure 6.2 depicts the pictorial representation in formation of the Al_2O_3-Blood Nanofluid.

6.2.1.2 Non-Newtonian Fluid Model (Power Law Fluid)

The Cauchy stress tensor for a power law fluid is given as [18]:

$$T^*=-pI+(\mu_{nf})_{\wp}(\Gamma\Pi)^{n-1}A_1. \quad (6.15)$$

Here p represents the pressure, I is the identity tensor, n represents the rheological power-law index ($n=1$ for Newtonian fluid, $n<1$ for pseudoplastic blood, $n>1$ for dilatant blood). The first Rivlin-Ericksen tensor is defined as $A_1=\nabla V+(\nabla V)^T$ and $\Pi=\sqrt{\frac{1}{2}tr(A_1)}$.

Use equations (6.15) and the above terms to get the stress tensor components are expressed as:

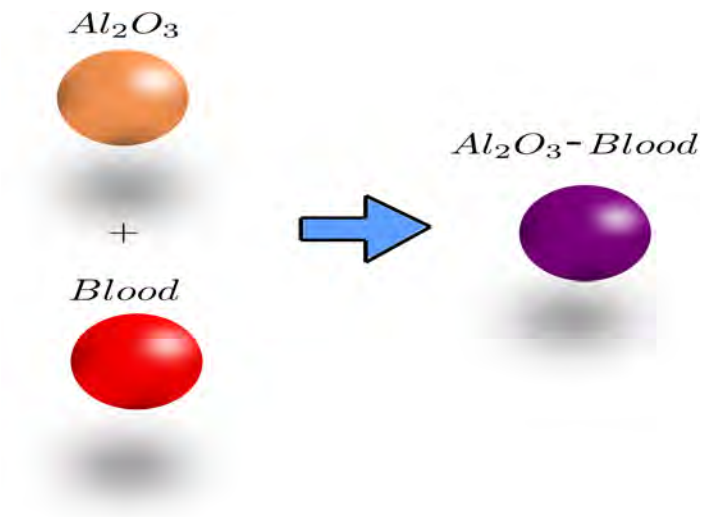

Figure 6.2: Formation of Al_2O_3-Blood Nanofluid by integration of Al_2O_3 nanoparticle with blood.

Table 6.1: Dimensionless parameters

$r = \frac{\tilde{r}}{R_0}$	$z = \frac{\tilde{z}}{L_0}$	$u_c = \frac{L_0 \tilde{u}_1}{\delta^* U_0}$	$R_1 = \frac{\tilde{R}_1}{R_0}$
$p = \frac{R_0^2 \tilde{p}}{(\mu_f)_p U_0 L_0}$	$C_c = \frac{\tilde{C}_c - \tilde{C}_0}{\tilde{C}_w - \tilde{C}_0}$	$T_c = \frac{\tilde{T}_c - \tilde{T}_0}{\tilde{T}_w - \tilde{T}_0}$	$T_p = \frac{\tilde{T}_p - \tilde{T}_0}{\tilde{T}_w - \tilde{T}_0}$
$w_c = \frac{\tilde{w}_c}{U_0}$	$Gr = \frac{g(\rho_f)_p \beta_f R_0^2 \Delta \tilde{T}}{U_0 (\mu_f)_p}$	$Re = \frac{(\rho_f)_p R_0 U_0}{(\mu_f)_p}$	$k_0 = \frac{(\kappa_f)_p}{(\kappa_f)_c}$
$M^2 = \frac{\sigma_f B_0^2 R_0^2}{(\mu_f)_p}$	$Sc = \frac{(\mu_f)_p}{(D_B)_p (\rho_f)_p}$	$Nr = \frac{16 \sigma_e \tilde{T}_1}{3 (\kappa_f)_p k_e}$	$N_t = \frac{(\rho C)_s (D_B)_p \Delta \tilde{T}}{\tilde{T}_0 (\kappa_f)_p}$
$Br = EcPr$	$(D_B)_0 = \frac{(D_B)_p}{(D_B)_c}$	$(D_T)_0 = \frac{(D_T)_p}{(D_T)_c}$	$Gc = \frac{g(\rho_f)_p \beta_f R_0^2 (\tilde{C}_w - \tilde{C}_0)}{U_0 (\mu_f)_p}$
$\Delta \tilde{T} = \tilde{T}_w - \tilde{T}_0$	$Da = \frac{K}{R_0^2}$	$S_{\tilde{z}\tilde{z}} = \frac{U_0 (\mu_f)_p}{L_0} S_{zz}$	$S_{\tilde{r}\tilde{z}} = \frac{U_0 (\mu_f)_p}{R_0} S_{rz}$
$We = \frac{\Gamma U_0}{R_0}$	$\Delta \tilde{C} = \tilde{C}_w - \tilde{C}_0$	$\xi = \frac{k_r^2 R_0^2 (\rho_f)_p}{(\mu_f)_p}$	$\Omega = \frac{\Delta \tilde{T}}{\tilde{T}_0}$
$\mu_0 = \frac{(\mu_f)_p}{(\mu_f)_c}$	$C_p = \frac{\tilde{C}_p - \tilde{C}_0}{\tilde{C}_w - \tilde{C}_0}$	$t = \frac{U_0 \tilde{t}}{R_0}$	$w_p = \frac{\tilde{w}_p}{U_0}$
$\rho_0 = \frac{(\rho_f)_p}{(\rho_f)_c}$	$Pr = \frac{C_p (\mu_f)_p}{(\kappa_f)_p}$	$S_{\tilde{r}\tilde{r}} = \frac{U_0 (\mu_f)_p}{L_0} S_{rr}$	$N_b = \frac{(\rho C)_s (D_B)_p \Delta \tilde{C}}{(\kappa_f)_p}$
$E^* = \frac{E_a}{\tilde{T}_0}$			

$$S_{\tilde{r}\tilde{r}} = (\mu_{nf})_{\wp}\left\{\zeta^*\frac{\partial \tilde{u}_{\wp}}{\partial \tilde{r}}\right\}, \tag{6.16}$$

$$S_{\tilde{z}\tilde{z}} = (\mu_{nf})_{\wp}\left\{\zeta^*\frac{\partial \tilde{w}_{\wp}}{\partial \tilde{z}}\right\}, \tag{6.17}$$

$$S_{\tilde{r}\tilde{z}} = (\mu_{nf})_{\wp}\left\{\zeta^*\left(\frac{\partial \tilde{w}_{\wp}}{\partial \tilde{r}}+\frac{\partial \tilde{u}_{\wp}}{\partial \tilde{z}}\right)\right\}. \tag{6.18}$$

Here, ζ^* is defined as:

$$\begin{aligned}\zeta^* &= (\Gamma\Pi)^{n-1}\\ &= \left\{\left|\Gamma\left(2\left(\frac{\partial \tilde{u}_{\wp}}{\partial \tilde{r}}\right)^2+2\left(\frac{\partial \tilde{w}_{\wp}}{\partial \tilde{z}}\right)^2+2\left(\frac{\tilde{u}_{\wp}}{\tilde{r}}\right)^2+\left(\frac{\partial \tilde{u}_{\wp}}{\partial \tilde{z}}+\frac{\partial \tilde{w}_{\wp}}{\partial \tilde{r}}\right)^2\right)^{\frac{1}{2}}\right|^{n-1}\right\}.\end{aligned} \tag{6.19}$$

6.3 Non-Dimensional Equations

By using the non-dimensionalize parameters mentioned in table 6.1 and mild-stenosis assumption ($\delta << 1$) with $O(1) = \varepsilon = \frac{R_0}{L_0}$, the governing equations reduced to:

For core region $0 < r \leq R_1(z)$

$$\frac{\partial p}{\partial r} = 0, \tag{6.20}$$

$$\frac{\rho_{nf}}{\rho_f}\frac{1}{\rho_0}Re\frac{\partial w_c}{\partial t} = -\frac{\partial p}{\partial z}+\left[\frac{1}{r}\frac{\partial}{\partial r}(rS_{rz})\right]+\frac{(\rho\beta)_{nf}}{(\rho\beta_f)}\frac{1}{\rho_0}GrT_c+\frac{(\rho\beta)_{nf}}{(\rho\beta_f)}\frac{1}{\rho_0}GcC_c-\frac{(\mu_{nf})_p}{\mu_f}\frac{1}{\mu_0}\frac{w_c}{Da} - \frac{\sigma_{nf}}{\sigma_f}M^2w_c, \tag{6.21}$$

$$RePr\frac{k_0}{\rho_0 s_0}\left\{\frac{\kappa_f}{\kappa_{nf}}\frac{(\rho C_p)_{nf}}{(\rho C_p)_f}\right\}\frac{\partial T_c}{\partial t} = \frac{\partial^2 T_c}{\partial r^2}+\frac{1}{r}\frac{\partial T_c}{\partial r}+\kappa_0\left(\frac{\kappa_f}{\kappa_{nf}}\right)\left\{\frac{N_b}{(D_B)_0}\frac{\partial T_c}{\partial r}\frac{\partial C_c}{\partial r}+\frac{N_t}{(D_T)_0}\left(\frac{\partial T_c}{\partial r}\right)^2 + Nr\left(\frac{\partial^2 T_c}{\partial r^2}+\frac{1}{r}\frac{\partial T_c}{\partial r}\right)+\frac{\mu_{nf}}{\mu_f}\frac{1}{\mu_0}Br\left(\frac{\partial w_c}{\partial r}\right)^2+\frac{\sigma_{nf}}{\sigma_f}M^2Brw_c^2\right\}, \tag{6.22}$$

$$ReSc(D_B)_0\frac{\partial C_c}{\partial t}=\frac{\partial^2 C_c}{\partial r^2}+\frac{1}{r}\frac{\partial C_c}{\partial r}+\frac{(D_B)_0}{(D_T)_0}\frac{N_t}{N_b}\left(\frac{\partial^2 T_c}{\partial r^2}+\frac{1}{r}\frac{\partial T_c}{\partial r}\right)-\xi Sc(D_B)_0(1+\Omega T_c)^{m_1}e^{-\frac{E^*}{1+\Omega T_c}}C_c. \tag{6.23}$$

For plasma region $R_1(z)<r\leq R(z)$

$$\frac{\partial p}{\partial r}=0, \tag{6.24}$$

$$\frac{\rho_{nf}}{\rho_f}Re\frac{\partial w_p}{\partial t}=-\frac{\partial p}{\partial z}+\frac{\mu_{nf}}{\mu_f}\left[\frac{1}{r}\frac{\partial}{\partial r}\left(r\frac{\partial w_p}{\partial r}\right)\right]+\frac{(\rho\beta)_{nf}}{(\rho\beta_f)}GrT_p+\frac{(\rho\beta)_{nf}}{(\rho\beta_f)}GcC_p-\frac{\mu_{nf}}{\mu_f}\frac{w_p}{Da}-\frac{\sigma_{nf}}{\sigma_f}M^2w_p, \tag{6.25}$$

$$\begin{aligned}RePr\left\{\frac{\kappa_f}{\kappa_{nf}}\frac{(\rho C_p)_{nf}}{(\rho C_p)_f}\right\}\frac{\partial T_p}{\partial t}=&\frac{\partial^2 T_p}{\partial r^2}+\frac{1}{r}\frac{\partial T_p}{\partial r}+\left(\frac{\kappa_f}{\kappa_{nf}}\right)\left\{N_b\frac{\partial T_p}{\partial r}\frac{\partial C_p}{\partial r}+N_t\left(\frac{\partial T_p}{\partial r}\right)^2\right.\\&\left.+Nr\left(\frac{\partial^2 T_p}{\partial r^2}+\frac{1}{r}\frac{\partial T_p}{\partial r}\right)+\frac{\mu_{nf}}{\mu_f}Br\left(\frac{\partial w_p}{\partial r}\right)^2+\frac{\sigma_{nf}}{\sigma_f}M^2Brw_p^2\right\},\end{aligned} \tag{6.26}$$

$$ReSc\frac{\partial C_p}{\partial t}=\frac{\partial^2 C_p}{\partial r^2}+\frac{1}{r}\frac{\partial C_p}{\partial r}+\frac{N_t}{N_b}\left(\frac{\partial^2 T_p}{\partial r^2}+\frac{1}{r}\frac{\partial T_p}{\partial r}\right)-\xi Sc(1+\Omega T_p)^{m_1}e^{-\frac{E^*}{1+\Omega T_p}}C_p. \tag{6.27}$$

The constant ζ^* is given as:

$$\begin{aligned}\zeta^*=&\left\{\left|\Gamma\left(2\left(\frac{\delta^* U_0}{R_0L_0}\right)^2\left(\frac{\partial u_{\wp}}{\partial r}\right)^2+2\left(\frac{U_0}{L_0}\right)^2\left(\frac{\partial w_{\wp}}{\partial z}\right)^2+2\left(\frac{\delta^* U_0}{R_0L_0}\right)^2\left(\frac{u_{\wp}}{r}\right)^2\right.\right.\\&\left.\left.+\left(\frac{\delta^* U_0}{L_0^2}\frac{\partial u_{\wp}}{\partial z}+\frac{U_0}{R_0}\frac{\partial w_{\wp}}{\partial r}\right)^2\right)^{\frac{1}{2}}\right|^{n-1}\right\}\end{aligned} \tag{6.28}$$

$$=\left\{\left|\Gamma\left(\frac{U_0}{R_0}\right)\left(2(\delta\varepsilon)^2\left(\frac{\partial u_{\wp}}{\partial r}\right)^2+2(\varepsilon)^2\left(\frac{\partial w_{\wp}}{\partial z}\right)^2+2(\delta\varepsilon)^2\left(\frac{u_{\wp}}{r}\right)^2+\left(\delta\varepsilon\frac{\partial u_{\wp}}{\partial z}+\frac{\partial w_{\wp}}{\partial r}\right)^2\right)^{\frac{1}{2}}\right|^{n-1} \tag{6.29}$$

The non-dimensionalize shear stress component S_{rz} is written as:

$$\begin{aligned} S_{rz} &= \frac{(\mu_{nf})_{\wp}}{(\mu_f)_p}\left\{\zeta^*\left(\frac{\partial w_{\wp}}{\partial r}\right)\right\} \\ &= \frac{(\mu_{nf})_{\wp}}{(\mu_f)_p}\left\{We^2\left|\frac{\partial w_{\wp}}{\partial r}\right|^2\right\}^{\left(\frac{n-1}{2}\right)}\frac{\partial w_{\wp}}{\partial r} \end{aligned} \tag{6.30}$$

Use equation (6.28) and (6.30) to get the momentum equations in core region as:

$$\begin{aligned} \frac{\rho_{nf}}{\rho_f}\frac{1}{\rho_0}Re\frac{\partial w_c}{\partial t} =& -\frac{\partial p}{\partial z} + \frac{\mu_{nf}}{\mu_f}\frac{1}{\mu_0}\left[\frac{1}{r}\frac{\partial}{\partial r}\left\{r\left[\left\{(We)^2\left|\frac{\partial w_c}{\partial r}\right|^2\right\}^{\frac{n-1}{2}}\left(\frac{\partial w_c}{\partial r}\right)\right]\right\}\right] \\ &+ \frac{(\rho\beta)_{nf}}{(\rho\beta)_f}\frac{1}{\rho_0}GrT_c + \frac{(\rho\beta)_{nf}}{(\rho\beta)_f}\frac{1}{\rho_0}GcC_c - \frac{\mu_{nf}}{\mu_f}\frac{1}{\mu_0}\frac{w_c}{Da} - \frac{\sigma_{nf}}{\sigma_f}M^2 w_c, \end{aligned} \tag{6.31}$$

The dimensionless formulation of boundary conditions are described as:

$$\begin{cases} w_{\wp} = T_{\wp} = C_{\wp} = 0 & \text{at} \quad t = 0, \\ \frac{\partial w_c}{\partial r} = 0, \quad \frac{\partial T_c}{\partial r} = 0, \quad \frac{\partial C_c}{\partial r} = 0, & \text{at} \quad r = 0, \\ w_c = w_p, \quad T_c = T_p, \quad C_c = C_p & \text{at} \quad r = R_1(z), \\ \tau_c = \tau_p, \quad \frac{\partial T_c}{\partial r} = \frac{\partial T_p}{\partial r}, \quad \frac{\partial C_c}{\partial r} = \frac{\partial C_p}{\partial r} & \text{at} \quad r = R_1(z), \\ w_p = 0, \quad T_p = 1, \quad C_p = 1 & \text{at} \quad r = R(z). \end{cases} \tag{6.32}$$

The dimensionless pressure gradient is written as:

$$-\frac{\partial p}{\partial z} = B_1(1 + e\cos(c_1 t)), \tag{6.33}$$

where, $B_1 = \frac{A_0 R_0^2}{(\mu_f)_p U_0}, e = \frac{A_1}{A_0}$ and $c_1 = \frac{2\pi R_0 \omega_p}{U_0}$.

6.3.1 Non-Dimensional Form for Geometry of Diseased Arterial Segment

The geometry of the stenosis in the core region is considered as:

$$R(z)=\begin{cases}1-\frac{6\delta}{5}\left\{11(z-d)^3-47(z-d)^2+72(z-d)-36(z-d)^4\right\}, & \text{for} \quad d<z\leq d+1,\\ 1, & \text{otherwise}\end{cases} \tag{6.34}$$

The geometry of the stenosis in the plasma region is considered as:

$$R_1(z)=\begin{cases}\bar{\beta}-\frac{6\delta}{5}\left\{11(z-d)^3-47(z-d)^2+72(z-d)-36(z-d)^4\right\}, & \text{for} \quad d<z\leq d+1,\\ \bar{\beta}, & \text{otherwise}\end{cases} \tag{6.35}$$

6.3.2 Quantities of Physical Interest

The radial transformation, denoted as $x_1=\frac{r}{R(z)}$, is employed within the governing equations for restraining the geometric effects. Then, the volumetric flow rate is defined as [109]:

$$\begin{aligned}Q^f =& R^2\int_0^1\int_0^\pi x_1 w dx_1 d\theta \\ =& R^2\left(\int_0^{\bar{\beta}}\int_0^\pi x_1 w_c dx_1 d\theta+\int_{\bar{\beta}}^1\int_0^\pi x_1 w_p dx_1 d\theta\right).\end{aligned} \tag{6.36}$$

Here, $\bar{\beta}=0.75$ is the interface between the plasma and core region. The resistance impedance is given as:

$$\lambda=\frac{\int_0^L(-\frac{\partial p}{\partial z})dz}{Q^f}. \tag{6.37}$$

The WSS, Nusselt (Nu) and Sherwood (Sh) are given as:

$$\tau_w=-\frac{1}{R}\left(\frac{\partial w}{\partial x_1}\right)_{x_1=1},\quad Nu=-\frac{1}{R}\left(\frac{\partial T}{\partial x_1}\right)_{x_1=1}\quad Sh=-\frac{1}{R}\left(\frac{\partial C}{\partial x_1}\right)_{x_1=1} \tag{6.38}$$

6.4 Numerical Method

The Method of Lines (MOL) represents a prominent numerical approach employed for the resolution of partial differential equations (PDEs) by discretizing along the spatial coordinates resulting into a system of ordinary differential equations (ODEs) which can be further solved by time-stepping methods [158, 160]. This particular approach, characterized by

the exclusive discretization of spatial coordinates while keeping the temporal domain continuous, is conventionally referred to as 'semi-discretization' method. The relevant partial differentials are defined as:

$$\frac{\partial f}{\partial x} = \frac{f_{i+1} - f_{i-1}}{2h} \tag{6.39}$$

$$\frac{\partial^2 f}{\partial x^2} = \frac{f_{i+1} - 2f_i + f_{i-1}}{h^2} \tag{6.40}$$

The Method of Lines (MOL) substitutes the exact or analytical solutions for the functions $w(r,t)$, $T(r,t)$, and $C(r,t)$ in the spatial domain with an approximate solution denoted as $w(t)$, $T(t)$, and $C(t)$ for a specific range of indices $i = 1,2,...,N+1$. This approximation is computed along a finite set of straight lines, as illustrated in Figure 6.3.

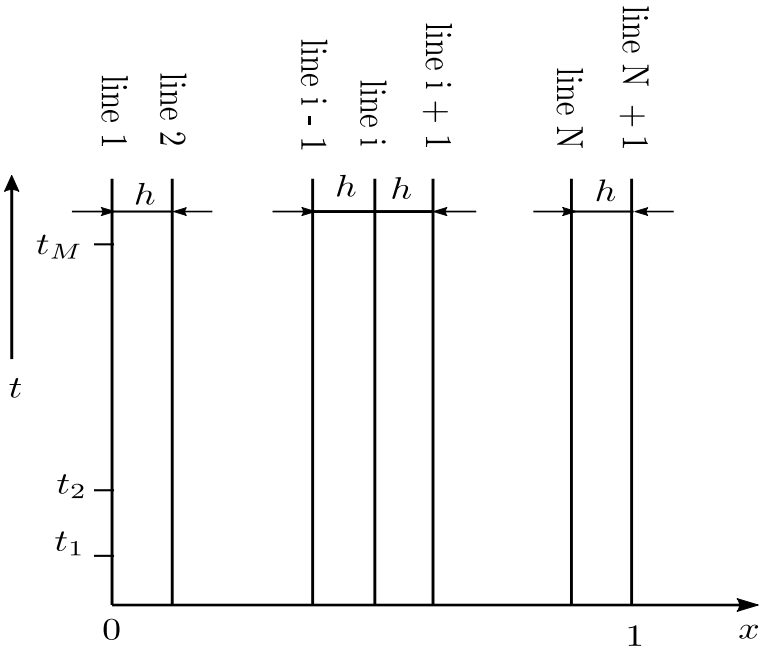

Figure 6.3: Computational domain for Method of Lines (MOL)

The radial transformation, denoted as $x_1 = \frac{r}{R(z)}$, is employed within the governing equations for restraining the geometric effects. This transformation is subsequently applied to equations (6.20) - (6.32). Afterward, equations (6.39) and (6.40) are introduced into the resulting equations, leading to the formulation of a system of first-order ordinary differential equations (ODEs) along the straight line i, where i ranges from 2 to N.

For core region $(0 < x_1 \leq 0.75)$,

$$\frac{dw_i}{dt} = \frac{1}{Re}\frac{\rho_0\rho_f}{\rho_{nf}}\left[\frac{\mu_{nf}}{\mu_f}\frac{1}{\mu_0}\frac{1}{R^{n+1}}\left\{\frac{1}{x_{1i}}\left(We\left|\frac{w_{i+1}-w_{i-1}}{2h}\right|\right)^{n-1}\left(\frac{w_{i+1}-w_{i-1}}{2h}\right)\right.\right.$$
$$+\left(\frac{w_{i+1}-2w_i+w_{i-1}}{h^2}\right)\left\{\left(We\left|\frac{w_{i+1}-w_{i-1}}{2h}\right|\right)^{n-1}+(n-1)We^{n-1}\left(\left|\frac{w_{i+1}-w_{i-1}}{2h}\right|\right)^{n-2}\right.$$
$$\left.\left.\left.\frac{w_{i+1}-w_{i-1}}{2h}\right\}\right\}\right]+\frac{1}{Re}\frac{(\beta)_{nf}}{(\beta)_f}GrT_i+\frac{1}{Re}\frac{(\beta)_{nf}}{(\beta)_f}GcC_i+\left(\frac{1}{Re}\frac{\rho_0\rho_f}{\rho_{nf}}\right)\left\{-\frac{\mu_{nf}}{\mu_f}\frac{1}{\mu_0}\frac{w_i}{Da}\right.$$
$$\left.+E_p(1+e\cos(c_1t))-\frac{\sigma_{nf}}{\sigma_f}M^2w_i\right\} \tag{6.41}$$

$$\frac{dT_i}{dt} = \left(\frac{\rho_0 s_0}{k_0}\frac{1}{RePr}\frac{\kappa_{nf}}{\kappa_f}\frac{(\rho C_p)_f}{(\rho C_p)_{nf}}\right)\frac{1}{R^2}\left\{\frac{T_{i+1}-2T_i+T_{i-1}}{h^2}+\frac{1}{x_{1i}}\frac{T_{i+1}-T_{i-1}}{2h}\right\}+\frac{(\rho_0 s_0)}{RePr}\frac{N_b}{(D_B)_0}$$
$$\frac{1}{R^2}\frac{(\rho C_p)_f}{(\rho C_p)_{nf}}\left\{\frac{T_{i+1}-T_{i-1}}{2h}\cdot\frac{C_{i+1}-C_{i-1}}{2h}\right\}+\frac{(\rho_0 s_0)}{RePr}\frac{1}{R^2}N_t\frac{(\rho C_p)_f}{(\rho C_p)_{nf}}\frac{1}{(D_T)_0}\left\{\left(\frac{T_{i+1}-T_{i-1}}{2h}\right)^2\right\}$$
$$+\left(\frac{1}{R^2}\frac{\rho_0 s_0}{RePr}\frac{(\rho C_p)_f}{(\rho C_p)_{nf}}\right)\left[Nr\left\{\frac{T_{i+1}-2T_i+T_{i-1}}{h^2}+\frac{1}{x_{1i}}\frac{T_{i+1}-T_{i-1}}{2h}\right\}+\frac{\mu_{nf}}{\mu_f}\frac{1}{\mu_0}Br\right. \tag{6.42}$$
$$\left.\left(\frac{w_{i+1}-w_{i-1}}{2h}\right)^2\right]+\left(\frac{\rho_0 s_0}{RePr}\frac{(\rho C_p)_f}{(\rho C_p)_{nf}}\right)\frac{\sigma_{nf}}{\sigma_f}M^2Brw_i^2,$$

$$\frac{dC_i}{dt} = \frac{1}{R^2}\frac{1}{ReSc(D_B)_0}\left\{\frac{C_{i+1}-2C_i+C_{i-1}}{h^2}+\frac{1}{x_{1i}}\frac{C_{i+1}-C_{i-1}}{2h}\right\}+\frac{1}{ReSc(D_T)_0}\frac{N_t}{N_b}\frac{1}{R^2}$$
$$\left\{\frac{C_{i+1}-2C_i+C_{i-1}}{h^2}+\frac{1}{x_{1i}}\frac{C_{i+1}-C_{i-1}}{2h}\right\}-\frac{\xi}{Re}(1+\Omega T_i)^{m_1}e^{-\frac{E^*}{1+\Omega T_i}}C_i \tag{6.43}$$

For plasma region $(0.75 < x_1 \leq 1)$,

$$\frac{dw_i}{dt} = \frac{1}{Re}\frac{\rho_f}{\rho_{nf}}\left[\frac{\mu_{nf}}{\mu_f}\frac{1}{R^2}\left\{\frac{1}{x(i)}\left(\frac{w_{i+1}-w_{i-1}}{2h}\right)+\frac{w_{i+1}-2w_i+w_{i-1}}{h^2}\right\}\right.$$
$$\left.+\frac{(\rho\beta)_{nf}}{(\rho\beta)_f}GrT_i+\frac{(\rho\beta)_{nf}}{(\rho\beta)_f}GcC_i+\left\{-\frac{\mu_{nf}}{\mu_f}\frac{w_i}{Da}\right\}+E_p(1+e\cos(c_1t))-\frac{\sigma_{nf}}{\sigma_f}M^2w_i\right] \tag{6.44}$$

$$\frac{dT_i}{dt} = \left(\frac{1}{RePr}\frac{\kappa_{nf}}{\kappa_f}\frac{(\rho C_p)_f}{(\rho C_p)_{nf}}\right)\frac{1}{R^2}\left\{\frac{T_{i+1}-2T_i+T_{i-1}}{h^2}+\frac{1}{x_{1i}}\frac{T_{i+1}-T_{i-1}}{2h}\right\}+\frac{1}{RePr}N_b\frac{1}{R^2}\frac{(\rho C_p)_f}{(\rho C_p)_{nf}}$$
$$\left\{\frac{T_{i+1}-T_{i-1}}{2h}\cdot\frac{C_{i+1}-C_{i-1}}{2h}\right\}+\frac{1}{RePr}\frac{1}{R^2}N_t\frac{(\rho C_p)_f}{(\rho C_p)_{nf}}\left\{\left(\frac{T_{i+1}-T_{i-1}}{2h}\right)^2\right\}$$
$$+\left(\frac{1}{R^2}\frac{1}{RePr}\frac{(\rho C_p)_f}{(\rho C_p)_{nf}}\right)\left[Nr\left\{\frac{T_{i+1}-2T_i+T_{i-1}}{h^2}+\frac{1}{x_{1i}}\frac{T_{i+1}-T_{i-1}}{2h}\right\}\right. \tag{6.45}$$
$$\left.+\frac{\mu_{nf}}{\mu_f}Br\left(\frac{w_{i+1}-w_{i-1}}{2h}\right)^2\right]+\left(\frac{1}{RePr}\frac{(\rho C_p)_f}{(\rho C_p)_{nf}}\right)\frac{\sigma_{nf}}{\sigma_f}M^2Brw_i^2,$$

$$\frac{dC_i}{dt} = \frac{1}{R^2}\frac{1}{ReSc}\left\{\frac{C_{i+1}-2C_i+C_{i-1}}{h^2}+\frac{1}{x_{1i}}\frac{C_{i+1}-C_{i-1}}{2h}\right\}+\frac{1}{ReSc}\frac{N_t}{N_b}\frac{1}{R^2}\left\{\frac{C_{i+1}-2C_i+C_{i-1}}{h^2}\right.$$
$$\left.+\frac{1}{x_{1i}}\frac{C_{i+1}-C_{i-1}}{2h}\right\}-\frac{\xi}{Re}(1+\Omega T_i)^{m_1}e^{-\frac{E^*}{1+\Omega T_i}}C_i \tag{6.46}$$

Furthermore, the initial conditions for ODEs mention from (6.41)-(6.46) is written in discrete form as:

$$w_i(0)=0,\;\; T_i(0)=0,\;\; C_i(0)=0 \tag{6.47}$$

Boundary Conditions:

The three-point forward finite difference formula for function f at $i=1(x=0)$ is given as:

$$\frac{\partial f}{\partial x}=\frac{-f(3)+4f(2)-3f(1)}{2h} \tag{6.48}$$

Use equation (6.32) and (6.48) to write the function w, T and C at $i=1$ as given below:

$$w_1=\frac{4w_2-w_3}{3},\quad T_1=\frac{4T_2-T_3}{3},\quad C_1=\frac{4C_2-C_3}{3}. \tag{6.49}$$

At $i=N+1$,

$$w_{N+1}=0,\quad T_{N+1}=0,\quad C_{N+1}=0. \tag{6.50}$$

Parameters	Ranges	Sources
Thermophoresis parameter (N_t)	0.1-0.8	[15, 16]
Brownian parameter (N_b)	0.1-0.8	[10, 15]
Schmidt number (Sc)	0-3	[1]
Ratio of density in core and plasma region (ρ_0)	1.05	[4, 5]
Ratio of viscosity in core and plasma region (μ_0)	1.2	[3, 4]
Magnetic field parameter (M)	0-$\sqrt{5}$	[33, 175]
Activation energy parameter (E_a)	0.08-1.8	[1, 10]
Weissenberg number (We)	1.5-3.5	[18]

Table 6.2: Values of the physical parameters with their sources

Parameters	ϕ_1	B_1	Gr	Gc	E_a	n	Da^{-1}	Re	$(D_T)_0$	$(D_B)_0$	m_1	ξ	Nr
Ranges	0.02	1.4	2	0.5	0.5	0.7	0.2	2	0.8	0.8	0.6	0.5	2

Table 6.3: Default value of emerging parameters

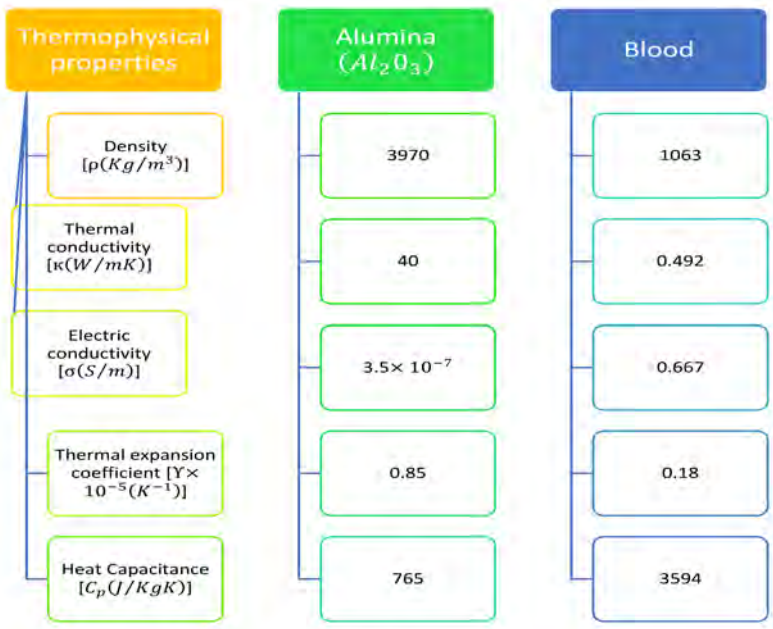

Figure 6.4: Thermophysical properties of blood and nanoparticle

The resulting system of ODEs are initial value problems (IVPs). In order to solve the system of ODEs , we employed the inbuilt MATLAB function 'ode15s,' which operates

through the utilization of a semi-implicit approach recognized as the 'stiff' ODE solver method. Figure 6.4 depicts the thermophysical properties of blood and nanoparticle.

Table 6.4: Thermophysical properties of nanofluid

Properties	Mathematical Expression for Nanofluid
Viscosity	$\mu_{nf} = \frac{\mu_f}{(1-\phi_1)^{2.5}}$
Density	$\rho_{nf} = (1-\phi_1)\rho_f + \phi_1\rho_{s_1}$
Heat Capacity	$(\rho C_p)_{nf} = (1-\phi_1)(\rho C_p)_f + \phi_1(\rho C_p)_{s_1}$
Thermal Conductivity	$\frac{k_{nf}}{k_f} = \frac{k_{s_1}+2k_f-2\phi_1(k_f-k_{s_1})}{k_{s_1}+2k_f+\phi_1(k_f-k_{s_1})}$
Electrical Conductivity	$\frac{\sigma_{nf}}{\sigma_f} = \frac{\sigma_{s_1}+2\sigma_f-2\phi_1(\sigma_f-\sigma_{s_1})}{\sigma_{s_1}+2\sigma_f+\phi_1(\sigma_f-\sigma_{s_1})}$
Thermal Expansion Coefficient	$\beta_{nf} = (1-\phi_1)\beta_f + \phi_1\beta_{s_1}$

6.5 Results and Graphical Analysis

In this section, we comprehensively explored the dynamic of the blood flow phenomena by delving into the graphical illustration and physical significance of different emerging parameters. This study helps in the providing the significant step for understanding the complex physiological phenomena. The present study focuses on the two-phase blood flow in the overlapping stenosed artery. The power law fluid model is adopted to simulate the blood flow in the core region and non-newtonian characteristic of blood has been considered in the plasma region. The Method of Lines (MOL) has been employed to simulate the numerical code. The numerical values of various emerging parameters are presented in table 6.2 and 6.3. The thermo-physical properties of nanofluid is displayed in table 6.4.

6.5.1 Validation

The validation of our work is complemented by the study conducted by Tripathi et al. [176] on two-phase MHD blood flow through a stenosed artery.

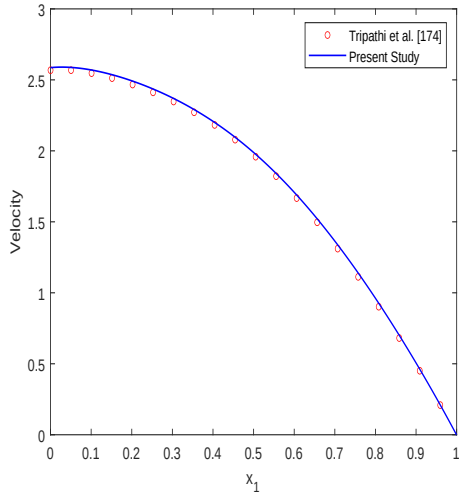

(a) Comparative result for velocity profile for $Gr = 2$

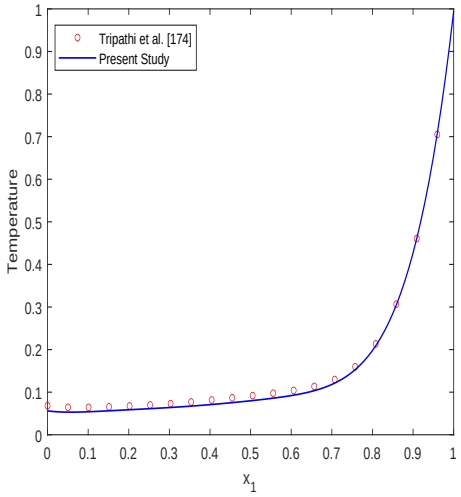

(b) Comparative result for temperature profile for $Nr = 9$

By making appropriate assumptions, we have substantiated the velocity and temperature profiles of our current research through a comparative analysis with the findings of Tripathi et al. [176], as shown in figure 6.5a and 6.5b. Notably, Tripathi et al.[176] employed an analytical methodology to derive solutions for the dimensionless governing equations in their investigation, resulting in exact solutions. In contrast, our study used the Method of Lines (MOL) approach. The ensuing graphical representations demonstrate a noteworthy agreement between our study and the earlier research, thus affirming the consistency of our velocity and temperature profiles with the established literature.

6.5.2 Axial Velocity Profiles

Blood contains iron, primarily in the form of haemoglobin. The presence of a magnetic field exerts a notable influence on the behaviour of blood, primarily attributed to the alignment of iron atoms within the protein molecule known as haemoglobin. The investigation of the influence of the magnetic field parameter M on the velocity profile is motivated by the observed phenomenon, as depicted in Figure 6.6a. The velocity profile exhibits a discernible pattern wherein a decreasing trend is observed as the magnetic field strength increases within the range of 0 to $\sqrt{5}$. This behaviour can be explained by the presence of a strong external magnetic field, which results in the generation of a resistive drag force known as the Lorentz

force, thereby retarding the fluid motion. This effect of magnetic fields on blood properties has notable applications in the biomedical field. A prominent example is magnetic resonance imaging (MRI) machines, which utilize strong magnetic fields to generate images of diseased arteries, including those affected by stenosis.

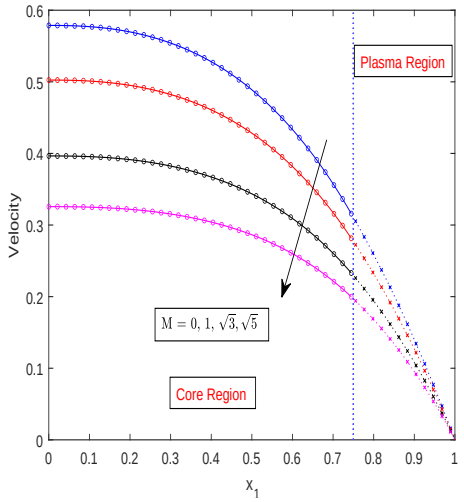

(a) Velocity profile by varying M

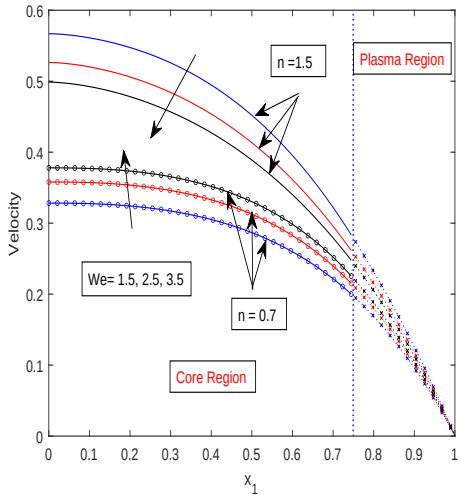

(b) Velocity profile by varying We

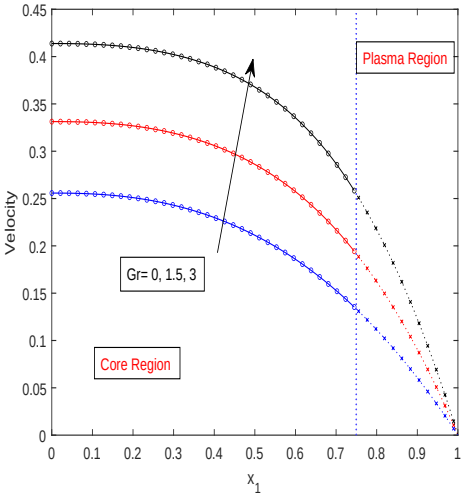

(c) Velocity profile by varying Gr

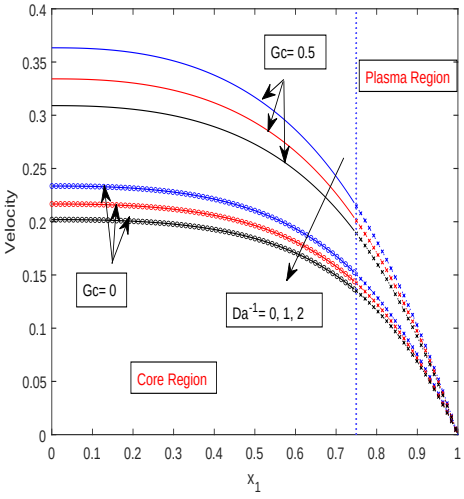

(d) Velocity profile by varying Da^{-1} and Gc

Figure 6.6: Velocity profile

Figure 6.6b depicts the manifestation of the velocity profile's fluctuation as a function of the Weissenberg number within the context of two-phase blood flow. The relationship between a material's relaxation time and deformation time scale is characterised by a dimensionless parameter known as the Weissenberg number. As depicted in the provided figure, it is evident that for a given value of $n = 1.5$, the velocity profile exhibits a noticeable pattern of diminishing magnitude with increasing Weissenberg number (We). The empirical

evidence gathered from the observations strongly indicates a positive correlation between the rise in resistance to deformation and the concurrent elevation in the Weissenberg number. In the realm of shear-thickening fluids, which exhibit a power-law index of $n = 1.5$, it has been noted that as the applied shear stress or strain rate increases, the fluid's resistance to flow becomes increasingly prominent.

In the context of a shear-thinning fluid exhibiting power-law behaviour with an exponent of $n = 0.7$, it has been observed that the velocity profile shows a discernible inclination towards higher values as the Weissenberg number is increased. The observed phenomenon can be ascribed to the distinctive attributes of shear-thickening fluids, which manifest diminished opposition to deformation. As a result, this phenomenon allows for enhanced fluid flow under conditions of increased stress or strain rates.

The impact of the Grashof number on the velocity profile is illustrated in Figure 6.6c. It is observed that the velocity profile exhibits a decreasing trend as the Grashof number (Gr) increases from 0 to 3. The observed phenomenon aligns with an increase in the prevalence of buoyancy forces in the constricted artery, which arises due to temperature fluctuations. The investigation examines the influence of two key parameters, namely the concentration gradient (Gc) and the inverse of the Darcy number (Da^{-1}), on the velocity profile. The visualisation of this relationship is presented in Figure 6.6d. The observed trend indicates that the velocity profile increases as the parameter Gc is augmented while concurrently displaying a decrease as the inverse Darcy number Da^{-1} rises. According to the study's findings, it has been proposed that the presence of a porous medium within the flow contributes to the resistance experienced by the fluid during its movement. Furthermore, in the scenario where ($Da \to \infty$), the porosity of the medium becomes negligible or effectively disappears. The inverse of the Darcy number, Da^{-1}, reflects the resistance offered by the porous medium. As Da^{-1} increases, the resistance intensifies, decreasing the velocity profile. On the other hand, increasing the Grashof number (Gc) from 0 to 0.5 results in a heightened concentration gradient within the fluid. The observed phenomenon of an increase in the velocity profile can be attributed to an amplified concentration gradient.

6.5.3 Temperature Profile

The investigation aims to analyse the impact of various parameters, precisely the Prandtl number (Pr), Radiation parameter (Nr), Thermophoresis parameter (N_t), and Brownian parameter (N_b), on the temperature profile, as illustrated in figure 6.7. The temperature profile shown in Figure 6.7a significantly decreases as the Prandtl number (Pr) increases from 19 to 27. The aforementioned tool is valuable in characterising the intricate relationship between momentum transport and thermal diffusivity within a fluid system.

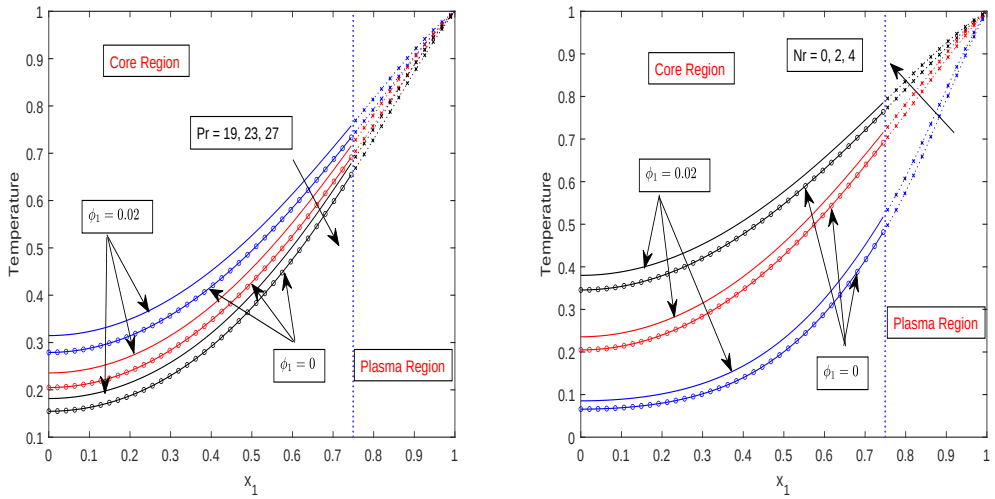

(a) Influence of Pr and ϕ_1 on temperature profile **(b)** Influence of Nr and ϕ_1 on temperature profile

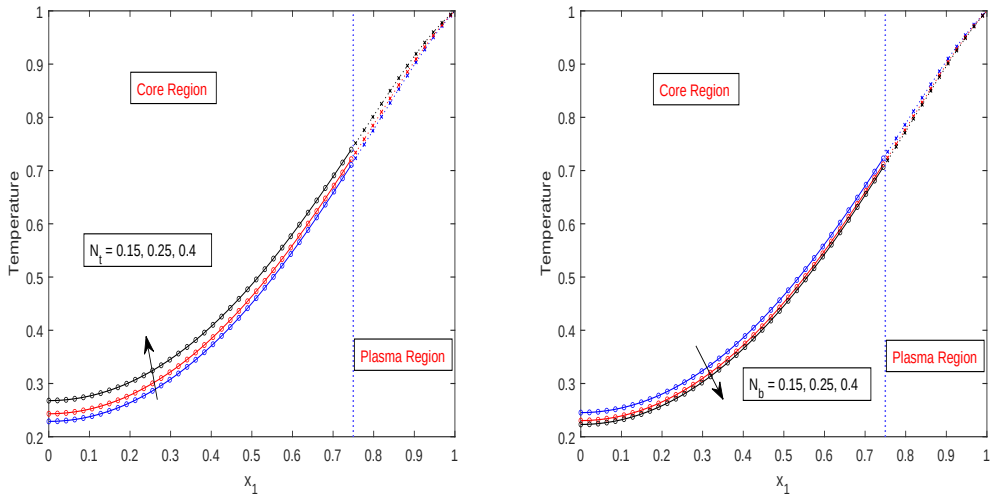

(c) Temperature profile by varying N_t **(d)** Temperature profile by varying N_b

Figure 6.7: Temperature profile

A higher Prandtl number indicates a comparatively lower thermal conductivity compared to a smaller Prandtl number. The empirical evidence gathered from this observation suggests a positive correlation between the Prandtl number and the temperature profiles exhibited by fluids. Specifically, fluids with smaller Prandtl numbers exhibit higher temperature profiles than those with larger Prandtl numbers. The correlation between the radiation parameter and the temperature profile is elucidated in Figure 6.7b. Based on the available evidence, it can be deduced that the presence of radiation serves as a catalyst for the generation of thermal energy, leading to a discernible elevation in the overall temperature profile. The utilization of radiation in biomedicine, particularly in the discipline of radiation therapy, entails the strategic deployment of this energy to manipulate the temperature distribution to eradicate

malignant cells with optimal efficacy. The observed phenomenon of the temperature profile increment is elucidated by the graphical representation provided in Figure 6.7c. This increment is directly correlated with the increase in the parameter N_t. As the value of the parameter N_t is incremented, a corresponding effect is observed in the motion of particles, which is driven by the temperature gradient. Consequently, this phenomenon gives rise to an elevation in the temperature profile. Figure 6.7d illustrates the diminishing characteristic of the temperature profile with the parameter N_b. An elevation in the Brownian parameter is directly associated with an amplification in the thermal conductivity of the fluid. This augmentation leads to a more balanced dispersion of thermal energy within the fluid, resulting in a reduced temperature gradient.

6.5.4 Concentration Profile

The concentration profile is illustrated in Figure 6.8, showcasing the impact of variables such as E, ξ, N_t, and N_b. The concept of activation energy refers to the minimum amount of energy that must be surpassed to initiate a chemical reaction. Thus, it is an important decisive factor in regulating the chemical reaction. The solutal chemical reaction exhibits a decrease in response to an increase in the variable E, thereby resulting in an augmentation of solute concentration as depicted in figure 6.8a. The influence of chemical reaction parameter on the concentration profile is illustrated in the figure 6.8b. The higher value of ξ associated with reduced molecular diffusion. The observed relationship between the parameter ξ and the molecular diffusivity of chemical species within a system suggests that an increase in ξ is associated with a decrease in diffusivity. Consequently, this leads to a reduction in the overall diffusion process, thus, lead to reduction in concentration profile. The concentration profile in the stenotic region for N_t is depicted in Figure 6.8c. The analysis of the figure reveals that there is a noticeable decrease in the concentration profile within both the core and plasma regions as the thermophoresis parameter increases from 0.15 to 0.4. The increase in the parameter N_t results in an elevation of the temperature gradient, which subsequently induces the accumulation of particles towards the region of higher temperature. This accumulation ultimately leads to an increase in the concentration profile. The concentration profile for N_b exhibits an opposite trend. An increase in the Brownian motion parameter results in a reduction in the concentration gradient, leading to the formation of a more uniform concentration profile.

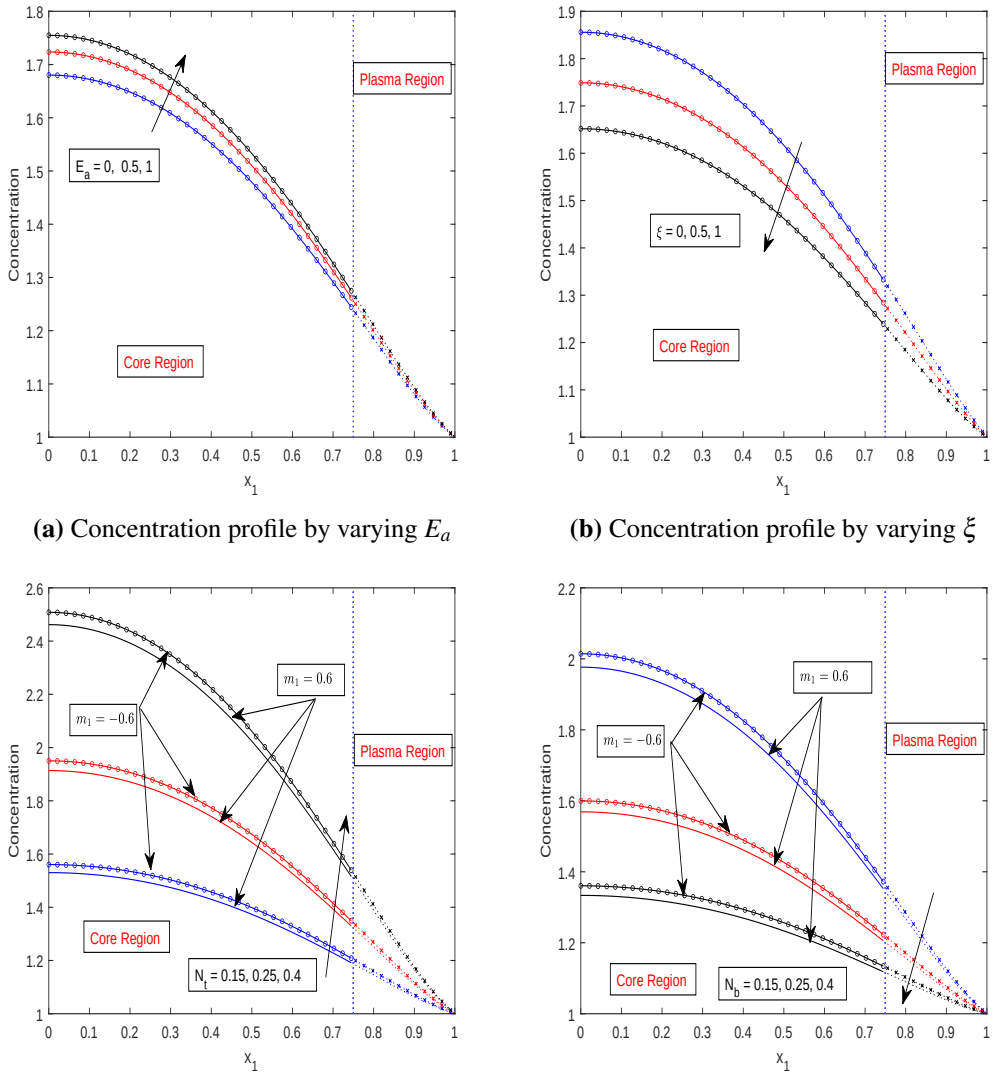

(a) Concentration profile by varying E_a

(b) Concentration profile by varying ξ

(c) Concentration profile by varying N_t

(d) Concentration profile by varying N_b

Figure 6.8: Concentration profile

6.5.5 Wall Shear Stress (WSS)

WSS is the frictional force acting tangentially to the surface. It is the key factors to understand the hemodynamic flow around the wall of the stenotic region. In biomedical field, the study of WSS helps the researchers to get insight to the mechanical force experienced by endothelial cells at the arterial wall. 6.9a potrays the influence of magnetic field parameter on the WSS profile. The WSS profile shows the declining nature for the increasing magnetic field parameter M.

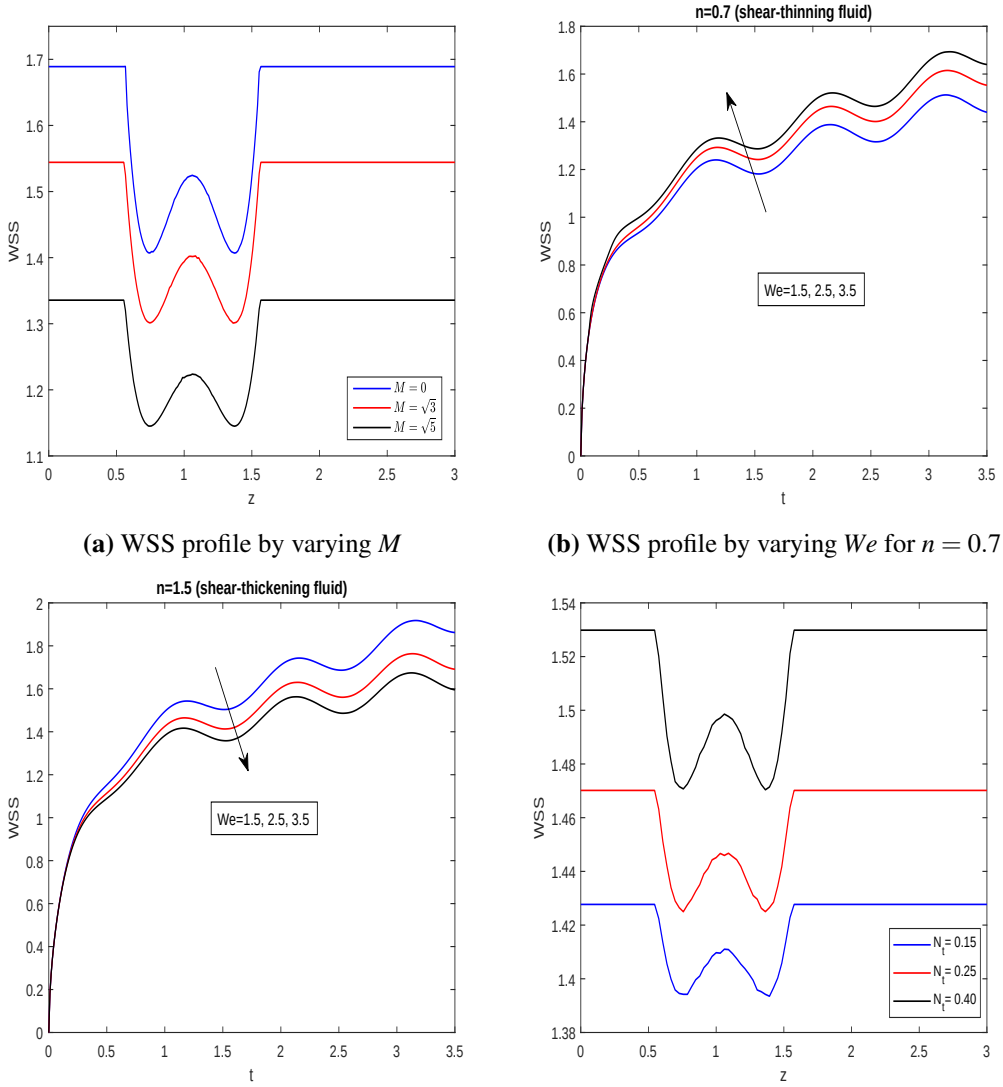

(a) WSS profile by varying M

(b) WSS profile by varying We for $n = 0.7$

(c) WSS profile by varying We for $n = 1.5$

(d) WSS profile by varying N_t

Figure 6.9: WSS profile

On enhancing the magnetic field the blood experience the resistive Lorentz flow that impede the fluid flow along the arterial wall and reduces the WSS profile. Figures 6.9b and 6.9c depict the influence of We on the time-series graph of the WSS profile for shear-thinning fluid and shear-thickening. The WSS profile increases for $n = 0.5$ and decreases for $n = 1.5$ as the We number increases from 1.5 to 3.5. respectively. This contrasting behaviour can be attributed to the varying rates of deformation concerning changes in We, which, for $n = 1.5$, lead to heightened deformation rates, while the opposite holds for $n = 0.5$.

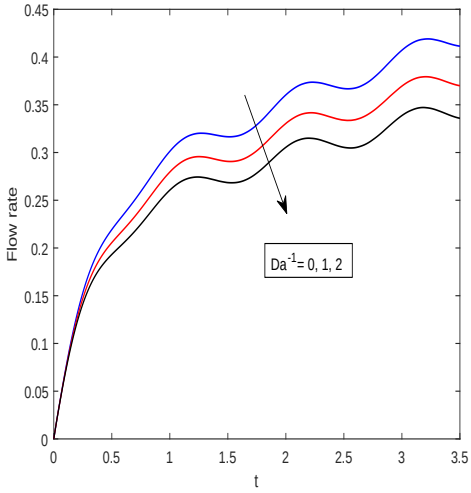

(a) Flow rate by varying Da^{-1}

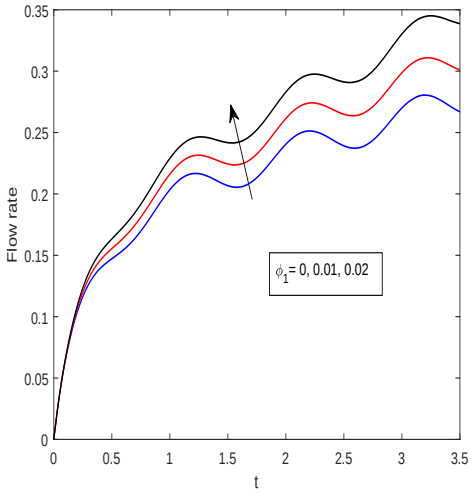

(b) Flow rate by varying ϕ_1

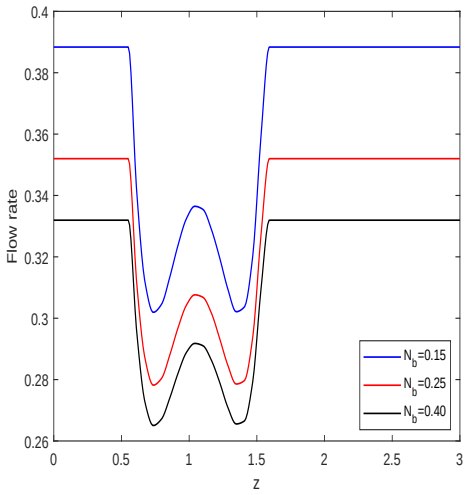

(c) Flow rate by varying N_b

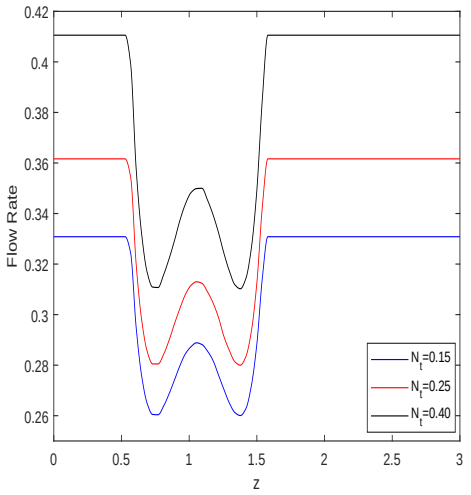

(d) Flow rate by varying N_t

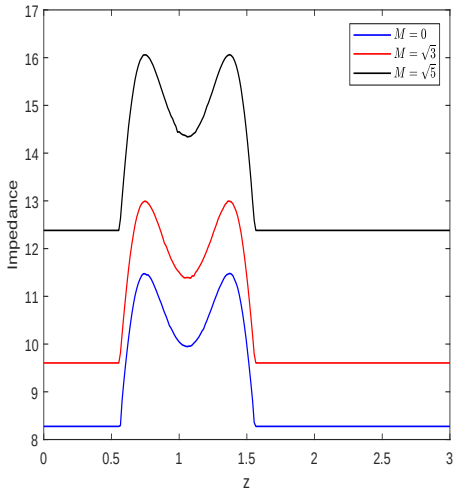

(e) Impedance by varying M

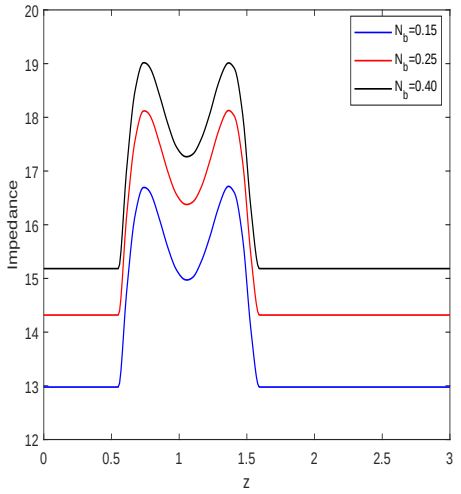

(f) Impedance profile by varying N_b

Figure 6.10: Flow rate and Impedance Profile

Consequently, these alterations in WSS profiles have implications for hemodynamic behaviour, potentially resulting in altered blood flow patterns near arterial walls. Figure 6.9d depict the influence of N_t on the WSS profile. Clearly, it can be observed form the figure that the WSS profile decreases as the magnitude of N_t increases from 0.15 to 0.40.

6.5.6 Flow Rate and Impedance

Flow rate is the amount of fluid that passes through the conduit (artery) per unit time. The influence of Da^{-1}, N_b, N_t and ϕ_1 on the flow rate profile. The influence of (Da^{-1}) on the flow rate is depicted in Figure 6.10a. This illustrates that the flow rate profile decreases as Da^{-1} decreases from 0 to 2. Permeability is a fundamental parameter used to measure the degree of ease with which blood can pass through a porous medium. As (Da^{-1}) increases, there is a corresponding decrease in permeability. This decrease in permeability reduces blood flow through stenotic regions, reducing the flow rate profile. The influence of the parameter ϕ_1 on the temporal progression of flow rate within a system is depicted in Figure 6.10b. The results described in the analysis showcase a notable trend in which the velocity of blood increases as the concentration of nanoparticles varies within the range of 0 to 0.02. It is worth noting that the fluid within the system exhibits a significant characteristic in its central region, as it conforms to a power law pattern with a power-law index denoted as $n = 0.7$.

This specific parameter $n = 0.7$ signifies the shear-thinning property of the fluid, wherein the viscosity of the fluid diminishes with an escalation in the shear rate. As a result, it can be observed that an increase in the concentration of nanoparticles leads to a corresponding decrease in the viscosity of the fluid and an improvement in the flow rate profile. Figure 6.10c portrays the decrement profile of flow rate with enhancement in Brownian motion parameter N_b while the reverse trend is observed for N_t as shown in 6.10c. A higher value of the variable N_b corresponds to a concomitant decrease in the nanoparticle's size; conversely, a lower value of N_b corresponds to an increase in nanoparticle size. The presence of these diminutive nanoparticles serves to decelerate the flow rate profile. The figure 6.10d illustrates the influence exerted by the thermophoresis parameter N_t on the blood flow velocity. In contrast to the prevailing trend resulting from the increase in the Brownian motion parameter, it is observed that the velocity profile experiences a significant enhancement as the thermophoresis parameter is elevated. The thermophoretic body force propels nanoparticles in response to a temperature gradient. The phenomenon mentioned above facilitates the progression of momentum, expedites the fluid motion and enhances the flow rate profile. Impedance is defined as the resistive force that a fluid experiences as it flows through a surface or body. Clearly, from figure 6.10e, it can be inferred that the impedance profile increases as the

magnetic field parameter increases. The composition of blood includes minute magnetic iron particles that are evenly dispersed throughout its plasma. The phenomenon of electromotive activity in blood gives rise to the rotational motion of charged particles in tandem with the magnetic components present within the blood. The aforementioned phenomenon induces the suspension of electrically charged particles as well as erythrocytes within the circulatory fluid, thereby leading to an elevation in its viscosity. Hence, the Lorentz force that arises from the interaction between moving particles and the applied magnetic field counteracts the velocity of blood, thereby augmenting the Impedance profile. Figure 6.10f exhibits a discernible trend of decline in the impedance profile as the value of N_b increases from 0.15 to 0.4. The observed phenomenon can be attributed to the simultaneous rise in resistive forces, ascribed to the reduction in size of the nanoparticles.

6.5.7 Velocity Contour

This section illustrates the velocity contours, which serve as visual representations of the velocity field inside a constricted artery. The presented contours give significant insights into the spatial fluctuations of velocity within the fluid, providing a complete comprehension of the velocity variations at various positions inside the artery. Figure 6.11 illustrates the influence of the magnetic field parameter, denoted as M, on the velocity contour profile. Notably, the fluid velocity shows a diminishing trend as the magnetic field strength increases, as shown in figures 6.11a - 6.11c. Specifically, the highest fluid velocity, reaching 0.6, is observed in the absence of a magnetic field, as depicted in figure 6.11a. Subsequently, as the magnetic field strength escalates from $M = 1$ to $M = 3$, a discernible reduction in the velocity field pattern within the contour becomes apparent. The observed decrease in velocity can be ascribed to the resistive Lorentz force exerted within the system, highlighting the complex interaction between magnetic fields and fluid dynamics within the framework of this investigation.

Figure 6.12 illustrates the influence of Da^{-1} on the velocity contour. The fluid velocity pattern decreases as The bolous reduces as Da^{-1} increases from 0 to 2. This has happened due to the dominance of the viscous forces over the inertial force. This results in the decrement in the velocity field as shwown in figure 6.12. The influence of varying nanoparticle concentration on the observed velocity patterns is visually depicted in figure 6.13. Nanoparticles have garnered considerable attention in biomedicine due to their small size, large surface area, and ability to be tailored with specific surface chemistry. These characteristics collectively enable the adequate transportation of therapeutic payloads.

In the current study, the utilisation of Al_2O_3 nanoparticles has been implemented to examine their impact on the dynamics of two-phase blood flow. The utilisation of Al_2O_3

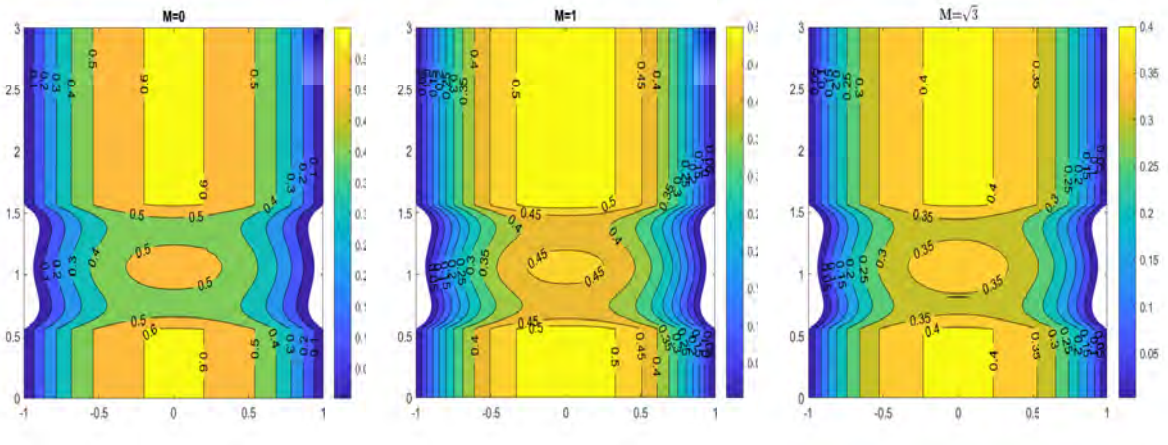

(a) **(b)** **(c)**

Figure 6.11: Velocity contour for M

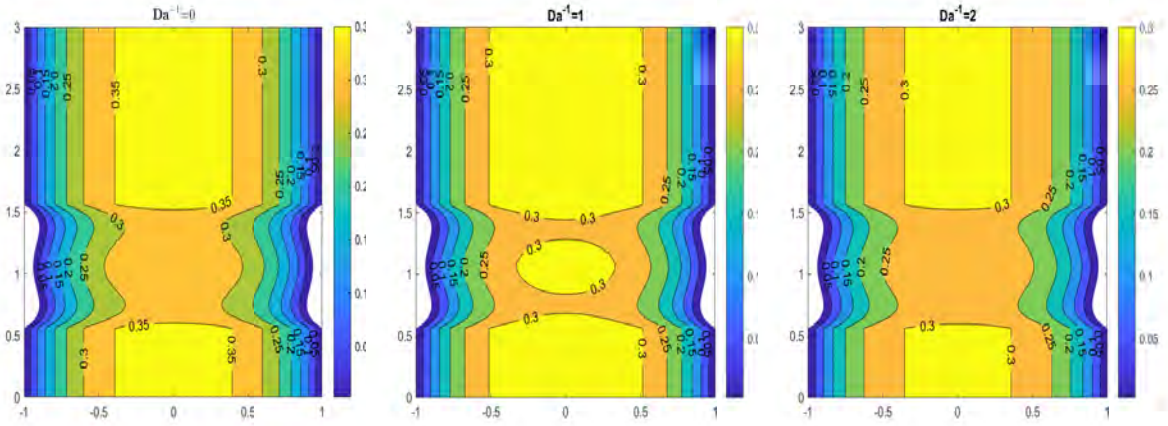

(a) **(b)** **(c)**

Figure 6.12: Velocity contour for Da^{-1}

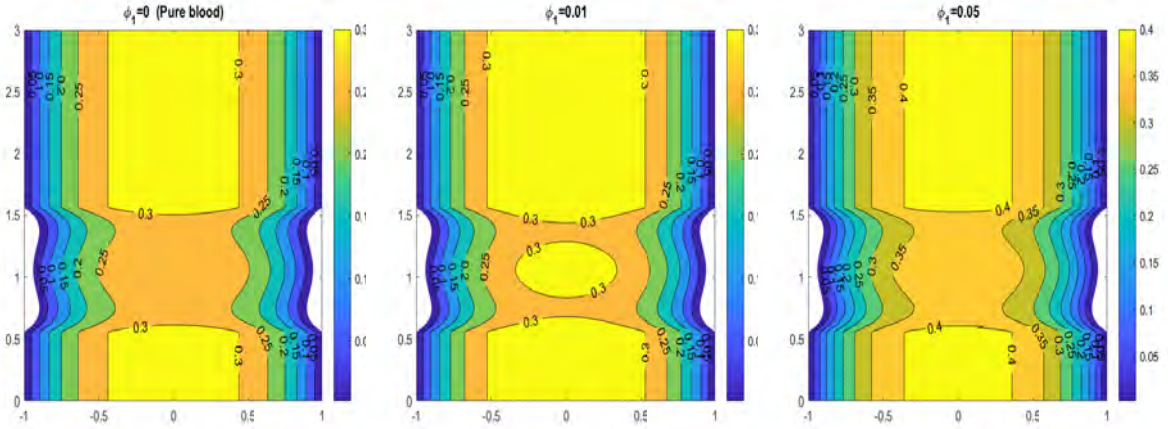

(a) **(b)** **(c)**

Figure 6.13: Velocity contour for nanoparticle concentration ϕ_1

nanoparticles has been explored for their potential in carrying therapeutic substances, including pharmaceuticals and genetic material. This unique characteristic allows for precise and targeted drug delivery, specifically to stenotic sites.

The utilisation of this particular approach serves to mitigate the occurrence of systemic side effects while concurrently enhancing the therapeutic efficacy. The blood flow within a stenosed artery devoid of nanoparticles is depicted in figure 6.13a. On the other hand, figures 6.13b and 6.13c offer valuable information regarding the velocity distribution in the artery with different concentrations of nanoparticles, ranging from 0 to 0.05. The increased fluid velocity observed can be attributed to a corresponding increase in the concentration of nanoparticles within the stenotic artery. This increase in concentration leads to localised temperature variations, contributing to the observed augmentation in fluid velocity. The aforementioned variations give rise to temperature gradients, which induce flow through buoyancy effects, ultimately boosting fluid velocity.

6.6 Conclusion

This research paper investigates the complex realm of magnetohydrodynamic (MHD) two-phase blood flow through a stenosed artery. The study incorporates different fluid models, with the core region modeled as a Power-law fluid and the plasma region as a Newtonian fluid. The study focuses on the potential of suspended Al_2O_3 nanoparticles in the base fluid (blood) as carriers for drug delivery applications. The nanoparticles are biocompatible and chemically stable, making them viable for long-term use in the medical field. The Method of Lines approach is effectively used to solve the governing equations within the proposed model, demonstrating its versatility, adaptability, and precision. This approach offers a practical and valuable avenue for addressing the complexities of partial differential equations, advancing our knowledge of multifaceted fluid dynamics and their applications in the medical domain. It is observed that the temperature profile increases as the thermophoresis and Brownian motion parameter enhances. In shear thinning fluid, the velocity profile depicts the declining nature for enhancemetn in the value of Weissenberg parameter We, while shows the reverse trend for shear thickening fluid. The velcoity profile shows the increasing trend for solutal Grashof number but decreases with an increase in the inverse Darcy number Da^{-1}. The concentration profile shows the increasing trend for activation parameter E, while depicts the reverse trend for reaction parameter ξ.

Chapter 7

Magnetically Targeted Drug Delivery for Two-Phase Blood Flow Through Composite Stenotic Artery Under the Influence of Hall and Ion Effects Using Method of Line Approach

7.1 Introduction

Targeted drug delivery, involving the binding of drugs to nanoparticles, represents an innovative approach in medicine. This method stands in contrast to conventional drug delivery practices, where drugs are diffused throughout the body, often resulting in reduced therapeutic efficacy and potential harm to healthy tissues. A notable technique in this domain is magnetically controlled drug delivery, where drugs are conjugated with magnetic nanoparticles and guided externally to specific target sites, as seen in applications such as stenosis. This approach provides a viable solution by enabling the precise delivery of therapeutic agents to afflicted areas, thereby augmenting treatment efficacy and curtailing adverse effects [177, 178]. Furlani et al. [179] formulated a mathematical model to analyse the magnetic drug targeting (MDT) process at the tumour sites. The model considered the influence of magnetic and fluidic forces on particles, enabling the prediction of their trajectory during the MDT process. In a study conducted by Shaw and Murthy [169], an investigation was undertaken to examine several factors that influence the targeted delivery of carrier particles. These factors encompass arterial inner wall permeability, carrier particle size, and microvessel diameter. Majee and Shit [165] focused on nanoparticle aggregation and flow patterns in targeted drug delivery (TDD) within stenosed arteries, discovering increased nanoparticle concentration downstream of stenosis, and forming vigorous flow circulation zones. In a study by Sharma et al. [48], the researchers examined the effects of an external magnetic field on various parameters related to blood and magnetic particle flow within a cylindrical tube. The experimental findings presented in their study provide evidence of reduced velocities observed in

both blood and magnetic particles when subjected to the external magnetic field. In a study by Ali et al. [180], a fractional model was formulated to describe the flow behaviour of Casson fluid within a cylindrical tube under the influence of an oscillating pressure gradient. This model aimed to provide a comprehensive understanding of the fluid dynamics in such systems. In a more recent investigation by Maiti et al. [181], a fractional-order model was proposed to analyse drug delivery processes involving the utilisation of magnetic nanoparticles by applying the fractional order model. The findings of their investigation revealed a notable augmentation in the Nusselt profile when subjected to intensified thermal radiation.

The quantitative analysis of blood flow necessitates a comprehensive understanding of the rheological properties of blood. Among the crucial characteristics of blood, the volume percentage of erythrocytes plays a pivotal role. Existing literature, derived from both in vivo and in vitro experiments, indicates the presence of a cell-free plasma layer near the arterial wall, attributed to the Fahraeus effect, especially in the context of blood flow through narrow arteries [4, 182]. Researchers such as Srivastava and Saxena [183] have proposed a two-phase blood flow model, wherein the core region is described as a Casson fluid enveloped by a peripheral layer of plasma governed by Newtonian fluid dynamics. Additionally, Ponalagusamy and Selvi [184] have delved into the complexities of two-phase blood flow in stenosed arteries, considering varying slip conditions at the arterial wall. Sharma and Yadav [8] have explored the dynamics of two-layer blood flow in constricted arteries, modeling the system as a circular tube surrounded by a two-layer porous region. Ranjit et al. [185] have investigated entropy generation and Joule heating effects in the context of electroosmotic flow of a two-layer fluid through micro-channels. Meanwhile, Kumawat et al. [28] have focused on entropy generation in two-phase blood flow, where the core region exhibits variable viscosity while the plasma region maintains constant viscosity. Their research findings have unveiled critical insights; specifically, factors like curvature and permeability can exacerbate the risk of atherosclerosis formation, whereas the presence of a heat source demonstrates a contrary effect, potentially mitigating this risk.

In the intricate landscape of biological systems, magnetohydrodynamics (MHD) emerges as a promising field, illuminating unique perspectives and avenues for exploration. Rao et al. delved into the magnetic field's impact on biological systems, revealing its profound influence. In a similar vein, Abbas et al. [138] scrutinized pulsatile MHD fluid flow through stenosed arteries, considering the presence of body acceleration. Their research unveiled a decline in velocity profile with increasing stenotic depth and magnetic field parameter, contrasting with the upward trend observed for the body acceleration parameter. Ponalagusamy and Priyadharshini [104] extended this exploration to the MHD flow of Casson fluid through bifurcated stenosed arteries. Subsequently, Kumar et al. [118] investigated MHD fluid flow

through permeable bifurcated arteries, accounting for magnetic field effects, heat source, and chemical reactions. Poonam et al. [82] delved into MHD fluid flow with Au-Al_2O_3 hybrid nanoparticles through curved stenosed arteries with aneurysms. Their study highlighted the potential use of radiation in thermal therapies, effectively mitigating arteriosclerosis and elevating fluid temperatures. Furthermore, Khanduri et al. [186] undertook a study on electroosmotic MHD flow through curved arteries afflicted with stenosis along the wall and thrombosis at the catheter's center. Numerous other researchers [118, 187, 33, 120] have also contributed to the understanding of MHD fluid flow through diseased arteries, collectively enhancing our comprehension of these intricate biological phenomena.

In recent years, researchers have delved into the various factors influencing blood flow patterns. Among these phenomena, the Hall and ion effects emerge as critical determinants shaping blood flow dynamics. The Hall effect arises from the interaction between the magnetic field and moving charged particles, while the ion effect plays a pivotal role in the electrochemical properties of blood. Mekheimer and El Kot [73] studied micropolar fluid flow through stenosed arteries, incorporating the Hall and magnetic field effects . Hayat et al. [188] investigated the impact of Hall and ion slip on Jeffery nanofluid in channels, revealing that velocity increases while temperature profiles decrease with Hall and ion slip parameters. Das et al. [189] utilized the homotopy analysis method to examine nanofluid flow in inclined stenosed arteries. Their findings indicated a decrease in wall shear stress profile with an increase in the Hall parameter. Moreover, Das et al. [77] extended their research by incorporating ion slip effects into electromagnetic blood flow hybrid nanoparticles. Numerous researchers [190, 191, 112, 121] have endeavoured to comprehend the influence of Hall and ion slip effects on blood flow, aiming to explore their biomedical applications. These studies contribute significantly to our understanding of the complexities involved in blood flow patterns, paving the way for innovative applications in the biomedical field.

In the previously mentioned studies, a noteworthy research gap emerges as there has been an absence of investigations pertaining to magnetic drug targeting in the stenosed artery within the framework of a two-phase blood flow model that incorporates essential factors such as Hall and ion effects, radiation, and viscous dissipation. Limited attention has been given to solving the resulting governing equations utilizing the Method of Lines approach, renowned for its robustness, accuracy, and precision. To fill the above-mentioned gaps, this study delves into the hemodynamic flow within a composite stenosed artery with radiation, viscous dissipation, Hall and ion effects, specifically emphasizing the application of magnetic drug targeting. The proposed model incorporates a two-phase system, where a power law fluid model characterizes the core region, and the plasma region is defined

using a Newtonian fluid model. The discretization of the governing equations and their subsequent solution through the Method of Lines form the fundamental methodology of this research effort. This approach is chosen for its well-documented effectiveness in handling complex fluid dynamics scenarios. Through this rigorous investigation, our study aims to bridge the existing knowledge gaps and enhance our understanding of magnetic drug targeting mechanisms within the intricate dynamics of stenosed arteries, thereby contributing valuable insights to biomedical fluid dynamics.

The novelty of the current research lies in the following aspects:

- Implementation of magnetic drug targeting within a stenosed artery.
- Adoption of a two-phase model incorporating various influencing factors such as Joule heating, viscous dissipation, Hall, and ion effects.
- Demonstrating the advanced computational prowess of the Method of Lines approach in solving the discretized governing equations, thereby elevating precision and accuracy in the analysis.

7.2 Mathematical Model

In this paper, we considered an unsteady, laminar, two dimensional incompressible blood flow through the stenosed artery as depicted in figure 7.1. The magnetic nanoparticles Fe_3O_4 is doped in the blood and uniformly distributed throughout the blood. The magnetic field is applied perpendicular to sheet. The magnetic Reynold number is asumed to be small to neglect the effect of induced magnetic field. The two-phase blood flow model is assumed where fluid nature in core region is represented by Ostwald-DeWaele power-law fluid model and the suspended peripheral layer of plamsa is assumed to be Newtonian. The viscosity of the blood in core and plasma region is represented as μ_c and μ_p, receptively.

7.2.1 Geometry

The geometry of the stenosis in the core region is considered as [40]:

$$\tilde{R}(\tilde{z}) = \begin{cases} R_0 - \frac{2\delta^*}{L_0}(\tilde{z}-\tilde{d}), & \text{for} \quad \tilde{d} < \tilde{z} \leq \tilde{d} + \frac{L_0}{2}, \\ R_0 + \frac{2\delta^*}{L_0}(\tilde{z}-\tilde{d}-L_0), & \text{for} \quad \tilde{d} + \frac{L_0}{2} < \tilde{z} \leq \tilde{d} + L_0, \\ R_0 + \frac{\delta^*}{L_0}\sin(\pi(\tilde{z}-\tilde{d})), & \text{for} \quad \tilde{d} + L_0 < \tilde{z} \leq \tilde{d} + 2L_0, \\ R_0, & \text{otherwise} \end{cases} \tag{7.1}$$

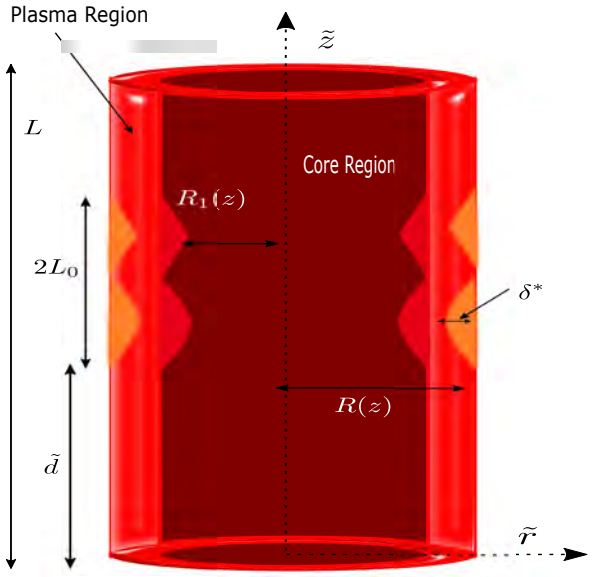

Figure 7.1: Pictorial representation of diseased artery

The geometry of the stenosis in the plasma region is considered as:

$$\bar{R}_1(\tilde{z}) = \begin{cases} \bar{\beta}R_0 - \frac{2\delta^*}{L_0}(\tilde{z}-\tilde{d}), & \text{for} \quad \tilde{d} < \tilde{z} \leq \tilde{d} + \frac{L_0}{2}, \\ \bar{\beta}R_0 + \frac{2\delta^*}{L_0}(\tilde{z}-\tilde{d}-L_0), & \text{for} \quad \tilde{d} + \frac{L_0}{2} < \tilde{z} \leq \tilde{d} + L_0, \\ \bar{\beta}R_0 + \frac{\delta^*}{L_0}\sin(\pi(\tilde{z}-\tilde{d})), & \text{for} \quad \tilde{d} + L_0 < \tilde{z} \leq \tilde{d} + 2L_0, \\ \bar{\beta}R_0, & \text{otherwise}, \end{cases} \tag{7.2}$$

where, $\tilde{R}(\tilde{z})$ represent the radius of the artery, $\tilde{R}_1(\tilde{z})$ represent the radius of core region, R_0 is the radius of normal artery, L_0 signifies the length of the stenosis, d is the location of stenosis and δ^* is the stenosis height.

7.2.2 Electrohydrodynamics (EHD)

The composition of blood is characterised by its intricate combination of ions, proteins, cellular components, and electrolytes. This unique composition makes blood an exceptional conductor of electrical current. The application of an external electric field to the fluid, specifically blood in this context, induces kinetic motion in its constituents. The occurrence of this motion encounters opposition from electrically charged particles that are distributed throughout the fluid, resulting in the dissipation of energy. This phenomenon is commonly referred to as Joule heating. This section illustrates the velocity contours, which represent the velocity field inside a constricted artery. The presented contours give significant insights into the spatial fluctuations of velocity within the fluid, providing a complete comprehension

of the velocity variations at various positions inside the artery. The generalized Ohm law is given as [77, 107]:

$$\mathbf{J} = \sigma_{nf}(\mathbf{E} + \mathbf{V} \times \mathbf{B}) - \frac{\beta_e}{B_0}(\mathbf{J} \times \mathbf{B}) + \frac{\beta_e \beta_i}{B_0^2}[(\mathbf{J} \times \mathbf{B}) \times \mathbf{B}], \tag{7.3}$$

where $q, \sigma_{nf}, B, \mathbf{J}, \beta_e, \beta_i$ are the velocity vector, effective electric conductivity of hybrid nanofluid, magnetic field vector, current density vector, Hall and ion slip parameter, respectively.

The maxwell equation is given as:

$$\nabla \times \mathbf{E} = -\frac{\partial \mathbf{B}}{\partial t}, \quad \nabla \cdot \mathbf{B} = 0, \quad \nabla \cdot \mathbf{J} = 0. \tag{7.4}$$

The induced magnetic field is negligible due to the small magnetic Reynold number. In the absence of magnetic field and using the equation (7.4), the equation (7.3) reduced to:

$$J_{\tilde{r}}(1 + \beta_e \beta_i) - \beta_e J_{\tilde{z}} = -\sigma_{nf} B_0 \tilde{w}_\rho, \tag{7.5}$$

$$J_{\tilde{z}}(1 + \beta_e \beta_i) + \beta_e J_{\tilde{r}} = -\sigma_{nf} B_0 \tilde{u}_\rho. \tag{7.6}$$

Solving the equations (7.5) and (7.6) gives:

$$J_{\tilde{r}} = \frac{\sigma_{nf} B_0}{\alpha_e^2 + \beta_e^2}[\tilde{u}_\rho \beta_e - \tilde{w}_\rho \alpha_e], \tag{7.7}$$

$$J_{\tilde{z}} = \frac{\sigma_{nf} B_0}{\alpha_e^2 + \beta_e^2}[\tilde{u}_\rho \alpha_e + \tilde{w}_\rho \beta_e]. \tag{7.8}$$

$$\tag{7.9}$$

Here, $\alpha_e = 1 + \beta_e \beta_i$ and $\beta_e = \omega_e t_e$ is the Hall parameter. The current density and Lorentz force is given as:

$$\frac{\mathbf{J} \cdot \mathbf{J}}{\sigma_{nf}} = \frac{\sigma_{nf} B_0^2}{\alpha_e^2 + \beta_e^2}\left[\tilde{u}_\rho^2 + \tilde{w}_\rho^2\right], \tag{7.10}$$

$$\mathbf{J} \times \mathbf{B} = \left(-\frac{\sigma_{nf} B_0^2}{\alpha_e^2 + \beta_e^2}\left\{\tilde{u}_\rho \alpha_e + \tilde{w}_\rho \beta_e\right\}, 0, \frac{\sigma_{nf} B_0^2}{\alpha_e^2 + \beta_e^2}\left\{\tilde{u}_\rho \beta_e - \tilde{w}_\rho \alpha_e\right\}\right).$$

7.2.3 Fluidic Force Formulation

Magnetic nanoparticles exhibit inherent non-invasive characteristics, which make them suitable for various applications such as drug binding and external manipulation using magnetic forces. Within the context of this investigation, our primary focus has been directed towards magnetite (Fe_3O_4) as the preferred magnetic nanoparticle for the purpose of accurately targeting drugs within affected arterial regions. The motion of these nanoparticles is determined by a combination of various forces, namely magnetic forces, inter-particle interactions, fluidic forces, inertial forces, and buoyant forces. The current flow regime exhibits a low Reynolds number, which consequently diminishes the impact of Brownian motion effects on the magnetic nanoparticles. The system dynamics are primarily governed by magnetic and viscous forces. Consequently, we formulate the equations of motion for the nanoparticles based on Newton's second law as follows:

$$m\frac{\partial \tilde{v}_{pr}}{\partial t} = F_{mr} + F_{fr} + F_{gr}, \tag{7.11}$$

$$m\frac{\partial \tilde{v}_{pz}}{\partial t} = F_{mz} + F_{fz} + F_{gz}, \tag{7.12}$$

where, m is the mass of the nanoparticle, $F_{fr}, F_{fz}, F_{mr}, F_{mz}, F_{gr}, F_{gz}$ are the fluidic, magnetic and graviataional forces along the radial and axial direction, certain assumptions are made based on the low magnetic Reynolds number hypothesis. Specifically, the magnetic forces are considered negligible, leading to the conditions $F_{mr} = 0$ and due to sub-micron size of the nano-magnetic particles the gravitational force can be neligible $F_{gr} = 0$.

The equations (7.11) and (7.12) becomes $F_{mr} + F_{fr} + F_{gr} = 0$ and $F_{mz} + F_{fz} + F_{gz} = 0$ when the interial forces are neglected due to nanoparticle sub-micron size. The fluidic force imposed by a nanoparticle is determined through the application of Stokes' law, which describes the viscous drag acting upon the spherical object as follows:

$$F_{fr} = -6\pi\mu_f \tilde{R}_p f_{\mathrm{DP}}(\tilde{v}_{pr} - \tilde{u}_\rho), \tag{7.13}$$

$$F_{fz} = -6\pi\mu_f \tilde{R}_p f_{\mathrm{DP}}(\tilde{v}_{pz} - \tilde{w}_\rho), \tag{7.14}$$

where, μ_f is the static viscosity, f_{DP} is drag coefficient and $\tilde{R}_p$ is the radius of nanoparticle.

In this work, we have neglected the gravitational impact on submicron nanoparticles, primarily focusing on investigating the magnetic and fluidic forces. Equations (7.11) and

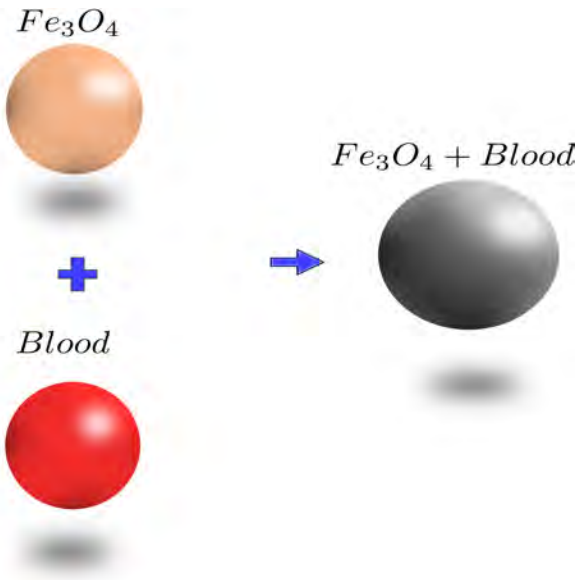

Figure 7.2: Formation of Fe_3O_4-Blood nanofluid through the integration of Fe_3O_4 nanoparticles with blood.

(7.12) can be simplified when the fluidic environment mainly influences the nanoparticle, resulting in subsequent expressions as [165]:

$$m\frac{\partial \tilde{v}_{pr}}{\partial \tilde{t}} = K_s(\tilde{u}_\rho - \tilde{v}_{pr}), \tag{7.15}$$

$$m\frac{\partial \tilde{v}_{pz}}{\partial \tilde{t}} = K_s(\tilde{w}_\rho - \tilde{v}_{pz}), \tag{7.16}$$

where, $K_s = 6\pi\mu\tilde{R}_p f_{\mathrm{DP}}$ is the Stroke's constant, $f_{\mathrm{DP}} = \frac{2F_D}{\rho u^2 A}$ is drag coefficient, where F_D is drag coefficient and $\bar{R}_p = 2.5 \times 10^7$ is effective hydrodynamics nanoparticle radius. Figure 7.2 shows the Fe_3O_4 nanoparticles doped with Blood to form the Fe_3O_4-Blood nanofluid.

7.2.4 Governing Equations

The blood flow model is designed in the cylindrical coordinate system, where velocity u and w are considered along the radial r and axial direction z, respectively. The azimuthal direction θ is neglected as blood flow is assumed to be axi-symmetrical. Under the assumption mentioned above and using the Boussinesq approximation, the resultant flow equations are given as [18]:

Continuity:

$$\frac{\partial \tilde{u}_\rho}{\partial \tilde{r}} + \frac{\tilde{u}_\rho}{\tilde{r}} + \frac{\partial \tilde{w}_\rho}{\partial \tilde{z}} = 0. \tag{7.17}$$

For core region:

Momentum ($\tilde{r}$-direction):

$$(\rho_{nf})_c \left[\frac{\tilde{D}\tilde{u}_c}{\tilde{D}\tilde{t}}\right] = -\frac{\partial \tilde{p}}{\partial \tilde{r}} + \left[\frac{1}{\tilde{r}}\frac{\partial}{\partial \tilde{r}}(\tilde{r}S_{\tilde{r}\tilde{r}}) + \frac{\partial}{\partial \tilde{z}}(S_{\tilde{r}\tilde{z}})\right] + \tilde{G}. \tag{7.18}$$

Momentum ($\tilde{z}$-direction):

$$(\rho_{nf})_c \left[\frac{\tilde{D}\tilde{w}_c}{\tilde{D}\tilde{t}}\right] = -\frac{\partial \tilde{p}}{\partial \tilde{z}} + \left[\frac{1}{\tilde{r}}\frac{\partial}{\partial \tilde{r}}(\tilde{r}S_{\tilde{r}\tilde{z}}) + \frac{\partial}{\partial \tilde{z}}(S_{\tilde{z}\tilde{z}})\right] + \tilde{F} \tag{7.19}$$

For plasma region:

Momentum ($\tilde{r}$-direction):

$$(\rho_{nf})_p \left[\frac{\tilde{D}\tilde{u}_p}{\tilde{D}\tilde{t}}\right] = -\frac{\partial \tilde{p}}{\partial \tilde{r}} + \frac{1}{\tilde{r}}\frac{\partial}{\partial \tilde{r}}\left\{(\mu_{nf})_p \frac{\partial \tilde{u}_p}{\partial \tilde{r}}\right\} + \frac{\partial}{\partial \tilde{z}}\left\{(\mu_{nf})_p \left(\frac{\partial \tilde{u}_p}{\partial \tilde{z}} + \frac{\partial \tilde{w}_p}{\partial \tilde{r}}\right)\right\} - 2(\mu_{nf})_p \frac{\tilde{u}_p}{\tilde{r}^2} + \tilde{G}. \tag{7.20}$$

Momentum ($\tilde{z}$-direction):

$$(\rho_{nf})_p \left[\frac{\tilde{D}\tilde{w}_p}{\tilde{D}\tilde{t}}\right] = -\frac{\partial \tilde{p}}{\partial \tilde{z}} + \frac{1}{\tilde{r}}\frac{\partial}{\partial \tilde{r}}\left\{\tilde{r}(\mu_{nf})_p \left(\frac{\partial \tilde{u}_p}{\partial \tilde{z}} + \frac{\partial \tilde{w}_p}{\partial \tilde{r}}\right)\right\} + \frac{\partial}{\partial \tilde{z}}\left\{2(\mu_{nf})_p \left(\frac{\partial \tilde{w}_p}{\partial \tilde{z}}\right)\right\} + \tilde{F}. \tag{7.21}$$

The body force term $\tilde{G}$ defined in the equations (7.18) and (7.20) and $\tilde{F}$ in equations (7.19) and (7.21) are expressed as:

$$\tilde{F} = \frac{\sigma_{nf} B_0^2}{\alpha_e^2 + \beta_e^2}\left\{\tilde{u}_\rho \beta_e - \tilde{w}_\rho \alpha_e\right\} + ((\rho\beta)_{nf})_\rho g(\tilde{T}_\rho - \tilde{T}_0) - \frac{(\mu_{nf})_\rho}{K}\tilde{w}_\rho + K_s N(\tilde{v}_{pz} - \tilde{w}_\rho), \tag{7.22}$$

$$\tilde{G} = -\frac{\sigma_{nf} B_0^2}{\alpha_e^2 + \beta_e^2}\left\{\tilde{u}_\rho \alpha_e + \tilde{w}_\rho \beta_e\right\} + K_s N(\tilde{v}_{pr} - \tilde{w}_\rho). \tag{7.23}$$

Energy equation:

$$((\rho Cp)_{nf})_\rho \left[\frac{\tilde{D}\tilde{T}_\rho}{\tilde{D}\tilde{t}}\right] =(\kappa_{nf})_\rho \left[\nabla^2 \tilde{T}_\rho\right] + \frac{\sigma_{nf} B_0^2}{\alpha_e^2+\beta_e^2}\left[u_\rho^2 + w_\rho^2\right] - \frac{1}{\tilde{r}}\left\{\frac{\partial}{\partial \tilde{r}}(\tilde{r} q_r)\right\} + \phi^* \quad (7.24)$$

where, the radiation term [33, 174],

$$q_r = -\frac{16\sigma_e \tilde{T}_0^3}{3k_e}\frac{\partial \tilde{T}_\rho}{\partial \tilde{r}}, \quad (7.25)$$

and, viscous dissipation term is defined as:

$$\phi^* = (\mu_{nf})_\rho \left[2\left(\frac{\partial \tilde{u}_\rho}{\partial \tilde{r}}\right)^2 + \left(\frac{\partial \tilde{u}_\rho}{\partial \tilde{z}} + \frac{\partial \tilde{w}_\rho}{\partial \tilde{r}}\right)^2 + 2\left(\frac{\partial \tilde{w}_\rho}{\partial \tilde{z}}\right)^2\right]. \quad (7.26)$$

Here, the operators $\frac{\tilde{D}}{\tilde{D}\tilde{t}} \equiv \left[\frac{\partial}{\partial \tilde{t}} + \tilde{u}_\wp \frac{\partial}{\partial \tilde{r}} + \tilde{w}_\wp \frac{\partial}{\partial \tilde{z}}\right]$ and $\nabla^2 \equiv \left[\frac{\partial^2}{\partial \tilde{r}^2} + \frac{1}{\tilde{r}}\frac{\partial}{\partial \tilde{r}} + \frac{\partial^2}{\partial \tilde{z}^2}\right]$.
The paramter ρ is represented as:

$$\rho = \begin{cases} c, & \text{if } 0 < \tilde{r} \le R_1(\tilde{z}) \qquad \text{(Core region)}, \\ p, & \text{if } R_1(\tilde{z}) < \tilde{r} \le R(\tilde{z}) \text{ (Plasma region)}. \end{cases} \quad (7.27)$$

The blood flow has the pulsatile nature due to the pumping action of the blood. Therefore, the pressure gradient can be taken in the following form [138]:

$$-\frac{\partial \tilde{p}}{\partial \tilde{z}} = A_0 + A_1 \cos(\omega_p \tilde{t}), \tilde{t} > 0. \quad (7.28)$$

Where, $\omega_p = 2\pi f_p$, the terms A_0 and A_1 signifies the amplitude of steady-state and pulsatile component. The term f_p signifies for heart pulse frequency.

Moreover, the non-dimensional form of equation (7.16) is given as:

$$G\frac{\partial v_{pz}}{\partial t} = w_\rho - v_{pz}, \quad (7.29)$$

where $G = \frac{mU_0}{K_s R_0}$ is the particle mas parameter.

7.2.4.1 Non-Newtonian Fluid Model (Power Law Fluid)

The Cauchy stress tensor for a power law fluid is given as [18, 192]:

$$T^* = -pI + \mu(\Gamma\Pi)^{n-1}\grave{A}_1. \quad (7.30)$$

Here p represents the pressure, I is the identity tensor, n represents the rheological power-law index ($n = 1$ for Newtonian fluid, $n < 1$ for pseudoplastic blood, $n > 1$ for dilatant blood). The first Rivlin-Ericksen tensor is defined as $\grave{A}_1 = \nabla\mathbf{V} + (\nabla\mathbf{V})^T$ and $\Pi = \sqrt{\frac{1}{2}tr(\grave{A}_1)}$.

Use equations (7.30) and the above terms to get the stress tensor components are expressed as:

$$S_{\tilde{r}\tilde{r}} = (\mu_{nf})_\rho \left\{ \zeta^* \frac{\partial \tilde{u}_\rho}{\partial \tilde{r}} \right\}, \tag{7.31}$$

$$S_{\tilde{z}\tilde{z}} = (\mu_{nf})_\rho \left\{ \zeta^* \frac{\partial \tilde{w}_\rho}{\partial \tilde{z}} \right\}, \tag{7.32}$$

$$S_{\tilde{r}\tilde{z}} = (\mu_{nf})_{\wp} \left\{ \zeta^* \left(\frac{\partial \tilde{w}_\rho}{\partial \tilde{r}} + \frac{\partial \tilde{u}_\rho}{\partial \tilde{z}} \right) \right\}. \tag{7.33}$$

Here, ζ^* is defined as:

$$\begin{aligned} \zeta^* &= (\Gamma\Pi)^{n-1} \\ &= \left\{ \left| \Gamma \left(2\left(\frac{\partial \tilde{u}_\rho}{\partial \tilde{r}}\right)^2 + 2\left(\frac{\partial \tilde{w}_\rho}{\partial \tilde{z}}\right)^2 + 2\left(\frac{\tilde{u}_\rho}{\tilde{r}}\right)^2 + \left(\frac{\partial \tilde{u}_\rho}{\partial \tilde{z}} + \frac{\partial \tilde{w}_\rho}{\partial \tilde{r}}\right)^2 \right)^{\frac{1}{2}} \right|^{n-1} \right\} \end{aligned} \tag{7.34}$$

7.3 Non-Dimensional Equations

By using the non-dimensionalize parameters mentioned in table 7.1 and mild-stenosis assumption ($\delta << 1$) with $O(1) = \varepsilon = \frac{R_0}{L_0}$, the governing equations reduced to:

For core region $0 < r \leq R_1(z)$

$$\frac{\partial p}{\partial r} = 0, \tag{7.35}$$

$$\begin{aligned} \frac{\rho_{nf}}{\rho_f}\frac{1}{\rho_0}Re\frac{\partial w_c}{\partial t} = -\frac{\partial p}{\partial z} + \left[\frac{1}{r}\frac{\partial}{\partial r}(rS_{rz})\right] + \left\{\frac{(\rho\beta)_{nf}}{(\rho\beta_f)}\right\}\frac{1}{\rho_0}GrT_c - \left\{\frac{\mu_{nf}}{\mu_f}\right\}\frac{1}{\mu_0}\frac{w_c}{Da} \\ - \frac{\sigma_{nf}}{\sigma_f}\frac{\alpha_e}{\alpha_e^2+\beta_e^2}M^2 w_c + R_p(v_{pz} - w_c), \end{aligned} \tag{7.36}$$

$$RePr\frac{k_0}{\rho_0 s_0}\left\{\frac{\kappa_f}{\kappa_{nf}}\frac{(\rho C_p)_{nf}}{(\rho C_p)_f}\right\}\frac{\partial T_c}{\partial t}=\frac{\partial^2 T_c}{\partial r^2}+\frac{1}{r}\frac{\partial T_c}{\partial r}+\kappa_0\left(\frac{\kappa_f}{\kappa_{nf}}\right)\left\{Nr\left(\frac{\partial^2 T_c}{\partial r^2}+\frac{1}{r}\frac{\partial T_c}{\partial r}\right)+\frac{\mu_{nf}}{\mu_f}\frac{1}{\mu_0}Br\left(\frac{\partial w_c}{\partial r}\right)^2+\frac{\sigma_{nf}}{\sigma_f}\frac{\alpha_e}{\alpha_e^2+\beta_e^2}M^2 Brw_c^2\right\}. \quad (7.37)$$

For plasma region $R_1(z) < r \leq R(z)$

$$\frac{\partial p}{\partial r}=0, \quad (7.38)$$

$$\frac{\rho_{nf}}{\rho_f}Re\frac{\partial w_p}{\partial t}=-\frac{\partial p}{\partial z}+\frac{\mu_{nf}}{\mu_f}\left[\frac{1}{r}\frac{\partial}{\partial r}\left(r\frac{\partial w_p}{\partial r}\right)\right]+\frac{(\rho\beta)_{nf}}{(\rho\beta_f)}GrT_p-\frac{\mu_{nf}}{\mu_f}\frac{w_p}{Da}-\frac{\sigma_{nf}}{\sigma_f}\frac{\alpha_e}{\alpha_e^2+\beta_e^2}M^2 w_p+R_p(v_{pz}-w_p), \quad (7.39)$$

$$RePr\left\{\frac{\kappa_f}{\kappa_{nf}}\frac{(\rho C_p)_{nf}}{(\rho C_p)_f}\right\}\frac{\partial T_p}{\partial t}=\frac{\partial^2 T_p}{\partial r^2}+\frac{1}{r}\frac{\partial T_p}{\partial r}+\left(\frac{\kappa_f}{\kappa_{nf}}\right)\left\{Nr\left(\frac{\partial^2 T_p}{\partial r^2}+\frac{1}{r}\frac{\partial T_p}{\partial r}\right)+\frac{\mu_{nf}}{\mu_f}Br\left(\frac{\partial w_p}{\partial r}\right)^2+\frac{\sigma_{nf}}{\sigma_f}\frac{\alpha_e}{\alpha_e^2+\beta_e^2}M^2 Brw_p^2\right\}. \quad (7.40)$$

The constant ζ^* is given as:

$$\zeta^*=\left\{\left|\Gamma\left(2\left(\frac{\delta^* U_0}{R_0 L_0}\right)^2\left(\frac{\partial u_{\wp}}{\partial r}\right)^2+2\left(\frac{U_0}{L_0}\right)^2\left(\frac{\partial w_{\wp}}{\partial z}\right)^2+2\left(\frac{\delta^* U_0}{R_0 L_0}\right)^2\left(\frac{u_{\wp}}{r}\right)^2+\left(\frac{\delta^* U_0}{L_0^2}\frac{\partial u_{\wp}}{\partial z}+\frac{U_0}{R_0}\frac{\partial w_{\wp}}{\partial r}\right)^2\right)^{\frac{1}{2}}\right|^{n-1}\right\} \quad (7.41)$$

$$=\left\{\left|\Gamma\left(\frac{U_0}{R_0}\right)\left(2(\delta\varepsilon)^2\left(\frac{\partial u_{\wp}}{\partial r}\right)^2+2(\varepsilon)^2\left(\frac{\partial w_{\wp}}{\partial z}\right)^2+2(\delta\varepsilon)^2\left(\frac{u_{\wp}}{r}\right)^2+\left(\delta\varepsilon^2\frac{\partial u_{\wp}}{\partial z}+\frac{\partial w_{\wp}}{\partial r}\right)^2\right)^{\frac{1}{2}}\right|^{n-1}\right\}. \quad (7.42)$$

The non-dimensionalize shear stress component S_{rz} is written as:

$$\begin{aligned} S_{rz} =& \frac{(\mu_{nf})_{\wp}}{(\mu_f)_p}\left\{\zeta^*\left(\frac{\partial w_{\wp}}{\partial r}\right)\right\} \\ =& \frac{(\mu_{nf})_{\wp}}{(\mu_f)_p}\left\{We^2\left|\frac{\partial w_{\wp}}{\partial r}\right|^2\right\}^{\left(\frac{n-1}{2}\right)}\frac{\partial w_{\wp}}{\partial r}. \end{aligned} \tag{7.43}$$

Use equation (7.41) and (7.43) to get the momentum equations in core region as:

$$\begin{aligned} \frac{\rho_{nf}}{\rho_f}\frac{1}{\rho_0}Re\frac{\partial w_c}{\partial t} =& -\frac{\partial p}{\partial z}+\frac{\mu_{nf}}{\mu_f}\frac{1}{\mu_0}\left[\frac{1}{r}\frac{\partial}{\partial r}\left\{r\left[\left\{(We)^2\left|\frac{\partial w_c}{\partial r}\right|^2\right\}^{\frac{n-1}{2}}\left(\frac{\partial w_c}{\partial r}\right)\right]\right\}\right] \\ &+\frac{(\rho\beta)_{nf}}{(\rho\beta)_f}\frac{1}{\rho_0}GrT_c-\frac{\mu_{nf}}{\mu_f}\frac{1}{\mu_0}\frac{w_c}{Da}-\frac{\sigma_{nf}}{\sigma_f}\frac{\alpha_e}{\alpha_e^2+\beta_e^2}M^2w_c, \end{aligned} \tag{7.44}$$

Table 7.1: Dimensionless parameters

$r=\frac{\tilde{r}}{R_0}$	$z=\frac{\tilde{z}}{L_0}$	$u_c=\frac{L_0\tilde{u}_c}{\delta^*U_0}$	$R_1=\frac{\tilde{R}_1}{R_0}$	$t=\frac{U_0\tilde{t}}{R_0}$
$p=\frac{R_0^2\tilde{p}}{(\mu_f)_pU_0L_0}$	$u_p=\frac{L_0\tilde{u}_p}{\delta^*U_0}$	$T_c=\frac{\tilde{T}_c-\tilde{T}_0}{\tilde{T}_w-\tilde{T}_0}$	$T_p=\frac{\tilde{T}_p-\tilde{T}_0}{\tilde{T}_w-\tilde{T}_0}$	$w_p=\frac{\tilde{w}_p}{U_0}$
$w_c=\frac{\tilde{w}_c}{U_0}$	$Gr=\frac{g(\rho_f)_p\beta_fR_0^2\Delta\tilde{T}}{U_0(\mu_f)_p}$	$Re=\frac{(\rho_f)_pR_0U_0}{(\mu_f)_p}$	$k_0=\frac{(\kappa_f)_p}{(\kappa_f)_c}$	$v_{pr}=\frac{\tilde{v}_{pr}}{U_0}$
$M^2=\frac{\sigma_fB_0^2R_0^2}{(\mu_f)_p}$	$v_{pz}=\frac{\tilde{v}_{pz}}{U_0}$	$Nr=\frac{16\sigma_e\tilde{T}_0}{3(\kappa_f)_pk_e}$	$R_p=\frac{K_sNR_0^2}{(u_f)_p}$	$\rho_0=\frac{(\rho_f)_p}{(\rho_f)_c}$
$Br=EcPr$	$\mu_0=\frac{(\mu_f)_p}{(\mu_f)_c}$	$We=\frac{\Gamma U_0}{R_0}$	$s_0=\frac{(C_{pf})_p}{(C_{pf})_c}$	$Pr=\frac{C_p(\mu_f)_p}{(\kappa_f)_p}$
$\Delta\tilde{T}=\tilde{T}_w-\tilde{T}_0$	$Da=\frac{K}{R_0^2}$	$S_{\tilde{z}\tilde{z}}=\frac{U_0(\mu_f)_p}{L_0}S_{zz}$	$S_{\tilde{r}\tilde{z}}=\frac{U_0(\mu_f)_p}{R_0}S_{rz}$	$S_{\tilde{r}\tilde{r}}=\frac{U_0(\mu_f)_p}{L_0}S_{rr}$
$R=\frac{\tilde{R}}{R_0}$	$R_1=\frac{\tilde{R}_1}{R_0}$			

The dimensionless formulation of boundary conditions are described as:

$$\begin{cases} w_\rho = v_{p_\rho} = T_\rho = 0 & \text{at} \quad t = 0, \\ \frac{\partial w_c}{\partial r} = 0, \quad \frac{\partial T_c}{\partial r} = 0, \quad \frac{\partial v_{p_c}}{\partial r} = 0, & \text{at} \quad r = 0, \\ w_c = w_p, \quad v_{p_c} = v_{p_p}, \quad T_c = T_p & \text{at} \quad r = R_1(z), \\ \tau_c = \tau_p, \quad \frac{\partial T_c}{\partial r} = \frac{\partial T_p}{\partial r}, \quad \frac{\partial v_{p_c}}{\partial r} = \frac{\partial v_{p_p}}{\partial r} & \text{at} \quad r = R_1(z), \\ w_p = 0, \quad v_{p_p} = 1, \quad T_p = 1 & \text{at} \quad r = R(z). \end{cases} \tag{7.45}$$

The dimensionless pressure gradient is written as:

$$-\frac{\partial p}{\partial z} = B_1(1 + e\cos(c_1 t)), \tag{7.46}$$

where, $B_1 = \frac{A_0 R_0^2}{(\mu_f)_p U_0}, e = \frac{A_1}{A_0}$ and $c_2 = \frac{2\pi R_0 \omega_b}{U_0}$.

7.3.1 Non-Dimension Form for Geometry of Stenosis

The geometry of the stenosis in the core region is considered as [40]:

$$R(z) = \begin{cases} 1 - 2\delta(z-d), & \text{for} \quad d < z \leq d + \frac{1}{2}, \\ 1 + 2\delta(z-d-1), & \text{for} \quad d + \frac{1}{2} < z \leq d + 1, \\ 1 + \delta\sin(\pi(z-d)), & \text{for} \quad d + 1 < z \leq d + 2, \\ 1, & \text{otherwise.} \end{cases} \tag{7.47}$$

The geometry of the stenosis in the plasma region is considered as:

$$R_1(z) = \begin{cases} \bar{\beta} - 2\delta(z-d), & \text{for} \quad d < z \leq d + \frac{1}{2}, \\ \bar{\beta} + 2\delta(z-d-1), & \text{for} \quad d + \frac{1}{2} < z \leq d + 1, \\ \bar{\beta} + \delta\sin(\pi(z-d)), & \text{for} \quad d + 1 < z \leq d + 2, \\ \bar{\beta}, & \text{otherwise.} \end{cases} \tag{7.48}$$

7.3.2 Quantities of Physical Interest

In order to address the potential impact of geometric effects, a radial transformation is introduced, represented by the equation $x_1 = \frac{r}{R(z)}$. Then, the volumetric flow rate is defined

as:

$$\begin{aligned} Q^f =& R^2 \int_0^1 \int_0^\pi x_1 w dx_1 d\theta \\ =& R^2 \left(\int_0^{\bar{\beta}} \int_0^\pi x_1 w_c dx_1 d\theta + \int_{\bar{\beta}}^1 \int_0^\pi x_1 w_p dx d\theta \right). \end{aligned} \tag{7.49}$$

Here, $\bar{\beta} = 0.75$ is the interface between the plasma and core region. The resistance impedance is given as:

$$\lambda = \frac{\int_0^L (-\frac{\partial p}{\partial z}) dz}{Q^f}, \tag{7.50}$$

The WSS and Nusselt (Nu_x) are given as:

$$WSS = -\frac{1}{R} \left(\frac{\partial w}{\partial x_1} \right)_{x_1=1}, \quad Nu_x = -\frac{1}{R} \left(\frac{\partial T}{\partial x_1} \right)_{x_1=1}. \tag{7.51}$$

7.3.3 Numerical Methodology

The commonly employed technique referred to as the 'semi-discretization' approach entails discretizing only the spatial coordinates while preserving continuity in the temporal domain. This method, termed the Method of Lines (MOL), serves as a prominent numerical technique employed in the resolution of partial differential equations (PDEs) [159, 160]. The achievement of the aforementioned objective is facilitated through the process of discretization along the spatial coordinates.

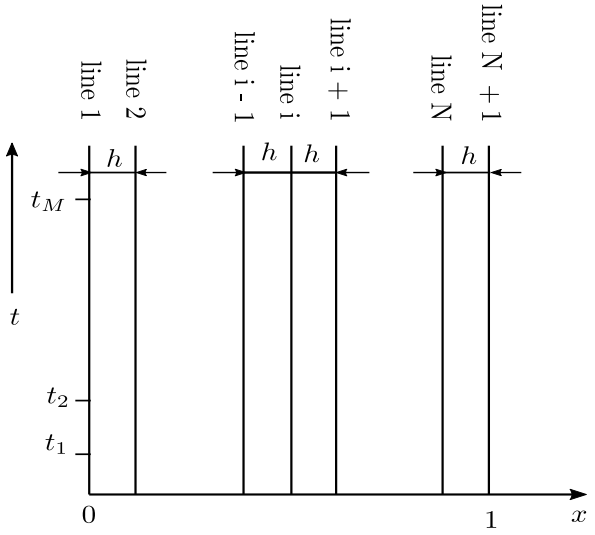

Figure 7.3: Computational domain for Method of Lines (MOL)

This discretization leads to the formulation of a system of ordinary differential equations (ODEs), which can then be effectively solved by employing time-stepping methods. The pertinent partial differentials are mathematically defined as follows:

$$\frac{\partial f}{\partial x} = \frac{f_{i+1} - f_{i-1}}{2h}, \tag{7.52}$$

$$\frac{\partial^2 f}{\partial x^2} = \frac{f_{i+1} - 2f_i + f_{i-1}}{h^2}. \tag{7.53}$$

The Method of Lines (MOL) is a technique that entails substituting the precise or analytical solutions for the functions $w(r,t)$, $T(r,t)$, and $C(r,t)$ in the spatial domain with an approximate solution denoted as $w(t)$, $T(t)$, and $C(t)$. This approximation is subject to certain limitations, as it is confined within a defined range of indices, namely $i = 1,2,...,N+1$. The determination of this approximation is based on a finite set of straight lines, as illustrated in Figure 7.3.

Incorporating equations (7.52) and (7.53) into the governing equations results in a system of first-order ordinary differential equations (ODEs) being formulated along a straight line marked as i, where i changes from 2 to N. In order to address the potential impact of geometric effects, a radial transformation is introduced, represented by the equation $x_1 = \frac{r}{R(z)}$. Following the preceding steps, the aforementioned transformation is then implemented on the equations denoted as (7.35) -(7.46).

For core region $(0 < x_1 \leq 0.75)$,

$$\begin{aligned}\frac{dw_i}{dt} =& \frac{1}{Re}\frac{\rho_0\rho_f}{\rho_{nf}}\left[\frac{\mu_{nf}}{\mu_f}\frac{1}{\mu_0}\frac{1}{R^{n+1}}\left\{\frac{1}{x_{1i}}\left(We\left|\frac{w_{i+1}-w_{i-1}}{2h}\right|\right)^{n-1}\left(\frac{w_{i+1}-w_{i-1}}{2h}\right)\right.\right.\\
&+\left(\frac{w_{i+1}-2w_i+w_{i-1}}{h^2}\right)\left\{\left(We\left|\frac{w_{i+1}-w_{i-1}}{2h}\right|\right)^{n-1}+(n-1)We^{n-1}\left(\left|\frac{w_{i+1}-w_{i-1}}{2h}\right|\right)^{n-2}\right.\\
&\left.\left.\left.\frac{w_{i+1}-w_{i-1}}{2h}\right\}\right\}\right]+\frac{1}{Re}\frac{(\beta)_{nf}}{(\beta)_f}GrT_i+\left(\frac{1}{Re}\frac{\rho_0\rho_f}{\rho_{nf}}\right)\left\{-\frac{\mu_{nf}}{\mu_f}\frac{1}{\mu_0}\frac{w_i}{Da}+E_p(1+e\cos(c_1t))\right.\\
&\left.-\frac{\sigma_{nf}}{\sigma_f}\frac{\alpha_e}{\alpha_e^2+\beta_e^2}M^2w_i+R_p(v_{pz}-w_i)\right\},\end{aligned} \tag{7.54}$$

$$\frac{dv_{p_i}}{dt} = \frac{(w_i - v_{p_i})}{G}. \tag{7.55}$$

$$\frac{dT_i}{dt} = \left(\frac{\rho_0 s_0}{k_0}\frac{1}{RePr}\frac{\kappa_{nf}}{\kappa_f}\frac{(\rho C_p)_f}{(\rho C_p)_{nf}}\right)\frac{1}{R^2}\left\{\frac{T_{i+1}-2T_i+T_{i-1}}{h^2}+\frac{1}{x_{1i}}\frac{T_{i+1}-T_{i-1}}{2h}\right\}$$
$$+\left(\frac{1}{R^2}\frac{\rho_0 s_0}{RePr}\frac{(\rho C_p)_f}{(\rho C_p)_{nf}}\right)\left[Nr\left(\left\{\frac{T_{i+1}-2T_i+T_{i-1}}{h^2}\right\}+\left\{\frac{1}{x_{1i}}\frac{T_{i+1}-T_{i-1}}{2h}\right\}\right)\right.$$
$$\left.+\frac{\mu_{nf}}{\mu_f}\frac{1}{\mu_0}Br\left(\frac{w_{i+1}-w_{i-1}}{2h}\right)^2\right]+\left(\frac{\rho_0 s_0}{RePr}\frac{(\rho C_p)_f}{(\rho C_p)_{nf}}\right)\frac{\sigma_{nf}}{\sigma_f}\frac{M^2 Br}{\alpha_e^2+\beta_e^2}w_i^2, \tag{7.56}$$

For plasma region $(0.75 < x_1 \leq 1)$,

$$\frac{dw_i}{dt} = \frac{1}{Re}\frac{\rho_f}{\rho_{nf}}\left[\frac{\mu_{nf}}{\mu_f}\frac{1}{R^2}\left\{\frac{1}{x(i)}\left(\frac{w_{i+1}-w_{i-1}}{2h}\right)+\frac{w_{i+1}-2w_i+w_{i-1}}{h^2}\right\}\right.$$
$$\left.+\frac{(\rho\beta)_{nf}}{(\rho\beta)_f}GrT_i+\left\{-\frac{\mu_{nf}}{\mu_f}\frac{w_i}{Da}\right\}+E_p(1+e\cos(c_1 t))-\frac{\sigma_{nf}}{\sigma_f}M^2 w_i\right], \tag{7.57}$$

$$\frac{dv_{p_i}}{dt} = \frac{(w_i - v_{p_i})}{G}. \tag{7.58}$$

$$\frac{dT_i}{dt} = \left(\frac{1}{RePr}\frac{\kappa_{nf}}{\kappa_f}\frac{(\rho C_p)_f}{(\rho C_p)_{nf}}\right)\frac{1}{R^2}\left\{\frac{T_{i+1}-2T_i+T_{i-1}}{h^2}+\frac{1}{x_{1i}}\frac{T_{i+1}-T_{i-1}}{2h}\right\}$$
$$+\left(\frac{1}{R^2}\frac{1}{RePr}\frac{(\rho C_p)_f}{(\rho C_p)_{nf}}\right)\left[Nr\left(\left\{\frac{T_{i+1}-2T_i+T_{i-1}}{h^2}\right\}+\frac{1}{x_{1i}}\frac{T_{i+1}-T_{i-1}}{2h}\right)\right.$$
$$\left.+\frac{\mu_{nf}}{\mu_f}Br\left(\frac{w_{i+1}-w_{i-1}}{2h}\right)^2\right]+\left(\frac{1}{RePr}\frac{(\rho C_p)_f}{(\rho C_p)_{nf}}\right)\frac{\sigma_{nf}}{\sigma_f}\frac{M^2 Br}{\alpha_e^2+\beta_e^2}w_i^2, \tag{7.59}$$

Furthermore, the initial conditions for ODEs mention from (7.54)-(7.59) is written in discrete form as:

$$w_i(0) = 0,\ \ v_{p_i} = 0,\ \ T_i(0) = 0. \tag{7.60}$$

Boundary Conditions:

The three-point forward finite difference formula for function f at $i = 1(x = 0)$ is given as:

$$\frac{\partial f}{\partial x} = \frac{-f(3)+4f(2)-3f(1)}{2h}. \tag{7.61}$$

Use equation (7.45) and (7.61) to write the function w, T and ϕ at $i = 1$ as given below:

$$w_1 = \frac{4w_2 - w_3}{3}, \quad v_{p1} = \frac{4v_{p2} - v_{p3}}{3}, \quad T_1 = \frac{4T_2 - T_3}{3}. \tag{7.62}$$

At $i = N+1$,

$$w_{N+1} = 0, \quad v_{pN+1} = 0, \quad T_{N+1} = 0. \tag{7.63}$$

The ensuing set of ODEs constitutes initial value problems (IVPs). To tackle the given system of ODEs, we have utilised the built-in MATLAB function 'ode15s.' This numerical solver is well-known for implementing a semi-implicit methodology, which is widely recognised as the 'stiff' ODE solver technique. The thermophysical characteristics of blood and nanoparticles are depicted in Figure 7.4.

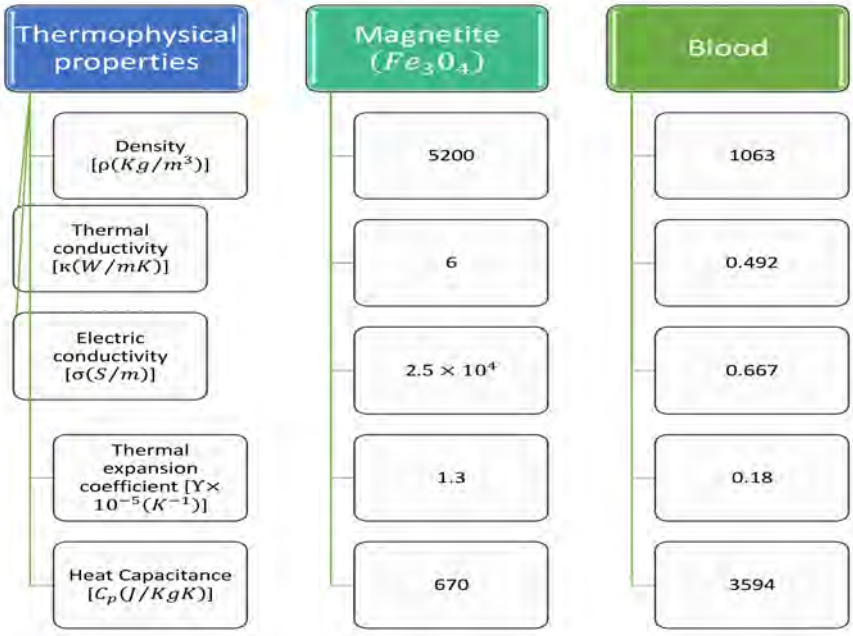

Figure 7.4: Thermophysical properties of blood and nanoparticle

The numerical values of various emerging parameters are presented in table 7.2 and 7.3. The thermo-physical properties of nanofluid is displayed in table 6.4.

7.4 Results and Graphical Analysis

In this segment, we extensively examined the dynamics of blood flow phenomena by analyzing graphical representations and the physical implications of various emerging parameters. This research serves as a crucial stride toward comprehending intricate physiological

processes. Specifically, our investigation centers on the two-phase blood flow within overlapping stenosed arteries. To simulate the blood flow in the core region, we employed the power law fluid model, while the non-Newtonian nature of blood was accounted for in the plasma region. The numerical code was simulated using the Method of Lines (MOL).

Parameters	Ranges	Sources
R_p	0.005-0.9	[180, 193]
G	0.02-0.9	[193]
Nr	0-5	[194]
Ratio of density in core and plasma region (ρ_0)	1.05	[4, 5]
Ratio of viscosity in core and plasma region (μ_0)	1.2	[3, 4]
Magnetic field parameter (M)	0-$\sqrt{5}$	[40, 121]
Weissenberg number (We)	1.5-3.5	[18]

Table 7.2: Values of the physical parameters with their sources

Parameters	ϕ_1	B_1	Gr	β_e	β_i	n	Da^{-1}	Re	Ec	κ_0
Ranges	0.02	1.4	2	0.5	0.7	0.7	0.2	5	0.5	0.5

Table 7.3: Default value of emerging parameters

7.4.1 Validation

The validation of our research is supported by a study conducted by Tripathi et al. [176] on two-phase magnetohydrodynamic (MHD) blood flow through a stenosed artery. Through appropriate assumptions, we have corroborated the velocity and temperature profiles of our current research by comparing them with the findings of Tripathi et al. [176], as depicted in figures 7.5a and 7.5b. It is worth noting that Tripathi et al. [176] utilized an analytical methodology to obtain exact solutions for the dimensionless governing equations in their study. In contrast, our research employed the Method of Lines (MOL) approach. The resulting graphical representations exhibit a significant agreement between our study and the prior research, confirming the consistency of our velocity and temperature profiles with the established literature.

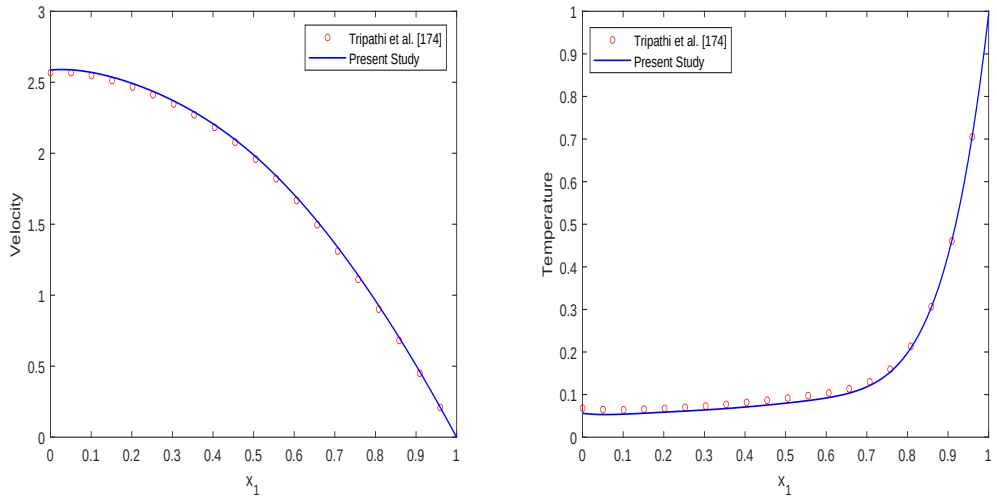

(a) Comparative result for velocity profile for $Gr = 2$

(b) Comparative result for temperature profile for $Nr = 9$

Figure 7.5: Validation for velocity and temperature profile for $Gr = 2$ and $Nr = 9$

7.4.2 Velocity Profile

Figures 7.6 and 7.7 depict the velocity profile for nanofluid (Fe_3O_4-Blood) and nanoparticle flowing though the stenosed artery. Figures 7.6a and 7.7a depict the velocity profile by varying Particle mass parameter G on both the nanofluid and nanoparticles velocity. The velocity profile in nanofluid is relatively more as compared to nanoparticle velocity in which both profile show the declining nature with increasing G. In targeting drug delivery both the nanoparticle and nanofluid influenced by the interaction of magnetic and viscous forces. The nanofluid (fluid with nanoparticles) will have a higher velocity compared to individual nanoparticles within it. This is because the nanoparticle experiences the drag force due to viscous resistance of the fluid while the fluid is less affected by this drag force and move freely. As Particle mass parameter G increases, it signifies the drag force experienced by the nanoparticle become more significant and they are less able to accelerate through influence of magnetic field resulting in the decline of nanoparticle velocity. The nanofluid velocity decreases as G increases due to the enhancement in the fluid viscosity which hinder the flow of the fluid more significantly due to their size and mass. Figures 7.6b and 7.7b depict the variation of Weissenberg number We on both the nanofluid and nanoparticles velocity. Both figures illustrate the variation in the velocity profile as a function of the Weissenberg number in the context of two-phase blood flow. The Weissenberg number, a dimensionless parameter representing the relationship between a material's relaxation time and deformation time scale, governs the material's behavior.

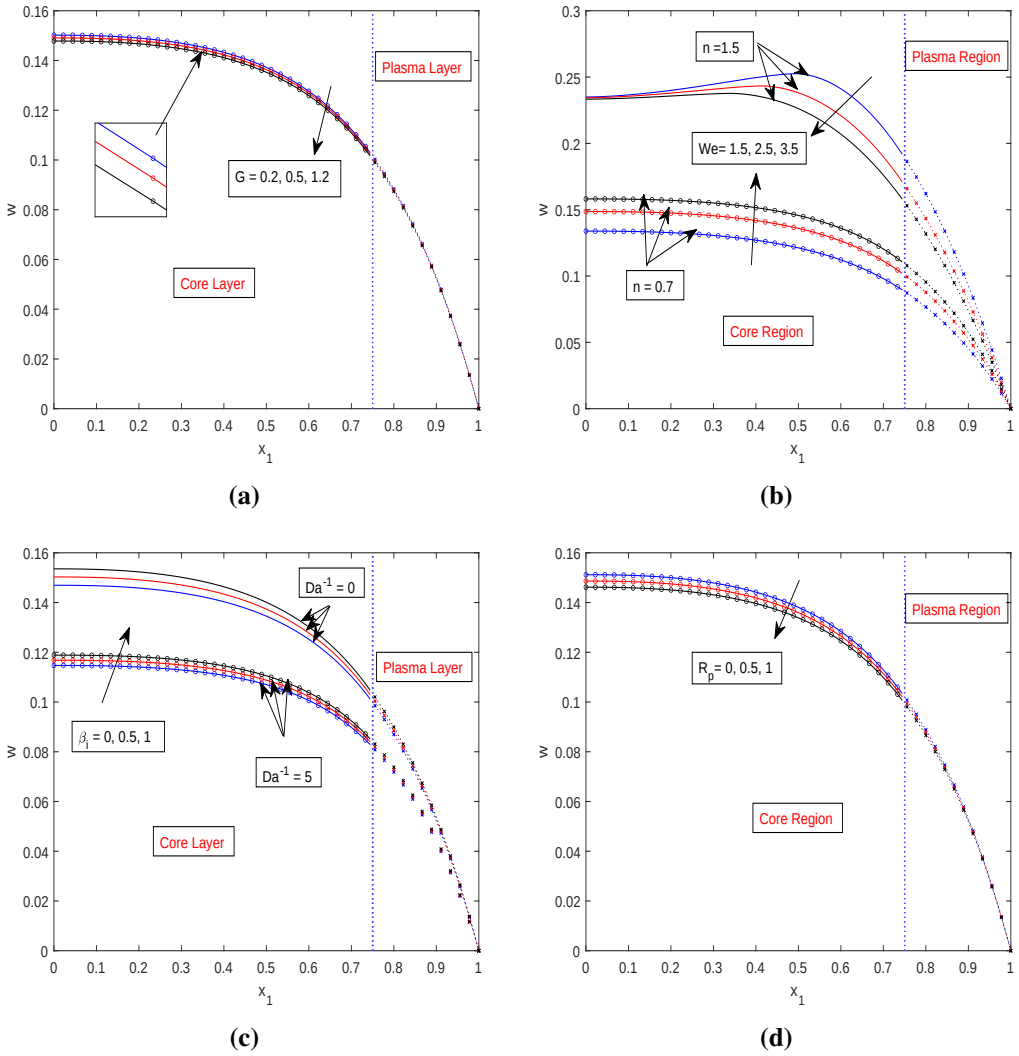

Figure 7.6: Blood flow velocity (a) Particle mass parameter G, (b) Weisenberg number We, (c) Ion parameter (d) Particle concentration parameter R_p

The provided figure demonstrates that, for a fixed value of $n = 1.5$, the velocity profile exhibits a distinct trend of decreasing magnitude with the increasing Weissenberg number (We). This trend implies a strong positive correlation between heightened resistance to deformation and an elevated Weissenberg number. In the domain of shear-thickening fluids characterized by a power-law index of $n = 1.5$ it has been observed that as the applied shear stress or strain rate increases, the fluid's resistance to flow becomes more pronounced. Conversely, in the case of a shear-thinning fluid exhibiting power-law behavior with an exponent of $n = 0.7$, an inclination towards higher velocity values is discernible as the Weissenberg number is augmented. This phenomenon can be attributed to the unique properties of shear-thinning fluids, which display reduced resistance to deformation. Consequently, this behavior facilitates enhanced fluid flow under conditions of escalated stress or strain rates.

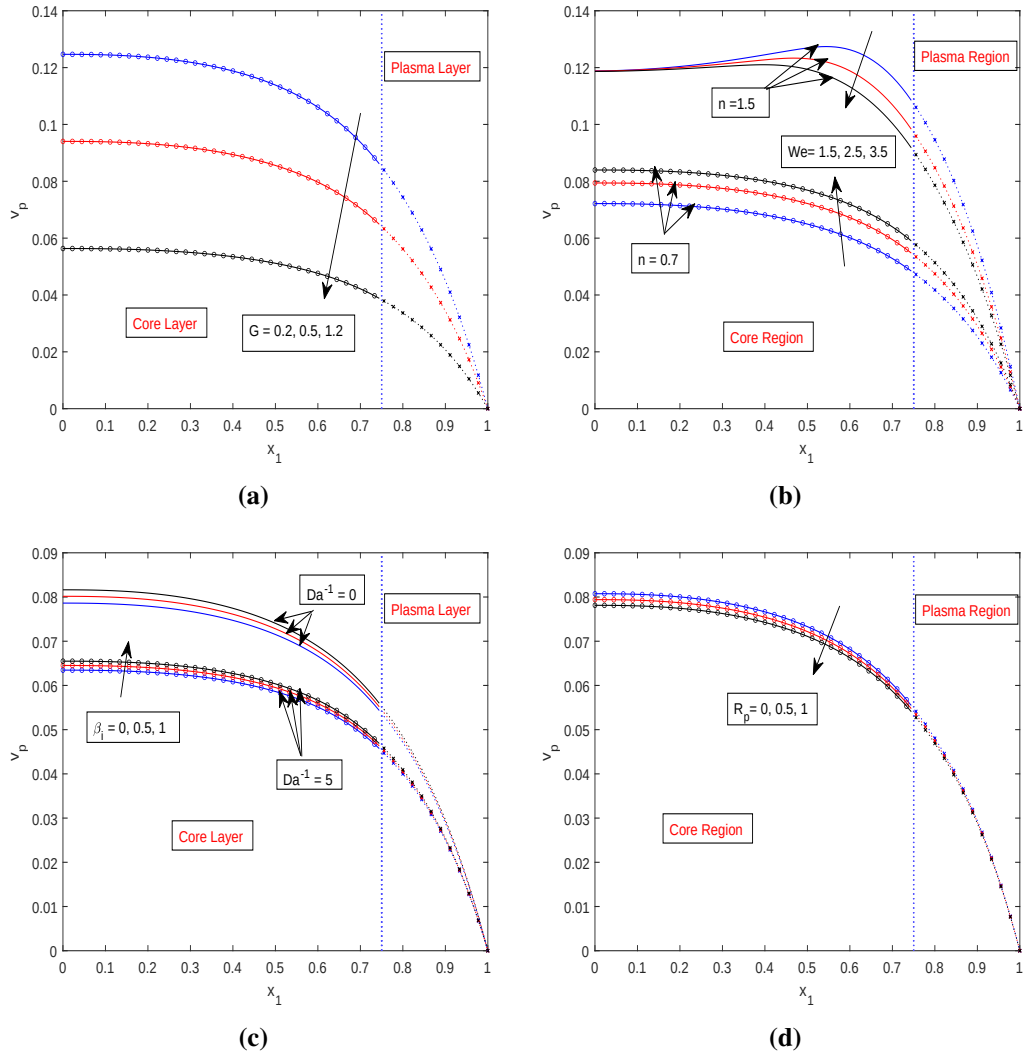

Figure 7.7: Nanoparticle velocity for (a) Particle mass parameter G, (b) Weisenberg number We, (c) Ion parameter (d) Particle concentration parameter R_p

Figures 7.6c and 7.7c illustrate the effect of Hall parameter β_e and inverse Darcy number Da^{-1} on the nanofluid and nanoparticle velocity, respectively. The velocity profile in both the cases increases as β_i increases from 0 to 1, while reverse trend is observed for Da^{-1}. The enhancement in the magnitude of β_e signifies the stonger electromagnetic force which assists the fluid motion, thus overpowering the viscous drag forces. The stronger electromotive forces on both the nanoparticle and surrounding fluid leads to enhancement in the fluid velocity. Thus, the combined effect of individual nanoparticle acceleration and the enhanced fluidic behavior results in a higher nanofluid velocity compared to the velocity of individual nanoparticles within the fluid. In both the figure , the velocity profile declines as Da^{-1} increases from 0 to 5. This has happened due the dominant effect of viscous forces over the inertial forces leading to a decline in the velocity profile.

Figures 7.6d and 7.7d illustrate the influence of particle concentration parameter R_p on the velocity profile of nanofluid and nanoparicles. In both the figure the velocity shows the declining nature as R_p increases from 0 to 1. The enhancement in R_p results in the overall increase in the viscosity of fluid. Thus, reducing the nanofluid velocity and the resulting drag force on the nanoparticle enhances that lead in decrement of the nanoparticle velocity profile. While individual nanoparticles experience reduced velocities, the nanofluid can maintain a relatively higher overall velocity due to its collective fluidic behavior. This contrast in velocities is a result of the complex interplay between interparticle interactions, fluid viscosity, and the behavior of particles in the magnetic drug targeting process.

7.4.3 Temperature Profile

Figure 7.8 depicts the temperature profile for the two phase blood flow thorugh stensoed artery by varying the Prandtl number Pr , magnetic field parameter M, Hall parameter β_e and radiation parameter Nr. The temperature profile, illustrated in Figure 7.8a, demonstrates a noticeable decline as the Prandtl number (Pr) increases within the range of 19 to 27. A higher Prandtl number, Pr, implies lower thermal conductivity within the fluid when compared to smaller Prandtl numbers. Smaller Prandtl numbers facilitate more efficient heat conduction, yielding steeper temperature gradients and, consequently, elevated temperature profiles. In contrast, higher Prandtl numbers correspond to decreased thermal conductivity, leading to less effective heat propagation and lower temperature gradients and, consequently, reduced temperature profiles. Figure 7.8b demonstrate the declining nature of the temperature profile with increase in the magnetic field parameter M. This has happened due to the enhancement in the thermal conductivity of the fluid that facilitate the conduction of heat away from the stenosed region leading to the decrement in the temperature profile. In the MDT , the targeted nanoparticle is guided by the external magnetic field which lead to providing medicine to particular targeted region. This could be beneficial for the medication of the temperature sensitive drug as lower temperature could enhance the stability and efficacy of drug on arrival at the particular site. Figure 7.8c potrayed the temperature profile for varying Hall parameter β_e. The Hall effect arises due to the interaction of the magnetic field and the motion of the charged particle. The enhancement in the Hall parameter leads to the transfer of the energy from the higher to cooler region. Additionally, the enhanced heat conduction facilitated from the enhancement of the Hall parameter lead to decline in the temperature profile. Also, it has been obeserved that the temperature profile decreases as the magntiude of Reynold number Re increases from 2 to 5. Figure 7.8d illustrates the enhancement in the temperature profile with both the radiation parameter Nr and Eckert number Ec. This has happened due to the generation of additional thermal energy as Nr

increases from 0 to 5. This ionized radiation can be beneficial in MDT by temporarly altering the permeability of the arterial wall making it easier for the drug-loaded nanoparticles to penetrate the stenosed artery.

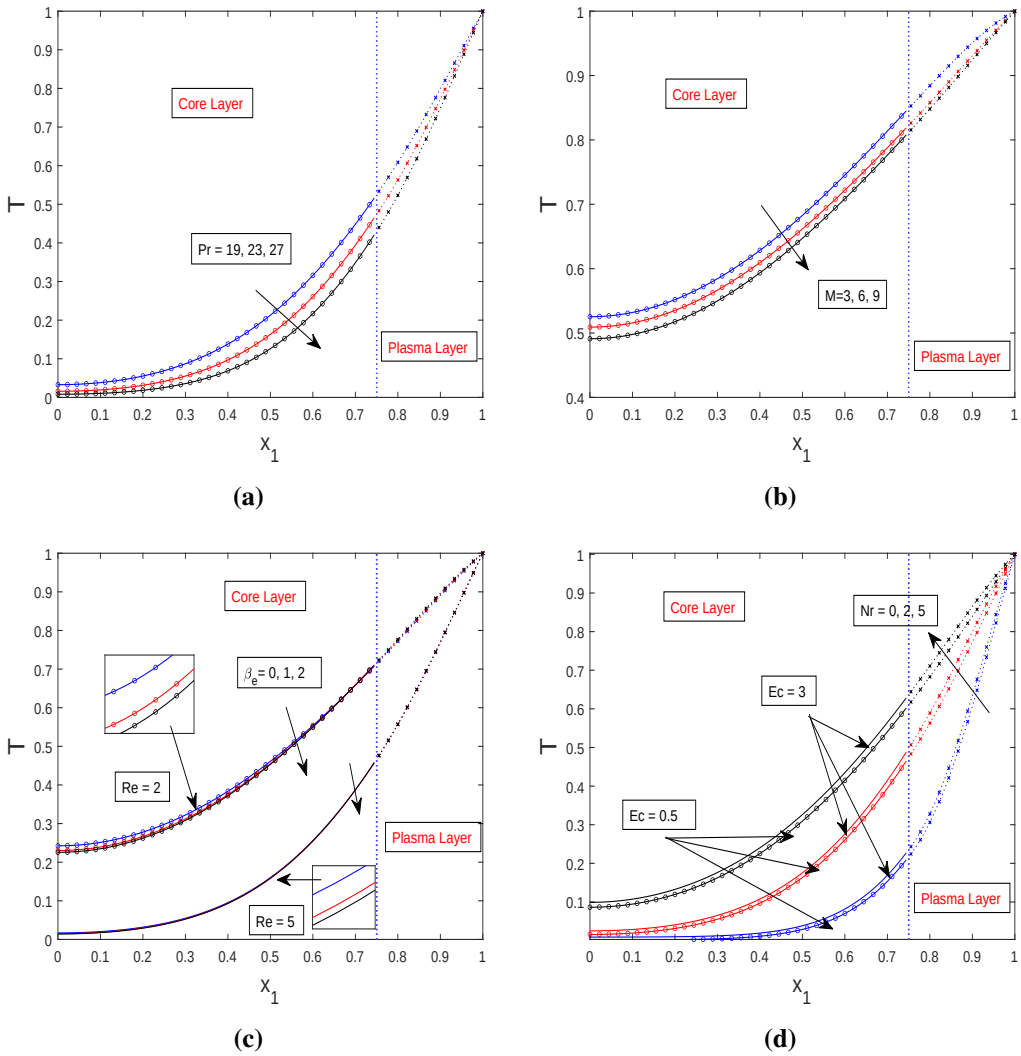

Figure 7.8: Temperature profile for (a) Prandtl number Pr, (b) Magnetic field parameter M, (c) Hall parameter β_e (d) Radiation parameter Nr

As the Ec increases from 0.5 to 3, this leads to the enahncemetn of the temperature profile as the kinetic energy get converted into thermal energy due to viscous dissipation.

7.4.4 Nusselt Profile

Figure 7.9 demonstrates the Nusselt profile, varying the magnetic field parameter M and radiation parameter Nr. Analyzing Figure 7.9a, it is evident that the Nu_x profile diminishes with an increase in the magnetic field strength from 0 to 2. This decline is attributed to the

emergence of Lorentz forces, impeding fluid motion near the surface. Consequently, this resistance diminishes convective heat transfer, leading to a reduction in the Nusselt profile. Conversely, Figure 7.9b indicates a rising trend in the Nu_x profile as Nr escalates from 0 to 2. A higher radiation parameter signifies the prevalence of radiative heat transfer over convective heat transfer.

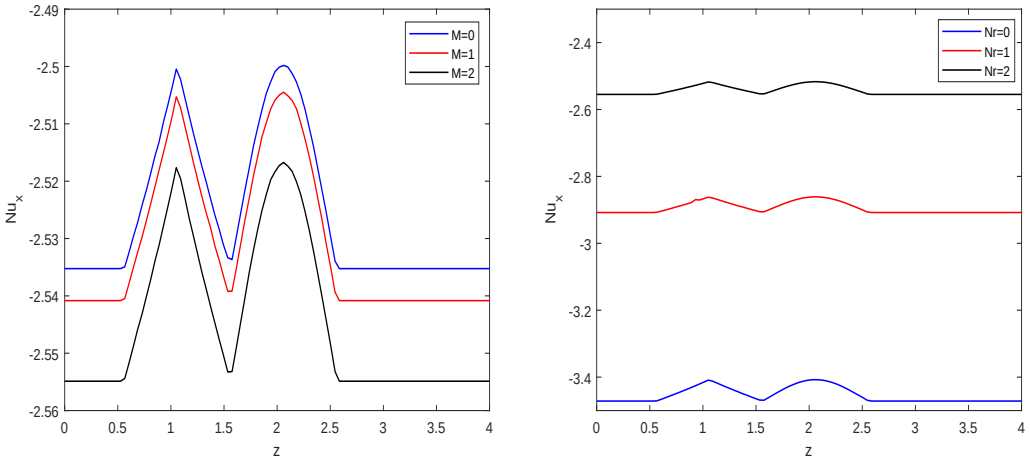

(a) **(b)**

Figure 7.9: Nusselt profile

Radiative heat transfer aids in redistributing heat within the fluid. Areas with elevated temperatures, such as stenosis, lose heat through radiation, while cooler regions absorb energy from radiation. This redistribution results in a more uniform temperature distribution, enhancing both heat transfer and the Nusselt profile. In the realm of medical diagnostics, professionals can discern conditions related to blood flow, inflammation, and skin temperature disorders by analyzing radiation patterns dependent on temperature distribution. Various heat transfer mechanisms, including radiation, influence these temperature profiles.

7.4.5 Flow Rate and Impedance

The circulatory system, a marvel bioengineering example which ensures the delivery of oxygen and nutrients to tissue and organ throughout the human body. A critical determinability of its proper functioning is flow rate and impedance that influence the vascular health and play a crucial role in understanding and managing the circulatory diseases. Figure 7.10a illustrates the influence of magnetic field parameter M on the flow rate profile. From the figure, we can observed that the flow rate profile decreases for M and near the stenotic zone. This behaviour is occured as a result of reistance offered by the Lorentz force.

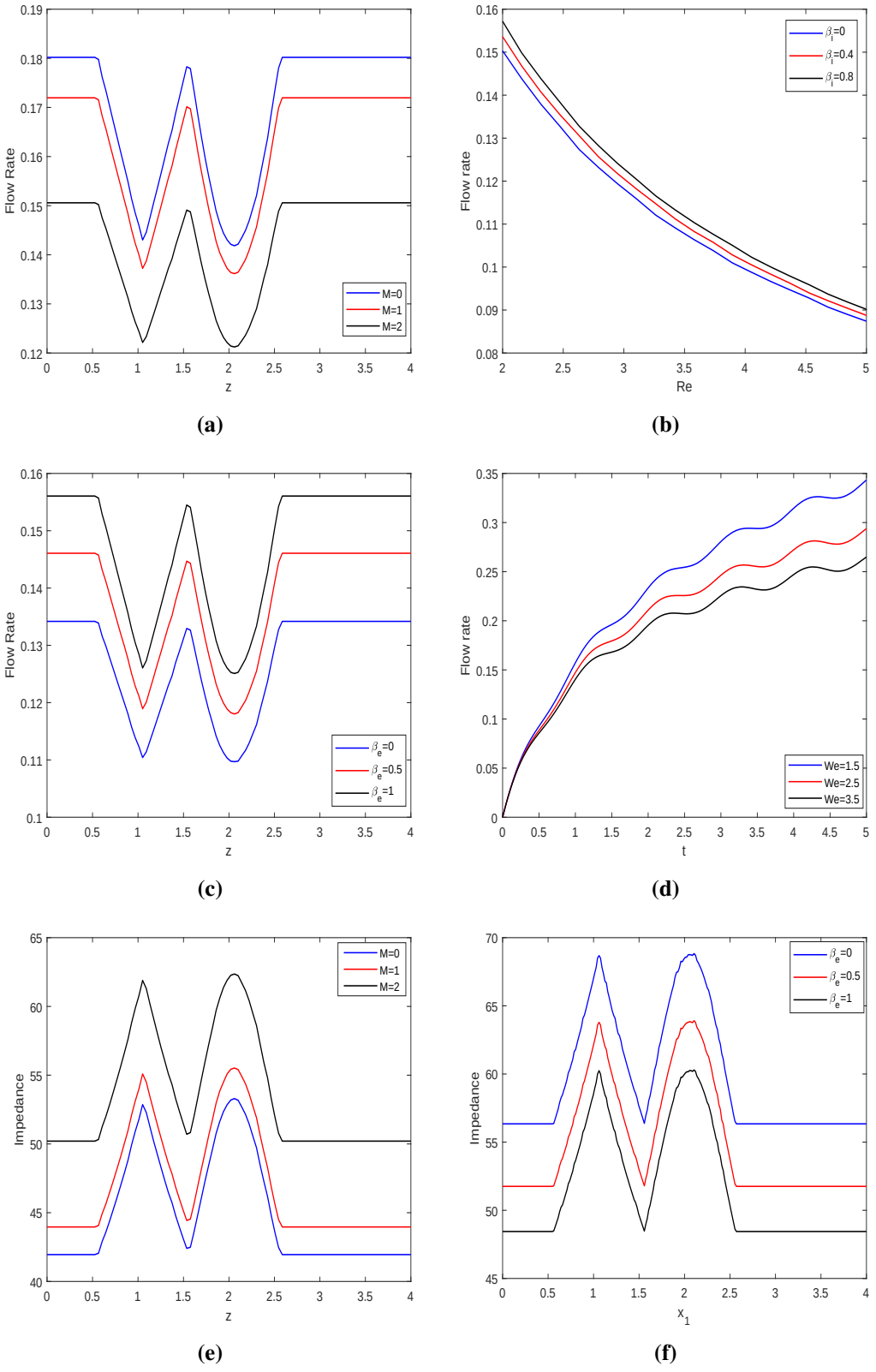

Figure 7.10: Flow rate profile for (a) Magnetic field parameter M, (b) Ion parameter β_i, (c) Hall parameter β_e (d) Weissenberg number We Impedance profile for (e) Magnetic field parameter M, (f) Hall parameter β_e

This additional force opposes the flow of blood, making it the lower movement of blood to pass through the stenosed artery. The magnetic field hinders the movement of blood creating a localized effect which is beneficial for the targeted drug delivery. Figure 7.10b shows the influence of β_i and Re on the flow rate profile. The flow rate profile falls down from 0.15 to 0.09 in the absence of ion effect $\beta_i = 0$ for increasing Re from 2 to 5. It can be inferred from the figure that flow rate profile increases as the value of β_i increases from 0 to 0.08. This leads to increasing ion effect which makes the higher conductivity of the fluid. The response to applied magnetic field becomes stronger as the concentration of ions (carriers) increases in the solution. Thus, this leads to further increase in the flow rate in the stenosed artery. Similarly, we can observed the enhancement in the flow rate profile for Hall parameter β_e. The magnetic force extered on the fluid become stronger in comparison with viscous forces as the Hall parameter increases from 0 to 1. This increase in the fluid velocity leads to enhancement of the flow rate. Figure 7.10d shows the time series graph of flow rate profile for Weisenber number We. In this case, we have consider shear thickening fluid $n = 1.5$ and plot the time series graph of flow rate profile, clearly, it can be seen that the flow rate profile decreases as We varies from 1.5 to 3.5. The elastic stress becomes predominant for higher value of Weissenberg number $We > 1$. The shear-thicknenig fluid tend to resist deformation under stress due to their increased viscosity with higher shear rates. The resistance occurs due the deformation results in a decrease in the flow rate profile. Figure 7.10e demonstrate the declining nature for the increasing strength of the magnetic field. As discussed in the figure 7.10a, the resistive force comes into the picture and resist the fluid motion which leads to the enhancement in the Impedance profile. Figure 7.10f depict the declining nature in the impedance profile for enhancing value of Hall parameter β_e. The dominance of the magnetic forces over the viscous forces leads to enhancement in the fluid velocity depicting the reverse trend on the Impedance profile. In magnetic drug targeting, an increases in the Hall parameter llow for more precise control over the movement of the magnetic particles carrying therapeutic agents.

7.4.6 Wall Shear Stress (WSS)

This improved control can be helpful in guiding the particle to be targeted more efficiently at the targeted sites such as stenosis, thrombosis and cancerous cells. WSS is one of the influential parameter to be study in the stenosed artery due to its impact on the vascular health, tissue remodeling and progression of arterial diseases . It is defined as the frictional force per unit area exerted on the flowing blood on the endothelial lining of the blood vessel. Figure 7.11a illustrates the WSS profile for the variation of magnetic field parameter and Grashof number Gr.

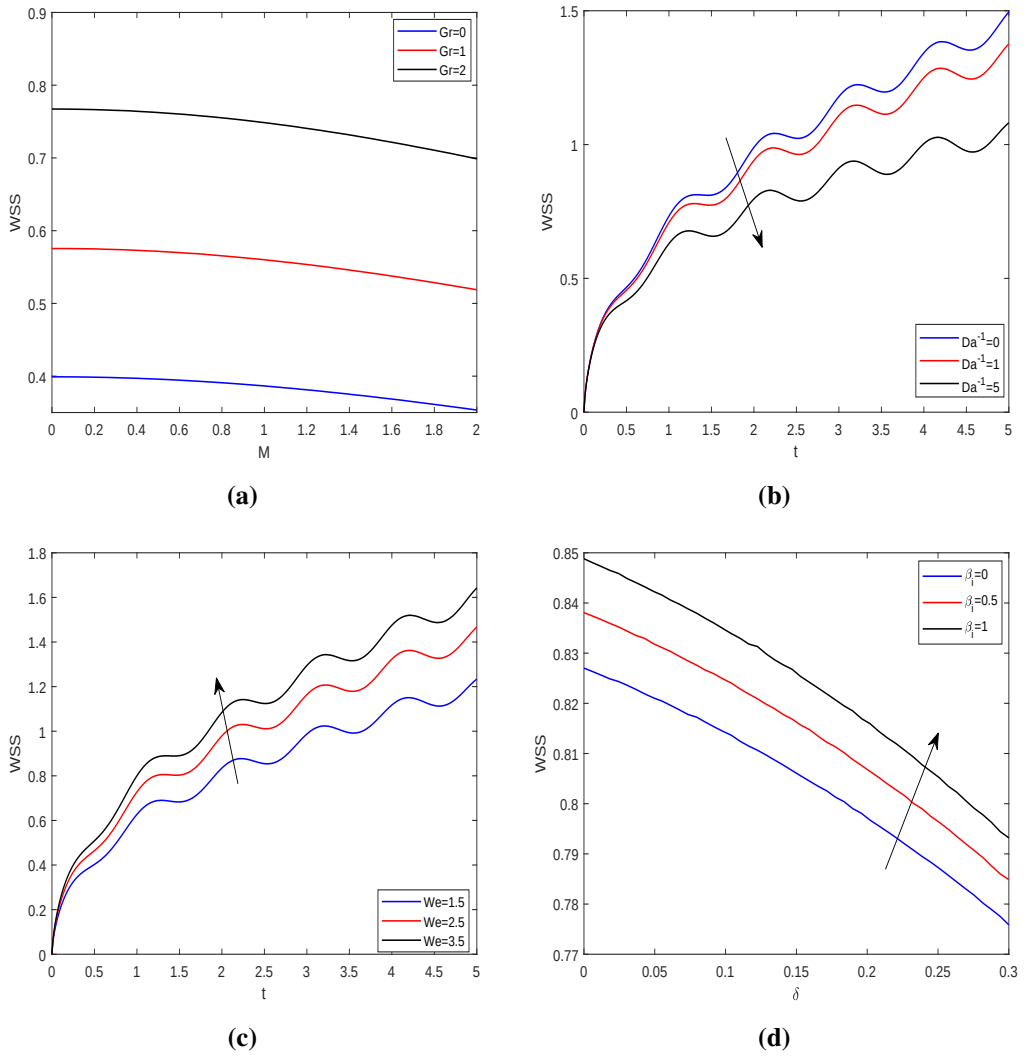

Figure 7.11: WSS profile for (a) Grashof number Gr, (b) Inverse Darcy number Da^{-1}, (c) Weissenberg number We (d) Ion parameter β_i

Enhancement in the value of Gr leads to the dominance of buoyancy forces over viscous forces. This lead to the increase in the velocity of fluid near the arterial wall and enhanced the WSS profile. While, it can be observed from the figure that the WSS profile shows the declining nature with enhancement in the value of magnetic field parameter M. The dominance of the magnetic field results in the reduction of the velocity gradient and shear within the fluid. As a result WSS profile decreases with increasing M. Figure 7.11b depict the variation in the time series graph of WSS profile with the inverse Darcy number Da^{-1}. The enhancement in the value of Da^{-1} represent the dominance of the viscous forces relative to the inertial forces. This lead to decrement in the velocity of fluid near the wall and decrease in WSS profile. Figure 7.11c shows the declining nature of the time series graph of WSS profile for increasing Weissenberg number. For $n = 1.5$, the fluid shows the shear

thinning nature where viscosity decreases with increase in the magnitude of We from 1.5 to 3.5. This results in the enhancement of the fluid velocity and WSS profile. Figure 7.11d depicts the wall shear stress (WSS) profile concerning the ion parameter β_i in relation to stenotic depth. The graph clearly illustrates that the WSS profile exhibits a declining trend as the stenotic depth values increase from 0 to 0.03. In the absence of stenosis, the WSS profile reaches its peak, registering values of 0.848, 0.838, and 0.827 for β_i values of 0, 0.5, and 1, respectively. Furthermore, the WSS profile displays an increasing pattern with higher values of β_i. This phenomenon arises due to the induced velocity gradient within the fluid, a consequence of the presence of a magnetic field. The velocity gradient becomes more pronounced with higher ion parameter values, a characteristic that is reflected in the WSS profile.

7.4.7 Contour

Velocity contour are the valuable tools in fluid dynamics that visually represent the distribution of velocity field within the given domain. In our case, it demonstrates the magnitude and direction of the fluid velocity around the stenosed artery. Moreover, the contour provides the valuable insights like recirculation zones and areas of low velcoity, highlighting the region prone to thrombus formation and artherosclerotic plaque formation. Figures7.12a-7.12c illustrate the velocity contour for variation in the magnetic field parameter M. The figure illustrates the decrement in the velocity pattern. Figure 7.12a eludicate the velocity field in the stenosed artery for $M = 0$ (absence of magnetic field). The maximum velocity attain by the fluid is 0.18 in the central part of the artery with no-slip boundary condition at the arterial walls. Although the maximum velocity attain by the fluid is same that is 0.14 in both the figure 7.12b and 7.12c but the central region occupied by the maximum velocity vary in both the case.

The reduction of the velocity field is due to the Lorentz force which comes into picture due to the interaction of the magnetic and electric field. This resistive force retard the fluid motion as depicted in the velocity contours. Figures 7.12d- 7.12f depict the nanoparticle velocity contour for particle concentration parameter R_p. Figure 7.12d shows the velocity field in the absence of particle concentration parameter R_p. Clearly, it can be observed from the figures 7.12d- 7.12f that the velocity decreases with increase in R_p from 0 to 1. If we compare all these three figures, we can intercept that the region occupied by the maximum nanoparticle velocity reduces from 7.12d to 7.12e, while it further reduces to 0.7 for $R_p = 1$ as depicted in the figure 7.12f. Researchers aim to optimize the particle concentration to achieve the balance between the effective drug delivery and maintaining an acceptable flow velocity.

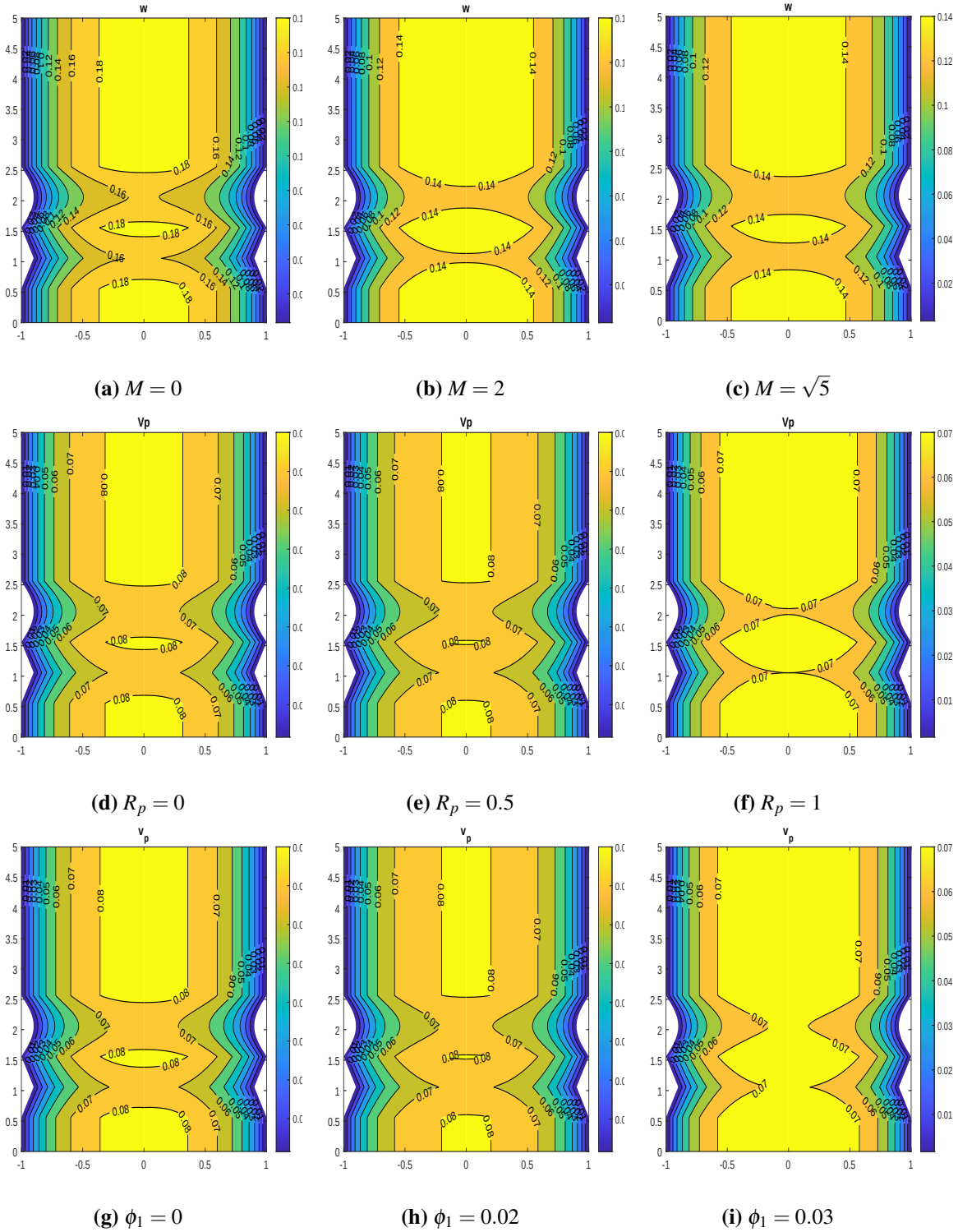

(a) $M = 0$ **(b)** $M = 2$ **(c)** $M = \sqrt{5}$

(d) $R_p = 0$ **(e)** $R_p = 0.5$ **(f)** $R_p = 1$

(g) $\phi_1 = 0$ **(h)** $\phi_1 = 0.02$ **(i)** $\phi_1 = 0.03$

Figure 7.12: Nanofluid velocity contour for (a) Magnetic field parameter M , Nanoparticle velocity contour for (b)Particle concentration parameter R_p, (c) volumetric concentration of nanoparticle ϕ_1.

Too high a particle concnetration might impede the fluid flow excessively, while too

low a concentration might result in inadequate drug targeting efficiency. The nanoparticle velocity contour are depicted in the figures 7.12g-7.12i. Figure 7.12g shows the nanoparticle velocity contour in the absence of nanoparticle (Pure blood case). The maximum velocity is 0.08 which occupied the central region of the stenosed artery. This region is further decreased while the maximum velocity remain the same. In both the cases a trapped bolus formed in the central part of the stenosed artery. From the figure 7.12i , it can be inferred that the maximum velocity reduces to 0.07 and the trapped bolus in the central part also disapper for $\phi_1 = 0.03$. This demonstrate that the enhancement in the nanoparticle concentration reducers the nanoparticle velocity.

7.4.8 Conclusion

This study delves into the hemodynamic flow characteristics involving the suspension of magnetite (Fe_2O_3) nanoparticles within blood flowing through stenosed arteries. The research employs a two-phase blood flow model, considering the core region's fluid nature using the Ostwald-DeWaele power-law fluid model and the peripheral layer of plasma as Newtonian. Specifically, the study focuses on the (Fe_2O_3-Blood) nanofluid, with direct applications in magnetic drug targeting. Important key findings emerge from this investigation:

- The velocities of both nanoparticles and the nanofluid decrease as the particle mass parameter G increases.
- Temperature profiles exhibit enhancement with rising radiation parameter Nr, while showcasing an inverse trend with the Prandtl number Pr.
- Wall shear stress (WSS) profiles decline with increasing stenotic depth but exhibit the opposite trend with the ion parameter β_i.
- The time series graph of flow rate profiles illustrates a declining trend for the Weissenberg parameter We concerning shear thickening fluid.
- Impedance profiles increase with a rise in the magnetic field parameter M due to the generation of the resistive Lorentz force.

These insights are not only valuable for understanding the fundamental dynamics of nanofluid flow in stenosed arteries but also hold significant promise in the biomedical field. The findings suggest practical applications, particularly in the realm of magnetic drug targeting delivery. By harnessing magnetite nanoparticles, this research paves the way for innovative approaches to targeted drug delivery, potentially revolutionizing treatments in the biomedical arena.

Chapter 8

Conclusions and Future work

This chapter discusses the primary findings of the thesis in the conclusion section and explores potential avenues for future research in the future work section.

8.1 Conclusions

The main motivation of this work is to explore the hemodynamic flow and its interaction with different physical phenomena through the stenosed artery. We have considered the different types of arterial geometry, the Newtonian and non-Newtonian fluid properties, the effect of nanoparticle shape and size and different types of pathological conditions like stenosis, thrombosis and aneurysm. Chapter 1 briefly explained the bio-fluid mechanics, pathological conditions, physical parameters and the numerical methodology. In Chapter 2, the study focuses on the flow of MHD hybrid nanofluid (Au-GO/blood) through a curved artery. The mathematical model is presented in the curvilinear coordinate system, considering the effects of Hall and ion slip, Joule heating, thermal radiation, and a viscosity model dependent on hematocrit. The results illustrate that the hybrid nanoparticles Au-GO exhibit a higher temperature profile compared to pure and individual nanoparticles. This increase is due to the heightened thermal conductivity with a rise in nanoparticle concentration. Chapter 3 delves into entropy generation optimisation in electroosmotic MHD fluid flow through a curved artery. The research explores blood flow containing suspended Al_2O_3 nanoparticles in irregular stenosis with thrombosis on catheter walls. The study investigates the impact of nanoparticle shape and size using the Crocine model. It is observed that the temperature profile rises with an increase in the nanoparticle shape parameter, attributed to the enhanced thermal conductivity. Moreover, as nanoparticle size increases, the velocity profile also rises due to the increase in surface area ratio. Consequently, fluid flow reduction occurs with a decrease in nanoparticle size due to the enhanced fluid velocity.

The human circulatory system is incredibly complex, comprising arteries that are not just straight or curved but also frequently bifurcated, meaning they split into two smaller branches. The stenosis and aneurysm usually occur at the bifurcation site; thus, understanding the flow dynamics in these bifurcations is critical for diagnosing and treating vascular diseases. Motivated by an issue regarding these physiological conditions, in chapter 4, we have discussed the hybrid nanofluid (Al_2O_3-Cu/Blood) flow through the bifurcated artery containing the gyrotactic microorganisms. In both sections of the bifurcated artery (Parent and daughter artery), mild stenosis is considered where the overlapping stenosis at the parent artery and irregular stenosis on the daughter artery. The effect of electroosmotic force, heat source, magnetic field and chemical reaction are studied on the blood flow through the bifurcated artery. It has been discovered that for change in the bifurcation angle, the impedance profile depicts no change in the parent artery but shows changes in the daughter artery as the bifurcated angle caused the fluid to change its behaviour and led the decreasing profile for an increasing bifurcation angle. The rise in the bioconvective Peclet number results in an increase in the speed of motile microorganisms, which decreases the density of microorganisms. In Chapter 5, the study delves deeper into entropy generation within bifurcated arteries during blood flow. The Casson fluid model depicts blood behaviour, considering pathological conditions like aneurysms and overlapping stenosis in both parent and daughter arteries. The research explores ternary hybrid nanoparticles (Au-CuO-GO), offering superior stability and prolonged circulation in the bloodstream. Notably, the ternary hybrid nanofluid (Au-CuO-GO) exhibits a higher velocity profile compared to the hybrid nanofluid (Au-CuO). This chapter also states that the entropy generation profile increases as the magnitude of Brinkmann number Br increases.

We have utilised a two-phase blood model outlined in Chapter 6 to depict the inherent characteristics of blood accurately. According to Haynes' theory, this model illustrates the tendency of red blood cells (RBCs) to concentrate at the centre of the vessel, leaving plasma, devoid of RBCs, to accumulate at the vessel's periphery. Our investigation focuses on the dynamics of two-phase nanofluid flow in the blood through a stenosed artery. This model incorporates a Power-law fluid characterisation for the core region and a Newtonian fluid description for the plasma region. Moreover, our analysis includes the integration of thermophoresis, Brownian motion, and activation energy into the flow analysis. The study emphasises explicitly the potential of suspended Al_2O_3 nanoparticles in the blood due to their biocompatible and chemically stable nature. The governing equations, derived under the assumption of mild stenosis, have been solved using the Method of Lines approach, a precise and adaptable numerical methodology known for its efficacy in addressing complex partial differential equations. Our findings indicate that introducing Al_2O_3 nanoparticles

into the blood enhances fluid velocity. Additionally, our investigation reveals a significant reduction in the concentration profile concerning the Thermophoresis parameter, while a reverse effect is observed for the Brownian motion parameter.

In Chapter 7, we investigated the effectiveness of targeted drug delivery mechanisms in unsteady blood flow by introducing the infusion of Fe_3O_4 magnetic nanoparticles within a stenosed artery. Conventional systemic drug delivery methods often lack efficiency in such situations due to limited drug targeting and high systemic toxicity. Magnetic drug targeting, however, offers an improved treatment approach without compromising healthy tissues. Motivated by the potential of targeted drug delivery, our study focused on incorporating Fe_3O_4 magnetic nanoparticles within a stenosed artery to explore their impact on unsteady blood flow. The study employed a two-phase mathematical model, incorporating a power law fluid model in the core region and a Newtonian model in plasma regions. Our findings revealed that an increase in the particle mass parameter (G) led to a reduction in both nanoparticle and nanofluid velocities. Moreover, a comprehensive time series analysis of flow rate profiles demonstrated a decreasing trend in the Weissenberg parameter (We), particularly in the context of shear-thickening fluid. This research significantly enhances our understanding of magnetic drug targeting, contributing valuable insights to biomedical fluid dynamics. These findings have substantial implications for developing targeted drug delivery systems and their potential applications in healthcare.

8.2 Future Scope

The mathematical model examined in this study focused on the different types of geometry for both stenosis and artery. The blood is represented by both Newtonian and non-Newtonian fluid model. In the clinical point of view, the following aspects of research work could be explore in the future course:

- Exploring the analysis of solute dispersion in two-phase blood flow through curved arteries.
- Investigating the fluid-structure interaction of non-Newtonian Power law fluids in bifurcated channels with stenosis and elastic walls.
- Extending the research presented in Chapter 6 to include magnetic drug-targeted blood flow in curved artery. This extension involves incorporating variable viscosity in both the core and plasma regions.
- Investigate nanofluid blood flow in stenosed bifurcated arteries and curved arteries with compliant walls using the vorticity-stream function approach.

- Examining the impact of drug carrier characteristics such as shape, size, porosity, and blood rheology on magnetic nanoparticle-based drug delivery within curved and bifurcated arteries.

Bibliography

[1] B. K. Sharma, U. Khanduri, N. K. Mishra, and A. J. Chamkha, "Analysis of arrhenius activation energy on magnetohydrodynamic gyrotactic microorganism flow through porous medium over an inclined stretching sheet with thermophoresis and brownian motion," *Proceedings of the Institution of Mechanical Engineers, Part E: Journal of Process Mechanical Engineering*, p. 09 544 089 221 128 768, 2022.

[2] A. Ahmed and S. Nadeem, "Effects of magnetohydrodynamics and hybrid nanoparticles on a micropolar fluid with 6-types of stenosis," *Results in physics*, vol. 7, pp. 4130–4139, 2017.

[3] M. Sharan and A. S. Popel, "A two-phase model for flow of blood in narrow tubes with increased effective viscosity near the wall," *Biorheology*, vol. 38, no. 5-6, pp. 415–428, 2001.

[4] A. Medvedev and V. Fomin, "Two-phase blood-flow model in large and small vessels," in *Doklady Physics*, SP MAIK Nauka/Interperiodica, vol. 56, 2011, pp. 610–613.

[5] B. Tripathi and B. K. Sharma, "Influence of heat and mass transfer on two-phase blood flow with joule heating and variable viscosity in the presence of variable magnetic field," *International Journal of Computational Methods*, vol. 17, no. 03, p. 1 850 139, 2020.

[6] A. Dubey, B Vasu, O Anwar Bég, R. S. Gorla, and A. Kadir, "Computational fluid dynamic simulation of two-fluid non-newtonian nanohemodynamics through a diseased artery with a stenosis and aneurysm," *Computer Methods in Biomechanics and Biomedical Engineering*, vol. 23, no. 8, pp. 345–371, 2020.

[7] B. Tripathi, B. K. Sharma, and M. Sharma, "Modeling and analysis of MHD two-phase blood flow through a stenosed artery having temperature-dependent viscosity," *The European Physical Journal Plus*, vol. 134, no. 9, p. 466, 2019.

[8] B. D. Sharma and P. K. Yadav, "A two-layer mathematical model of blood flow in porous constricted blood vessels," *Transport in Porous Media*, vol. 120, pp. 239–254, 2017.

[9] K. S. Mekheimer and M. El Kot, "Suspension model for blood flow through catheterized curved artery with time-variant overlapping stenosis," *Engineering Science and Technology, an International Journal*, vol. 18, no. 3, pp. 452–462, 2015.

[10] N. Saleem, S. Munawar, and D. Tripathi, "Thermal analysis of double diffusive electrokinetic thermally radiated tio2-ag/blood stream triggered by synthetic cilia under buoyancy forces and activation energy," *Physica Scripta*, vol. 96, no. 9, p. 095 218, 2021.

[11] R Ponalagusamy and S Priyadharshini, "Numerical investigation on two-fluid model (micropolar-newtonian) for pulsatile flow of blood in a tapered arterial stenosis with radially variable magnetic field and core fluid viscosity," *Computational and Applied Mathematics*, vol. 37, no. 1, pp. 719–743, 2018.

[12] C. Kumawat, B. Sharma, and K. Mekheimer, "Mathematical analysis of two-phase blood flow through a stenosed curved artery with hematocrit and temperature dependent viscosity," *Physica Scripta*, vol. 96, no. 12, p. 125 277, 2021.

[13] I. Shahzadi, S. Suleman, S. Saleem, and S. Nadeem, "Utilization of cu-nanoparticles as medication agent to reduce atherosclerotic lesions of a bifurcated artery having compliant walls," *Computer methods and programs in biomedicine*, vol. 184, p. 105 123, 2020.

[14] P. Jalili, A. Sadeghi Ghahare, B. Jalili, and D. Domiri Ganji, "Analytical and numerical investigation of thermal distribution for hybrid nanofluid through an oblique artery with mild stenosis," *SN Applied Sciences*, vol. 5, no. 4, p. 95, 2023.

[15] N. Saleem and S. Munawar, "Significance of synthetic cilia and arrhenius energy on double diffusive stream of radiated hybrid nanofluid in microfluidic pump under ohmic heating: An entropic analysis," *Coatings*, vol. 11, no. 11, p. 1292, 2021.

[16] B. Sharma, U. Khanduri, N. K. Mishra, and K. S. Mekheimer, "Combined effect of thermophoresis and brownian motion on mhd mixed convective flow over an inclined stretching surface with radiation and chemical reaction," *International Journal of Modern Physics B*, vol. 37, no. 10, p. 2 350 095, 2023.

[17] B. Tripathi and B. K. Sharma, "Two-phase analysis of blood flow through a stenosed artery with the effects of chemical reaction and radiation," *Ricerche di Matematica*, pp. 1–27, 2021.

[18] J. Tripathi, B Vasu, O. A. Bég, B. R. Mounika, and R. S. R. Gorla, "Numerical simulation of the transport of nanoparticles as drug carriers in hydromagnetic blood flow through a diseased artery with vessel wall permeability and rheological effects," *Microvascular research*, vol. 139, p. 104 241, 2022.

[19] M. J. Sarnak and A. S. Levey, "Cardiovascular disease and chronic renal disease: A new paradigm," *American journal of kidney diseases*, vol. 35, no. 4, S117–S131, 2000.

[20] P. Walsh and C. McLachlan, "Stenosis and thrombosis," *Wiley Encyclopedia of Biomedical Engineering*, 2006.

[21] J. Strony, A. Beaudoin, D. Brands, and B. Adelman, "Analysis of shear stress and hemodynamic factors in a model of coronary artery stenosis and thrombosis," *American Journal of Physiology-Heart and Circulatory Physiology*, vol. 265, no. 5, H1787–H1796, 1993.

[22] A. Tanveer, T. Hayat, and A. Alsaedi, "Peristaltic flow of MHD jeffery nanofluid in curved channel with convective boundary conditions: A numerical study," *Neural Computing and Applications*, vol. 30, no. 2, pp. 437–446, 2018.

[23] A. Ahmed and S. Nadeem, "Shape effect of Cu-nanoparticles in unsteady flow through curved artery with catheterized stenosis," *Results in physics*, vol. 7, pp. 677–689, 2017.

[24] I. Shahzadi and N Kousar, "Hybrid mediated blood flow investigation for atherosclerotic bifurcated lesions with slip, convective and compliant wall impacts," *Computer Methods and Programs in Biomedicine*, vol. 179, p. 104 980, 2019.

[25] S. Changdar and S. De, "Analytical investigation of nanoparticle as a drug carrier suspended in a MHD blood flowing through an irregular shape stenosed artery," *Iranian Journal of Science and Technology, Transactions A: Science*, vol. 43, no. 3, pp. 1259–1272, 2019.

[26] W. Alghamdi, A. Alsubie, P. Kumam, A. Saeed, and T. Gul, "MHD hybrid nanofluid flow comprising the medication through a blood artery," *Scientific Reports*, vol. 11, no. 1, pp. 1–13, 2021.

[27] B. Sharma, C. Kumawat, and O. Makinde, "Hemodynamical analysis of MHD two phase blood flow through a curved permeable artery having variable viscosity with heat and mass transfer," *Biomechanics and Modeling in Mechanobiology*, pp. 1–29, 2022.

[28] C. Kumawat, B. Sharma, Q. M. Al-Mdallal, and M. Rahimi-Gorji, "Entropy generation for MHD two phase blood flow through a curved permeable artery having variable viscosity with heat and mass transfer," *International Communications in Heat and Mass Transfer*, vol. 133, p. 105 954, 2022.

[29] K. S. Mekheimer, I. Shahzadi, S Nadeem, A. Moawad, and A. Zaher, "Reactivity of bifurcation angle and electroosmosis flow for hemodynamic flow through aortic bifurcation and stenotic wall with heat transfer," *Physica Scripta*, vol. 96, no. 1, p. 015 216, 2020.

[30] S. I. Abdelsalam, K. S. Mekheimer, and A. Zaher, "Alterations in blood stream by electroosmotic forces of hybrid nanofluid through diseased artery: Aneurysmal/stenosed segment," *Chinese Journal of Physics*, vol. 67, pp. 314–329, 2020.

[31] S. Akhtar, L. B. McCash, S. Nadeem, S. Saleem, and A. Issakhov, "Mechanics of non-newtonian blood flow in an artery having multiple stenosis and electroosmotic effects," *Science Progress*, vol. 104, no. 3, p. 00 368 504 211 031 693, 2021.

[32] J. Akram, N. S. Akbar, and D. Tripathi, "Analysis of electroosmotic flow of silver-water nanofluid regulated by peristalsis using two different approaches for nanofluid," *Journal of Computational Science*, vol. 62, p. 101 696, 2022.

[33] U. Khanduri, B. K. Sharma, M. Sharma, N. K. Mishra, and N. Saleem, "Sensitivity analysis of electroosmotic magnetohydrodynamics fluid flow through the curved stenosis artery with thrombosis by response surface optimization," *Alexandria Engineering Journal*, vol. 75, pp. 1–27, 2023.

[34] R. Manchi and R Ponalagusamy, "Pulsatile flow of emhd micropolar hybrid nanofluid in a porous bifurcated artery with an overlapping stenosis in the presence of body acceleration and joule heating," *Brazilian Journal of Physics*, vol. 52, no. 2, pp. 1–25, 2022.

[35] A. Zaher, K. K. Ali, and K. S. Mekheimer, "Electroosmosis forces eof driven boundary layer flow for a non-newtonian fluid with planktonic microorganism: Darcy forchheimer model," *International Journal of Numerical Methods for Heat & Fluid Flow*, vol. 31, no. 8, pp. 2534–2559, 2021.

[36] S. Lee and S. U. Choi, "Application of metallic nanoparticle suspensions in advanced cooling systems," Argonne National Lab.(ANL), Argonne, IL (United States), Tech. Rep., 1996.

[37] N. S. Akbar and A. W. Butt, "Magnetic field effects for copper suspended nanofluid venture through a composite stenosed arteries with permeable wall," *Journal of Magnetism and magnetic materials*, vol. 381, pp. 285–291, 2015.

[38] M. H. Shahzad, A. U. Awan, S. Akhtar, and S. Nadeem, "Entropy and stability analysis on blood flow with nanoparticles through a stenosed artery having permeable walls," *Science Progress*, vol. 105, no. 2, p. 00 368 504 221 096 000, 2022.

[39] R. Gandhi, B. Sharma, C. Kumawat, and O. A. Bég, "Modeling and analysis of magnetic hybrid nanoparticle Au-Al_2 O 3/blood based drug delivery through a bell-shaped occluded artery with Joule heating, viscous dissipation and variable viscosity effects," *Proceedings of the Institution of Mechanical Engineers, Part E: Journal of Process Mechanical Engineering*, p. 09 544 089 221 080 273, 2022.

[40] B. Sharma, R. Gandhi, and M. M. Bhatti, "Entropy analysis of thermally radiating MHD slip flow of hybrid nanoparticles Au-Al2O3/blood) through a tapered multi-stenosed artery," *Chemical Physics Letters*, p. 139 348, 2022.

[41] A. Bejan, "A study of entropy generation in fundamental convective heat transfer," 1979.

[42] I. Aoki, "Entropy flow and entropy production in the human body in basal conditions," *Journal of theoretical biology*, vol. 141, no. 1, pp. 11–21, 1989.

[43] N. S. Akbar and A. W. Butt, "Entropy generation analysis in convective ferromagnetic nano blood flow through a composite stenosed arteries with permeable wall," *Communications in Theoretical Physics*, vol. 67, no. 5, p. 554, 2017.

[44] R. Gandhi, B. K. Sharma, and O. D. Makinde, "Entropy analysis for mhd blood flow of hybrid nanoparticles (au–al2o3/blood) of different shapes through an irregular stenosed permeable walled artery under periodic body acceleration: Hemodynamical applications," *ZAMM-Journal of Applied Mathematics and Mechanics/Zeitschrift für Angewandte Mathematik und Mechanik*, e202100532, 2022.

[45] R. H. Haynes, "Physical basis of the dependence of blood viscosity on tube radius," *American Journal of Physiology-Legacy Content*, vol. 198, no. 6, pp. 1193–1200, 1960.

[46] R. Chebbi, "Dynamics of blood flow: Modeling of the fåhræus–lindqvist effect," *Journal of biological physics*, vol. 41, pp. 313–326, 2015.

[47] R. E. Wells, E. W. Merrill, *et al.*, "Influence of flow properties of blood upon viscosity-hematocrit relationships," *The Journal of clinical investigation*, vol. 41, no. 8, pp. 1591–1598, 1962.

[48] S. Sharma, U. Singh, and V. Katiyar, "Magnetic field effect on flow parameters of blood along with magnetic particles in a cylindrical tube," *Journal of Magnetism and Magnetic materials*, vol. 377, pp. 395–401, 2015.

[49] J Doffin and F Chagneau, "Oscillating flow between a clot model and a stenosis," *Journal of biomechanics*, vol. 14, no. 3, pp. 143–148, 1981.

[50] J. Vanherweghem, "Thrombosis and stenosis of central venous access in hemodialysis," *Nephrologie*, vol. 15, no. 2, pp. 117–121, 1994.

[51] T. Elnaqeeb, K. S. Mekheimer, and F. Alghamdi, "Cu-blood flow model through a catheterized mild stenotic artery with a thrombosis," *Mathematical Biosciences*, vol. 282, pp. 135–146, 2016.

[52] A. Ahmed and S. Nadeem, "Biomathematical study of time-dependent flow of a Carreau nanofluid through inclined catheterized arteries with overlapping stenosis," *Journal of Central South University*, vol. 24, no. 11, pp. 2725–2744, 2017.

[53] M. M. Bhatti, A. Zeeshan, and R. Ellahi, "Heat transfer analysis on peristaltically induced motion of particle-fluid suspension with variable viscosity: Clot blood model," *Computer Methods and Programs in Biomedicine*, vol. 137, pp. 115–124, 2016.

[54] A. Saleem, S. Akhtar, S. Nadeem, A. Issakhov, and M. Ghalambaz, "Blood flow through a catheterized artery having a mild stenosis at the wall with a blood clot at the centre," *Computer Modeling in Engineering & Sciences*, vol. 125, no. 2, pp. 565–577, 2020.

[55] S. Akhtar, L. McCash, S. Nadeem, and A. Saleem, "Scientific breakdown for physiological blood flow inside a tube with multi-thrombosis," *Scientific reports*, vol. 11, no. 1, pp. 1–14, 2021.

[56] A. Saleem, S. Akhtar, S. Nadeem, and M. Ghalambaz, "Microphysical analysis for peristaltic flow of swcnt and mwcnt carbon nanotubes inside a catheterised artery having thrombus: Irreversibility effects with entropy," *Int J Exergy*, vol. 34, pp. 301–314, 2021.

[57] A. Zidan, L. McCash, S. Akhtar, A. Saleem, A. Issakhov, and S. Nadeem, "Entropy generation for the blood flow in an artery with multiple stenosis having a catheter," *Alexandria Engineering Journal*, vol. 60, no. 6, pp. 5741–5748, 2021.

[58] A. Saleem, S. Akhtar, and S. Nadeem, "Bio-mathematical analysis of electro-osmotically modulated hemodynamic blood flow inside a symmetric and nonsymmetric stenosed artery with joule heating," *International Journal of Biomathematics*, vol. 15, no. 02, p. 2 150 071, 2022.

[59] I. Shahzadi and S Nadeem, "Stimulation of metallic nanoparticles under the impact of radial magnetic field through eccentric cylinders: A useful application in biomedicine," *Journal of Molecular Liquids*, vol. 225, pp. 365–381, 2017.

[60] I. Shahzadi and S Nadeem, "A comparative study of cu nanoparticles under slip effects through oblique eccentric tubes, a biomedical solicitation examination," *Canadian Journal of Physics*, vol. 97, no. 1, pp. 63–81, 2019.

[61] I. Shahzadi and S Nadeem, "Analysis of ag/blood-mediated transport in curved annulus with exclusive nature of convective boundary," *Physica Scripta*, vol. 94, no. 11, p. 115 011, 2019.

[62] K. G. Kumar, M. G. Reddy, A. Aldalbahi, M. Rahimi-Gorji, M. Rahaman, *et al.*, "Application of different hybrid nanofluids in convective heat transport of carreau fluid," *Chaos, Solitons & Fractals*, vol. 141, p. 110 350, 2020.

[63] M. Imran, A Shaheen, E.-S. M. Sherif, M. Rahimi-Gorji, and A. H. Seikh, "Analysis of peristaltic flow of jeffrey six constant nano fluid in a vertical non-uniform tube," *Chinese Journal of Physics*, vol. 66, pp. 60–73, 2020.

[64] D. F. Jamil *et al.*, "Analysis of non-newtonian magnetic casson blood flow in an inclined stenosed artery using caputo-fabrizio fractional derivatives," *Computer Methods and Programs in Biomedicine*, vol. 203, p. 106 044, 2021.

[65] M. Hassan, E. R. El-Zahar, S. U. Khan, M. Rahimi-Gorji, and A. Ahmad, "Boundary layer flow pattern of heat and mass for homogenous shear thinning hybrid-nanofluid: An experimental data base modeling," *Numerical Methods for Partial Differential Equations*, vol. 37, no. 2, pp. 1234–1249, 2021.

[66] T. Elnaqeeb, N. A. Shah, and K. S. Mekheimer, "Hemodynamic characteristics of gold nanoparticle blood flow through a tapered stenosed vessel with variable nanofluid viscosity," *BioNanoScience*, vol. 9, no. 2, pp. 245–255, 2019.

[67] L. Sarwar and A. Hussain, "Flow characteristics of Au-blood nanofluid in stenotic artery," *International Communications in Heat and Mass Transfer*, vol. 127, p. 105 486, 2021.

[68] M. M. Bhatti and S. I. Abdelsalam, "Bio-inspired peristaltic propulsion of hybrid nanofluid flow with tantalum (ta) and gold (au) nanoparticles under magnetic effects," *Waves in Random and Complex Media*, pp. 1–26, 2021.

[69] M. Khazayinejad, M. Hafezi, and B. Dabir, "Peristaltic transport of biological graphene-blood nanofluid considering inclined magnetic field and thermal radiation in a porous media," *Powder Technology*, vol. 384, pp. 452–465, 2021.

[70] I. Ocsoy *et al.*, "DNA-guided metal-nanoparticle formation on graphene oxide surface," *Advanced Materials*, vol. 25, no. 16, pp. 2319–2325, 2013.

[71] J.-W. Kim, M. Kim, K. K. Lee, K. H. Chung, and C.-S. Lee, "Effects of graphene oxide-gold nanoparticles nanocomposite on highly sensitive foot-and-mouth disease virus detection," *Nanomaterials*, vol. 10, no. 10, p. 1921, 2020.

[72] S. Kang *et al.*, "Gold nanoparticle/graphene oxide hybrid sheets attached on mesenchymal stem cells for effective photothermal cancer therapy," *Chemistry of Materials*, vol. 29, no. 8, pp. 3461–3476, 2017.

[73] K. S. Mekheimer and M. El Kot, "Influence of magnetic field and Hall currents on blood flow through a stenotic artery," *Applied Mathematics and Mechanics*, vol. 29, no. 8, pp. 1093–1104, 2008.

[74] N. N. Anika, M. M. Hoque, S. I. Hossain, and M. M. Alam, "Thermal diffusion effect on unsteady viscous MHD micropolar fluid flow through an infinite vertical plate with Hall and ion-slip current," *Procedia Engineering*, vol. 105, pp. 160–166, 2015.

[75] J. Misra and S. Ghosh, "Flow of a Casson fluid in a narrow tube with a side branch," *International journal of engineering science*, vol. 38, no. 18, pp. 2045–2077, 2000.

[76] M. Ramzan, H. Gul, J. D. Chung, S. Kadry, and Y.-M. Chu, "Significance of Hall effect and ion slip in a three-dimensional bioconvective tangent hyperbolic nanofluid flow subject to Arrhenius activation energy," *Scientific Reports*, vol. 10, no. 1, pp. 1–15, 2020.

[77] S Das, B Barman, R. Jana, and O. Makinde, "Hall and ion slip currents' impact on electromagnetic blood flow conveying hybrid nanoparticles through an endoscope with peristaltic waves," *BioNanoScience*, vol. 11, no. 3, pp. 770–792, 2021.

[78] G. K. Snyder, "Influence of temperature and hematocrit on blood viscosity," *American Journal of Physiology-Legacy Content*, vol. 220, no. 6, pp. 1667–1672, 1971.

[79] G. Shit, M Roy, and A Sinha, "Mathematical modelling of blood flow through a tapered overlapping stenosed artery with variable viscosity," *Applied Bionics and Biomechanics*, vol. 11, no. 4, pp. 185–195, 2014.

[80] B Tripathi and B. Sharma, "Effect of variable viscosity on MHD inclined arterial blood flow with chemical reaction," *International Journal of Applied Mechanics and Engineering*, vol. 23, no. 3, 2018.

[81] J. Akram, N. S. Akbar, and D. Tripathi, "Thermal analysis on MHD flow of ethylene glycol-based bnnts nanofluids via peristaltically induced electroosmotic pumping in a curved microchannel," *Arabian Journal for Science and Engineering*, pp. 1–17, 2021.

[82] Poonam, B. Sharma, C. Kumawat, and K. Vafai, "Computational biomedical simulations of hybrid nanoparticles (au-al2o3/blood-mediated) transport in a stenosed and aneurysmal curved artery with heat and mass transfer: Hematocrit dependent viscosity approach," *Chemical Physics Letters*, p. 139 666, 2022.

[83] M. K. Sharma, K. Bansal, and S. Bansal, "Pulsatile unsteady flow of blood through porous medium in a stenotic artery under the influence of transverse magnetic field," *Korea-Australia Rheology Journal*, vol. 24, no. 3, pp. 181–189, 2012.

[84] A. Tiwari and S. S. Chauhan, "Effect of varying viscosity on two-layer model of pulsatile flow through blood vessels with porous region near walls," *Transport in Porous Media*, vol. 129, no. 3, pp. 721–741, 2019.

[85] F. Ishtiaq, R. Ellahi, M. M. Bhatti, and S. Z. Alamri, "Insight in thermally radiative cilia-driven flow of electrically conducting non-newtonian jeffrey fluid under the influence of induced magnetic field," *Mathematics*, vol. 10, no. 12, p. 2007, 2022.

[86] N. Ahmed, U. Khan, S. T. Mohyud-Din, *et al.*, "Influence of shape factor on flow of magneto-nanofluid squeezed between parallel disks," *Alexandria engineering journal*, vol. 57, no. 3, pp. 1893–1903, 2018.

[87] S Ijaz and S Nadeem, "Shape factor and sphericity features examination of Cu and Cu-Al2O3/blood through atherosclerotic artery under the impact of wall characteristic," *Journal of Molecular Liquids*, vol. 271, pp. 361–372, 2018.

[88] D. Young, "Effect of a time-dependent stenosis on flow through a tube," 1968.

[89] N. Mustapha, N. Amin, S. Chakravarty, and P. K. Mandal, "Unsteady magneto-hydrodynamic blood flow through irregular multi-stenosed arteries," *Computers in Biology and Medicine*, vol. 39, no. 10, pp. 896–906, 2009.

[90] R Ghandi, B. Sharma, C Kumawat, O. Beg, *et al.*, "Modeling and analysis of magnetic hybrid nanoparticle (au-al2o3/blood) based drug delivery through a bell-shaped occluded artery with joule heating, viscous dissipation and variable viscosity effects," *Proceedings of the Institution of Mechanical Engineers, Part E: Journal of Process Mechanical Engineering*, 2022.

[91] A Kolin, "An electromagnetic flowmeter. principle of the method and its application to bloodflow measurements," *Proceedings of the Society for Experimental Biology and Medicine*, vol. 35, no. 1, pp. 53–56, 1936.

[92] J. R. Melcher and H. H. Woodson, "Electromechanical dynamics," *Part I: Discrete Systems; John Wiley & Sons, Inc.: Hoboken, NJ, USA*, 1968.

[93] C. L. Rice and R. Whitehead, "Electrokinetic flow in a narrow cylindrical capillary," *The Journal of Physical Chemistry*, vol. 69, no. 11, pp. 4017–4024, 1965.

[94] S Noreen, S Waheed, and A Hussanan, "Peristaltic motion of mhd nanofluid in an asymmetric micro-channel with joule heating, wall flexibility and different zeta potential," *Boundary Value Problems*, vol. 2019, no. 1, pp. 1–23, 2019.

[95] I. Shahzadi, F. Z. Duraihem, S Ijaz, C. Raju, and S Saleem, "Blood stream alternations by mean of electroosmotic forces of fractional ternary nanofluid through the oblique stenosed aneurysmal artery with slip conditions," *International Communications in Heat and Mass Transfer*, vol. 143, p. 106 679, 2023.

[96] A Zaman, A. A. Khan, and N. Kousar, "Simulation of magneto-hydrodynamics effects on cross fluid (blood) model with entropy generations in multiple stenosed (aneurysm) curved channel," *Chinese Journal of Physics*, 2022.

[97] B. K. Sharma, Poonam, and A. J. Chamkha, "Effects of heat transfer, body acceleration and hybrid nanoparticles (au–al2o3) on mhd blood flow through a curved artery with stenosis and aneurysm using hematocrit-dependent viscosity," *Waves in Random and Complex Media*, pp. 1–31, 2022.

[98] M. M.-S. Lih *et al.*, *Transport phenomena in medicine and biology*. Wiley, 1975.

[99] O. K. Baskurt and H. J. Meiselman, "Blood rheology and hemodynamics," in *Seminars in thrombosis and hemostasis*, Copyright© 2003 by Thieme Medical Publishers, Inc., 333 Seventh Avenue, New . . ., vol. 29, 2003, pp. 435–450.

[100] J. Tripathi, B Vasu, and O. A. Bég, "Computational simulations of hybrid mediated nano-hemodynamics (ag-au/blood) through an irregular symmetric stenosis," *Computers in Biology and Medicine*, vol. 130, p. 104 213, 2021.

[101] J. Akram, N. S. Akbar, and D. Tripathi, "Thermal analysis on mhd flow of ethylene glycol-based bnnts nanofluids via peristaltically induced electroosmotic pumping in a curved microchannel," *Arabian Journal for Science and Engineering*, pp. 1–17, 2022.

[102] M. Corcione, "Empirical correlating equations for predicting the effective thermal conductivity and dynamic viscosity of nanofluids," *Energy conversion and management*, vol. 52, no. 1, pp. 789–793, 2011.

[103] A. Zaman, N. Ali, and M. Sajjad, "Effects of nanoparticles (cu, tio2, al2o3) on unsteady blood flow through a curved overlapping stenosed channel," *Mathematics and Computers in Simulation*, vol. 156, pp. 279–293, 2019.

[104] R Ponalagusamy and S Priyadharshini, "Pulsatile mhd flow of a casson fluid through a porous bifurcated arterial stenosis under periodic body acceleration," *Applied Mathematics and Computation*, vol. 333, pp. 325–343, 2018.

[105] B. K. Sharma and C. Kumawat, "Impact of temperature dependent viscosity and thermal conductivity on mhd blood flow through a stretching surface with ohmic effect and chemical reaction," *Nonlinear Engineering*, vol. 10, no. 1, pp. 255–271, 2021.

[106] B. Sharma, U. Khanduri, N. K. Mishra, and K. S. Mekheimer, "Combined effect of thermophoresis and brownian motion on mhd mixed convective flow over an inclined stretching surface with radiation and chemical reaction," *International Journal of Modern Physics B*, p. 2 350 095, 2022.

[107] U. Khanduri and B. K. Sharma, "Hall and ion slip effects on hybrid nanoparticles (au-go/blood) flow through a catheterized stenosed artery with thrombosis," *Proceedings of the Institution of Mechanical Engineers, Part C: Journal of Mechanical Engineering Science*, vol. 237, no. 10, pp. 2256–2278, 2023.

[108] U. Khanduri and B. K. Sharma, "Entropy analysis for mhd flow subject to temperature-dependent viscosity and thermal conductivity," in *Nonlinear Dynamics and Applications*, Springer, 2022, pp. 457–471.

[109] B. K. Sharma, C. Kumawat, U. Khanduri, and K. S. Mekheimer, "Numerical investigation of the entropy generation analysis for radiative mhd power-law fluid flow of blood through a curved artery with hall effect," *Waves in Random and Complex Media*, pp. 1–38, 2023.

[110] N. S. Akbar, S Nadeem, T Hayat, and A. A. Hendi, "Effects of heat and chemical reaction on jeffrey fluid model with stenosis," *Applicable Analysis*, vol. 91, no. 9, pp. 1631–1647, 2012.

[111] G. Shit and M Roy, "Effect of induced magnetic field on blood flow through a constricted channel: An analytical approach," *Journal of Mechanics in Medicine and Biology*, vol. 16, no. 03, p. 1 650 030, 2016.

[112] U. Khanduri and B. Sharma, "Mathematical analysis of hall effect and hematocrit dependent viscosity on au/go-blood hybrid nanofluid flow through a stenosed catheterized artery with thrombosis," in *International workshop of Mathematical Modelling, Applied Analysis and Computation*, Springer, 2022, pp. 121–137.

[113] Y. B. Tan, N. Mustapha, and Sarifuddin, "Blood flow through a stenosed artery bifurcation under the effects of gravity," in *AIP Conference Proceedings*, American Institute of Physics, vol. 1635, 2014, pp. 241–248.

[114] D Srinivasacharya and G Madhava Rao, "Modeling of blood flow through a bifurcated artery using nanofluid," *BioNanoScience*, vol. 7, pp. 464–474, 2017.

[115] D Srinivasacharya and G. M. Rao, "Pulsatile flow of couple stress fluid through a bifurcated artery," *Ain Shams Engineering Journal*, vol. 9, no. 4, pp. 883–893, 2018.

[116] H. Shahzad *et al.*, "Fluid structure interaction study of non-newtonian casson fluid in a bifurcated channel having stenosis with elastic walls," *Scientific Reports*, vol. 12, no. 1, p. 12 219, 2022.

[117] T. M. Joshua, K Anwar, and N Abdullah, "Numerical study of magnetohydrodynamic blood flow through an artery with multiple stenosis," in *IOP Conference Series: Materials Science and Engineering*, IOP Publishing, vol. 864, 2020, p. 012 199.

[118] D. Kumar, B Satyanarayana, R. Kumar, S. Kumar, and N. Deo, "Application of heat source and chemical reaction in mhd blood flow through permeable bifurcated arteries with inclined magnetic field in tumor treatments," *Results in Applied Mathematics*, vol. 10, p. 100 151, 2021.

[119] R. Manchi and R Ponalagusamy, "Modeling of pulsatile emhd flow of au-blood in an inclined porous tapered atherosclerotic vessel under periodic body acceleration," *Archive of Applied Mechanics*, vol. 91, no. 7, pp. 3421–3447, 2021.

[120] N. K. Mishra, M. Sharma, B. Sharma, and U. Khanduri, "Soret and dufour effects on mhd nanofluid flow of blood through a stenosed artery with variable viscosity," *International Journal of Modern Physics B*, p. 2 350 266, 2023.

[121] M. Sharma, B. K. Sharma, U. Khanduri, N. K. Mishra, S. Noeiaghdam, and U. Fernandez-Gamiz, "Optimization of heat transfer nanofluid blood flow through a stenosed artery in the presence of hall effect and hematocrit dependent viscosity," *Case Studies in Thermal Engineering*, p. 103 075, 2023.

[122] R Ellahi, S. U. Rahman, S. Nadeem, and N. S. Akbar, "Blood flow of nanofluid through an artery with composite stenosis and permeable walls," *Applied Nanoscience*, pp. 919–926, 2014.

[123] H. T. Basha, K. Rajagopal, N. A. Ahammad, S Sathish, and S. R. Gunakala, "Finite difference computation of au-cu/magneto-bio-hybrid nanofluid flow in an inclined uneven stenosis artery," *Complexity*, vol. 2022, pp. 1–18, 2022.

[124] R. Gandhi and B. Sharma, "Modelling pulsatile blood flow using casson fluid model through an overlapping stenotic artery with au-cu hybrid nanoparticles: Varying viscosity approach," in *International workshop of Mathematical Modelling, Applied Analysis and Computation*, Springer, 2022, pp. 155–176.

[125] M. Bhatti, A Zeeshan, and R Ellahi, "Simultaneous effects of coagulation and variable magnetic field on peristaltically induced motion of jeffrey nanofluid containing gyrotactic microorganism," *Microvascular research*, vol. 110, pp. 32–42, 2017.

[126] F. Alharbi, M. Naeem, M. Zubair, M. Jawad, W. U. Jan, and R. Jan, "Bioconvection due to gyrotactic microorganisms in couple stress hybrid nanofluid laminar mixed convection incompressible flow with magnetic nanoparticles and chemical reaction as carrier for targeted drug delivery through porous stretching sheet," *Molecules*, vol. 26, no. 13, p. 3954, 2021.

[127] K. S. Mekheimer, R. Abo-Elkhair, S. I. Abdelsalam, K. K. Ali, and A. Moawad, "Biomedical simulations of nanoparticles drug delivery to blood hemodynamics in diseased organs: Synovitis problem," *International Communications in Heat and Mass Transfer*, vol. 130, p. 105 756, 2022.

[128] D. R. Mostapha and N. T. El-Dabe, "Peristaltic transfer of nanofluid with motile gyrotactic microorganisms with nonlinear thermic radiation," *Scientific Reports*, vol. 13, no. 1, p. 7054, 2023.

[129] R. Ellahi, M. Raza, and K. Vafai, "Series solutions of non-newtonian nanofluids with reynolds' model and vogel's model by means of the homotopy analysis method," *Mathematical and Computer Modelling*, vol. 55, no. 7-8, pp. 1876–1891, 2012.

[130] B Vasu, A. Dubey, O. A. Bég, and R. S. R. Gorla, "Micropolar pulsatile blood flow conveying nanoparticles in a stenotic tapered artery: Non-newtonian pharmacodynamic simulation," *Computers in Biology and Medicine*, vol. 126, p. 104 025, 2020.

[131] B. Zhang, J. Gu, M. Qian, L. Niu, H. Zhou, and D. Ghista, "Correlation between quantitative analysis of wall shear stress and intima-media thickness in atherosclerosis development in carotid arteries," *BioMedical Engineering OnLine*, vol. 16, no. 1, pp. 1–17, 2017.

[132] H. A. Hogan and M. Henriksen, "An evaluation of a micropolar model for blood flow through an idealized stenosis," *Journal of biomechanics*, vol. 22, no. 3, pp. 211–218, 1989.

[133] I. Marshall, S. Zhao, P. Papathanasopoulou, P. Hoskins, and X. Y. Xu, "Mri and cfd studies of pulsatile flow in healthy and stenosed carotid bifurcation models," *Journal of biomechanics*, vol. 37, no. 5, pp. 679–687, 2004.

[134] A. Raptis, M. Xenos, E. Tzirtzilakis, and M. Matsagkas, "Finite element analysis of magnetohydrodynamic effects on blood flow in an aneurysmal geometry," *Physics of Fluids*, vol. 26, no. 10, 2014.

[135] O. U. Mehmood, S. Bibi, A. Zeeshan, M. M. Maskeen, and F. Alzahrani, "Electroosmotic impacts on hybrid antimicrobial blood stream through catheterized stenotic aneurysmal artery," *The European Physical Journal Plus*, vol. 137, no. 5, p. 585, 2022.

[136] I. Cherkaoui, S. Bettaibi, A. Barkaoui, and F. Kuznik, "Magnetohydrodynamic blood flow study in stenotic coronary artery using lattice boltzmann method," *Computer Methods and Programs in Biomedicine*, vol. 221, p. 106 850, 2022.

[137] S. Majee and G. Shit, "Numerical investigation of mhd flow of blood and heat transfer in a stenosed arterial segment," *Journal of Magnetism and Magnetic Materials*, vol. 424, pp. 137–147, 2017.

[138] Z Abbas, M. Shabbir, and N Ali, "Numerical study of magnetohydrodynamic pulsatile flow of sutterby fluid through an inclined overlapping arterial stenosis in the presence of periodic body acceleration," *Results in Physics*, vol. 9, pp. 753–762, 2018.

[139] R. Gandhi, B. K. Sharma, N. K. Mishra, and Q. M. Al-Mdallal, "Computer simulations of emhd casson nanofluid flow of blood through an irregular stenotic permeable artery: Application of koo-kleinstreuer-li correlations," *Nanomaterials*, vol. 13, no. 4, p. 652, 2023.

[140] A. Dubey, B Vasu, O. A. Bég, and R. Gorla, "Finite element computation of magnetohemodynamic flow and heat transfer in a bifurcated artery with saccular aneurysm using the carreau-yasuda biorheological model," *Microvascular Research*, vol. 138, p. 104 221, 2021.

[141] S. C. Hossain, M. Ferdows, M. Z. I. Bangalee, and M. S. Alam, "Two-phase bionanofluid flow through a bifurcated artery with magnetic field interaction," *International Journal of Thermofluids*, vol. 15, p. 100 194, 2022.

[142] N. M. Zain and Z. Ismail, "Numerical solution of magnetohydrodynamics effects on a generalised power law fluid model of blood flow through a bifurcated artery with an overlapping shaped stenosis," *Plos one*, vol. 18, no. 2, e0276576, 2023.

[143] R Ellahi, S. Rahman, S Nadeem, and N. S. Akbar, "Blood flow of nanofluid through an artery with composite stenosis and permeable walls," *Applied Nanoscience*, vol. 4, pp. 919–926, 2014.

[144] A. Sharifi, S. Y. Motlagh, and H. Badfar, "Numerical investigation of magnetic drug targeting using magnetic nanoparticles to the aneurysmal vessel," *Journal of Magnetism and Magnetic Materials*, vol. 474, pp. 236–245, 2019.

[145] G. BJ and P. BC, "Scrutinization of different shaped nanoparticle of molybdenum disulfide suspended nanofluid flow over a radial porous fin," *International Journal of Numerical Methods for Heat & Fluid Flow*, vol. 30, no. 7, pp. 3685–3699, 2020.

[146] E. Y. Gürbüz, H. İ. Variyenli, A. Sözen, A. Khanlari, and M. Ökten, "Experimental and numerical analysis on using cuo-al2o3/water hybrid nanofluid in a u-type tubular heat exchanger," *International Journal of Numerical Methods for Heat & Fluid Flow*, vol. 31, no. 1, pp. 519–540, 2021.

[147] Z. Mahmood, Z. Iqbal, M. A. Alyami, B. Alqahtani, M. F. Yassen, and U. Khan, "Influence of suction and heat source on mhd stagnation point flow of ternary hybrid nanofluid over convectively heated stretching/shrinking cylinder," *Advances in Mechanical Engineering*, vol. 14, no. 9, p. 16 878 132 221 126 278, 2022.

[148] A. S. Alnahdi, S. Nasir, and T. Gul, "Blood-based ternary hybrid nanofluid flow-through perforated capillary for the applications of drug delivery," *Waves in Random and Complex Media*, pp. 1–19, 2022.

[149] S. Dolui, B. Bhaumik, and S. De, "Combined effect of induced magnetic field and thermal radiation on ternary hybrid nanofluid flow through an inclined catheterized artery with multiple stenosis," *Chemical Physics Letters*, vol. 811, p. 140 209, 2023.

[150] R. S. Ransing, "Thermal irreversibility demystified," *International Journal of Numerical Methods for Heat & Fluid Flow*, vol. 33, no. 2, pp. 682–711, 2023.

[151] N. S. Akbar, M Raza, and R Ellahi, "Peristaltic flow with thermal conductivity of h2o+ cu nanofluid and entropy generation," *Results in Physics*, vol. 5, pp. 115–124, 2015.

[152] T. Tayebi and A. J. Chamkha, "Entropy generation analysis during mhd natural convection flow of hybrid nanofluid in a square cavity containing a corrugated conducting block," *International Journal of Numerical Methods for Heat & Fluid Flow*, vol. 30, no. 3, pp. 1115–1136, 2019.

[153] S. Marzougui, F. Mebarek-Oudina, M. Magherbi, and A. Mchirgui, "Entropy generation and heat transport of cu–water nanoliquid in porous lid-driven cavity through magnetic field," *International Journal of Numerical Methods for Heat & Fluid Flow*, vol. 32, no. 6, pp. 2047–2069, 2022.

[154] E. A. Algehyne *et al.*, "Entropy optimization and response surface methodology of blood hybrid nanofluid flow through composite stenosis artery with magnetized nanoparticles (au-ta) for drug delivery application," *Scientific Reports*, vol. 13, no. 1, p. 9856, 2023.

[155] D. Das, S. Shaw, K. K. Mondal, and R. R. Kairi, "Analyzing the impact of boundary slip and absorption effects on the dispersion of solute in a pulsatile channel flow of casson fluid under magnetic field," *The European Physical Journal Plus*, vol. 138, no. 5, p. 372, 2023.

[156] S. C. Reddy and L. N. Trefethen, "Stability of the method of lines," *Numerische Mathematik*, vol. 62, no. 1, pp. 235–267, 1992.

[157] U Nowak, J Frauhammer, and U Nieken, "A fully adaptive algorithm for parabolic partial differential equations in one space dimension," *Computers & chemical engineering*, vol. 20, no. 5, pp. 547–561, 1996.

[158] V. R. Subramanian and R. E. White, "Semianalytical method of lines for solving elliptic partial differential equations," *Chemical engineering science*, vol. 59, no. 4, pp. 781–788, 2004.

[159] G Ozen and N. Selçuk, "Sensitivity of radiation modeling to property estimation techniques in the freeboard of lignite-fired bubbling fluidized bed combustors (bfbcs)," *Combustion Science and Technology*, vol. 186, no. 4-5, pp. 684–697, 2014.

[160] G. Pantoleontos, I. M. Anagnostara, M. Syrigou, and A. G. Konstandopoulos, "Solutions of the mass continuity equation in hollow fibers for fully developed flow with some notes on the lévêque correlation," *Carbon Capture Science & Technology*, vol. 2, p. 100 027, 2022.

[161] J. Misra and S Chakravarty, "Flow in arteries in the presence of stenosis," *Journal of Biomechanics*, vol. 19, no. 11, pp. 907–918, 1986.

[162] S. Siddiqui, N. Verma, S. Mishra, and R. Gupta, "Mathematical modelling of pulsatile flow of casson's fluid in arterial stenosis," *Applied Mathematics and Computation*, vol. 210, no. 1, pp. 1–10, 2009.

[163] A Zaman, F Mabood, A. Khan, A Abbasi, M. Nadeem, and I. Badruddin, "Simulations of unsteady blood flow through curved stenosed channel with effects of entropy generations and magneto-hydrodynamics," *International Communications in Heat and Mass Transfer*, vol. 127, p. 105 569, 2021.

[164] R Ponalagusamy and S Priyadharshini, "Numerical modelling on pulsatile flow of casson nanofluid through an inclined artery with stenosis and tapering under the influence of magnetic field and periodic body acceleration," *Korea-Australia Rheology Journal*, vol. 29, pp. 303–316, 2017.

[165] S. Majee and G. Shit, "Modeling and simulation of blood flow with magnetic nanoparticles as carrier for targeted drug delivery in the stenosed artery," *European Journal of Mechanics-B/Fluids*, vol. 83, pp. 42–57, 2020.

[166] A. Zaman, N. Ali, and A. A. Khan, "Computational biomedical simulations of hybrid nanoparticles on unsteady blood hemodynamics in a stenotic artery," *Mathematics and Computers in Simulation*, vol. 169, pp. 117–132, 2020.

[167] M. Varmazyar, M. Habibi, M. Amini, A. H. Pordanjani, M. Afrand, and S. M. Vahedi, "Numerical simulation of magnetic nanoparticle-based drug delivery in presence of atherosclerotic plaques and under the effects of magnetic field," *Powder Technology*, vol. 366, pp. 164–174, 2020.

[168] J. Ramana Reddy, D Srikanth, and S. K. Das, "Modelling and simulation of temperature and concentration dispersion in a couple stress nanofluid flow through stenotic tapered arteries," *The European Physical Journal Plus*, vol. 132, pp. 1–22, 2017.

[169] S. Shaw and P. Murthy, "Magnetic targeting in the impermeable microvessel with two-phase fluid model—non-newtonian characteristics of blood," *Microvascular research*, vol. 80, no. 2, pp. 209–220, 2010.

[170] S Nadeem and S Ijaz, "Nanoparticles analysis on the blood flow through a tapered catheterized elastic artery with overlapping stenosis," *The European Physical Journal Plus*, vol. 129, pp. 1–14, 2014.

[171] K. M. Prasad and P. R. Yasa, "Flow of non-newtonian fluid through a permeable artery having non-uniform cross section with multiple stenosis," *Journal of Naval Architecture and Marine Engineering*, vol. 17, no. 1, pp. 31–38, 2020.

[172] M. Hussain, M. Shabbir, and Z. Abbas, "Effects of thermophoresis and brownian motion on the pulsating nano-fluid in a curved diseased arterial segment," *Physica Scripta*, 2023.

[173] M. Ibrahim, "Numerical simulation to the activation energy study on blood flow of seminal nanofluid with mixed convection effects," *Computer Methods in Biomechanics and Biomedical Engineering*, vol. 26, no. 3, pp. 315–325, 2023.

[174] A. S. M. Aljaloud, L. Manai, and I. Tlili, "Bioconvection flow of cross nanofluid due to cylinder with activation energy and second order slip features," *Case Studies in Thermal Engineering*, vol. 42, p. 102 767, 2023.

[175] B. Sharma, A. Kumar, R. Gandhi, and M. Bhatti, "Exponential space and thermal-dependent heat source effects on electro-magneto-hydrodynamic jeffrey fluid flow over a vertical stretching surface," *International Journal of Modern Physics B*, vol. 36, no. 30, p. 2 250 220, 2022.

[176] B. Tripathi, B. K. Sharma, and M. Sharma, "Mhd pulsatile two-phase blood flow through a stenosed artery with heat and mass transfer," *arXiv preprint arXiv:1705.09794*, 2017.

[177] K. J. Widder, A. E. Senyei, and D. G. Scarpelli, "Magnetic microspheres: A model system for site specific drug delivery in vivo," *Proceedings of the Society for Experimental Biology and Medicine*, vol. 158, no. 2, pp. 141–146, 1978.

[178] A. Senyei, K. Widder, and G. Czerlinski, "Magnetic guidance of drug-carrying microspheres," *Journal of Applied Physics*, vol. 49, no. 6, pp. 3578–3583, 1978.

[179] E. J. Furlani and E. P. Furlani, "A model for predicting magnetic targeting of multifunctional particles in the microvasculature," *Journal of Magnetism and Magnetic Materials*, vol. 312, no. 1, pp. 187–193, 2007.

[180] F. Ali, N. A. Sheikh, I. Khan, and M. Saqib, "Magnetic field effect on blood flow of casson fluid in axisymmetric cylindrical tube: A fractional model," *Journal of Magnetism and Magnetic Materials*, vol. 423, pp. 327–336, 2017.

[181] S. Maiti, S. Shaw, and G. Shit, "Fractional order model of thermo-solutal and magnetic nanoparticles transport for drug delivery applications," *Colloids and Surfaces B: Biointerfaces*, vol. 203, p. 111 754, 2021.

[182] J. H. Barbee and G. R. Cokelet, "The fahraeus effect," *Microvascular research*, vol. 3, no. 1, pp. 6–16, 1971.

[183] V. Srivastava and M Saxena, "A two-fluid model of non-newtonian blood flow induced by peristaltic waves," *Rheologica Acta*, vol. 34, pp. 406–414, 1995.

[184] R Ponalagusamy and R. T. Selvi, "A study on two-layered model (casson–newtonian) for blood flow through an arterial stenosis: Axially variable slip velocity at the wall," *Journal of the Franklin Institute*, vol. 348, no. 9, pp. 2308–2321, 2011.

[185] N. Ranjit, G. Shit, and D Tripathi, "Entropy generation and joule heating of two layered electroosmotic flow in the peristaltically induced micro-channel," *International Journal of Mechanical Sciences*, vol. 153, pp. 430–444, 2019.

[186] B. K. Sharma, U. Khanduri, N. K. Mishra, I. Albaijan, and L. M. Pérez, "Entropy generation optimization for the electroosmotic mhd fluid flow over the curved stenosis artery in the presence of thrombosis," *Scientific Reports*, vol. 13, no. 1, p. 15 441, 2023.

[187] M. F. Alrehili *et al.*, "Numerical computing of soret and linear radiative effects on mhd casson fluid flow toward a vertical surface through a porous medium: Finite element analysis," *Modern Physics Letters B*, vol. 36, no. 32n33, p. 2 250 170, 2022.

[188] T Hayat, M. Shafique, A Tanveer, and A Alsaedi, "Hall and ion slip effects on peristaltic flow of jeffrey nanofluid with joule heating," *Journal of Magnetism and Magnetic Materials*, vol. 407, pp. 51–59, 2016.

[189] S Das, T. Pal, R. Jana, and B Giri, "Significance of hall currents on hybrid nano-blood flow through an inclined artery having mild stenosis: Homotopy perturbation approach," *Microvascular Research*, vol. 137, p. 104 192, 2021.

[190] S. I. Abdelsalam and M. Bhatti, "The study of non-newtonian nanofluid with hall and ion slip effects on peristaltically induced motion in a non-uniform channel," *RSC advances*, vol. 8, no. 15, pp. 7904–7915, 2018.

[191] S Das, T. Pal, R. Jana, and B Giri, "Ascendancy of electromagnetic force and hall currents on blood flow carrying cu-au nps in a non-uniform endoscopic annulus having wall slip," *Microvascular Research*, vol. 138, p. 104 191, 2021.

[192] A. Zaman and A. Khan, "Unsteady biomedical investigation of nano-fluid flow via a bent stenosed blood vessel (with aneurysm) using the sisko model," *Waves in Random and Complex Media*, pp. 1–18, 2022.

[193] R Ponalagusamy, R. T. Selvi, and R Padma, "Modeling of pulsatile emhd flow of non-newtonian blood with magnetic particles in a tapered stenosed tube: A comparative study of actual and approximated drag force: Emhd flow of bingham fluid," *The European Physical Journal Plus*, vol. 137, no. 2, p. 230, 2022.

[194] N. S. Akbar, D. Tripathi, and O. A. Bég, "Variable-viscosity thermal hemodynamic slip flow conveying nanoparticles through a permeable-walled composite stenosed artery," *The European Physical Journal Plus*, vol. 132, pp. 1–11, 2017.

List of Publications

The published/communicated work includes:

1. **U. Khanduri**, and B. K. Sharma, Hall and ion slip effects on hybrid nanoparticles (Au-GO/blood) flow through a catheterized stenosed artery with thrombosis, Proceedings of the Institution of Mechanical Engineers, Part C: Journal of Mechanical Engineering Science, vol. 237, no. 10, pp. 2256-2278, 2023.

2. B. K. Sharma, **U. Khanduri**, N. K. Mishra, I. Albaijan, and L.M. Pérez, Entropy generation optimization for the electroosmotic MHD fluid flow over the curved stenosis artery in the presence of thrombosis," Scientific Reports , vol. 13, no.1, pp. 15441, 2023.

3. B. K. Sharma, **U. Khanduri**, N. K. Mishra, and Ali J. Chamkha , "Analysis of Arrhenius activation energy on magnetohydrodynamic gyrotactic microorganism flow through porous medium over an inclined stretching sheet with thermophoresis and Brownian motion." Proceedings of the Institution of Mechanical Engineers, Part E: Journal of Process Mechanical Engineering vol. 237, no. 5, pp. 1900-1914, 2023.

4. **U. Khanduri**, B. K. Sharma, M. Sharma, N. K. Mishra, and N. Saleem, "Sensitivity analysis of electroosmotic magnetohydrodynamics fluid flow through the curved stenosis artery with thrombosis by response surface optimization." Alexandria Engineering Journal vol. 75 , pp. 1-27, 2023.

5. N. K. Mishra, M. Sharma, B. K. Sharma, and **U. Khanduri**, "Soret and Dufour effects on MHD nanofluid flow of blood through a stenosed artery with variable viscosity," International Journal of Modern Physics B, 2350266, 2023.

6. B. K. Sharma, **U. Khanduri**, N. K. Mishra, and K. S. Mekheimer, "Combined effect of thermophoresis and Brownian motion on MHD mixed convective flow over an inclined stretching surface with radiation and chemical reaction," International Journal of Modern Physics B, vol. 37 , no. 10, pp. 2350095, 2023.

7. M. Sharma, B. K. Sharma, and **U. Khanduri**, N. K. Mishra, S. Noeiaghdam, U. Fernandez-Gamiz, "Optimization of heat transfer nanofluid blood flow through a stenosed artery in the presence of Hall effect and hematocrit dependent viscosity," Case Studies in Thermal Engineering, vol no. 47, pp. 103075, 2023.

8. B. K. Sharma, C. Kumawat, **U. Khanduri**, and K. S. Mekheimer, "Numerical investigation of the entropy generation analysis for radiative MHD power-law fluid flow of blood through a curved artery with Hall effect," Waves in Random and Complex Media, pp. 1-38, 2023.

9. R. Gandhi, B. K. Sharma, and **U. Khanduri**, "Electromagnetohydrodynamics Casson pulsatile nanofluid flow through a bifurcated stenosed artery: Magnetically targeted drug delivery," Journal of applied physics, vol. 134 , no. 18, pp. 184701, 2023.

10. **U. Khanduri**, B. K. Sharma, T. Muhammad, and L.M. Pérez, Electroosmotic and gyrotactic microorganisms effects on MHD Al_2O_3-Cu/Blood hybrid nanofluid flow through multi-stenosed bifurcated artery. (Accepted)

11. B. K. Sharma, **U. Khanduri**, R. Gandhi, and T. Muhammad , Entropy Generation Analysis of a Ternary Hybrid Nanofluid (Au-CuO-GO/Blood) Containing Gyrotactic Microorganisms in Bifurcated Artery , vol. 34 No. 2, pp. 980-1020.

12. **U. Khanduri**, and B. K. Sharma , Method of Lines Analysis of Magnetohydrodynamics Two-Phase Nanofluid Blood flow Through Overlapping Stenosed Artery with Activation Energy. (Communicated)

13. B. K. Sharma , **U. Khanduri**, and C. Kumawat, Magnetically targeted drug delivery for two-phase blood flow through composite stenotic artery under the influence of Hall and ion effects using method of line approach. (Communicated)

Conferences/ Workshop Attended

1. Presented the paper with title *"Computational analysis of Al_2O_3-Cu/Blood hybrid nanofluid containing gyrotactic gyrotactic microorganisms through the bifurcated artery"*, **International Conference on Recent Advances in Fluid Mechanics and Nanoelectronics**, Manipal Institute of Technology Bengaluru (July 12-14, 2023)

2. Presented the paper with title *"Mathematical analysis of Hall effect and hematocrit dependent viscosity on Au/GO-blood hybrid nanofluid flow through a stenosed catheterized artery with thrombosis,"* **International Conference On Mathematical Modelling, Applied Analysis And Computation (ICMMAAC-23)**, JECRC University, Jaipur (August 3-5, 2023).

3. Presented the paper with title *"Analysis of MHD mixed convective flow over a stretching surface with radiation, chemical reaction, Thermophoresis and Brownian motion."* in the online national seminar on **"Mathematical Sciences: Repositories of Logical Thoughts and Analytical Tools"**, Department of Mathematics & Statistics, Ch. Charan Singh Haryana Agricultural University, Hisar. (22 Dec 2022)

4. Presented the paper with title *Entropy analysis for MHD flow subject to temperature-dependent viscosity and thermal conductivity*, International Conference on Nonlinear Dynamics and Applications, Sikkim Manipal Institute of Technology, Majitar, East-Sikkim. (9 Mar 2022)

5. Presented the paper with title *"Influence of thermophoresis and Brownian motion on MHD mixed convective flow over an inclined stretching surface in non-Darcian porous medium."* in the three day online international conference on **Recent Advances in Computational Mathematics** & **Engineering**, B K Birla Institute of Engineering and Technology, Pilani. (March 19-21, 2021)

6. Attended the online webinar **"An Introductory Course on Fluid Dynamics"** organized by the Department of Mathematics, CHRIST (Deemed to be University), Bangalore during 17-20 August, and 24-28 August 2020.

7. Participated in the CEP course on **"OpenSource Computational Fluid Dynamics (CFD)"** conducted by IIT Bombay during January 9 - 13, 2023.

Brief Biography of the Candidate

Mr. Umesh Khanduri has been a dedicated full-time research scholar in the Department of Mathematics at BITS Pilani, Pilani Campus, Rajasthan, since January 2020. He earned his Bachelor of Science (B.Sc.) degree in 2014 from PGDAV College, Delhi University, and completed his Master's degree in Mathematics from the same institution in 2016. Subsequently, he pursued his Doctor of Philosophy (Ph.D.) in Biomechanics at Birla Institute of Technology and Sciences Pilani, Pilani Campus, under the supervision of Prof. Bhupendra Kumar Sharma. To his credit, Mr. Khanduri has authored 11 research papers published in esteemed international journals and has presented 2 papers at international conferences.

Brief Biography of the Supervisor

Dr. Bhupendra Kumar Sharma is a Professor & former Head, Department of Mathematics, Birla Institute of Technology and Science, Pilani, (BITS Pilani) Pilani Campus, Rajasthan, India. His research interest includes Heat and Mass Transfer, Arterial Blood Flow, Magnetic Targeting Drug Delivery, Porous Medium, Boundary Layer Theory, Micro-polar Fluid, Differential Equations etc. He has published more than 100 international/national journals of repute, and authored two books on Engineering Mathematics. He is member of editorial board, advisory board of a number of journal of reputes. Prof Sharma is a member of various academic committees of many Institutes/ Universities such as advisory committee, selection committee etc. He has also participated in many conferences and workshops.